FITTING AND PHENOMENOLOGY IN TYPE IA SUPERNOVA COSMOLOGY: GENERALIZED LIKELIHOOD ANALYSES FOR MULTIPLE EVOLVING POPULATIONS AND OBSERVATIONS OF NEAR-INFRARED LIGHTCURVES INCLUDING HOST GALAXY PROPERTIES

by

Kara A. Ponder

B. S. in Physics and Astronomy, University of Georgia, 2012

M. S. in Physics, University of Pittsburgh, 2014

Submitted to the Graduate Faculty of
the Kenneth P. Dietrich School of Arts and Sciences in partial
fulfillment
of the requirements for the degree of

Doctor of Philosophy

University of Pittsburgh

2017

UNIVERSITY OF PITTSBURGH

KENNETH P. DIETRICH SCHOOL OF ARTS AND SCIENCES

This dissertation was presented

by

Kara A. Ponder

It was defended on

July 19th, 2017

and approved by

W. Michael Wood-Vasey, University of Pittsburgh

Andrew Zentner, University of Pittsburgh

Ayres Freitas, University of Pittsburgh

Rachel Mandelbaum, Carnegie Mellon University

Jeffrey Newman, University of Pittsburgh

Dissertation Advisors: W. Michael Wood-Vasey, University of Pittsburgh,

Andrew Zentner, University of Pittsburgh

FITTING AND PHENOMENOLOGY IN TYPE IA SUPERNOVA COSMOLOGY: GENERALIZED LIKELIHOOD ANALYSES FOR MULTIPLE EVOLVING POPULATIONS AND OBSERVATIONS OF NEAR-INFRARED LIGHTCURVES INCLUDING HOST GALAXY PROPERTIES

Kara A. Ponder, PhD

University of Pittsburgh, 2017

In the late 1990s, Type Ia supernovae (SNeIa) led to the discovery that the Universe is expanding at an accelerating rate due to dark energy. Since then, many different tracers of acceleration have been used to characterize dark energy, but the source of cosmic acceleration has remained a mystery. To better understand dark energy, future surveys such as the ground-based Large Synoptic Survey Telescope and the space-based Wide-Field Infrared Survey Telescope will collect thousands of SNeIa to use as a primary dark energy probe. These large surveys will be systematics limited, which makes it imperative for our insight regarding systematics to dramatically increase over the next decade for SNeIa to continue to contribute to precision cosmology. I approach this problem by improving statistical methods in the likelihood analysis and collecting near infrared (NIR) SNeIa with their host galaxies to improve the nearby data set and search for additional systematics.

Using more statistically robust methods to account for systematics within the likelihood function can increase accuracy in cosmological parameters with a minimal precision loss. Though a sample of at least 10,000 SNeIa is necessary to confirm multiple populations of SNeIa, the bias in cosmology is $\sim 2\ \sigma$ with only 2,500 SNeIa. This work focused on an example systematic (host galaxy correlations), but it can be generalized for any systematic that can be represented by a distribution of multiple Gaussians.

The SweetSpot survey gathered 114 low-redshift, NIR SNeIa that will act as a crucial anchor sample for the future high redshift surveys. NIR observations are not as affected by dust contamination, which may lead to increased understanding of systematics seen in optical wavelengths. We obtained spatially resolved spectra for 32 SweetSpot host galaxies to test for local host galaxy correlations. For the first time, we probe global host galaxy correlations with NIR brightnesses from the current literature sample of SNeIa with host galaxy data from publicly available catalogs. We find inconclusive evidence that more massive galaxies host SNeIa that are brighter in the NIR than SNeIa hosted in less massive galaxies.

TABLE OF CONTENTS

LIST OF TABLES

LIST OF FIGURES

1.0 INTRODUCTION

The Universe is vast and dark with only small pockets of shining light that one can observe. Though we cannot see it, the Universe is, in reality, a very crowded place. The light and matter that we see make up a mere 4% of our Universe. 26% comes from a mysterious particle or several particles dubbed “dark matter” as we have only detected its (or their) interactions with normal matter through gravity and not through electromagnetic interactions that would allow us to observe it directly. The rest of the Universe, the other 70%, is an unknown component similarly called “dark energy”. Dark energy is responsible for the accelerated expansion of our Universe; however, we know almost nothing else about it.

This dissertation is focused on how to characterize dark energy using exploding stars referred to as supernovae. I explore improved statistical techniques and examine phenomenological correlations which will lead to improved models for supernova cosmology.

1.1 SUPERNOVA COSMOLOGY

1.1.1 Constraining Dark Energy

Cosmology refers to the study of the origin, evolution, and constituents of the Universe as a whole. One way to probe the evolution of the Universe is by using supernovae in their capacity as standard candles. If one knows the absolute brightness of an object, it can be compared to the observed brightness with the difference between them determining a relative distance. The distance is relative and not absolute because the rate of expansion is not well constrained by this method, but the relative distance provides enough information to resolve the density of dark energy and matter in the Universe.

Distance is affected by the composition and evolution of the Universe. If the Universe were dominated by matter, the gravitational attraction would cause it to contract after its initial expansion. The Universe was expected to be matter dominated since matter was the only thing previously observed by astronomers. However, we found that when we looked at the distant Universe, objects (such as supernovae) appeared fainter and thus farther away from us than expected for a matter dominated Universe. This dimming of distant objects is attributed to a dark energy that is stretching space itself, which is causing objects to recede from each other and thus increasing the relative distance between them.

Not only is dark energy stretching space, but it is doing so at an accelerating rate (Riess et al., 1998; Perlmutter et al., 1999), which means that objects farther away from us are moving away from us at a faster rate than objects closer to us. For example, if there were objects located 1, 2, and 3 Gpc away from Earth, over the same time interval they would move to 2, 4, and 6 Gpc away, respectively. The expansion is homogeneous and isotropic meaning that is happening in every direction and is seen as the same effect everywhere in the Universe, i.e. the object that is 1 Gpc away will see the Earth move to 2 Gpc away in the same time interval. Gravitationally bound objects such as the solar system, the Milky Way, or even the local group of galaxies are not affected by the accelerating expansion.

There are many different theories about what dark energy may be (this discussion based on reviews from Weinberg et al., 2013; Arun et al., 2017; Zhan & Tyson, 2017). The currently accepted theory is that dark energy is Einstein's cosmological constant that is interpreted as an additional energy component of the Universe with the equation of state parameter $w = -1$. Another way to describe dark energy is through the quintessence model (Peebles & Ratra, 1988), which describes it as a field with negative pressure that evolves with time. In this case, the equation of state parameter is limited to $-1 < w < 1$. Quintum dark energy (Huterer & Cooray, 2005; Cai et al., 2010) is also a common way to describe dark energy that evolves with redshift and introduces two new scalar fields that allow w to be greater than -1 but evolve to less than -1. The alternative to framing dark energy as a new component of the Universe is that the theory of gravity is wrong or incompatible at cosmological scales. Dvali-Gabadadze-Porrati (DGP) gravity (Dvali et al., 2000) allows gravity to leak into a fifth dimension and lessen its effect on matter. $f(R)$ gravity (Capozziello & Fang, 2002; Carroll et al., 2004) modifies the Ricci scalar to be a function. Tracing expansion and growth of structure with time can distinguish between these different models; however, some parameterizations of a new energy component and modified gravity may not be discernible.

One way to trace the expansion of the Universe is through the redshift (z). When a photon is emitted from a source and starts traveling towards the Earth, the Universe is expanding around it and causes the photon to lose energy. Redshift is defined as $z = (\lambda_{\text{observed}} - \lambda_{\text{emit}})/\lambda_{\text{emit}}$, which traces the energy lost during travel from the amount of expansion the photon experienced. Galaxies also experience motions relative to other galaxies called peculiar velocities due to gravitational effects. At $z < 0.03$, which corresponds to a recessional velocity of 8990 km/s at a distance of 128 Mpc away[1], peculiar velocities are the dominant source of error in the redshift.

If the absolute luminosity of an object is known, we can track its change in brightness as a function of distance to map the evolution of the Universe through the luminosity distance defined as:

$$d_L^2 = \frac{L}{4\pi F}, \tag{1.1}$$

where L is the luminosity and F is the measured flux. Most observations in astronomy are measured in "magnitudes" where a magnitude is related logarithmically to an object's flux. Expressing the luminosity distance in terms of magnitudes gives the distance modulus (μ):

$$\mu \equiv 5 \log_{10}(d_L/10 \text{ pc}) = m - M, \tag{1.2}$$

where m is the apparent magnitude, which is related logarithmically to the observed flux, and M is the absolute magnitude of an object located 10 pc away, which is related logarithmically to the intrinsic luminosity. The luminosity distance is divided by 10 pc to mirror the absolute magnitude by setting the distance relative to 10 pc away, i.e. the distance modulus would be zero if the object were 10 pc away. This equation is only valid for bolometric luminosities and magnitudes. Section 1.2.2 discusses the additional term that is added to Equation 1.2 for it to be true over different wavelength ranges.

---

[1] Assuming the Hubble constant is 70 km/s/Mpc

Luminosity distance is related to the comoving distance that describes the distance between two objects that stays constant as the Universe expands. We can express the comoving distance and thus the luminosity distance using the Friedmann-Robertson-Walker (FRW) metric with cosmological parameters such as the energy density of matter (baryons plus dark matter) Ω_M, the energy density of dark energy $\Omega_{\rm DE}$, and the equation of state parameter w:

$$d_L(z) = (1+z)\;\chi(z), \tag{1.3}$$

assuming the Universe is flat. $\chi(z)$ is the comoving distance defined as

$$\chi(z) = \frac{c}{H_0}\int_0^z \frac{dz'}{[\Omega_M(1+z')^3 + \Omega_{\rm DE}(1+z')^{3(1+w)}]^{1/2}}, \tag{1.4}$$

where H_0 is the Hubble constant that describes the expansion of the Universe at the present day and c is the speed of light. Equation 1.4 assumes the Universe is homogenous, isotropic, and flat with $\Omega_M + \Omega_{DE} = 1$. Here w is also assumed to be constant; however, one could choose a different functional form to describe dark energy that evolves with redshift. The current best fit cosmology for the Universe corresponds approximately to the ΛCDM model where $\Omega_M \sim 0.3$, $\Omega_{\rm DE}$ is Einstein's cosmological constant (Λ) with $\Omega_\Lambda \sim 0.7$, and $w \sim -1$ (Betoule et al., 2014; Planck Collaboration et al., 2016).

By using Equation 1.3 in Equation 1.2, the observed redshift, the observed flux in magnitudes m, and the absolute luminosity in magnitudes M, we can find the cosmology that best explains the observed data. Figure 1.1 illustrates this by plotting three different models of the Universe on what is called the Hubble diagram (distance modulus versus redshift). The red line is a dark energy-only Universe, the blue line is a matter only Universe, and the black line is the current best-fit cosmology. All of these models assume a flat universe with $w = -1$. If the Universe were matter dominated, we would see distant objects brighter than if the Universe had dark energy. If we can put data points on this plot, we can determine which cosmology corresponds the best to our Universe. This formulation is dependent on an intrinsic luminosity that is constant throughout space and time, which we believe applies to the majority of Type Ia Supernovae (SNeIa).

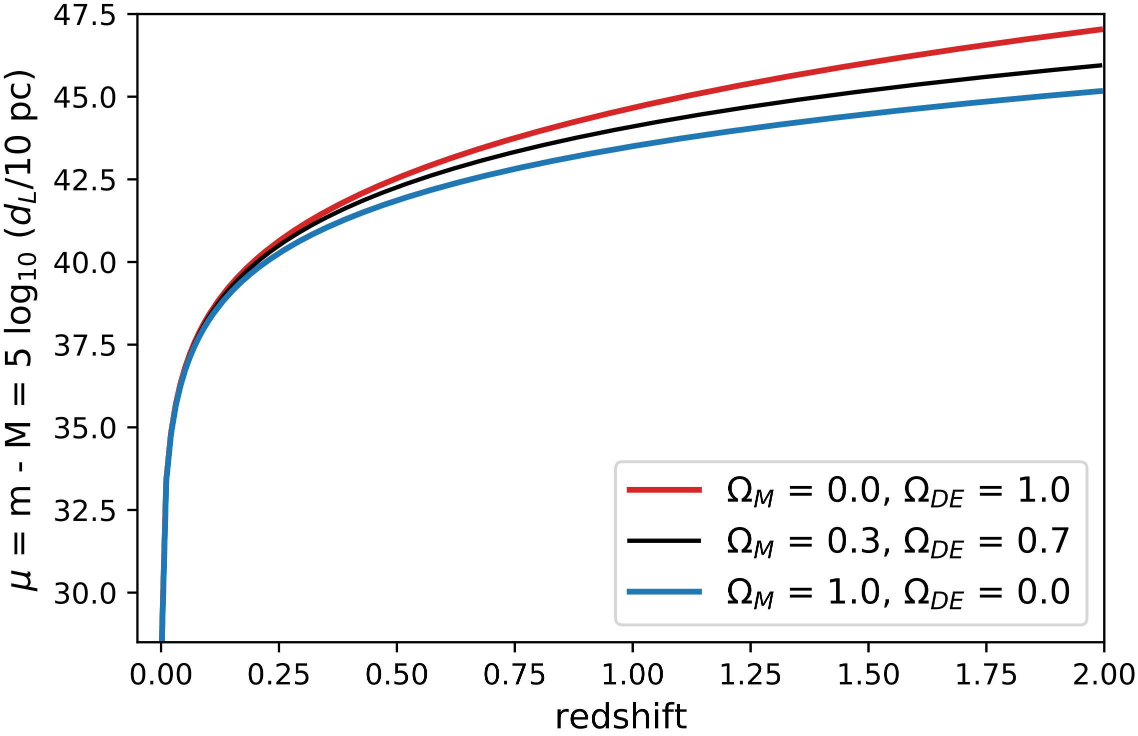

Figure 1.1 Distance modulus versus redshift, commonly referred to as Hubble Diagram. The three lines correspond to 3 different models of the flat Universe. The red line is a Universe consisting of only dark energy, the black line represents the current standard model, and the blue line represents a Universe with only matter. Note that in the magnitude system, lower numbers are brighter.

1.1.2 Supernovae

A supernova is an exceptionally luminous explosion of a star and can be produced by two different mechanisms: core collapse or thermonuclear runaway.

Core-Collapse Supernovae (ccSNe) occur in stars with mass greater than 8 times the mass of our Sun ($M_\odot$) (Carroll & Ostlie, 2006, pgs 529–543). An explosion results when a star can no longer fuse smaller elements into more massive elements to produce energy. Once a star's core consists of iron, fusion stops because iron takes energy to fuse instead of creating it, and the star can no longer counteract the force of gravity such that it collapses in on itself. As the outer layers begin to fall in, they hit the core and are rebounded off causing a massive explosion called a supernova. This release of energy is so large that it can be seen out to ~ 4.5 Gpc [2] away and leaves the core of the star as either a black hole or neutron star depending on its initial mass. The explosion can be identified by its spectrum or by measuring its flux as a function of time (lightcurve). These types of explosions usually exhibit large amounts of hydrogen, though certain types (stripped envelope supernovae) have had their outer layer of hydrogen removed but can still be separated from thermonuclear explosions by their lack of silicon lines. ccSNe can be distinguished by their lightcurve because they do not get as bright as SNeIa and they have a lower decline rate than SNeIa.

Though the explosion is bright, it is not very uniform. ccSNe brightness is dependent on initial mass, which could range from 8–100 $M_\odot$. This variation causes a large intrinsic scatter between the luminosity output from different explosions and makes them poor distance indicators.

The second kind of explosion is referred to as a thermonuclear runaway. A star with a mass less than 8 $M_\odot$ is not hot enough to fuse elements beyond carbon and oxygen after it leaves the main sequence of hydrogen burning; therefore, this star never experiences the explosive end that larger stars do (Carroll & Ostlie, 2006, pgs 457–474). Once it stops fusing hydrogen into helium, the center of the star shrinks and the outer layers expand and cool down. Material falls onto the core causing it to heat up which forms a hydrogen burning shell, then it shrinks and heats up until it starts burning helium. The star briefly burns

---

[2] https://sne.space/sne/SDSS-II%20SN%2020450/

brighter and hotter but slowly loses its outer layers as they float off to become a planetary nebula. Once the core has finished burning the helium into carbon and oxygen, it shrinks until it is held up by electron degeneracy pressure and slowly cools forever (Carroll & Ostlie, 2006, pgs 559–569). These carbon-oxygen white dwarfs (CO WDs) typically form with a mass of 0.42–0.7 $M_\odot$ with a peak around 0.56 $M_\odot$.

CO WDs are the progenitors of type Ia supernovae (SNeIa). From fundamental laws of quantum mechanics (the Heisenberg Uncertainty principle and Pauli exclusion principle), the electron degenerate nature of a WD can only support a mass up to 1.4 $M_\odot$, the Chandrasekhar limit (Carroll & Ostlie, 2006, pgs 569–572). A result of using electron degeneracy pressure to counteract the force of gravity is that the CO WD mass becomes inversely related to its volume such that there is a finite mass that leads to a volume of zero. Once a WD obtains this mass, the electrons become unstable, and electron degeneracy fails. The CO WD then collapses causing the temperature to increase enough to begin carbon fusion which then causes nuclear fusion to propagate throughout the WD in a massive release of energy that has been seen up to $\sim$ 15.8 Gpc (Jones et al., 2013) away. These explosions produce no hydrogen lines but do have a recognizable silicon line in their spectra.

It is because all CO WDs have the same fundamental mass limit that they explode with a similar energy which makes them excellent standard candles. In the 1990s, SNeIa were used in this capacity to discover that our Universe is expanding at an accelerating rate (Riess et al., 1998; Perlmutter et al., 1999).

1.1.2.1 The Progenitor Problem

As outlined in the previous section, there is a fundamental mass limit for CO WDs; however, if they form with a mass $\sim$ 0.6 $M_\odot$, then how does it get additional material? This question has plagued researchers that study SNeIa explosion models and supernova cosmologists alike. No progenitor system has ever been directly observed though multiple scenarios have been suggested.

Up to 50% of stars form in binary systems. When one star dies, the other star can continue to be gravitationally bound to its remnant. The two most popular theories for the SN Ia progenitor system are the Single Degenerate (SD) and the Double Degenerate

(DD) scenarios. The SD scenario supposes that there is a single CO WD and either a main sequence or a red giant branch companion star (Whelan & Iben, 1973), hence one degenerate object. The WD and companion star can be so close together that their gravitational fields are interlocked causing mass from the companion star to overflow onto the surface of the WD (Roche lobe overflow) until the WD reaches the Chandrasekhar limit. This scenario presents multiple problems such as how a WD would increase in total mass when adding matter would first cause small explosions (novae) from nuclear fusion on its surface that would leave the WD with *less* mass. Also, the companion star would not be destroyed in the explosion and should still be observable; however, there has been no concrete evidence that a companion has been found.

The DD scenario occurs when two CO WDs, two degenerate objects, orbit around each other and slowly fall into one another by losing angular momentum through gravitational waves (Webbink, 1984). The smaller WD can be ripped apart and fall onto the surface of the larger WD, or two WDs can directly merge into one "super-massive" ($> 1.4\ M_{\odot}$) WD that will then explode. However, theoretically, these mergers could result in a direct collapse into a neutron star instead of a supernova. Since this explosion leaves nothing behind, astronomers search for super-Chandrasekhar mass objects that are about to explode, but no unambiguous candidates have been found.

Though both SD and DD scenarios present theoretical and observational challenges, in 2015 two papers were published that presented convincing observational evidence for both scenarios. Cao et al. (2015), for the intermediate Palomar Transient Factory (iPTF), observed an SN Ia within four days of the explosion and showed an increase of flux in the ultraviolet (UV) than what is expected from typical explosion models. This extra UV flux is attributed to ejecta from the supernova hitting the companion star. Olling et al. (2015) used the Kepler satellite to observe three SNeIa within a half hour of their explosions and continued to observe them at 30-minute intervals over the next 60 days. They report no additional flux in the lightcurve that is unaccounted for by the supernova explosion and thus no flux from ejecta interacting with a companion star. It is highly likely that at least these two scenarios do form SNeIa. If there are different explosion mechanisms, then it is conceivable that SNeIa may exhibit increased intrinsic variations; i.e., our standard candles are not very standard.

1.2 STANDARDIZING TYPE IA SUPERNOVAE

SNeIa are at their most luminous 15–20 days after the initial explosion and the flux of SNeIa when they are at their brightest is used for cosmology. Since SNeIa must first be discovered but the night sky spans 41,253 square degrees to search through, it is not always possible to observe an SNeIa exactly at peak luminosity. Monitoring an SN Ia many over several weeks make it possible to estimate its apparent magnitudes at the time of maximum light. SNeIa start to dim at the time of the explosion, increase to peak brightness of ~ -19.3 magnitudes in 15–20 days, decline by ~ 3 mags in a month, then steadily decline by 1 magnitude per month until it is no longer visible. In the near infrared (NIR), SNeIa experience a second peak in brightness 20–30 days after the initial peak before they start to fade continuously. Supernovae stay bright enough to be observed for $\sim 1-3$ months. When nuclear fusion is triggered, carbon and oxygen fuse to form ^{56}Ni, which powers supernova lightcurves through the decay chain of ^{56}Ni$\rightarrow$^{56}Co$\rightarrow$^{56}Fe. The second hump in the NIR is from the recombination of cobalt and iron from doubly ionized to singly ionized as the supernova cools (Kasen, 2006).

Large surveys such as the ESSENCE survey (Wood-Vasey et al., 2007; Miknaitis et al., 2007), Lick Observatory Supernova Search (Li et al., 2000; Filippenko et al., 2001), Palomar Transient Factory/intermediate Palomar Transient Factory (Rau et al., 2009), Panoramic Survey Telescope and Rapid Response System (Pan-STARRS; Rest et al., 2014; Scolnic et al., 2014), Sloan Digital Sky Survey II Supernova Search (Frieman et al., 2008; Sako et al., 2014), and SuperNova Legacy Survey (Astier et al., 2006; Guy et al., 2010) have all made use of sky searches that can return to the same patch of sky within a week in order to find any object that has changed. They continue to observe the same areas of the sky every few days to gather large samples of lightcurves. The latest survey, Pan-STARRS, observed 70 square degrees on the sky every 3 nights for 4 years and gathered ~ 1000 SNeIa though not all are spectroscopically confirmed (Jones et al., 2017).

The observations of the SNeIa are then compared with templates of lightcurves previously collected to determine the time and apparent magnitude at peak brightness. At this point, the scatter in peak brightness is roughly 0.6 magnitudes. Two lightcurve correlations help to decrease this scatter: stretch- and color-corrections. Phillips (1993) showed that brighter SNeIa take longer to fade than dimmer SNeIa ("brighter-broader" effect). This correlation uses the full lightcurve information to measure the stretch. To further standardize the lightcurves, Riess et al. (1996) and Tripp (1998) showed that bright SNeIa were also bluer than dimmer SNeIa ("brighter-bluer" effect). By applying these two empirical correlations, the scatter in the peak brightness of the lightcurves was reduced to 0.15 mag, which corresponds to an error in distance of only $\sim 7\%$.

After these two corrections have been applied, there is evidence that more correlations may be impacting the scatter of the distribution. Many papers have explored how the stretch- and color-corrected luminosities may be correlated with different host galaxy properties (Sullivan et al., 2006; Gallagher et al., 2008; Kelly et al., 2010; Sullivan et al., 2010; Lampeitl et al., 2010; Gupta et al., 2011; D'Andrea et al., 2011; Hayden et al., 2013; Johansson et al., 2013; Childress et al., 2013a,b; Rigault et al., 2013; Pan et al., 2014; Kim et al., 2014; Rigault et al., 2015; Kelly et al., 2015; Jones et al., 2015; Moreno-Raya et al., 2016; Wolf et al., 2016; Campbell et al., 2016; Roman et al., 2017). The most statistically significant trend found has been with host galaxy mass (e.g., Sullivan et al., 2010; Johansson et al., 2013; Campbell et al., 2016). It is best parameterized by a step function (Childress et al., 2013b) and indicates that SNeIa exploding in galaxies with mass $> 10^{10}\ M_\odot$ are brighter than SNeIa hosted in less massive galaxies by ~ 0.1 mag. Most likely this trend is reflecting a more fundamental property such as metallicity (Hayden et al., 2013), but this is still an active area of investigation. It has also been shown that the brightness is more correlated with properties within 1–2 kpc of the supernova explosion site than with global characteristics (Rigault et al., 2013, 2015). Much research supports some correlation with host galaxy properties, but some claim this is an error on the human side of the analysis with insufficient lightcurve fitters (Kim et al., 2014) or inconsistent sample cuts (Jones et al., 2015).

The addition of lightcurve and host galaxy corrections may create a more precise distance indicator, but they also serve to obfuscate what is truly being used for cosmological analyses. For example, both interceding dust from the supernova host galaxy and the intrinsic color differences between SNeIa cause the "brighter-bluer" effect; however, most analyses do not distinguish between these two properties. (Guy et al., 2007, 2010; Betoule et al., 2014; Rest et al., 2014).

1.2.1 SNeIa in the NIR: The true standard candles?

The stretch and color corrections are undoubtedly useful when observing optical lightcurves; however, NIR lightcurves ($0.8 < \lambda < 2.2$ μm) do not need these corrections to produce a scatter of only 0.15–0.2 mag (Kasen, 2006; Folatelli et al., 2010; Kattner et al., 2012; Wood-Vasey et al., 2008; Barone-Nugent et al., 2012). Being able to use the apparent magnitude instead of a corrected magnitude reduces the systematics introduced in the analysis such as the distinction between intrinsic color and dust since dust does not affect the NIR. Theoretical evidence from Kasen (2006) shows that the first peak in the NIR, and especially the H-band centered at $\lambda = 1.6$ μm, is less sensitive to initial ^{56}Ni mass and progenitor metallicity. There is some evidence that applying a stretch or decline rate parameter will improve precision in fitting for a lightcurve template, but no correlation between stretch and NIR brightness has been found (Kattner et al., 2012; Burns et al., 2014). No studies of correlations between host galaxy properties have been conducted with NIR lightcurves. To test for these possible correlations, more NIR SNeIa need to be gathered to increase the current public data set, which is ~ 200 SNeIa. With the dedicated surveys currently running in the NIR such as Carnegie Supernova Project (Contreras et al., 2010; Stritzinger et al., 2011; Kattner et al., 2012) and SweetSpot (Weyant et al., 2014, 2017), we will be able to further explore these possible natural standard candles to a greater extent.

1.2.2 K-corrections

K-corrections are necessary for any observation to transform the flux from observer frame to restframe and allows the comparison of nearby to distant objects (Oke & Sandage, 1968; Hogg et al., 2002). As one looks further into the Universe, the light from astronomical objects is experiencing more expansion causing the redshift to increase – meaning that the light shifts into redder wavelengths. A supernova or galaxy that may be bright at optical wavelengths in the nearby Universe may appear dim in optical wavelengths at higher redshifts but bright in the infrared. K-corrections are used for photometric observations to account for the flux shifted out of or into a particular filter utilizing the spectral energy distribution (SED) and redshift of an object. It provides an additional term to the distance modulus ($\mu = m - M - K$) to shift the observed magnitude to the restframe magnitude. However, the K-correction is highly dependent on the validity of the SED for an object. SNeIa at optical wavelengths have been studied in depth and have robust templates (Kim et al., 1996; Nugent et al., 2002; Hsiao et al., 2007). In the NIR, this correction needs more research and more well-observed SEDs. The latest publicly available templates are from Hsiao et al. (2007) with other studies utilizing their unpublished templates (e.g., Stanishev et al., 2015). K-corrections must be applied to SN Ia lightcurves so that SNeIa at varying redshifts can be compared and used for cosmological analyses.

1.3 FUTURE IN LARGE SURVEYS

The future of SNeIa cosmology lies in large, wide-field surveys. The Large Synoptic Survey Telescope (LSST, LSST Science Collaboration et al., 2009) will conduct a wide, fast, and deep 10-year survey that can record the entire observable night sky in the Southern Hemisphere every 4 days. LSST will observe at least 10,000 well-sampled SNeIa, 100,000 decently sampled SNeIa, and over 1 million SNeIa detected in *ugrizy* bands, which span wavelengths of $\sim 0.350 - 1.060 \mu$m. This telescope is currently being built in Chile, will have first light in 2020, and will begin full survey operations in 2023. This ground based telescope will focus on the night sky in optical wavelengths whereas an upcoming space-based telescope, the Wide-Field Infrared Survey Telescope (WFIRST, Spergel et al., 2015), will observe the night sky at NIR wavelengths. WFIRST is focused on cosmology and exoplanets while LSST will be optimized to observe asteroids, dark energy probes, the Milky Way, and transients. The WFIRST satellite is planned to launch in the mid-2020s with operations soon to follow. It is expected to collect roughly 2,500 high redshift SNeIa with filters that range in wavelengths of $0.76 - 2.0$ μm. Both of these surveys will be operational by the mid to late 2020s, so the time to prepare for them is now.

SN Ia cosmology has not been limited by statistical error for ~ 10 years. The only way to improve the precision of cosmological parameters derived using these large data sets is to understand the remaining systematics. Systematics are errors and biases that cannot be removed by adding more SNeIa and reflect technical challenges or a lack of understanding in astrophysical processes.

A few of the current dominant systematics include flux calibration, Milky Way dust, selection bias, and host galaxy correlations (Conley et al., 2011; Scolnic et al., 2014; Betoule et al., 2014). The largest systematic today is that of flux calibration and calibration between observational surveys. This systematic is being addressed by building better telescopes/detectors and having large teams design better algorithms to reduce the data. With the upcoming large surveys, it will be possible to use only one survey for the high redshift sample to do precision cosmology thus reducing one of the primary sources of error. Dust from the Milky Way causes a 10% correlated uncertainty in all reddening corrections from converting the dust column density to extinction (Conley et al., 2011); however, large NIR surveys would circumvent this problem as the NIR is unaffected by dust. The correction for selection bias, including Malmquist bias (Malmquist, 1936), is dependent on observing strategy and changes based on the survey or even the individual running the telescope on a given night. This bias is estimated for large surveys by assuming targets are randomly selected. Smaller surveys used as low redshift anchors will produce higher errors from selection biases due to low number statistics and more significant variations in observing. Finally, the systematic focused on in this thesis is host galaxy correlations, which could potentially affect every sample of SNeIa. In the literature, host galaxy correlations have best been parameterized by a step function, but this model is not astrophysically motivated. More SNeIa with a variety of host galaxy properties measured are needed to create better models to understand and correct for this bias.

WFIRST will additionally be constrained because the low redshift, restframe NIR sample of SNeIa is much smaller than the optical sample of SNeIa. Higher redshift SNeIa probe different dark energy models more effectively, but low-redshift SNeIa are crucial to anchor the Hubble diagram. Having a smaller low-redshift sample would result in increased errors on dark energy constraints.

1.4 DISSERTATION OVERVIEW

This dissertation presents several efforts to prepare for the future large scale surveys through improved statistical techniques, new observations, and phenomenological studies. To begin, I develop a framework to more robustly determine cosmological parameters and add astrophysical models directly to the analysis. I then update the status of the SweetSpot survey, which aimed to gather a larger sample of low redshift NIR SNeIa. I begin to explore correlations between local and global host galaxy properties and NIR SNeIa with spectroscopic observations and catalogs of publicly available data. A summary of each chapter is presented below.

In Chapter 2, we present a Bayesian analysis for determining cosmological parameters. This framework incorporates the full distribution of the SN Ia population that would be necessary if the distribution was non-Gaussian. Previous analyses have assumed that the underlying probability density function of the luminosity of SNeIa is Gaussian, which reduces the computational difficulty of fitting for dark energy. However, if the fundamental distribution of SNeIa is not a single Gaussian, then additional biases are being added to cosmology. We explore the consequences of having multiple populations of SNeIa expressed through a Gaussian Mixture Model (GMM). Empirical findings expressed in host galaxy correlations and several possible progenitor systems suggests that there may be more than one population of SNeIa. We find that even though multiple populations may bias the cosmological parameters, the existence and characteristics of a non-Gaussian distribution may not be constrained. We would need 10,000 SNeIa to statistically confirm a GMM distribution with a difference in luminosity of 0.1 magnitude, but the cosmology will be noticeably biased with only 2,500 SNeIa. This chapter was published in the Astrophysical Journal in 2016 (Ponder et al., 2016).

I outline my observational work in Chapter 3. Since 2014 I have been the lead graduate student for the SweetSpot survey that was introduced by Weyant et al. (2014). This survey collected 114 SNeIa over 88 nights in 3 years to expand the NIR data set in the nearby smooth Hubble Flow ($0.03 < z < 0.08$). These SNeIa will be instrumental in exploring the standard nature of SNeIa in NIR and providing a well-calibrated restframe data set. To study local host galaxy properties in the NIR, I observed 32 galaxies that previously hosted SweetSpot supernovae with an integral field unit (IFU) that yields spatially resolved spectra. I continue in Chapter 3 to outline the observations, data reductions, and some results from these spectra.

Chapter 4 uses publicly available galaxy photometry to search for global host galaxy correlations with NIR brightnesses for the first time. We used optical photometry of galaxies that hosted SNeIa from the Sloan Digital Sky Survey (SDSS; SDSS Collaboration et al., 2016) and the Panoramic Survey Telescope and Rapid Response System (Pan-STARRS; Chambers et al., 2016; Flewelling et al., 2016; Magnier et al., 2016) with supporting NIR data from the Two Micron All-Sky Survey (2MASS; Skrutskie et al., 2006) and UV data from the Galaxy Evolution Explorer[3] (GALEX). We explore correlations between host galaxy mass, restframe $g-r$ color, and absolute r band magnitude and both NIR brightnesses and optical brightnesses that correspond to our NIR data set. We confirm the ~ 0.1 mag host galaxy mass step at $10^{10} M_{\odot}$ with the standardized brightness of optical SNeIa with the SNooPy fitter, but only find conclusive evidence for a correlation with H-band brightness. However, our sample contains an outlier population of NIR bright SNeIa in the nearby smooth Hubble flow that are hosted by massive ($> 10^{10} M_{\odot}$), red ($g-r > 0.6$ mag), and bright ($M_r < 21.0$ mag) galaxies. I summarize my results and conclusion in Chapter 5.

---

[3] `http://galex.stsci.edu/GR6/`

2.0 INCORPORATING ASTROPHYSICAL SYSTEMATICS INTO A GENERALIZED LIKELIHOOD FOR COSMOLOGY WITH TYPE IA SUPERNOVAE

This chapter was published in the Astrophysical Journal in July 2016 and was authored by K.A.P, W. Michael Wood-Vasey, and Andrew R. Zentner (Ponder et al., 2016).

Traditional cosmological inference using Type Ia supernovae (SNeIa) have used stretch- and color-corrected fits of SN Ia light curves and assumed a resulting fiducial mean and symmetric intrinsic dispersion for the resulting relative luminosity. As systematics become the main contributors to the error budget, it has become imperative to expand supernova cosmology analyses to include a more general likelihood to model systematics to remove biases with losses in precision. To illustrate an example likelihood analysis, we use a simple model of two populations with a relative luminosity shift, independent intrinsic dispersions, and linear redshift evolution of the relative fraction of each population. Treating observationally viable two-population mock data using a one-population model results in an inferred dark energy equation of state parameter w that is biased by roughly 2 times its statistical error for a sample of N $\gtrsim$ 2500 SNeIa. Modeling the two-population data with a two-population model removes this bias at a cost of an approximately $\sim$ 20% increase in the statistical constraint on w. These significant biases can be realized even if the support for two underlying SNeIa populations, in the form of model selection criteria, is inconclusive. With the current observationally-estimated difference in the two proposed populations, a sample of N $\gtrsim$10,000 SNeIa is necessary to yield conclusive evidence of two populations.

2.1 INTRODUCTION

Type Ia supernovae (SNeIa) are excellent standardizable candles that enabled the discovery of the expansion of the Universe in the late 1990s by Riess et al. (1998) and Perlmutter et al. (1999). Originally, SNeIa were used as standard candles from empirical evidence with a scatter of only ∼0.3 magnitudes (Baade, 1938; Kowal, 1968). As data sets grew, patterns appeared in the light curves yielding the brighter-slower (Phillips, 1993) and brighter-bluer (Riess et al., 1996; Tripp, 1998) relationships, which standardized the supernovae further by reducing their scatter down to ∼ 0.15 magnitudes.

The goal of this paper is to create a framework to properly model effects that change the *distribution* of expected SN Ia apparent brightness at each redshift. If unmodeled, these effects lead to systematic biases in cosmological inference. We propose using general and flexible likelihood functions that have the ability to handle insufficiently modeled systematics. As an example, we simulate a simplistic toy model of two SN Ia populations with a small relative shift in absolute magnitude. The relative rate of these two populations changes linearly with redshift. We examine the systematic errors in cosmological parameters caused by incorrectly fitting multiple populations with a single Gaussian model and show that these errors can be eliminated by using a multiple population model to fit the SN Ia magnitude–redshift relation. In this paper, we focus on this toy model to demonstrate the validity of this framework. The consideration of more complex multiple-population models or other astrophysical or observational effects that lead to shifting magnitude distributions with redshift will be considered in subsequent papers.

Though the two population model is intended as an example, there are several motivators for multiple populations of SNeIa. For instance, after adjusting the light curves with these observed relationships, there is still an unaccounted for feature in the corrected brightness residual with respect to the distance-redshift relationship (Hubble residual) that appears to be correlated with host galaxy properties. In the last five years, there have been myriad studies (Kelly et al., 2010; Sullivan et al., 2010; Lampeitl et al., 2010; Gupta et al., 2011; Johansson et al., 2013; Childress et al., 2013b; Rigault et al., 2013, 2015; Kelly et al., 2015) comparing host galaxy mass, metallicity, and/or star formation rate to residuals in the Hubble diagram. Rigault et al. (2013) examined the relationship between global and local star formation rates through H-alpha and found that SNeIa in locally passive environments were brighter than those in locally star forming environments. Rigault et al. (2015) and Kelly et al. (2015) used *GALEX* ultraviolet observations and confirmed this correlation between Hubble residual and local star-formation rate.

It is possible that the host galaxy correlations are caused by something more fundamental such as the nature of the progenitor. Though the evidence for host galaxy correlations may be controversial (Jones et al., 2015), there is increasing evidence that there are two different progenitor channels that could create a multiple population effect (Greggio, 2005; Cao et al., 2015; Olling et al., 2015).

The most recent analysis of SNeIa for cosmology comes from Betoule et al. (2014) with the Joint Lightcurve Analysis (JLA). They account for the observed correlation between Hubble residual and host galaxy mass by creating a step function for the absolute magnitude of each supernova based on the host galaxy mass. They then implicitly assume a Gaussian likelihood and fit for parameters using a χ^2 method. We will expand this method by defining a continuous function for absolute magnitude and finding the most probable parameter regions with a generalized likelihood through Markov Chain Monte Carlo (MCMC) techniques.

Being able to identify and accurately correct for systematics is becoming more important as the number of SNeIa drastically increases with current surveys such as Dark Energy Survey (DES)[1], Panoramic Survey Telescope and Rapid Response System (Pan-STARRS, Scolnic et al., 2014; Rest et al., 2014). The amount of SN Ia data available for cosmological analyses will continue to increase into the future with surveys such as the Large Synoptic Survey Telescope (LSST, LSST Science Collaboration et al., 2009), Wide-Field Infrared Survey Telescope-Astrophysics Focused Telescope Asset (WFIRST-AFTA, Spergel et al., 2015), and the European Space Agency's Euclid[2] mission on the horizon (Astier et al., 2014). Supernova cosmology is no longer statistically limited and is rapidly becoming systematically limited. Now is the time to explore different avenues for undertaking unbiased cosmological

---

[1] `http://www.darkenergysurvey.org/`

[2] `http://sci.esa.int/euclid/`

analyses with large data sets.

In Section 2.2 we discuss non-Gaussian error distributions as modeled by multiple Gaussian populations. Section 2.3 defines how mock SN Ia data sets are generated. Here, we introduce a toy model that represents a redshift evolution of the populations to probe uses of the framework. In Section 2.4 we define the likelihood to be used in the MCMC and the different model selection techniques. Section 2.5 shows that both population and cosmological parameters are biased if multiple populations are not included in the analysis. Though it has more model parameters, the Gaussian mixture model recovers input cosmology with only a $\sim 1-3\%$ loss in precision. We show that current and future data sets will have the cosmology biased before there are enough statistics to characterize the underlying systematic or to robustly require a more complicated model. Section 2.6 discusses how the models presented here relate to current cosmological analyses and presents possible astrophysical motivations for multiple populations. In Section 2.7 we summarize our results and discuss ways to improve and expand this framework.

2.2 NON-GAUSSIAN ERROR DISTRIBUTIONS

The most commonly used method for cosmological parameter estimation in supernova cosmology is χ^2 minimization. Implicit in this method is the assumption that the overall probability density function (PDF) of supernovae follows a Gaussian distribution or can be linearly corrected to do so. With motivations such as the host galaxy correlations, complexities in the analysis from Malmquist bias, and uncertainties about dust, there are too many unknowns within supernova cosmology for SNeIa to be adequately described by a single point estimator in a Gaussian PDF. The PDF of SNeIa needs to be expanded to be able to more fully model the systematic effects underlying the observed luminosity distribution of SNeIa.

Here we will explore one possible expansion to the PDF of SNIa luminosity. While this example is inspired by the recent discussions of correlations between SNIa corrected luminosity and host galaxy properties, its use here is intended as a demonstration of the framework.

We are not arguing for any particular specific model as being representative of the SNIa population extant in the Universe.

2.2.1 Gaussian Mixture Models

Karl Pearson popularized using multiple Gaussians to describe non-Gaussian data in 1894 when he showed that two Gaussians were a better fit to crab morphologies which strengthened the claim for evolution (Pearson, 1894).[3]

A distribution consisting of multiple Gaussian populations with different peaks and/or dispersions is referred to as a Gaussian mixture model (GMM) and the probability density function (PDF) that describes it is

$$p_{\mathrm{GMM}}(x) = \sum_{j=1}^{\mathcal{N}} \frac{n_j}{\sqrt{2\pi\sigma_j^2}} \exp\left(\frac{-(x-\lambda_j)^2}{2\sigma_j^2}\right) \tag{2.1}$$

where $\mathcal{N}$ is the number of populations; and for each population j: n_j is the relative normalization $\left(\sum_{j=1}^{\mathcal{N}} n_j = 1\right)$; λ_j is the mean; and σ_j is the standard deviation.

For the sake of simplicity and because it is motivated by current observational literature, in this paper we focus on a model with only two populations: A and B. Under this model Eq. 2.1 then becomes

$$\begin{aligned} p_{\mathrm{GMM}}(x) \quad = \quad & \frac{n_A}{\sqrt{2\pi\sigma_A^2}} \exp\left(\frac{-(x-\lambda_A)^2}{2\sigma_A^2}\right) + \\ & \frac{n_B}{\sqrt{2\pi\sigma_B^2}} \exp\left(\frac{-(x-\lambda_B)^2}{2\sigma_B^2}\right). \end{aligned} \tag{2.2}$$

There are five parameters that need to be specified: λ_A, λ_B, σ_A, σ_B, and n_A (n_B is implicitly specified under the constraint that $n_A + n_B = 1$). Once the PDF has been defined, the log-likelihood function for the two-population model, $\mathcal{L}$, is simply

$$\begin{aligned} \mathcal{L} = \ln L = \sum_{i=1}^{N} \ln \Bigg[\quad & \tfrac{n_A}{\sqrt{2\pi\sigma_A^2}} \exp\left(\tfrac{-(x_i-\lambda_A)^2}{2\sigma_A^2}\right) + \\ & \tfrac{n_B}{\sqrt{2\pi\sigma_B^2}} \exp\left(\tfrac{-(x_i-\lambda_B)^2}{2\sigma_B^2}\right) \Bigg], \end{aligned} \tag{2.3}$$

---

[3] Thanks to S. Peng Oh for this reference.

where N is the total number of objects included in the analysis, x_i is some observed quantity per object, and (λ_A, σ_A), (λ_B, σ_B) are the model mean and standard deviation for the populations A and B.

In the case of SN Ia cosmology, x_i is the observed width-color-corrected apparent magnitude of supernovae, and (λ_A, σ_A), (λ_B, σ_B) would correspond to models of two different SN Ia populations with different absolute magnitudes and intrinsic dispersions, each propagated through the same cosmological model for the luminosity distance modulus.

2.3 GENERATING MOCK DATA SETS

We begin exploring a two-population GMM for SNeIa by generating a sample of mock SN Ia data sets from Eq. 2.2. We represent the difference in the two populations as a difference in absolute magnitude M_X for $X = A$ or B populations. The parameters in Eq. 2.2 can thus be redefined as: $\lambda_A \to M_A$, $\lambda_B \to M_B$. While we will discuss absolute magnitude distributions in this section in order to emphasize the different populations, later we will consider fitting the mock data as "observed" apparent magnitudes. We define the relative mean magnitude shift between the populations such that $\Delta M \equiv M_A - M_B$ and re-parameterize M_B in terms of M_A and ΔM as $M_B = M_A - \Delta M$. The relative magnitude difference ΔM is thus applicable to either absolute or apparent magnitude, and the overall normalization of the absolute magnitude – which is generally marginalized over – is absorbed into one term for both populations. The variance of each population (σ_X^2) is defined as $\sigma_X^2 = \sigma_{\text{int},X}^2 + \sigma_{\text{phot}}^2$ including the intrinsic dispersion of the population $\sigma_{\text{int},X}$ and the dispersion introduced from observational errors σ_{phot}.

Figure 2.1 illustrates graphically the five parameters of our two-population GMM: M_A, ΔM, σ_A, σ_B, and n_A and the two parameters of a single-Gaussian model (SGM): M and σ fit to the GMM-generated data. For visual clarity, this example has $n_A = 0.7$ and shows an extreme shift of $\Delta M = 1.0$ mag. We expect realistic models to be on the order of $\Delta M \lesssim 0.1$ mag.

We simulate mock data sets assuming the peaks of the populations average to the

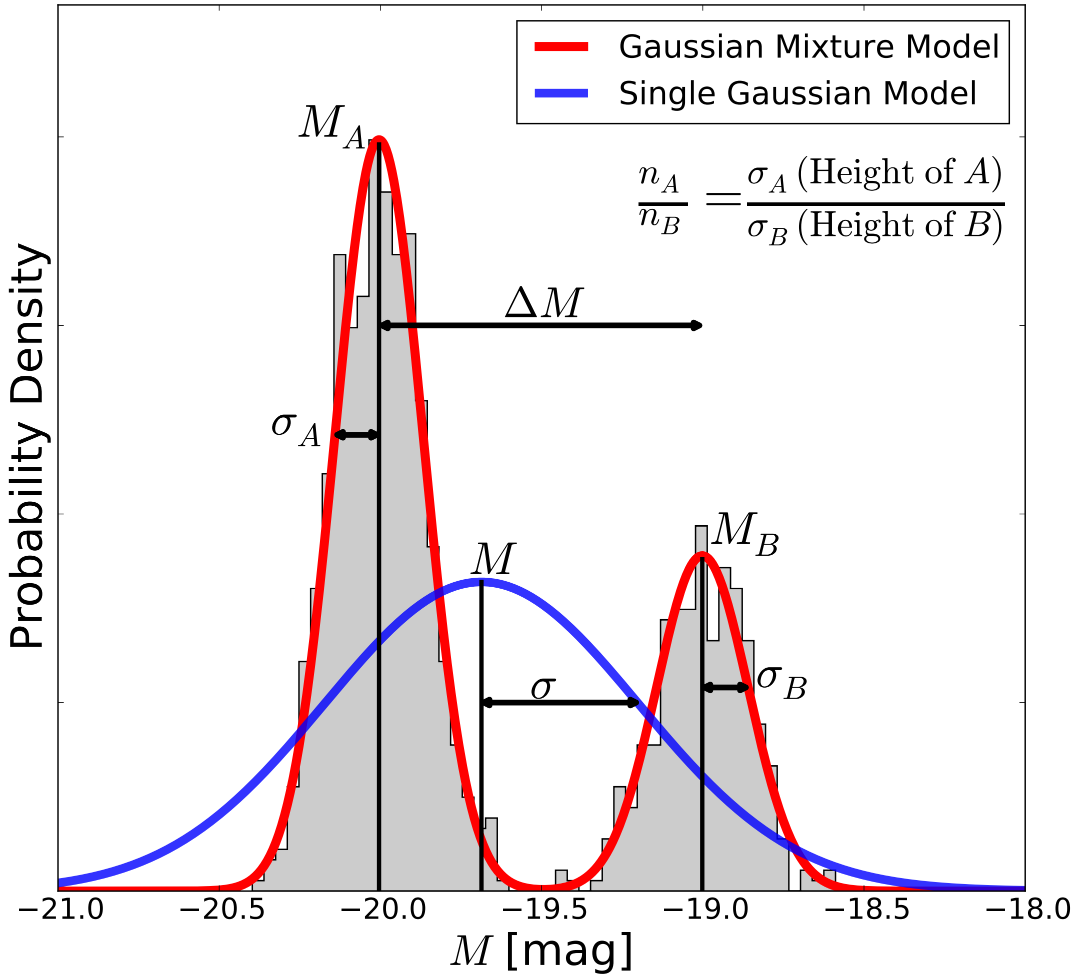

Figure 2.1 A histogram of mock supernovae with two populations are shown in grey and fit with a GMM and SGM. M and σ are the peak and dispersion from a SGM. The GMM model includes the location of both peaks, M_A and M_B, and the dispersion of both populations, σ_A and σ_B. ΔM is the different between M_A and M_B in magnitudes. The relative number of SNeIa in each population is n_A/n_B (where $n_A + n_B = 1$). In this example, $\Delta M = 1.0$ mag and $n_A = 0.7$.

estimated value of M such that $(M_A + M_B)/2 = -19.5$ mag with intrinsic dispersions of $\sigma_{\mathrm{int},X} = 0.1$ mag and $\sigma_{\mathrm{phot}} = 0.1$ mag for both populations. σ_{phot} was chosen to reflect the observational error that JLA achieved (~ 0.115 mag). The supernovae are constrained to a redshift range of $0.05 < z < 1.5$ to cover the low redshift anchors and the high redshift cosmology probes.

Because host galaxy properties are on average different at $z \sim 0$ and $z \sim 1$, it becomes sensible to explore the possibility of redshift evolution between the relative number of SNeIa in each population. As a toy model we simulate a redshift dependence of the relative normalizations by having the populations evolve linearly in redshift: $n_A = n'_{A,0}z + n_{A,0}$. Where $n_{A,0}$ is $n_A(z)$ evaluated at $z = 0$ and $n'_{A,0}$ is the first derivative of $n_A(z)$ evaluated at $z = 0$. We then impose boundary conditions such that the total population of supernova is dominated by a single population at the lowest redshift $n_A(z_{\mathrm{min}} = 0.05) = 1$ and the other population dominates the total population at the highest redshift $n_A(z_{\mathrm{max}} = 1.5) = 0$ to get $n_{A,0} = 1.003$ (no units) and $n'_{A,0} = -0.627$ in units of 1/redshift. The two populations have an equal number of supernovae at $z = 0.775$ as set by the slope and intercept of $n_A(z)$. This value is derived only from relative normalizations and is independent of other supernova population parameters.

A linear evolution with redshift is an overly simplistic model. The evolution of multiple populations or other astrophysical systematics will likely be a smooth, potentially monotonic, function of redshift. While a power law or logarithmic function might suggest itself as a good model for a variety of phenomena, a linear dependence is at least a reasonable description of a function for which we have a strong bias that should be varying slowly. As such, it is informative to explore a linear model, which is likely to capture a significant amount of the overall trend of the true astrophysical systematics. In Greggio et al. (2008), Figure 7 (top panel) shows the relative rates of the single degenerate channel versus double degenerate channels as a function of redshift. These are clear parallels to our relative population parameters, and one of the models shows a linear trend. The modeling of SNeIa progenitors is still incomplete and different models can provide drastically different rates. The GMM does not rely on a linear model for the evolution of the relative populations and can easily be constructed with different forms such as a power law or logarithmic function.

We randomly draw a redshift from a uniform distribution in the range $0.05 < z < 1.5$, then generate a GMM PDF corresponding to that redshift, and randomly draw an absolute magnitude from that PDF.

Figure 2.2 illustrates how the absolute magnitude distribution of SNeIa evolves with redshift for two different ΔMs. While the redshift evolution is a small effect for small ΔM, the shift between different populations becomes understandably more clear when $\Delta M = 0.5$ mag.

We generate 108 different data sets with a range of number of supernovae in each set: $N = 100,\ 1000,\ 2500,\ 10000$ and a range of shifts between the two supernovae populations: $\Delta M = 0.0,\ 0.01,\ 0.02,\ 0.05,\ 0.1,\ 0.2,\ 0.3,\ 0.4,\ 0.5$ mag. Each permutation of N with ΔM is performed three times to help average over random fluctuations in the data sets. The number of supernovae correspond to a small sample, the order of current data sets (1000), and the expected yields from WFIRST-AFTA (2500) and LSST $(10,000)$.[4] $\Delta M = 0.0$ mag is consistent with a single Gaussian population while $\Delta M = 0.1$ mag is close to the number quoted from Rigault et al. (2015) for the difference in brightness between supernovae located in active versus passive local environments. Though this framework is discussed with a specific systematic as an example motivation, it is general and can be applied to any systematic that can be described by an effective distribution in the likelihood.

In order to use apparent magnitudes instead of absolute magnitude, we add the cosmological distance modulus $\mu(z; \Omega_M, w)$ to produce an apparent magnitude (m). We chose our default cosmology to be that of WMAP9 with $\Omega_M = 0.2865$, $\Omega_L = 0.7134$, $w = -1$, $H_0 = 69.32$ km Mpc^{-1} s^{-1} (Hinshaw et al., 2013). We do not simulate a distribution of stretch and color or the resulting correction process. This process is thus rather generically applicable to any luminosity distance indicator with no particular restriction to SNeIa beyond the parameters chosen for the GMM.

In the present work, we also neglect the effects of gravitational lensing on SN Ia analyses. Though the dispersion induced by lensing may be non-negligible in forthcoming analyses (Zentner & Bhattacharya, 2009), lensing does not shift the average brightness (setting aside observational selection effects for the moment) and is unlikely to bias cosmological results

---

[4] Current estimates of cosmologically useful SNeIa from LSST range from 10,000s to 100,000. We have chosen a very conservative value here.

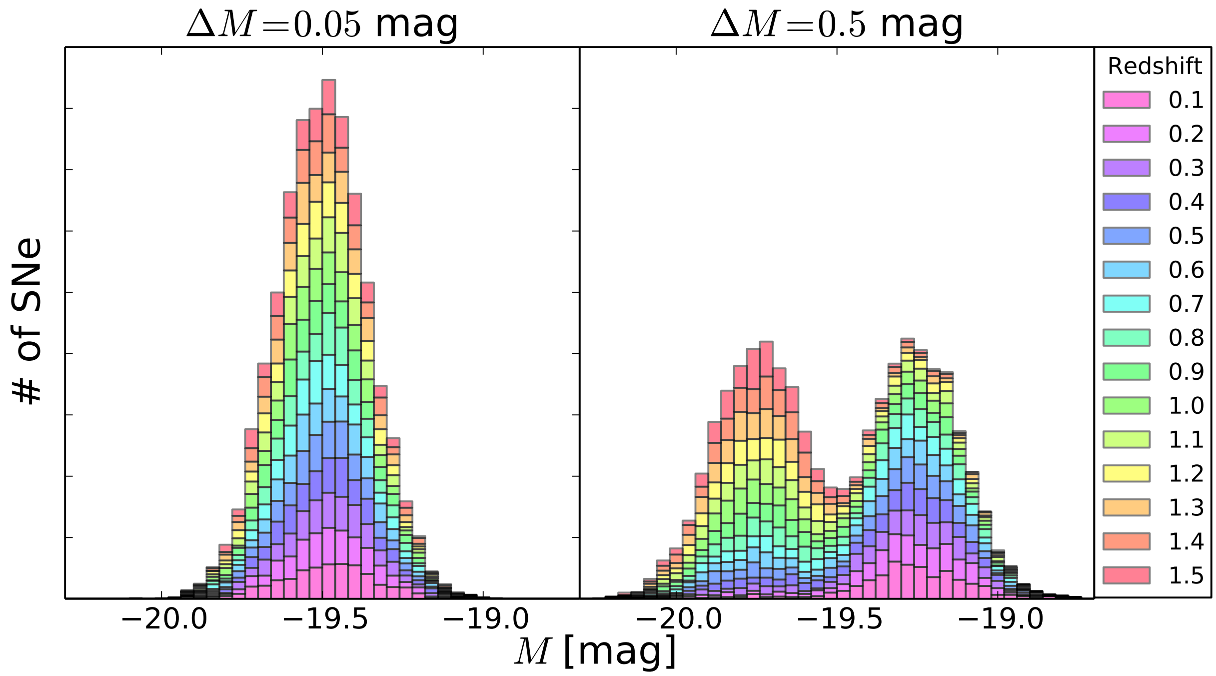

Figure 2.2 Absolute magnitude distribution of 10,000 mock SNeIa separated into 15 redshift bins denoted by color. A histogram is generated at each redshift then stacked upon the previous redshift's histogram. *Left:* A small separation of $\Delta M = 0.05$ mag is a subtle shift. *Right:* A exaggerated separation of $\Delta M = 0.5$ mag makes the evolution visually obvious.

(Helbig, 2015). We defer a more complex analysis including lensing to future work.

2.4 METHODS

2.4.1 Markov Chain Monte Carlo

We use standard Markov Chain Monte Carlo (MCMC; Metropolis et al., 1953) techniques to fit for model parameters. In particular, we utilize the affine-invariant ensemble sampler from Goodman & Weare (2010) and implemented in `python` with `emcee` (Foreman-Mackey et al., 2013). We test the convergence of our chains by checking that the autocorrelation of points sampled from the posterior approaches zero for large lags (Box & Jenkins, 1976).

The likelihood including cosmology used for the MCMC analysis is defined as

$$\begin{aligned} \mathcal{L} &= \sum_{i=1}^{N} \ln \Bigg[\frac{n_A(z)}{\sqrt{2\pi\sigma_A^2}} \exp\left(\frac{-(m_i - m_A)^2}{2\sigma_A^2}\right) + \\ &\qquad \frac{(1 - n_A(z))}{\sqrt{2\pi\sigma_B^2}} \exp\left(\frac{-(m_i - m_B)^2}{2\sigma_B^2}\right)\Bigg] \end{aligned} \tag{2.4}$$

where:

- N is the number of supernovae in the mock data set;
- $n_A(z)$ is the relative normalization of population A,

$$n_A(z) = n'_{A,0} z + n_{A,0} \quad ;$$

- σ_X is the standard deviation of the two populations such that

$$\sigma_X^2 = {\sigma_{\mathrm{phot}}}^2 + \sigma_{\mathrm{int},X}^2 \quad \text{where } X = A \text{ or } B;$$

- m_i is the generated "observed" apparent magnitude for supernova i in the mock data set;

Table 2.1. Flat Priors

Ω_M	w	$\mathcal{M}/\mathcal{M}_A$	ΔM	$\sigma_{\mathrm{int},X}$	$n'_{A,0}$	$n_{A,0}$
[0,1]	[-3,1]	[-10, 5]	[0, 5]	[0.0, 0.3]	[-1,0]	[0, 2]

- m_A and m_B are predicted apparent magnitudes based on cosmological parameters through the Hubble constant-free luminosity distance,

$$\begin{aligned} m_A &= 5\log(\mathcal{D}_L(z;\Omega_M,w)) + \mathcal{M}_A \\ &\quad \text{where} \quad \mathcal{M}_A = 25 - 5\log H_0 + M_A \\ &\quad\quad \text{and} \\ m_B &= 5\log(\mathcal{D}_L(z;\Omega_M,w)) + \mathcal{M}_B \\ &\quad \text{where} \quad \mathcal{M}_B = \mathcal{M}_A - \Delta M. \end{aligned}$$

We assume a flat Universe ($\Omega_M + \Omega_\Lambda = 1$) and fit for the matter density Ω_M and the dark energy equation of state parameter w. In the case of the GMM fits, we also fit for six nuisance parameters: $\mathcal{M}_A$, ΔM, $\sigma_{\mathrm{int},A}$, $\sigma_{\mathrm{int},B}$, $n'_{A,0}$ and $n_{A,0}$ which incapsulate the information about the underlying SN Ia populations. However, since we used the Hubble constant free luminosity distance, we must still specify H_0 to completely describe the underlying populations.

In addition to our GMM analysis, we also fit each data set using a single-Gaussian model (SGM) for the underlying SN Ia population; these fits have just two nuisance parameters: $\mathcal{M}$ and σ_{int}.

For all parameters we use the flat priors defined in Table 2.1 and an extra prior in the GMM on the combination of $n'_{A,0}$ and $n_{A,0}$ such that $0 \leq n_A(z) \leq 1$.

2.4.2 Model Comparison

We have introduced a GMM to treat the cosmological analyses of SN Ia data. The GMM is more complex than the SGM as evidenced, in part, by the fact that the GMM has four more nuisance parameters. The question arises whether or not the additional complexity is

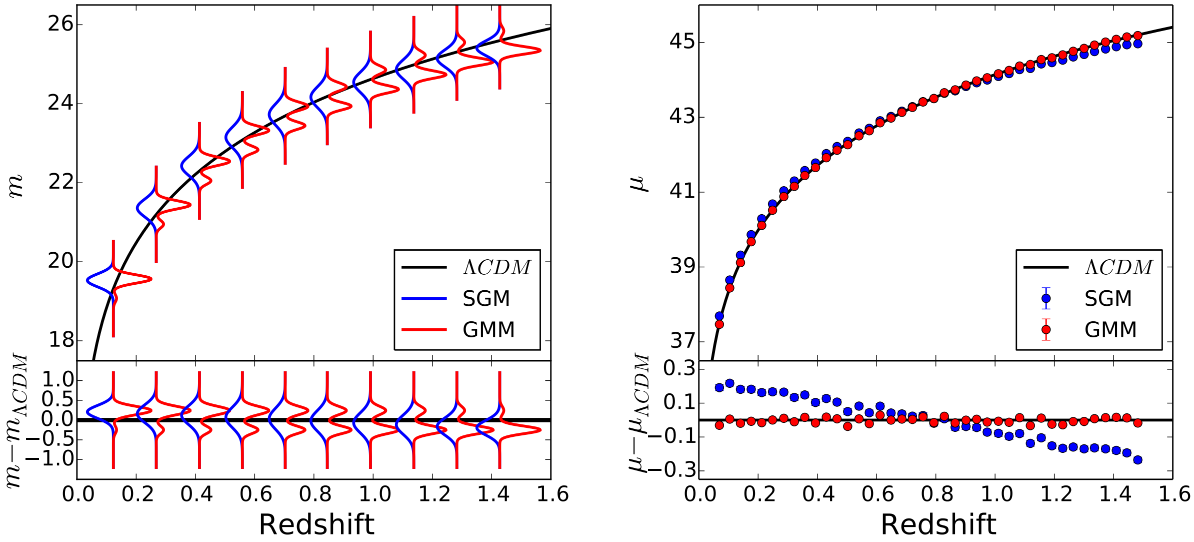

Figure 2.3 *Left:* Apparent magnitude versus redshift (top panel) and the Hubble residual (bottom panel) for parameter inferences using a GMM with $\Delta M = 0.5$ mag and $N = 10,000$ SNeIa. The black line cutting across the data is the expected magnitude redshift relation in our fiducial ΛCDM cosmology. At each of ten evenly-spaced redshift bins the blue (left-directed) curves show the PDFs of m inferred from a SGM fit to the GMM mock data while the red (right-directed) curves show the PDFs of m inferred by fitting the data with a GMM. Clearly the inferred m are biased in the SGM fits to the GMM mock data. *Right:* Luminosity distance modulus versus redshift (top panel) and residual (bottom panel) for $\Delta M = 0.5$ mag with $N = 10,000$. The line is the distance modulus calculated from ΛCDM. The data points are the mock data sets minus the model for absolute magnitude ($\mu = m - M_{\rm model}$) using the SGM (blue) with $M_{\rm model} \equiv M$ and the GMM (red) with $M_{\rm model} \equiv n_A M_A + n_B M_B$ with values derived from fit models holding cosmology and H_0 constant. 1 σ error bars have been plotted but are too small to see.

demanded by the data or, in our case, by the mock data used to mimic forthcoming analyses. We employ three statistical tests to indicate whether or not the additional complexity is required by the data: the Akaike Information Criterion (AIC; Akaike, 1974); the Bayesian or Schwartz Information Criterion (BIC; Schwarz, 1978); and the Deviance Information Criterion (DIC; Spiegelhalter et al., 2002). For a review of these three methods we refer the interested reader to Liddle (2007) and for a more in-depth discussion of AIC and DIC see Gelman et al. (2014).

The AIC and BIC are calculated from the maximum likelihood $\mathcal{L}_{\rm max}$, the number of model parameters k, and the number of data points N as

$$\mathrm{AIC} = -2\ln\mathcal{L}_{\rm max} + 2k + \frac{2k(k+1)}{N-k-1} \tag{2.5}$$

and

$$\mathrm{BIC} = -2\ln\mathcal{L}_{\rm max} + k\ln N. \tag{2.6}$$

Models with lower values of these information criteria are favored. Both the AIC and BIC penalize models with a greater number of parameters (greater k) because $\mathcal{L}_{\rm max}$ can only increase with increased parameter freedom, while the BIC also penalizes larger data sets (greater N) to reduce the risk of over fitting.

The DIC is more suited for analyses with MCMC outputs because it directly uses the resulting samples from the posterior. The DIC can be computed from these samples in the MCMC chain as

$$\mathrm{DIC} = 2\overline{D(\boldsymbol{\theta})} - D(\tilde{\boldsymbol{\theta}}), \tag{2.7}$$

where $\boldsymbol{\theta}$ is the set of parameters directly from the samples in the chain (in our case these are the cosmological parameters w and $\Omega_{\rm M}$ along with the parameters of either the SGM or GMM), $D(\boldsymbol{\theta})$ is the deviance,

$$D(\boldsymbol{\theta}) = -2\ln\mathcal{L}(\boldsymbol{\theta}) + C, \tag{2.8}$$

$\mathcal{L}(\boldsymbol{\theta})$ is the likelihood evaluated at parameters $\boldsymbol{\theta}$, and C is a normalizing constant that cancels when comparing different models. $\overline{D(\boldsymbol{\theta})}$ is the average of the deviance evaluated at each step in the chain and $D(\tilde{\boldsymbol{\theta}})$ is the deviance evaluated at the mean, median, or some other summary point in parameter space $\tilde{\boldsymbol{\theta}}$. In our samples, we find that the median is a better representation of our data because many of the posterior distributions are non-Gaussian, which can result in a mean value strongly influenced by tails.

2.5 RESULTS

2.5.1 An Illustration of Parameter Bias

We illustrate the potential for bias in the inferred cosmological parameters due to multiple SN Ia populations by first presenting Hubble diagrams. We consider data generated from an underlying GMM but fit with both a SGM likelihood and a GMM likelihood. The fit using a SGM likelihood function is intended to mimic an analysis in which there is no mechanism to account for two distinct populations.

Figure 2.3 shows the results of a comparison between a SGM and GMM analysis using one data set with an exaggerated shift in the magnitude difference between the two populations, $\Delta M = 0.5$ mag. We use this large shift here for illustrative purposes and more realistic values are $\Delta M \lesssim 0.1$. The upper panel of the left figure in Figure 2.3 shows, within ten evenly-spaced redshift bins, the PDF of apparent magnitude inferred from both the SGM and GMM fits to the underlying, multi-modal, GMM mock data. The parameters of these PDFs are determined by the fits through the MCMC process described in Section 2.4 with the cosmological parameters held constant for simplicity. The SGM was fit at each redshift bin while the GMM was fit using all the data at once to constrain the parameters of redshift evolution. The peak of the SGM PDF in the residual ($m_{\rm data} - m_{\Lambda{\rm CDM}}$) exhibits a linear evolution getting brighter as redshift increases, which is the result of the redshift evolution in the data set.

The right plot in Figure 2.3 shows the same data set and MCMC fit (with cosmology constant) converted into distance modulus versus redshift. Simply subtracting the absolute magnitude derived from the MCMC fit of the mock data yields this information. The absolute magnitude for the SGM can be taken straight from the chains ($M_{\rm SGM} = M$); however, the absolute magnitude for the GMM is a function of redshift and multiple fitted parameters ($M_{\text{GMM}}(z) = n_A(z)M_A + n_B(z)M_B$). The inferred SN Ia population parameters M and σ for the SGM have no way to account for the relative shift between the two SN Ia populations as a function of redshift and so the SGM fits show a systematic, redshift-dependent deviation in the distance modulus as a function of redshift. Notice that the mock GMM data set was generated such that at $z = 0.775$, the two populations have an equal number of SNeIa and, as expected, $M_{\text{SGM}} = M_{\text{GMM}}$ at $z = 0.775$. The population parameters are recovered well for the GMM fit and there is clearly no bias in this case.

2.5.2 Cosmological Parameters

From the perspective of exploiting SNeIa as a probe of cosmology, the greatest concern caused by multiple populations of SNeIa is that insufficiently accurate modeling of the multiple populations will lead to biased cosmological parameters. Exploring this possibility is the primary purpose of this paper. To explore the potential importance of multiple SN Ia populations on cosmology, we fit each of the 108 mock data sets described in Section 2.3 for the cosmological parameters, Ω_{M} and w, and SN Ia population parameters simultaneously.

Figure 2.4 displays the Hubble diagram inferred from both SGM and GMM fits to a GMM model from a single data set with $N = 10,000$ SNeIa and an extreme value of $\Delta M = 0.5$ mag. This large value of ΔM is used to produce this figure only because it has the pedagogical value of making the influence of the two-populations model on inferred cosmology obvious. Clearly the GMM fits yield an unbiased Hubble diagram and we infer unbiased values of both Ω_{M} and w.

On the other hand, the SGM fits to the GMM produces a biased inferred Hubble diagram and biased inferences for the cosmological parameters. Compare Fig. 2.4 to the right plot of Fig. 2.3. Notice that the results of the two fits no longer cross near $z = 0.775$ once cosmological parameters are fit simultaneously with SN Ia population parameters. The SGM fits to the GMM mock data result in cosmological parameters and SN Ia population parameters that are simultaneously significantly biased. As a result, the inferred Hubble diagram differs from the true underlying dependence of distance modulus on redshift. Most

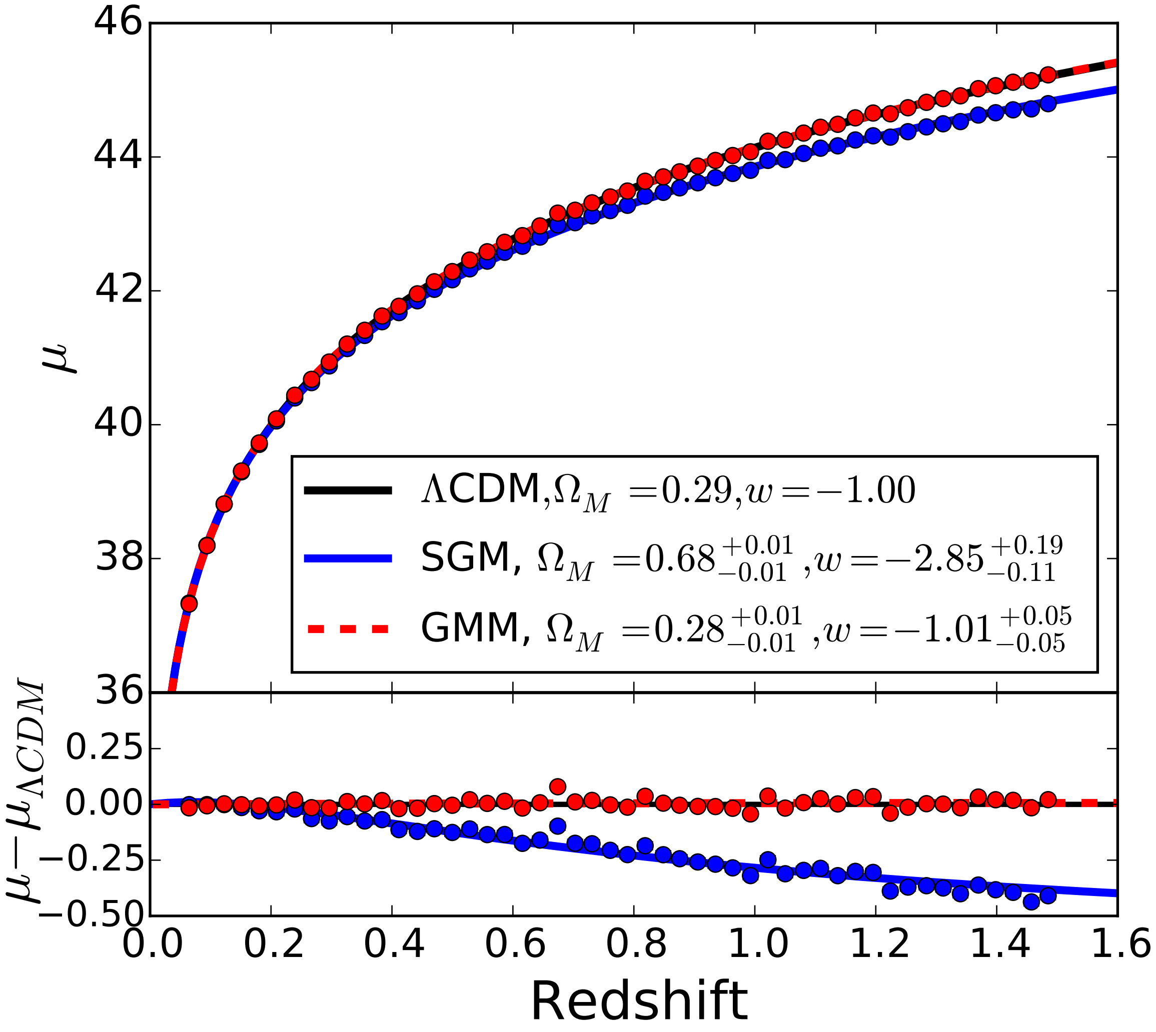

Figure 2.4 Hubble constant-free luminosity distance modulus versus redshift (top panel) and residual (bottom panel) for $\Delta M = 0.5$ mag with $N = 10,000$. The lines are the distance modulus calculated from cosmology derived from the MCMC fits. The data points are the mock data sets minus the model for absolute magnitude ($\mu = m - M_{\rm model}$) using the SGM (blue) with $M_{\rm model} \equiv M$ and the GMM (red) with $M_{\rm model} \equiv n_A M_A + n_B M_B$ with values derived from fit models. The data points correspond in color to their model. 1 σ error bars have been plotted but are too small to see.

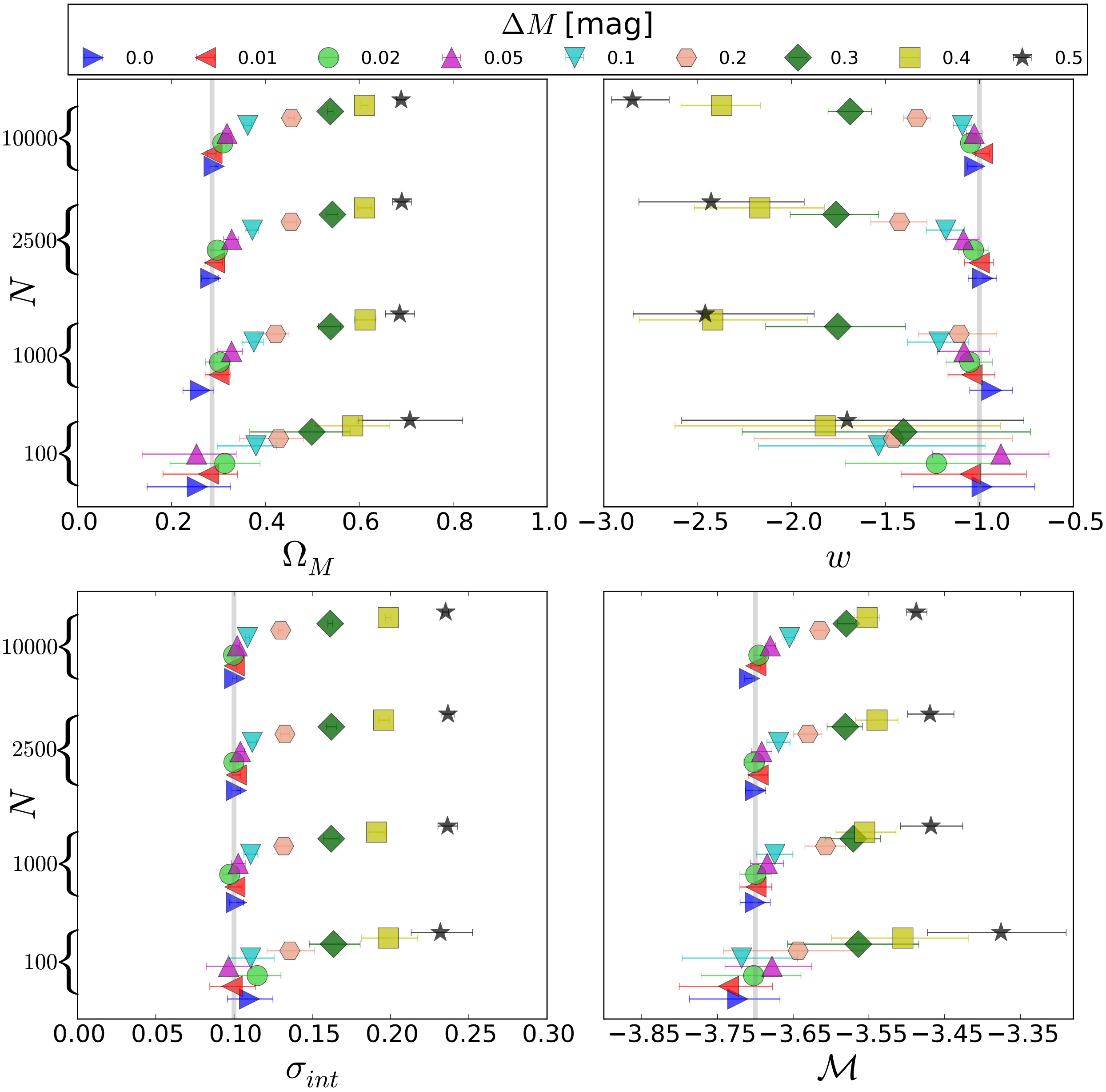

Figure 2.5 The median and 68% confidence region from the MCMC analysis using a SGM likelihood plotted within the limits of each prior (except $\mathcal{M}$). Each ΔM is given its own color and shape. To avoid overlap in the error bars, we present the increasing ΔM values with a small offset in ordinate value within each N bracket. The grey vertical line in each plot marks the fiducial value of that parameter.

importantly, the bias in the cosmological parameters is significant. We infer $\Omega_{\rm M} = 0.69 \pm 0.01$ and $w = -2.85^{+0.19}_{-0.11}$ and rule out the true underlying cosmology with high confidence. Of course, this model with $\Delta M = 0.5$ mag is extreme, but we will now move on to a discussion of inferred cosmological parameters in each of our 108 mock data sets and show that viable two-population SN Ia models yield biases in cosmology that are non-negligible compared to statistical errors.

We present medians and 68% confidence regions of the fitted parameters by combining the MCMC results from the 3 different data sets at each value of N and at each value of ΔM. We define the 68% confidence region as the area contained within the $16^{\rm th}$ and $84^{\rm th}$ percentiles, which enforces an equal probability in the tails at either end of the posterior distribution. In order to combine the three data sets, we calculate the average of the medians, and we calculate the $16^{\rm th}$ and $84^{\rm th}$ percentiles as

$$\sigma_{\%} = \sqrt{\frac{\sigma^2_{\%,1} + \sigma^2_{\%,2} + \sigma^2_{\%,3}}{3}}, \tag{2.9}$$

where $\sigma_{\%}$ is the $16^{\rm th}$ or $84^{\rm th}$ percentile and $\sigma_{\%,i}$ corresponds to the $16^{\rm th}$ or $84^{\rm th}$ percentile calculated from the $i^{\rm th}$ data set.

Fig. 2.5 shows the medians and 68% confidence regions in the inferred parameters in our fits using a SGM to describe GMM mock data. As Fig. 2.5 clearly shows, for $\Delta M = 0$, the inferred parameters are unbiased: the true, underlying value of each of the cosmological parameters is inferred to within statistical precision. This is unsurprising. We have assumed that both sub-populations have the same intrinsic dispersion, so a model in which $\Delta M = 0$ is tantamount to a SGM for SNeIa. This is nothing more than a validation of this procedure for a single population of SNeIa. Models with $\Delta M \neq 0$ correspond to GMM models. Both cosmological and SN Ia population model parameters exhibit increasing biases as ΔM increases. Moreover, many of these biases are quite statistically significant suggesting that it is possible to rule out the correct underlying models due to these systematic errors. We note that in some cases ($\Delta M \gtrsim 0.4$) the inferred values of w are strongly influenced by the hard prior $w > -3$ that we have enforced. Table 2.2 summarizes only the results for cosmological parameters with 68% confidence regions for SGM and GMM results.

Fig. 2.6 is an analogous plot focusing on the inferred values of w, which is the primary

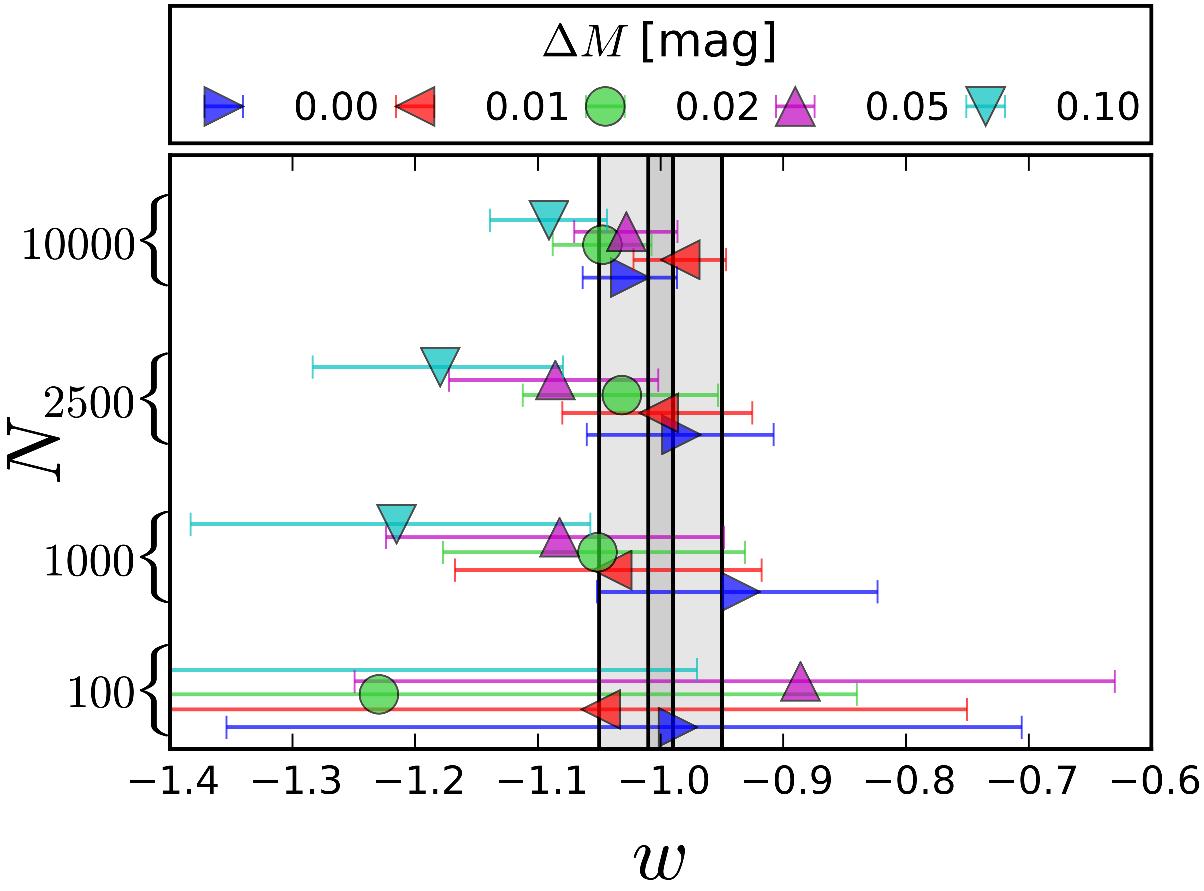

Figure 2.6 A close up view of the Top Right panel from Figure 2.5 to show the induced bias on w. We here only focus on the empirically plausible values $0.0 < \Delta M < 0.1$ mag. The vertical lines indicate ranges of ±0.05 and ±0.01 in w for reference.

Table 2.2. The median and 68% confidence region of Ω_M and w for all N and ΔM.

N	Model	Ω	$\Delta M = 0.0$	0.01	0.02	0.05	0.1	0.2	0.3	0.4	0.5
100	GMM	Ω_M	$0.234^{+0.071}_{-0.099}$	$0.265^{+0.061}_{-0.093}$	$0.295^{+0.075}_{-0.104}$	$0.23^{+0.083}_{-0.106}$	$0.356^{+0.049}_{-0.087}$	$0.408^{+0.056}_{-0.088}$	$0.406^{+0.122}_{-0.138}$	$0.428^{+0.112}_{-0.126}$	$0.303^{+0.089}_{-0.089}$
100	SGM	Ω_M	$0.255^{+0.071}_{-0.107}$	$0.279^{+0.062}_{-0.097}$	$0.314^{+0.075}_{-0.117}$	$0.253^{+0.085}_{-0.116}$	$0.38^{+0.044}_{-0.082}$	$0.428^{+0.053}_{-0.084}$	$0.499^{+0.082}_{-0.132}$	$0.586^{+0.079}_{-0.084}$	$0.708^{+0.112}_{-0.111}$
100	GMM	w	$-0.988^{+0.265}_{-0.346}$	$-1.047^{+0.286}_{-0.357}$	$-1.189^{+0.352}_{-0.470}$	$-0.875^{+0.231}_{-0.331}$	$-1.46^{+0.513}_{-0.627}$	$-1.471^{+0.615}_{-0.721}$	$-1.265^{+0.513}_{-0.758}$	$-1.447^{+0.626}_{-0.740}$	$-1.341^{+0.466}_{-0.554}$
100	SGM	w	$-0.986^{+0.28}_{-0.368}$	$-1.049^{+0.298}_{-0.369}$	$-1.23^{+0.389}_{-0.485}$	$-0.886^{+0.256}_{-0.363}$	$-1.538^{+0.567}_{-0.638}$	$-1.459^{+0.634}_{-0.742}$	$-1.404^{+0.676}_{-0.859}$	$-1.821^{+0.933}_{-0.800}$	$-1.705^{+0.941}_{-0.881}$
1000	GMM	Ω_M	$0.247^{+0.032}_{-0.040}$	$0.282^{+0.030}_{-0.038}$	$0.285^{+0.028}_{-0.036}$	$0.314^{+0.027}_{-0.035}$	$0.363^{+0.025}_{-0.035}$	$0.361^{+0.052}_{-0.061}$	$0.289^{+0.040}_{-0.048}$	$0.287^{+0.036}_{-0.043}$	$0.295^{+0.033}_{-0.041}$
1000	SGM	Ω_M	$0.261^{+0.029}_{-0.037}$	$0.301^{+0.024}_{-0.030}$	$0.303^{+0.024}_{-0.030}$	$0.328^{+0.023}_{-0.029}$	$0.376^{+0.020}_{-0.025}$	$0.422^{+0.028}_{-0.039}$	$0.539^{+0.021}_{-0.026}$	$0.612^{+0.023}_{-0.023}$	$0.686^{+0.032}_{-0.030}$
1000	GMM	w	$-0.92^{+0.108}_{-0.113}$	$-1.014^{+0.117}_{-0.125}$	$-1.025^{+0.116}_{-0.122}$	$-1.06^{+0.129}_{-0.139}$	$-1.184^{+0.155}_{-0.167}$	$-0.994^{+0.173}_{-0.197}$	$-0.993^{+0.152}_{-0.170}$	$-1.003^{+0.146}_{-0.162}$	$-1.014^{+0.140}_{-0.150}$
1000	SGM	w	$-0.935^{+0.112}_{-0.117}$	$-1.039^{+0.122}_{-0.128}$	$-1.051^{+0.120}_{-0.126}$	$-1.082^{+0.134}_{-0.142}$	$-1.215^{+0.158}_{-0.168}$	$-1.108^{+0.200}_{-0.217}$	$-1.755^{+0.362}_{-0.383}$	$-2.42^{+0.505}_{-0.392}$	$-2.46^{+0.580}_{-0.384}$
2500	GMM	Ω_M	$0.267^{+0.024}_{-0.028}$	$0.281^{+0.020}_{-0.024}$	$0.285^{+0.020}_{-0.025}$	$0.311^{+0.021}_{-0.027}$	$0.36^{+0.017}_{-0.023}$	$0.318^{+0.032}_{-0.029}$	$0.296^{+0.024}_{-0.027}$	$0.298^{+0.024}_{-0.028}$	$0.239^{+0.029}_{-0.032}$
2500	SGM	Ω_M	$0.284^{+0.017}_{-0.020}$	$0.292^{+0.017}_{-0.020}$	$0.298^{+0.016}_{-0.019}$	$0.328^{+0.015}_{-0.017}$	$0.372^{+0.013}_{-0.016}$	$0.455^{+0.012}_{-0.013}$	$0.543^{+0.012}_{-0.012}$	$0.611^{+0.015}_{-0.015}$	$0.691^{+0.020}_{-0.020}$
2500	GMM	w	$-0.967^{+0.073}_{-0.077}$	$-0.988^{+0.075}_{-0.078}$	$-1.012^{+0.077}_{-0.080}$	$-1.057^{+0.083}_{-0.087}$	$-1.16^{+0.100}_{-0.104}$	$-1.095^{+0.100}_{-0.116}$	$-1.02^{+0.094}_{-0.102}$	$-0.994^{+0.098}_{-0.103}$	$-0.865^{+0.083}_{-0.091}$
2500	SGM	w	$-0.983^{+0.075}_{-0.077}$	$-1.001^{+0.076}_{-0.079}$	$-1.032^{+0.078}_{-0.081}$	$-1.086^{+0.084}_{-0.087}$	$-1.18^{+0.100}_{-0.104}$	$-1.425^{+0.146}_{-0.154}$	$-1.763^{+0.226}_{-0.245}$	$-2.17^{+0.345}_{-0.349}$	$-2.429^{+0.496}_{-0.385}$
10000	GMM	Ω_M	$0.285^{+0.010}_{-0.013}$	$0.28^{+0.011}_{-0.014}$	$0.303^{+0.010}_{-0.013}$	$0.312^{+0.011}_{-0.015}$	$0.321^{+0.033}_{-0.031}$	$0.307^{+0.015}_{-0.014}$	$0.28^{+0.013}_{-0.014}$	$0.286^{+0.012}_{-0.013}$	$0.283^{+0.012}_{-0.012}$
10000	SGM	Ω_M	$0.291^{+0.008}_{-0.009}$	$0.286^{+0.009}_{-0.009}$	$0.309^{+0.008}_{-0.009}$	$0.318^{+0.009}_{-0.009}$	$0.363^{+0.008}_{-0.009}$	$0.456^{+0.007}_{-0.007}$	$0.538^{+0.006}_{-0.006}$	$0.611^{+0.008}_{-0.008}$	$0.689^{+0.010}_{-0.010}$
10000	GMM	w	$-1.016^{+0.039}_{-0.040}$	$-0.976^{+0.038}_{-0.039}$	$-1.037^{+0.041}_{-0.042}$	$-1.017^{+0.044}_{-0.044}$	$-1.028^{+0.055}_{-0.061}$	$-1.028^{+0.047}_{-0.050}$	$-0.98^{+0.046}_{-0.048}$	$-1.014^{+0.048}_{-0.050}$	$-0.991^{+0.045}_{-0.048}$
10000	SGM	w	$-1.025^{+0.038}_{-0.039}$	$-0.984^{+0.038}_{-0.038}$	$-1.047^{+0.040}_{-0.041}$	$-1.028^{+0.042}_{-0.042}$	$-1.091^{+0.047}_{-0.048}$	$-1.333^{+0.070}_{-0.072}$	$-1.688^{+0.114}_{-0.118}$	$-2.372^{+0.207}_{-0.217}$	$-2.848^{+0.196}_{-0.111}$

science goal of dark energy probes, and observationally-plausible values of $\Delta M \leq 0.1$. Even in this restricted range of ΔM it is apparent that neglecting the possibility of multiple populations can lead to biases in the inferred value of w that are non-negligible compared to the statistical errors in these parameters. This is clearly a challenge to precision measurements of the dark energy equation of state that must be overcome in order to fully exploit SNeIa.

In comparison, the inferred parameters in the GMM model fits to the GMM mock data can be seen in Figure 2.7 and Figure 2.8. In *all* such cases we recover the correct cosmological parameters to within statistical precision. Indeed this is not entirely surprising because this is now a fit with a model that correctly describes the mock data. Indeed, we are able to infer all of the model parameters in an unbiased way except for $n'_{A,0}$ and $n_{A,0}$ when $\Delta M \lesssim 0.2$ mag. The fiducial values are recovered within the 99% confidence region for the intercept $n_{A,0}$ and within $\sim 99.9\%$ confidence region for the slope $n'_{A,0}$. It is clear that $n'_{A,0}$ and $n_{A,0}$ are biased in Figure 2.7 in a way that favors less redshift dependence (smaller $n'_{A,0}$) except for large shifts in peaks of the two populations. Even though these parameters are biased, they do not introduce an increase in the variance of cosmological parameters. This counter intuitive result can be explained through Figure 2.10, which shows that the posterior distributions of the population versus cosmological parameters are parallel to the population parameters meaning they have little to no degeneracy with cosmological parameters. When ΔM is sufficiently small, data with the precision and size of our mock data sets cannot clearly distinguish the two peaks because the separation between the peaks is comparable to the dispersion in any one of the sub-populations. It is important to note that cosmological parameters can be strongly biased despite the fact that a fit to the underlying data *cannot* clearly distinguish the two populations. This is relevant to the results of the following subsection.

Clearly, an underlying model in which $\Delta M = 0$ and $\sigma_A = \sigma_B$ can be described by a SGM with no bias. Using a GMM model to describe such data introduces additional parameters and necessarily leads to less restrictive constraints on the cosmological parameters of interest. This loss in precision is the cost of using a model with the parameter freedom to account for the possibility of multiple SNeIa sub-populations. For a data set with the precision expected of $N = 2500$ ($N = 10,000$) SNeIa, the loss of precision in $\Omega_{\rm M}$ is $\sim 20\%$ ($\sim 25\%$) while the

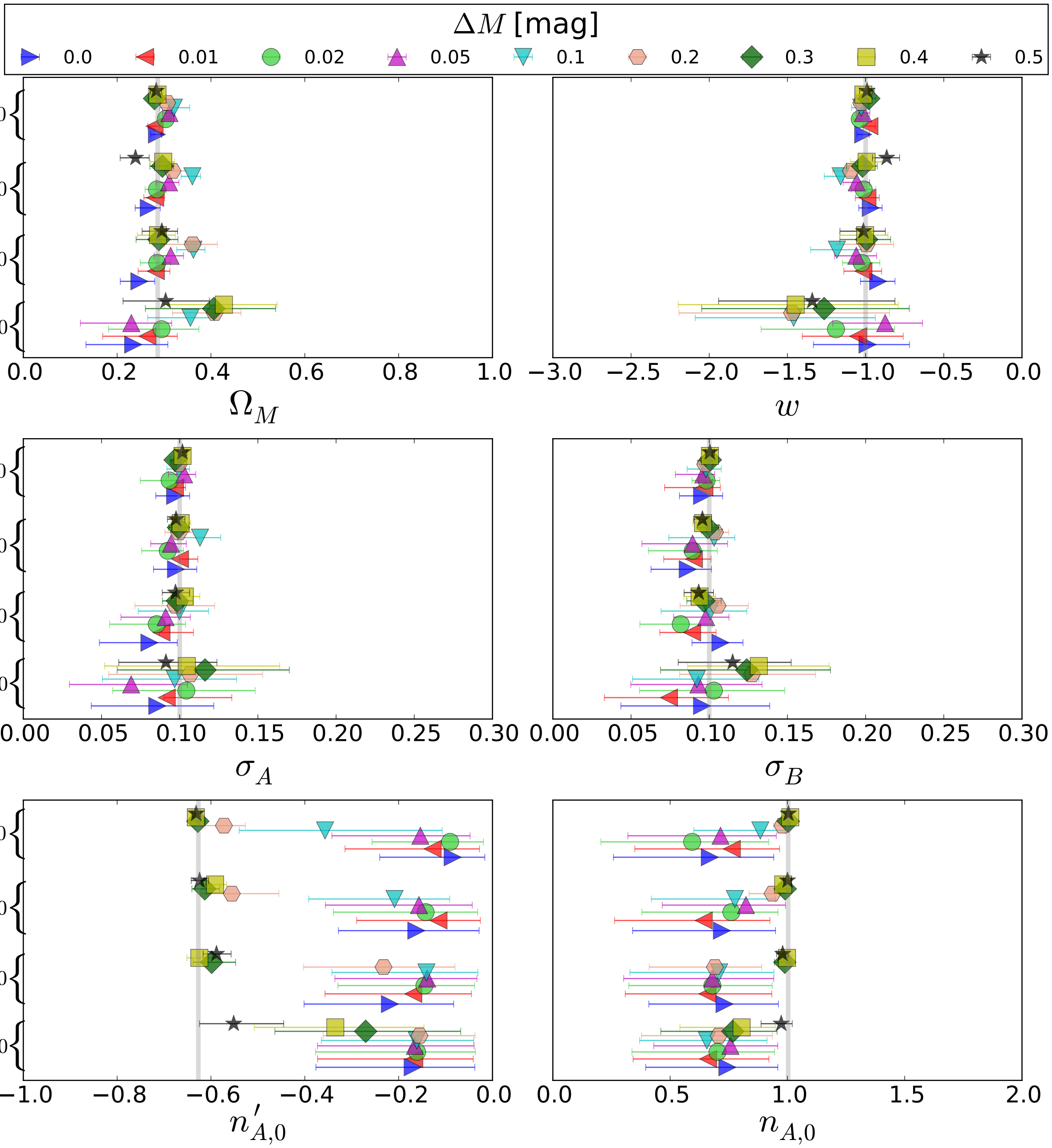

Figure 2.7 The GMM fit results for the same simulations as in Figure 2.5 and displayed with the same ordinate offsets. The GMM model correctly recovers the fiducial cosmology and accounts for the multiple input populations. The multiple-population parameters (σ_A, σ_B) are not well constrained for small ΔM, and the normalization factors ($n_{A,0}$ and $n'_{A,0}$) are even clearly biased at low ΔM due to the reduced leverage they have on the output. But the resulting cosmological parameters are well-constrained when marginalizing over the multiple-population parameters.

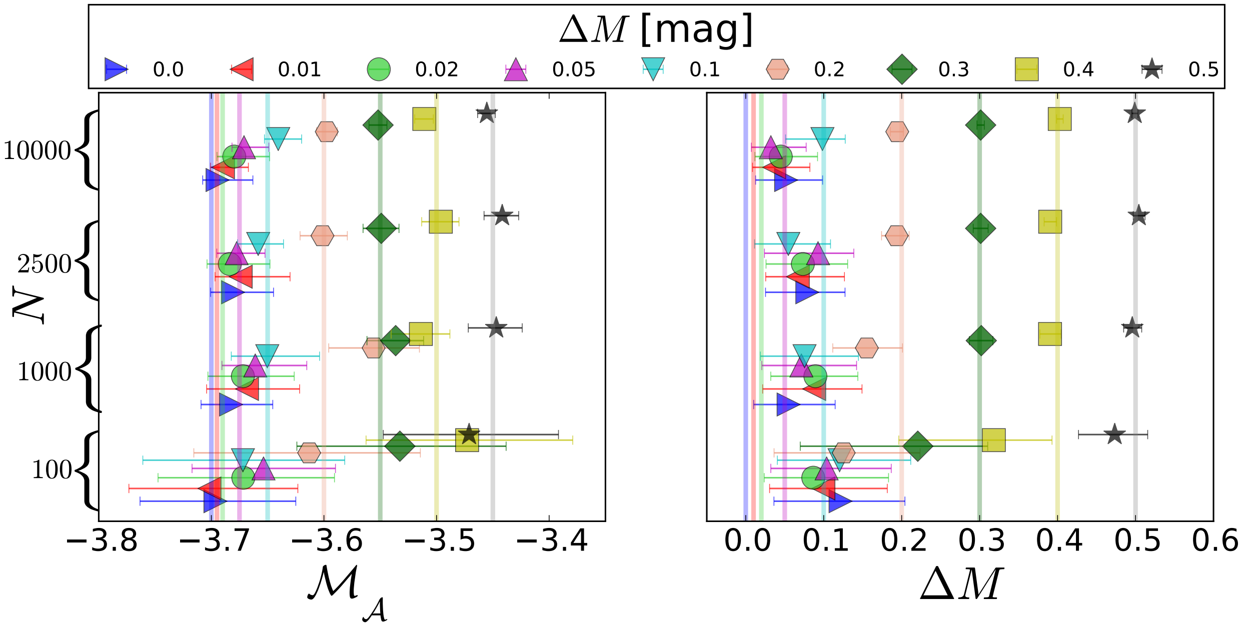

Figure 2.8 The GMM fit results for parameters dependent on ΔM from the same simulations as in Figures 2.5 and 2.7 and displayed with the same ordinate offsets. Each specific ΔM has a vertical line denoting the different fiducial values. While Figure 2.5 and Figure 2.7 are plotted over the entire range of the uniform prior, in this figure we focus on a range much smaller than the prior to show the detailed effect.

loss of precision in w is approximately $\lesssim 1\%$ ($\lesssim 3\%$). This very moderate cost in precision greatly outweighs the potential $\sim 2\sigma$ statistical error that can be induced by treating a two populations of SNeIa with $\Delta M \sim 0.1$ as a single populations (see Table 2). This finding reaffirms that the precision does not significantly decrease when these population parameters are added to the model.

Figure 2.9 shows the cosmological parameter posteriors from one data set for the interesting case of $N = 1,000$ and $\Delta M = 0.1$ mag. These numbers are interesting since the JLA has ~ 1000 SNeIa, and the current estimated discrepancy in Hubble residuals is equivalent to $\Delta M \sim 0.1$ mag. The contours continue to show that the GMM is less biased but also slightly less precise. These are not large offsets, but it could lead to a small systematic error in the next stages of observational cosmology.

2.5.3 Model Selection

To determine if the additional complexity of a given model is demanded by the (mock) data, we use the information criteria described in Section 2.4.2. In order to compare two models, one can compute the information criteria for each and take the difference between the two results. For example, if we compute the AIC for each model, we would compute $\Delta\text{AIC} = \text{AIC}_{\text{GMM}} - \text{AIC}_{SGM}$ where AIC_{GMM} is the value of AIC in the GMM model and likewise for AIC_{SGM}. We follow this convention, subtracting the SGM criteria from the GMM criteria, so that lower values of the difference between information criteria (IC) favor the GMM model. With these conventions, any change in information criteria (generically, Δ IC) will favor the GMM if $\Delta\text{IC} < 0$ and strongly favor the GMM if $\Delta\text{IC} < -5$. Conversely, a positive Δ IC favors the SGM while $\Delta\text{IC} > 5$ strongly favors the SGM.

We look for the minimum ΔM for each N that strongly favors the GMM. The results of this comparison are summarized Table 2.3 for all of the IC and in Fig. 2.11 for the AIC alone. The AIC, BIC, and DIC all give very comparable results. Notice that ΔM must be relatively large in order for the IC to indicate that the data demand a two-population model of SNeIa. Indeed, a data set of $N \gtrsim 10,000$ SNeIa is required in order for the IC to prefer

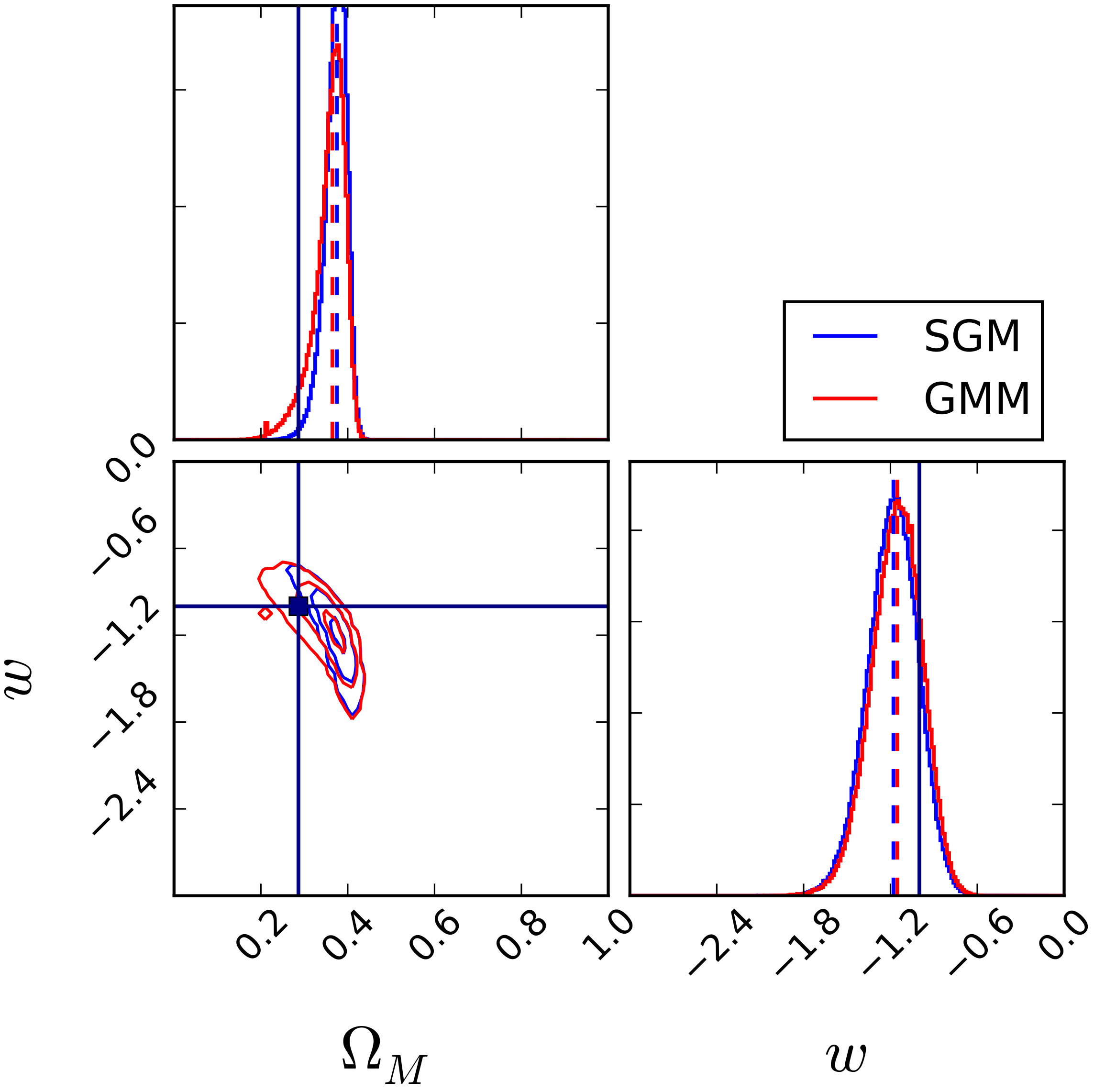

Figure 2.9 Cosmological contours for $\Delta M = 0.1$ mag and $N = 1000$. Made with `triangle.py` from Foreman-Mackey et al. (2014). The blue contours and histograms correspond to the mock data being fit with SGM likelihood and the red contours and histograms correspond to the GMM likelihood. The dashed lines are the medians of the populations. The dark navy lines are the fiducial values. The GMM is less precise but also less biased.

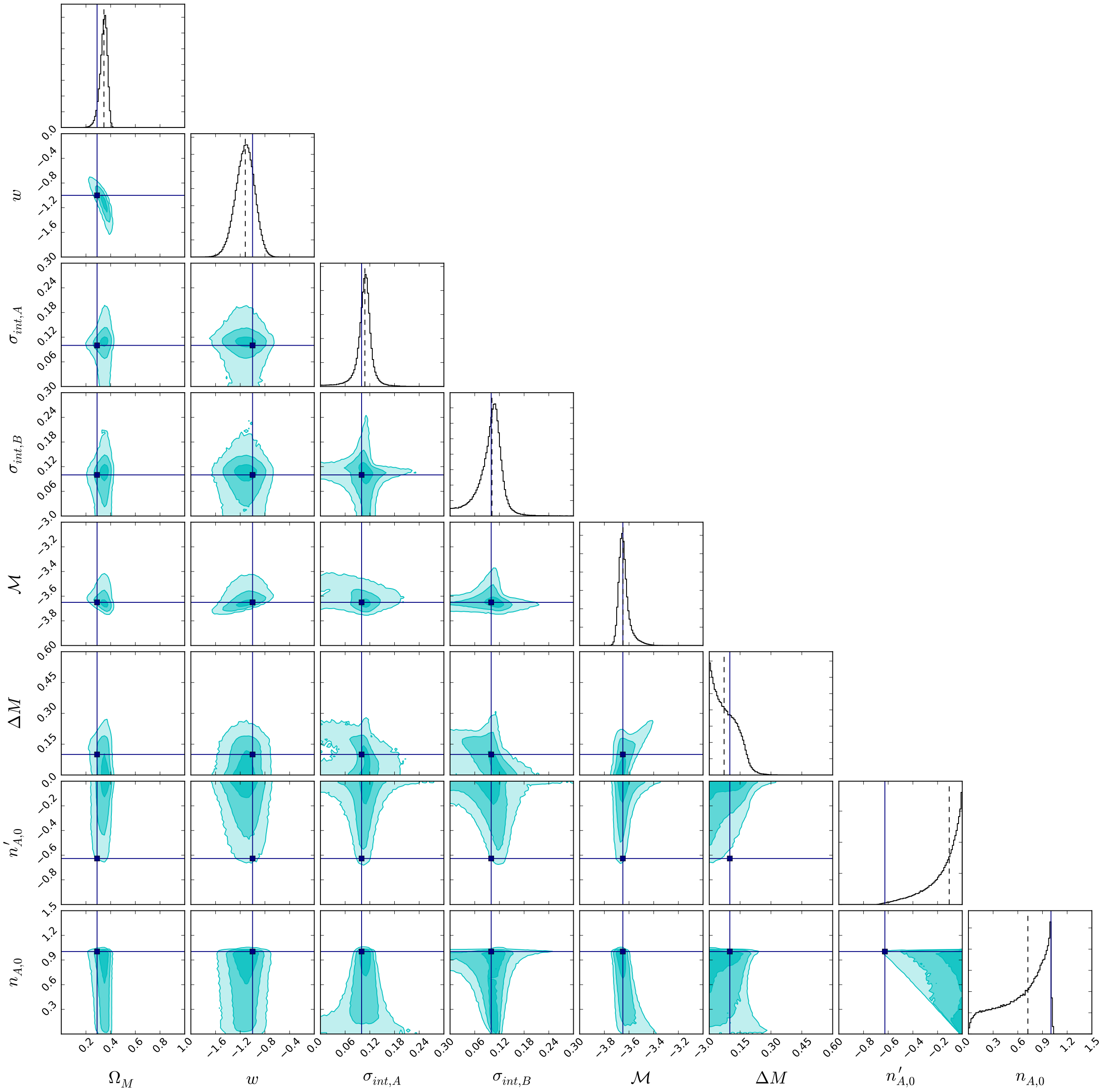

Figure 2.10 Full triangle plot of posterior distributions from a GMM likelihood for a single data set with $N = 1,000$ and $\Delta M = 0.1$ mag. Made with `triangle.py` from Foreman-Mackey et al. (2014)

Table 2.3. Minimum ΔM (in mag) with strong evidence for GMM.

N	AIC	BIC	DIC
100	0.40	0.45	0.41
1000	0.21	0.25	0.23
2500	0.12	0.21	0.23
10000	0.10	0.14	0.10

strongly the GMM with $\Delta M \sim 0.1$ over the SGM.

There is an important point regarding the interpretation of the results of this section in conjunction with those of the previous subsections. The fact that the data may not *demand* a GMM to describe SNeIa does *not* mean that a multiple-population SNeIa model is not *necessary*. As we have shown, statistically significant biases in cosmological parameters can be inferred when two-population data are analyzed as a single population, even when the information criteria do not unambiguously demand the GMM rather than the SGM. If by "necessary" one means that the model is needed in order to infer unbiased cosmological parameters, then the GMM may be necessary even when the IC yield only marginal evidence. IC that do not clearly demand the more complex model (the GMM in this case) are not sufficient justification for using only the simpler model (the SGM in this case) in cosmological analyses because significant parameter biases may still be realized using the simpler approach.

2.6 DISCUSSION

2.6.1 Usage of the SGM

The SGM was meant to be representative of the latest supernova cosmology analysis, namely the Joint Lightcurve Analysis (JLA); however, the SGM cannot be directly compared to the JLA. Unlike the SGM, the JLA further standardizes each supernova by applying an offset to the absolute magnitude of each supernova using an empirically-derived step function in host galaxy mass. This standardization follows from the observed Hubble residual trend

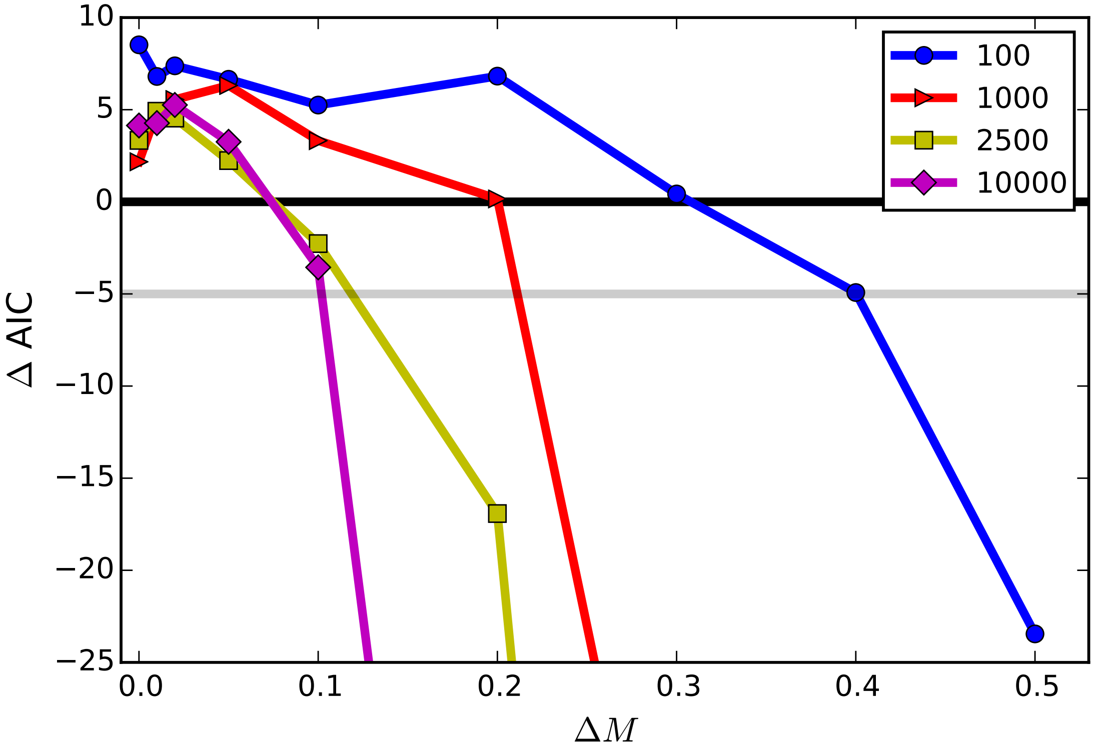

Figure 2.11 AIC(GMM)−AIC(SGM) for N=[100,1000,2500,1000] as a function of the separation of peaks. GMM is considered strongly favored once ΔAIC<-5.

with host galaxy properties that was one of the motivations for introducing multiple populations. Leaving out the host galaxy standardization enables this present study to avoid any unintended bias from using the step function, conceptually compare the SGM to the GMM, and create a general framework that can be applied to other systematics. The goal of this paper is not to implement a new model for the correlation between the SN Hubble residual and host-galaxy properties, but to introduce a statistical framework in which to implement a future model.

The likelihoods for the SGM and JLA are the same except that the JLA utilizes the host galaxy mass standardization and a full covariance matrix. JLA uses a χ^2 minimization for parameter estimation, which is equivalent to maximizing a Gaussian likelihood. The JLA uses a frequentist approach with χ^2 minimization, but we use the SGM to explore parameter space through Bayesian statistics with MCMC. However, χ^2 minimization and the SGM likelihood analysis both use a Gaussian single-point estimate of the SN corrected brightness to infer cosmological parameters. Using single-point estimate (μ, σ) does not provide framework to deal with insufficient population modeling and data with large error bars on parameters used for systematics modeling[5], both of which are found in the current data sets. This present paper shows that updating the likelihood to incorporate non-Gaussian effects can remove bias on cosmology without precise modeling of the underlying populations.

2.6.2 Connection To Astrophysical Properties

A relationship with host galaxy mass is currently used to correct SN Ia apparent brightness; however, host mass must be an indicator of a different galactic property that has a connection to the brightness of a supernova such as local metallicity, star formation rate, and stellar population age (Johansson et al., 2013). One possible explanation for the host mass effect is different progenitor ages. The overall mass of the galaxy is correlated with progenitor age through stellar population ages. SNeIa occur in both active and passive star forming regions, which implies that they have both short delay times ($\sim 100-500$ Myr) and long delay times (~ 5 Gyr) between progenitor formation and supernova event (Mannucci et al., 2005;

---

[5] The mass of each host galaxy is determined from photometry in the JLA sample has a typical uncertainty of ~ 0.8 dex.

Scannapieco & Bildsten, 2005; Mannucci et al., 2006; Sullivan et al., 2006). The different progenitor ages could be motivated by different channels for a thermonuclear explosion: single degenerate (SD) where a white dwarf accretes matter from a main sequence or red giant companion (Whelan & Iben, 1973) and double degenerate (DD) where two white dwarfs merge (Webbink, 1984). The SD and DD can both explain the population with short delay times; however, SD models do not support the long delay times (Greggio, 2005, see Maoz et al. (2014) for comprehensive review).

Several papers have begun to examine the connections between host galaxy mass and stellar population ages. Johansson et al. (2013) showed that the stretch-host galaxy mass relationship is caused by the correlation between host galaxy mass and stellar population age. Childress et al. (2013b) fit the Hubble residual versus host galaxy mass with different functional forms and examined different physical causes of the relationship. They found the best physical link to the step function was the evolution of the prompt fraction of SN Ia progenitors, but the fit is not adequate enough to be the only source of the effect. Childress et al. (2014) focused on modeling stellar population age as a function of host galaxy mass at different redshifts. The paper showed a bimodal distribution in progenitor age versus stellar mass and that this bimodality is evident out to a redshift $\lesssim 0.5$. These results clearly motivate adopting a GMM approach where the two populations changing with redshift. Unfortunately, the way the populations evolve with redshift is determined through star formation histories and delay time distributions, which is considerably more complicated than the simple linear evolution probed here. Creating better astrophysical models for the evolution of systematics is an active area of research, and we present this generalized PDF approach as the appropriate framework to incorporate them into.

2.7 CONCLUSION

This paper explored expanding supernovae analyses into a broader scope with a generalized likelihood model. For illustration we used a toy example of two-population GMM with a simple linear evolution in relative population with redshift. We explored different distributions of likelihood functions and showed that in mock data sets using our toy GMM example multiple SNeIa sub-populations may lead to significant biases in cosmological parameters inferred from SNeIa data. In particular, when $N = 1,000$ and $\Delta M = 0.1$ mag, biases may be 2-4 times that of the statistical uncertainty. Incorporate this model into the PDF removes systematic errors (biases) in inferred cosmological parameters at a small statistical cost, roughly 2% in the marginalized uncertainty on w. Large data sets (N $>$ 10,000) are necessary to yield unambiguous evidence of multiple populations according to various model selection criteria. However, even when model selection does not clearly favor multiple populations, the presence of multiple populations in the data can severely bias cosmological parameters. Our approach of modeling the possibility of multiple populations not only mitigates biases from them, but also yields a small penalty in precision if there is only one population.

The existence of multiple populations is still being debated as seen in Jones et al. (2015), which advocates for a single population; however, a GMM likelihood has the capability of determining if there is only one population and thus is a more rigorous way to analyze the data to ensure more systematics are included.

We have assumed an example model of two populations with a difference in the absolute magnitude, but there are clearly other channels in which separate populations might be expressed depending on the astrophysical cause. It is possible that a different supernova property can better parameterize the stellar population age of the progenitor. If we did not use the width-color-corrected apparent magnitude, then the apparent magnitudes would be defined as $M_X \equiv M_{\mathrm{Bband},X} - \alpha x_1 + \beta \mathcal{C}$, where x_1 is the stretch calculated from each supernova light curve, α is the stretch parameter determined for the entire supernova population, $\mathcal{C}$ is the color of each supernova at time of maximum light, and β is the color parameter determined for the entire supernova population. One example has been provided by Milne et al. (2015) which shows two different populations with a difference in near ultraviolet (NUV) $u - v$ color of 0.4 magnitudes (0.1 mag in $b - v$) with the relative fractions of populations evolving with redshift. This color dependence would fit nicely into our framework since we could alternatively model the absolute magnitude as $M_X \equiv M_{\mathrm{Bband}} - \alpha x_1 + \beta_X \mathcal{C}$.

This framework is tested with the host galaxy mass dependence as an example; however, it is suitable for accounting for any systematic that may have multiple values based on supernova parameters. For example, surveys with different selection effects could also be included as different PDFs, either in intrinsic distribution or in redshift evolution, for each survey. Corrections for Malmquist bias (Malmquist, 1936) could be handled more cleanly by using the full PDF instead of using the mean computed correction for the sample (e.g., Perrett et al., 2010; Conley et al., 2011; Rest et al., 2014; Scolnic et al., 2014; Betoule et al., 2014)) or priors on the light-curve fitting parameters applied on per-object basis (e.g., Wood-Vasey et al., 2007). Currently forward-modeling approaches that simulate entire surveys (e.g., SNANA; Kessler et al., 2009, 2010) carry through this modeling all the way; we believe there can be significant gains in translating much of this information into empirical PDFs that can then be interpolated and used in a generalized full-likelihood fitting (work towards this has begun in Rubin et al. (2015)).

Supernova cosmology would benefit from incorporating a non-Gaussian likelihood with an MCMC analysis to model the many systematics involved in order to remove biases with a minimal precision loss.

2.8 ACKNOWLEDGEMENTS

We thank the referee for constructive comments, which have improved this paper. We thank Phil Marshall and Carles Badenes for useful discussions. KAP was supported in this work by NSF AST-1028162, and by the U.S. Department of Energy, Office of Science, Office of Workforce Development for Teachers and Scientists, Office of Science Graduate Student Research (SCGSR) program. The SCGSR program is administered by the Oak Ridge Institute for Science and Education for the DOE under contract number DE-AC05-06OR23100. M.W.-V. was supported in part by DOE DE-SC0011834 and through sabbatical support from Stanford/SLAC. The work of ARZ is supported in part by the DOE through grant DE-SC0007914 and by the Pittsburgh Particle physics, Astrophysics, and Cosmology Center (Pitt PACC) at the University of Pittsburgh.

3.0 PHOTOMETRIC OBSERVATIONS AND SPECTROSCOPIC DATA REDUCTIONS FOR THE SWEETSPOT SURVEY

The portions of this chapter that outline HexPak data reductions and results will be submitted to the American Astronomical Society Journals authored by K.A.P., W. Michael Wood-Vasey, Lori Allen, Lluís Galbany, Saurabh W. Jha, Richard Joyce, and Thomas Matheson.

We present an overview of the SweetSpot survey that collected 115 supernovae in the NIR. We observed 32 galaxies that previously hosted SweetSpot SNeIa with an integral field unit (IFU) spectrograph with the primary goal of measuring Hα emission lines. Included here are detailed data reductions and spatial maps of Hα equivalent widths, Hα surface brightness, Hα velocities, and reconstructed SDSS r-band flux.

3.1 INTRODUCTION

The cosmological usefulness of Type Ia supernovae (SNeIa) lies in their uniformity of luminosity at peak brightness. Current evidence (Kasen, 2006; Folatelli et al., 2010; Kattner et al., 2012; Wood-Vasey et al., 2008; Barone-Nugent et al., 2012) suggests that SNeIa are more standard at near infrared wavelengths (NIR). They require fewer lightcurve corrections such as stretch (Phillips, 1993) and color (Riess et al., 1996; Tripp, 1998) that are critical for optical SNeIa. This phenomenon is partially due to the decreased dust extinction experienced at these wavelengths and partially because the explosion models show decreased sensitivity to initial nickel mass (Kasen, 2006). However, the current sample size of NIR lightcurves is only ~ 200 SNeIa whereas there are over 1000 well-observed SNeIa at optical wavelengths.

Several surveys have already been done, and some are still on going to increase this sample size including CSP-I, II (Contreras et al., 2010; Stritzinger et al., 2011; Kattner et al., 2012), CfA (Wood-Vasey et al., 2008; Friedman et al., 2015), and RAISINS (Kirshner, 2012). Work has also been done on a more individual scale from Kevin Krisciunas (Krisciunas et al., 2000, 2004a,b, 2009) (to name a few), Barone-Nugent et al. (2012), hereafter BN12, and Stanishev et al. (2015), hereafter S15. Except for BN12, RAISINS, and S15, all of the supernovae have been gathered at redshifts less than 0.03. Below $z = 0.03$ the peculiar velocities of host galaxies are a significant source of error when determining distances. BN12 observed 12 SNeIa at $0.0312 < z < 0.0817$, RAISINS uses the Hubble Space Telescope to observe the second peak in NIR lightcurves at $0.2 < z < 0.5$ but have not yet published any data, and S15 observed 16 SNeIa with $0.037 < z < 0.183$. SweetSpot was created to help fill in the redshift space in the nearby smooth Hubble flow.

SweetSpot was a National Optical Astronomy Observatory (NOAO) survey program to gather NIR lightcurves of SNeIa located in the nearby smooth Hubble flow at redshifts $0.03 - 0.08$. Its goal was to collect 144 SNeIa in 72 nights over three years during the NOAO semesters 2012B - 2015A at the WIYN 3.5-m Observatory[1] located at Kitt Peak using the WIYN High Resolution Infrared Camera (WHIRC; Meixner et al., 2010; Smee et al., 2011). The primary goals of this survey are to extend the Hubble diagram out to a redshift of 0.08 in H-band, quantify how standard SNeIa are in the NIR with a focus on the H-band, improve understanding of NIR colors, and provide a well-calibrated NIR restframe sample for future higher-redshift surveys such as WFIRST. Among the currently published data sets, SweetSpot will not only increase the sample size by 50% but will also be the largest data set from a single survey.

A current major area of research with optical lightcurves is exploring how host galaxy properties correlate with the brightness of SNeIa. Optical studies have shown that after correcting lightcurves for stretch and color, there still appears to be a correlation with characteristics of its host galaxy such as mass, metallicity, age, and local and global star formation

---

[1] These observations were taken when the WIYN Observatory was a joint facility of the University of Wisconsin-Madison, Indiana University, Yale University, and the National Optical Astronomy Observatory. `http://www.wiyn.org`

rates (SFRs) (Sullivan et al., 2006; Gallagher et al., 2008; Kelly et al., 2010; Sullivan et al., 2010; Lampeitl et al., 2010; Gupta et al., 2011; D'Andrea et al., 2011; Hayden et al., 2013; Johansson et al., 2013; Childress et al., 2013a,b; Rigault et al., 2013, 2015; Moreno-Raya et al., 2016; Campbell et al., 2016). These analyses have not been conducted using NIR lightcurves as the data sample has not been sufficiently large. However, the addition of SweetSpot SNeIa will drastically increase the NIR sample size reducing the statistical noise as well as reducing systematics since all of the SweetSpot SNeIa will be calibrated to the same system. Chapter 4 will explore global correlations between NIR lightcurves and global host galaxy properties using publicly available data. Rigault et al. (2013, 2015) showed a strong correlation with local (within 1-2 kpc of the supernova site) star formation rates, which is more significant than trends with global SFRs. This analysis was done using integral field spectroscopy (IFS) that yields spatially resolved spectra. Since similar data for most host galaxies is not publicly or even privately available, we began a campaign to collect this information.

We gathered 32 host galaxies in 4 telescope nights using the fiber bundle HexPak (Wood et al., 2012) mounted on the WIYN 3.5-m telescope. These observations were taken in 2015B after all of our SNeIa had faded to below detection threshold so that their flux did not contaminate our observations. Our goal was to measure Hα emission lines to determine star formation rates in the local area around the supernova explosion site. We here present our observations, data reductions, and Hα surface brightness maps. Future work will carry out the calculations for SFRs within 1-2 kpc of the explosion site and analyze host galaxy correlations.

This chapter is organized as follows: We briefly describe the telescope in Section 3.2 then outline the main SweetSpot survey in Section 3.3. All other sections will focus on the observations and data reductions of HexPak spectra for host galaxies of 32 SNeIa in the SweetSpot survey. The HexPak analysis is organized as follows: We outline the instrument and observational set up in Section 3.4. We detail the data reduction process in Section 3.5. Section 3.6 presents methods for and results from measuring Hα. We briefly conclude SweetSpot photometric and spectroscopic observations in Section 3.7.

3.2 WIYN 3.5-M TELESCOPE

We used the WIYN 3.5-m Telescope for both our NIR photometric observations and optical spectroscopic observations. (Hα is at optical wavelengths, 6572–7022 Å, for all redshifts that we observed.) Located at the Kitt Peak National Observatory (KPNO), this facility had first light in 1994 and was funded through the joint partnership of University of Wisconsin-Madison, Indiana University, Yale University, and the NOAO. It is a Ritchey-Chrétien design with an altitude-azimuth mount. The Ritchey-Chrétien design allows it to be shorter than traditional Newtonian telescopes and less affected by comas and spherical aberrations. The altitude-azimuth mount moves the telescope along both the vertical and horizontal axes to track objects as the Earth rotates. The primary mirror is 3.5-m, the secondary mirror is 1.2-m, and the tertiary mirror is 1.2-m by 0.8-m and is flat whereas the first two mirrors are hyperbolic. The WIYN 3.5-m has several ports to hold multiple detectors at the same time. The current list of all possible detectors includes two optical imagers: the One Degree Imager with a partially-filled focal plane (pODI; Harbeck et al., 2014) and NASA Exoplanet Star (and) Speckle Imager[2] (NESSI); the NIR imager WHIRC; and the WIYN Bench Spectrograph (Bershady et al., 2008) with several IFUs: HexPak/GradPak (Wood et al., 2012), SparsePak (Bershady et al., 2004, 2005), and Hydra (Barden et al., 1994).

3.3 SWEETSPOT SURVEY

3.3.1 WHIRC and WTTM

SweetSpot used the WHIRC (Meixner et al., 2010; Smee et al., 2011) NIR detector mounted on the WIYN Tip/tilt Module (WTTM) port (Claver et al., 2003). It has three broad band filters of J, H, and K_S centered at 1.250 μm, 1.651 μm, and 2.168 μm, respectively. WHIRC has several narrow band filters as well, but we did not make use of them. The instrument has a 2048x2048 Raytheon Virgo HgCdTe detector with a 3.3 arc minute (') field of view

---

[2] `http://www.wiyn.org/Instruments/wiynnessi.html`

and a 0.1 arc second (") pixel scale. The WTTM tip/tilt correction can provide image stabilization that improved the seeing of our images by $\sim 0.1 - 0.2$". However, the weather must be mostly clear with native seeing at or below $\sim$ 1.5", and it requires there to be a bright star within the field of view that stays in the field of view during any dithers.

The WTTM mirror was recoated in the summer of 2013 between our 2013A and 2013B semesters. This update significantly improved the signal levels and led to a noticeable difference in our measured zero points between 2011B–2013A data and 2013B data in SweetSpot's first data release (Weyant et al., 2017).

3.3.2 Survey Strategy

SweetSpot did not discover any of the supernovae used in its survey. We were reliant upon the supernova community to find, spectroscopically classify, and publish young SNeIa. We made use of Astronomer's Telegrams[3], IAU Central Bureau for Astronomical Telegrams (CBETs)[4], and the website Bright Supernova[5] managed by David Bishop to find supernovae that had been spectroscopically classified as Type Ia, within redshift of 0.03–0.08, and would be within two weeks of maximum light for their first observation.

Our goal was to collect 3–6 lightcurve points in J and H for the majority of our objects and 6–10 lightcurve points in J, H, and K_S for objects $z < 0.03$. The background sky and the detector plus telescope noise in the K_S filter is too bright to observe higher redshift objects. Figure 3.1 shows that we reached a median of 3 light curve points for H and J, but less frequently observed K_S.

In the NIR, not only is the night sky bright, but the detector and the telescope system also provide significant noise. Because of the contamination from the observing set up itself, we dithered our observations instead of exposing for longer times to drive down noise from the night sky and the detector plus telescope system and to remove any detector defects. A single integration was one minute, and we dithered in 3 patterns: 3x3 with 30" offsets, 4x4 with 20" offsets, and 5x5 with 15" offsets. These cover about 4' by 4' on the sky. Along with

---

[3] http://www.astronomerstelegram.org/

[4] http://www.cbat.eps.harvard.edu/

[5] http://www.rochesterastronomy.org/snimages/

dithering on our main science images, we also observed and dithered on Persson standard stars (Persson et al., 1998) to use for calibration.

For the latest data processing and more in-depth information about observing strategy, see DR1 (Weyant et al., 2017).

3.3.3 Statistics from Survey

SweetSpot was awarded 88.5 nights and observed 114 SNeIa, with an additional 12.5 nights to gather host galaxy templates, and in total used 1.8 megaseconds of open shutter time (see Table 3.1 for break down of seconds integrated and number of science frames taken). We also collected 1 type Ibn supernova on request from Isaac Shivvers whose resulting paper has already been accepted for publication (Shivvers et al., 2017). Figure 3.2 shows the location of our supernova projected on the sky in Right Ascension (RA) and Declination (Dec). Our sample is uniform on the night sky that is observable from Kitt Peak except for the overcrowded plane of the Milky Way. Figure 3.3 contains postage stamps for all 115 of the SweetSpot supernovae in order of increasing redshift. Our lowest redshifted SNeIa is at $z = 0.00068$ (SN 2014J) and our highest redshifted SNeIa is at $z = 0.094$. Our sample's median redshift is 0.035, and Figure 3.4 shows the full redshift distribution. The current literature sample (excluding S15) has a median redshift of only 0.026, which is where peculiar velocities are still the dominant source of error in distances.

Many of our supernovae exploded in locations that were heavily contaminated by their host galaxy flux. To correct for this flux, we returned to a field roughly one year after the explosion when the flux of the SNeIa was not visible. We took host galaxy templates with exposure times 3 times as long as the longest exposure on the supernovae. For example, if we had 9 minutes of total integration time on a target, we collected a host galaxy observation that was 25 minutes, and if we took a 50-minute exposure, the host galaxy template had to be at least 150 minutes. Due to the time-consuming collection of host galaxies, we did not observe the planned 144 SNeIa. We were not able to collect all of our host galaxy only exposures during the main part of the survey and were awarded an extra 12.5 night (not included in the original 88.5 nights) to complete them.

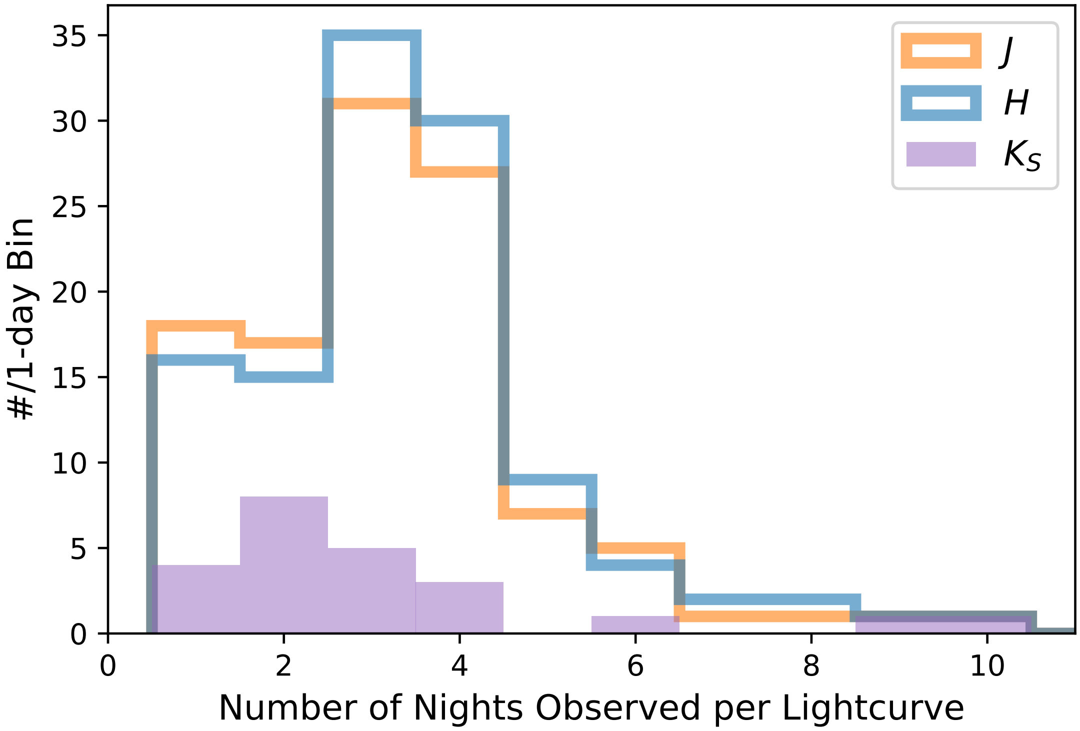

Figure 3.1 Histogram of the number of lightcurve points taken per filter per object. Median number of lightcurve points in $(J, H, K_S) = (3.0, 3.0, 2.0)$.

Table 3.1. SweetSpot Survey Summary of Total On-Sky Time

Category	Total	J	H	K_S
Total Number of Seconds integrated	1,858,790	909,611	788,068	107,479
Total Number of Science Frames	38,717	15,856	18,005	4,316
Total Number of Standard Star Science Frames	7,021	2,341	2,409	2,270
Total Science Frames in Preliminary	2,656	1,022	1,439	94
Total Science Frames in Main Survey	40,375	14,996	18,037	5,828
Total Science Frames in Template Follow-up	6,103	2,165	2,660	798

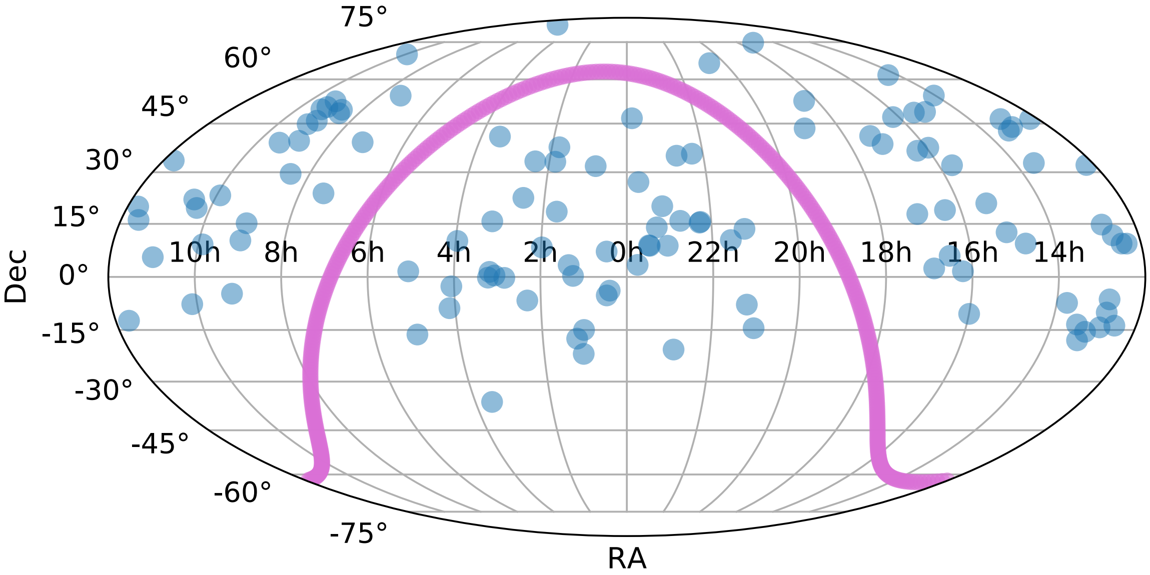

Figure 3.2 Location of the 115 SweetSpot supernova projected on to the sky. The purple line shows the path of the Milky Way.

Weyant et al. (2014), hereafter W14, presented the first results from the pilot semester of the SweetSpot Survey from 2011B semester. W14 presented 13 out of 18 SNeIa that were observed in Fall 2011. They showed that using SweetSpot SNeIa located in the nearby smooth Hubble flow ($0.03 < z < 0.1$) resulted in a scatter of only 0.16 mag without any lightcurve corrections. The lightcurves only had 1–4 points per band, which showed that sparsely-sampled NIR lightcurves could do precision cosmology. Using a combined literature dataset of 108 SNeIa, W14 constructed the most up-to-date Hubble diagram with the highest redshift NIR SNeIa at that time ($z = 0.094$) and found the scatter in all of the literature data set to be 0.22 mag.

Table 3.2 summarizes the number of nights awarded per semester, number of supernovae, and number of host galaxy templates or spectra observed. The pilot semester and the single night from 2012A are listed as "preliminary" as they are not part of the main survey that was from 2012B–2015A. The nominal time for Data Release 1 (DR1) is SNeIa observed between 2011B–2013B and the time for DR2 is supernovae observed between 2014A–2015A, which split our survey in half. 74 SNeIa and 33 lightcurves have been made public in DR1 (Weyant

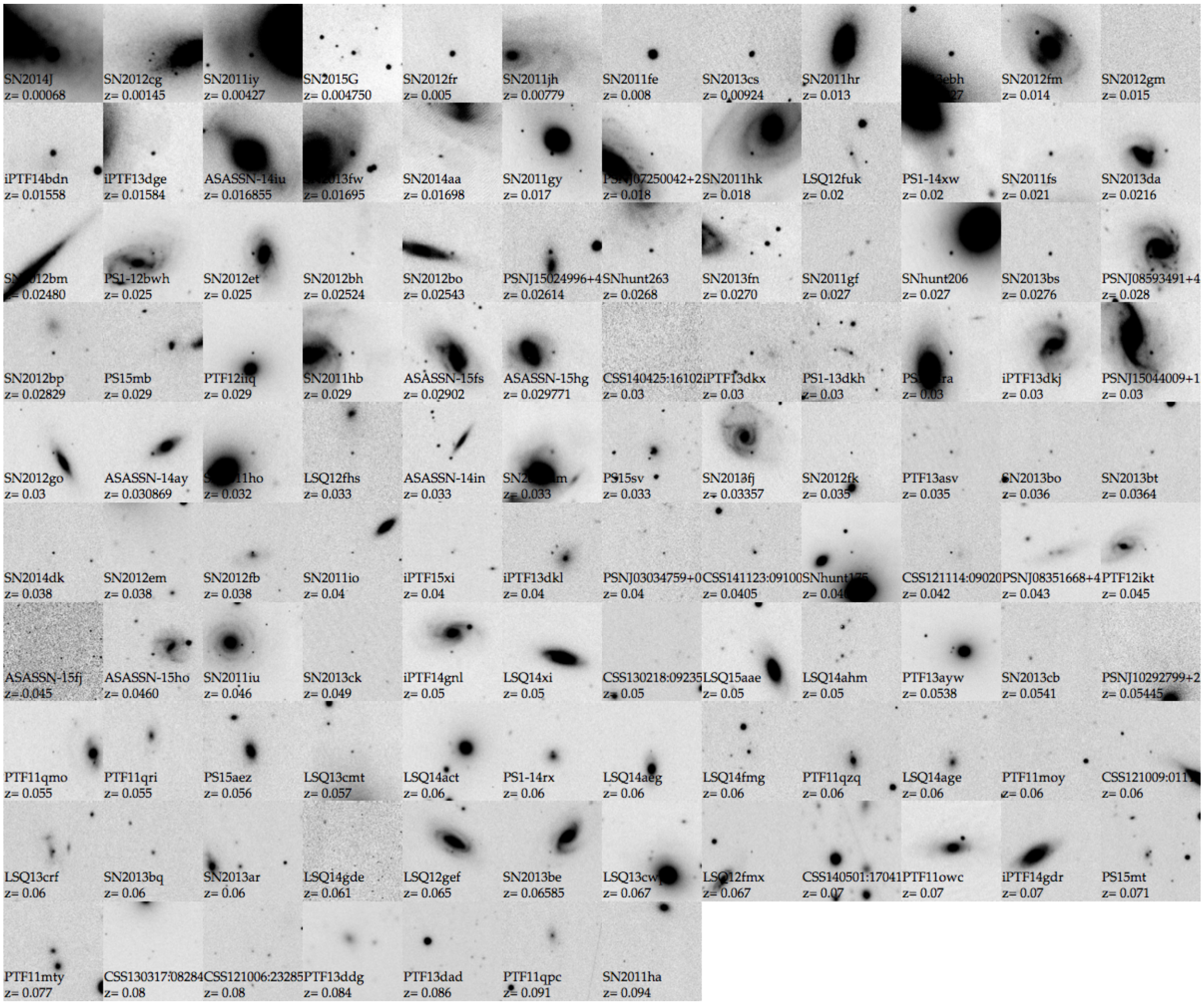

Figure 3.3 20" by 20" cutouts of all 115 supernovae ordered by increasing redshift.

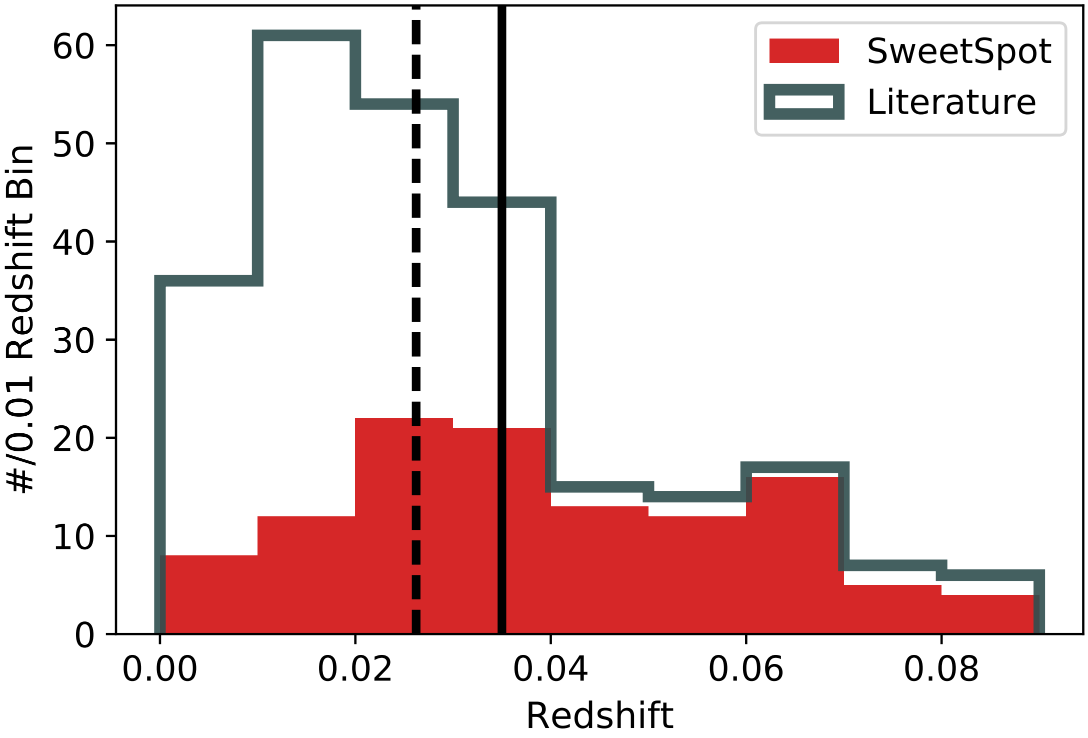

Figure 3.4 Redshifts of SweetSpot supernovae versus the literature data set (taken from Weyant et al. (2014)). This literature data set does not include the 16 SNeIa from S15. Median redshifts of the SweetSpot survey and literature data set are noted in the solid and dashed black lines, respectively.

et al., 2017), which was submitted to American Astronomical Journals in March 2017. Anja Weyant carried out most of the observations from 2011B–2013B and K.A.P. did the majority of the observing from 2014A–2017A. Michael Wood-Vasey also observed at least 10 nights and Jessica Kroboth observed for 7 nights. Also recorded in this table are the 4 nights that we gathered spectra from our host galaxies after the SNeIa had faded with HexPak.

3.3.4 Status of Data and Science Releases

DR1, presenting data from 2011B–2013B, was submitted for publication in March 2017, and we are working on the referee's comments. DR2 is planned for early 2018 and will contain all, or most, host galaxy subtractions for DR1 and DR2 SNeIa. We are planning to take more observations to quantify if all of our objects need host galaxy subtractions or if only the most contaminated SNeIa need them. DR3 will be our final data release and will contain improved host galaxy subtractions and calibration.

One driving factor of not completing the analysis of host galaxy correlations with local properties is that DR1 only released 3 lightcurves and all others need host galaxy templates or will be released in DR2. The cause of this delay is partially by the design of the HexPak observations as we wanted to observe galaxies that hosted SNeIa with obvious host galaxy flux near the location of the explosion site, but this has caused a delay in the release of the scientific analysis.

3.4 HEXPAK DATA RELEASE OF 32 SWEETSPOT HOST GALAXIES: OBSERVATIONS

3.4.1 Description of HexPak

HexPak (Wood et al., 2012) is a variable-pitch (containing multiple fiber sizes) integral field unit (IFU) mounted on the WIYN 3.5-m telescope. HexPak and its companion GradPak are the first variable-pitch IFUs ever built. They share a single cable and mount, but only one unit may be used at one time. Both of these use the same slit to feed into the WIYN

Table 3.2. SweetSpot Survey Summary of Nights Observed

	Semester	# of Nights	# of SNe	# of Hosts
Preliminary	2011B[a]	7	18	–
	2012A[a]	1	4	4
DR1	2012B[a]	8	19	5
	2013A[a]	11	16	–
	2013B[b]	10.5	15	6
DR2	2014A	20.5	16	12
	2014B	16.5	14	13
	2015A	14	12	7
HexPak	2015B	4	–	32
Template	2015B	6	–	11
Follow-up	2016A	5	–	7
	2017A	1.5	–	2
Total		110	115	99[c]

[a] Anja Weyant carried out the majority of these observations.

[b] Anja Weyant carried out the majority these observations with K.A.P. assisting on 3 nights and leading on 1.

[c] These are not unique host galaxy observations. Some were observed in multiple semesters if the template was not observed with satisfactory seeing.

Bench Spectrograph[6]. HexPak consists of "small" fibers with a diameter 0.94 arc second (") arranged in a circle surrounded by "large" fibers with diameters of 2.9" arranged in a hexagonal pattern, see Figure 3.5. This configuration is optimal for face-on galaxies. The large fibers span roughly 41" by 36", and small fibers span about 6" in diameter. There are 7 large sky fibers and 2 small sky fibers which are located over 43" to the right and above the configuration seen in Figure 3.5. The large fibers were recycled from DensePak (Barden et al., 1998), and SparsePak (Bershady et al., 2004) and have varying levels of sensitivity as a function of wavelength.

3.4.2 Configuration of the WIYN Bench Spectrograph

HexPak feeds into the WIYN Bench Spectrograph using the Hydra red cable. We used the 600@10.1 grating, 600 lines/mm with a blaze angle of 10.1° at order 1, with a spectral resolution of 3.35. Our setup centered at 6000 Å and ranged from 4600 Å to 7400 Å. The Bench uses the STA1 Charge-Coupled Device (CCD) with 2600 by 4000 pixels, and we used the medium gain of 0.4 electrons/ADU. For one night (2015 November 16), we did not bin the CCD; however, on the other three nights, we used 2x2 binning. The observations with 1x1 binning are noisier resulting in approximately 2.4 times greater error in Hα surface brightness for large fibers and 3.2 times higher in the smaller fibers.

3.4.3 Wifoe Camera

The Wifoe Camera[7] is used to determine pointing. It consists of an Allied GigE GT3300 CCD with a default 5x5 binning giving a scale of 0.258" per pixel. To determine pointing, we took a short exposure of the current field and looked for objects with which to align. Then we turned on the back illuminator to project the locations of the fibers on to the CCD, see Figure 3.6. From this, we determined if the pointing was sufficient or if we needed to put in offsets. Unfortunately, when switching from the Wifoe camera to the main science setup, the positions might change by a few arc seconds. We saved both the longer images of the

---

[6] `ftp://ftp.noao.edu/kpno/hydra/hydrawiynmanual.pdf`

[7] `http://www.wiyn.org/Instruments/WifoeCameraInterface.pdf`

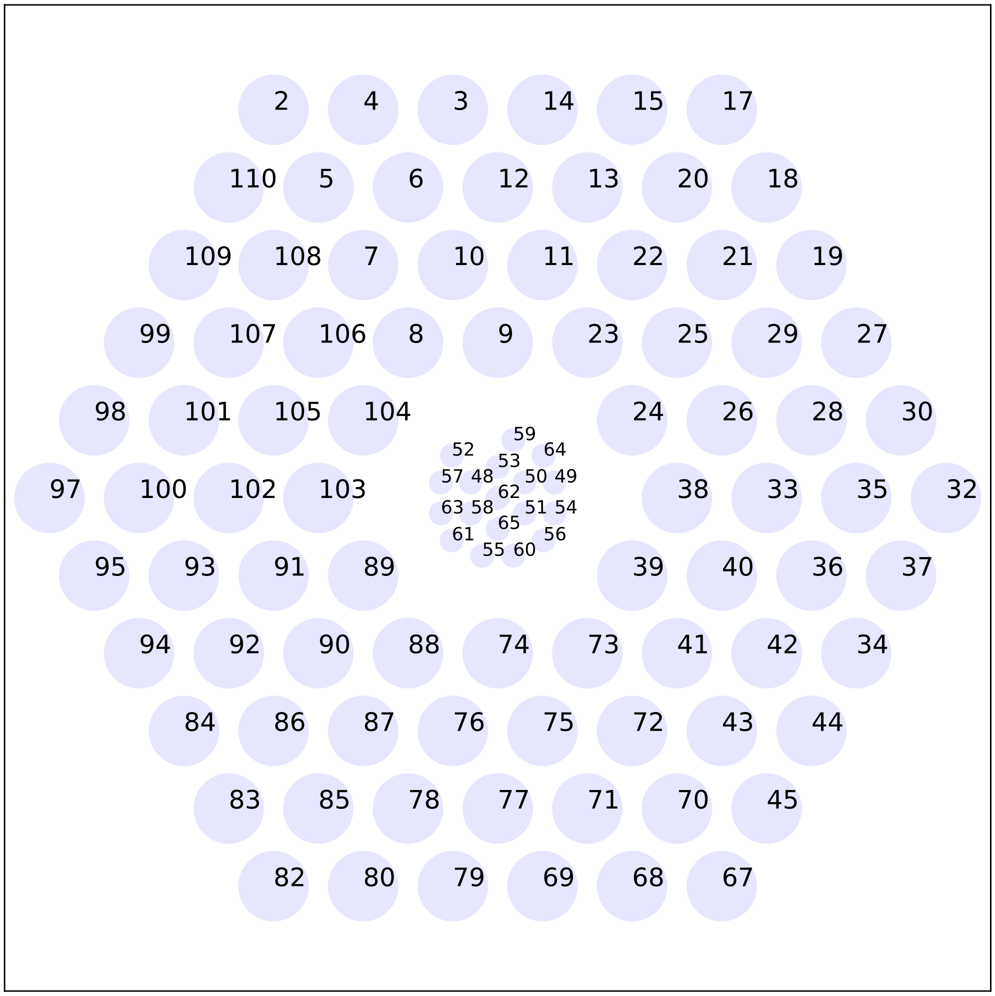

Figure 3.5 Bundle configuration and fiber locations. The small fibers in the middle are 0.94” and the large fibers around them are 2.9”. The missing small fiber in the upper left side was dead upon arrival. The numbers correspond to the ordering of the spectra on the CCD. Small fibers are projected onto the middle of the CCD. Not included here are the 9 sky fibers (2 small and 7 large) that are located to the right and above this configuration.

field of view and the shorter images with the fibers on sky for all pointings.

3.4.4 Calibration Observations

Due to the variable-pitch nature of the bundle, we had to take calibration observations of different lengths to accommodate the different collecting areas. Since on 2015-11-16 we used 1x1 binning and the other 3 nights we used 2x2 binning, we took different calibrations for the first night versus the other three.

Calibration images taken each night:

- **Bias:** We collected 5-10 exposures during the free time in the night (long slewing time, using a different detector, etc.).
- **Darks:** 11 exposures were taken at 1200 seconds each morning after observations.
- **Domeflats:** These were taken each afternoon before the run. We gathered 30-second and 10-second exposures for 1x1 and 2x2 binning, respectively, to have a good signal in the small fibers. Given the different collecting areas, these exposures saturated the large fibers, so we took additional 5-second and 2-second exposures. For every exposure time, we saved 6 frames.
- **Comparison Lamps:** We used the Copper Argon lamp and took these twice during each night: once in the afternoon and once in the middle of the night. In both binning modes we collected 3 frames at 10 and 60 seconds; however, sometimes the second comparison lamp was only exposed for 60 seconds. On nights with 2x2 binning, we occasionally took 1- or 2-second comparison lamps, but the data reduction process did not use them.
- **Twilight Flats:** Taken at the beginning of the night, except for 2015-11-16 when we took them in the morning. We observed these at varying exposure times depending on the amount of light in the fibers. Longer exposures often gave a good signal in the small fibers but saturated the large fibers.
- **Standard Stars:** We observed BD+284211, a blue star, and Hiltner 600, a red star, once per night at different times. Most nights, they were observed on multiple fibers to improve flux calibration.

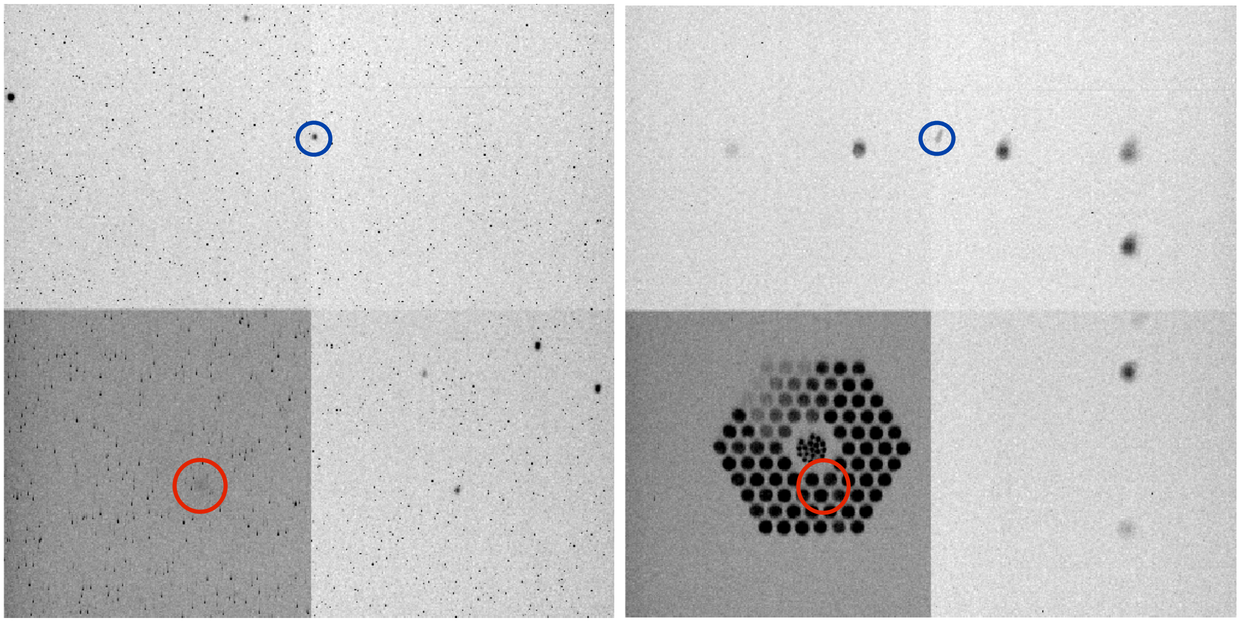

Figure 3.6 Wifoe images of field SN 2013fj / PGC 68419. *Left:* A 5 second exposure with the pointing camera. The galaxy is in the lower left hand panel as a faint, poorly-resolved, slightly darker smear and is circled in red. We also circled a star in blue that is within the aperture of one of the sky fibers. *Right:* A 0.2 second exposure with the back illuminator on to indicate where the fibers fall on the field of view. The location of the star in the Left plot is again circled in blue and on top of it is an imprint from a small fiber. This is the only object where a star fell into the field of view of a sky fiber. The location of the galaxy is also circled in red.

3.4.5 Descriptions of Observations and Host galaxy sample

Rigault et al. (2013) referred to as R13, showed a greater dependence on local star formation rates (SFRs) than on global SFRs. Figure 5 in R13 illustrates the relationship between local and global SFRs with globally star-forming galaxies hosting regions of passive and active star formation while globally passive galaxies are locally passive. Our goal in this study is to examine spiral galaxies that hosted supernovae in the SweetSpot sample, for this reason, HexPak was the ideal instrument. However, this means that our sample is biased and all conclusions from it will need to account for this. We observed 32 host galaxies with 27 spiral and star-forming galaxies and 5 elliptical galaxies. All of the spirals are face-on or slightly inclined, i.e. no edge on galaxies. One of the spiral galaxies is in a merging system, but the location of the supernova explosion is well removed from the area of interaction. Most of our fields contain supernovae that were heavily contaminated by host galaxy flux though several are quite removed. We also preferentially chose galaxies that would span several fibers, so our sample is biased towards massive, low-redshift galaxies. Table 3.3 gives a summary of the fields observed, and Figure 3.7 shows the redshift distribution of our sample. Citations for supernova and host galaxy properties can be found in Appendix A.1 in Table A1.

We took either three 10-minute exposures, two 10-minute and one 20-minute exposure, or two 10-minute and two 20-minute exposures. The exposure time depended on the redshift of the host galaxy, the size of the galaxy, and if Hα was visible in the raw spectrum. We did not dither our observations; however, if the host galaxy is exceptionally big (SN 2011hb/NGC 7674) or interesting (SN 2014dm/NGC 1516A), we took additional exposures at new pointings that target the galaxy as a whole instead of the site of the supernova. If we took multiple pointings of a galaxy, some pointings would only have two 10 minute exposures. We gathered 41 pointings of 32 different host galaxies. Table 3.4 details number of targets observed per night. All nights were clear, but 2015-11-16 and 2015-11-17 had seeing of 1.5–2.5”, which is important to note as the small fibers are only 1” and will affect absolute flux calibrations. Note on 2015-11-30: During this night we switched detectors from HexPak to WHIRC to observe a host galaxy template for the main SweetSpot survey.

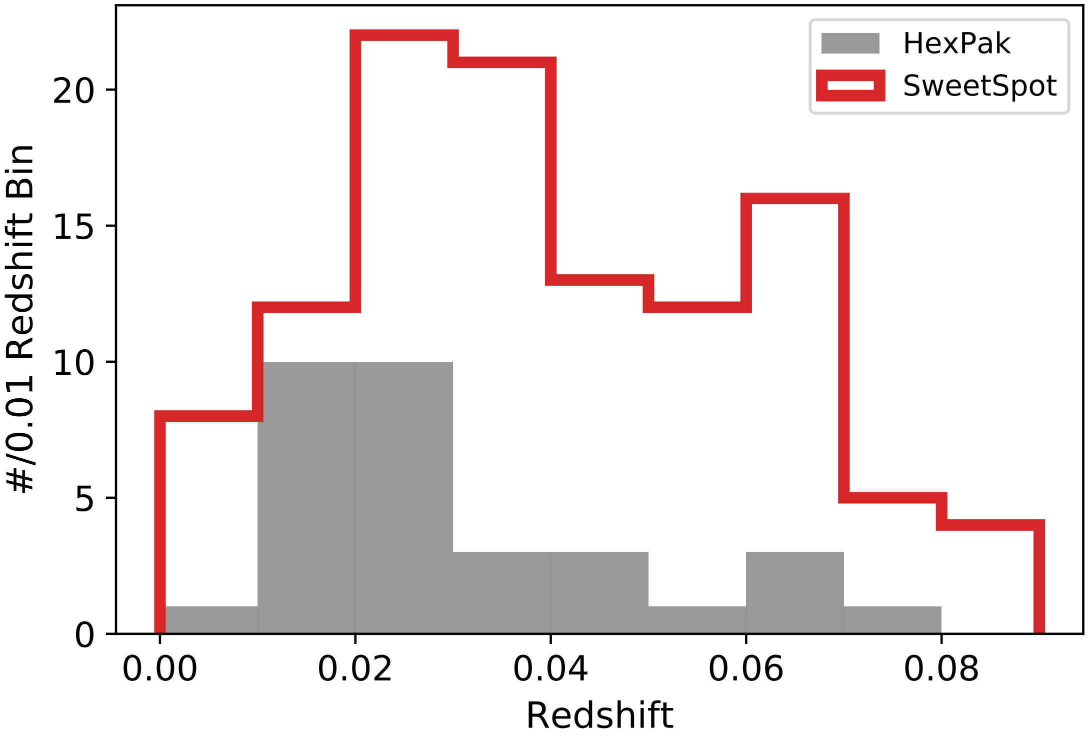

Figure 3.7 Redshift distribution of the supernovae observed in HexPak host galaxies versus the distribution from the full SweetSpot survey with 114 SNeIa.

Table 3.3. Targets Observed with HexPak

Name[a]	Host Name	R.A.	Dec.	Host R.A.	Host Dec.	Offset (")	z_{SN}	z_{Host}	Type
ASASSN-15hg[a]	CGCG 063-098	09:53:48.62	+09:11:37.8	09:53:49.2	+09:11:38	8.59	0.029771	0.029771	Ia
ASASSN-15ho	2MASXi J0909234-044327	09:09:23.89	-04:43:30.10	09:09:23.4	-04:43:27	7.95	0.046	0.041	Ia
LSQ12gef	2MASX J01403375+1830406	01:40:33.751	+18:30:36.74	01:40:33.7	+18:30:41	4.32	0.065	0.0648	Ia
LSQ14aeg	2MASX J10193682+1933131	10:19:36.79	+19:33:20.3	10:19:36.8	+19:33:14	6.30	0.06	0.064676	Ia
PS1-12bwh	CGCG 205-021	07:09:24.29	+39:06:15.8	07:09:24.8	+39:06:12	7.05	0.023	0.023203	Ia Pec
PS15mb	SDSS J085940.13+151113.5	08:59:40.20	+15:11:12.5	08:59:40.13	+15:11:14	1.81	0.029	0.028724	Ia
PSN J07250042+2347030[a]	NGC 2370	07:25:00.408	+23:47:03.15	07:25:01.6	+23:47:00	16.66	0.018	0.018346	Ia
PSN J08593491+4555343	UGC 4709	08:59:34.91	+45:55:34.3	08:59:34.6	+45:55:36	3.65	0.0281	0.028101	Ia
PSN J10292799+2200468	UGC 5691	10:29:27.99	+22:00:46.8	10:29:27.5	+22:00:29	19.06	0.05	0.054453	Ia
PTF12iiq	2MASX J02500784-0016014	02:50:07.786	-00:15:54.04	02:50:07.8	-00:16:01	6.96	0.0291	0.029142	Ia
PTF12ikt	2MASX J01144386+0017100	01:14:43.13	+00:17:07.1	01:14:43.8	+00:17:10	10.46	0.045	0.045185	Ia
iPTF13dge[a]	NGC 1762	05:03:35.091	+01:34:17.03	05:03:37.0	+01:34:24	29.46	0.01584	0.015854	Ia
iPTF13dkj	CGCG 454-001	23:08:50.737	+20:04:08.59	23:08:50.7	+20:04:12	3.45	0.03	0.036232	Ia
iPTF13ebh	NGC 890	02:21:59.98	+33:16:13.7	02:22:01.0	+33:15:58	20.25	0.01327	0.013269	Ia
iPTF14gdr	2MASX J00275880-0513014	00:27:58.35	-05:12:59.5	00:27:58.8	-05:13:01	6.89	0.07	0.0695	Ia
SN 2011gy	MCG +07-08-15	03:29:35.319	+40:52:02.93	03:29:35.1	+40:52:08	5.64	0.017	0.016882	Ia
SN 2011hb[a]	NGC 7674	23:27:55.508	+08:46:45.45	23:27:56.7	+08:46:45	17.68	0.029	0.028924	Ia
SN 2011hk	NGC 881	02:18:45.801	-06:38:30.45	02:18:45.3	-06:38:21	12.04	0.018	0.017555	Ia Pec
SN 2011hr	NGC 2691	08:54:46.056	+39:32:16.02	08:54:46.3	+39:32:19	4.10	0.013	0.013279	Ia Pec
SN 2011iu	UGC 12809	23:51:02.342	+46:43:21.55	23:51:03.2	+46:43:25	9.47	0.046	0.045985	Ia
SN 2012cg	NGC 4424	12:27:12.826	+09:25:12.93	12:27:11.6	+09:25:14	18.17	0.001458	0.001458	Ia
SN 2012et	CGCG 476-117	23:42:38.747	+27:05:31.02	23:42:38.4	+27:05:31	4.63	0.025	0.024961	Ia
SN 2012fm	UGC 3528	06:56:13.39	+84:04:50.2	06:56:10.9	+84:04:44	7.30	0.014	0.014553	Ia
SN 2012gm	NGC 7580	23:17:37.055	+14:00:08.89	23:17:36.4	+14:00:04	10.71	0.015	0.01479	Ia
SN 2013be	IC 3573	12:36:27.638	+11:45:27.96	12:36:27.2	+11:45:33	8.17	0.06585	0.065846	Ia
SN 2013fj	PGC 68419	22:15:28.48	+15:34:03.19	22:15:28.7	+15:34:10	7.51	0.03357	0.03357	Ia
SN 2013fn	IC 1342	21:00:23.673	-14:29:52.42	21:00:25.4	-14:29:45	26.15	0.027	0.026975	Ia
SN 2013fw[a]	NGC 7042	21:13:44.763	+13:34:33.33	21:13:45.8	+13:34:30	15.48	0.01695	0.016952	Ia-HV
SN 2014aa	NGC 3861	11:45:03.58	+19:58:25.4	11:45:03.9	+19:58:25	4.53	0.01698	0.016982	Ia
SN 2014dm[a]	NGC 1516A	04:08:07.13	-08:49:37.2	04:08:07.4	-08:49:45	8.77	0.03	0.03318	Ia
SNhunt206	NGC 766	01:58:42.759	+08:20:39.51	01:58:41.9	+08:20:48	15.32	0.027	0.027032	Ia
SNhunt263	UGC 4798	09:08:42.48	+44:48:13.2	09:08:42.6	+44:48:38	24.83	0.0268	0.026762	Ia

[a] Multiple pointings were observed.

Table 3.4. Nights Observed with HexPak

Date[a]	# Observations[b] Galaxies	Stars	Seeing
2015-11-16	11	4	Bad
2015-11-17	10	8	Bad
2015-11-30	8	7	Good
2015-12-01	12	10	Good

[a] YYYY-MM-DD of local evening at KPNO (MST).

[b] Number of pointings, not number of objects.

3.5 HEXPAK DATA RELEASE OF 32 SWEETSPOT HOST GALAXIES: PROCESSING OF IFU DATA

Data processing is based on the **Guide to Reducing IFU Data, 2015, with Specific Application to "Pak" Family of IFUs Feeding the Bench Spectrograph at WIYN** shared privately by Eric Hooper. The reduction steps are done using PyRAF.

1. **Data Transfer and Uncompression:** We followed steps 1 and 2 from SweetSpot Data Release 1 (Weyant et al., 2017) to transfer and uncompress images from the NOAO Science Archive. We used ftp directly to transfer the Wifoe images from the computers on Kitt Peak to University of Pittsburgh computers.
2. **Overscan Correction:** The overscan correction is used to remove the bias level and the read noise and is implemented with `noao.imred.ccdred.ccdproc` with `oversca = yes` in PyRAF. This process creates a smooth function from averages of the overscan region with interactive fitting to a 100th order Legendre polynomial. The program marked

3σ outliers and removed by hand which resulted in the order of the polynomial to be adjusted down based on the number of deleted points. The mean of the bias ranged from 15595 to 15678 counts. We removed pixels that biased the fits to the overscan region for the comparison lamp exposures, which contained structured outliers, and the dome flat exposures (usually only a few close to the edge). All other exposure types either needed no outliers removed or very few.

3. **Bias/Zero Correction:** Bias frames are used to remove electronic background characteristics of the CCD that are present in every frame. We median combine using `images.immatch.imcombine` with the `ccdclip` algorithm, which utilizes CCD noise parameters from header keywords to create a Poisson noise model to remove outliers. Since bias frames can vary over time, we scaled each frame by a small additive offset calculated from their median values. Since there should not be cosmic rays due to the short exposure time, only 5σ outliers were rejected. After combining the bias frames, we subtract the master Bias from all remaining files (flats, comparison lamps, darks, objects) using `noao.imred.ccdred.ccdproc`.

4. **Dark Correction:** Dark frames are long exposures that are used to remove thermally generated electrons in the CCD. We median combine these frames using `images.immatch.imcombine` with `sigclip`, which calculates outliers based on the standard deviation of the pixels. This method is sensitive to the number of frames combined such that there must be at least 9 frames to remove 3σ outliers on a per-pixel basis. Only the darks have enough frames (11 per night) to use this outlier rejection method. Removing 3σ outliers should be sufficient to remove cosmic rays. We used a median scaling but note that all the scales came out close to 1 (1–1.6). A dark correction is only needed for exposures long enough to accrue electrons from thermal effects and any exposure less than a minute will not be dark corrected. All darks were 1200 second exposures, so to correct exposures that are 180–600 seconds, we multiplied the master Dark by an appropriate factor, i.e. 0.5 for 600 seconds. The master Darks are subtracted from object files (including standard star observations) with `noao.imred.ccdred.ccdproc` using the equivalent exposure time. All dome flats, twilight flats, and comparison lamps have exposure times that are too short to require dark corrections.

5. **Cosmic Ray Removal on All Other Exposures:** We had too few images to use `images.immatch.imcombine sigclip` on flats, comparison lamps, and object files, and we found that `ccdclip` removed a large amount of real data. To remove cosmic rays without removing real data, we used `pycosmic` (Husemann et al., 2012), which is for integral field spectroscopy (IFS). Because the large and small fibers caused inconsistent counts in different areas of the CCD, we treated the areas separately by splicing out the middle of the fits file containing these fibers. Figure 3.8 shows a raw object frame to illustrate why we spliced out the "middle" of the fits file. `pycosmic` is then run separately on the large and small fibers, and the two fits files are then spliced back together for one image containing all the full CCD range. For twilight flats and object frames, we also masked several strong telluric lines, as the program consistently marked them as outliers, and then unmasked them in the final output file.
6. **Combine Comparison Lamps:** These images are used to wavelength calibrate object and twilight flat images. For comparison lamps, we did not stack all of the frames from all exposure times together due to the varying levels of saturation of the large fibers. We median combined all images with the same exposure time (typically 3 frames). We primarily used the 10-second or 60-second exposures to identify lines.
7. **Combine Dome Flats:** The Dome Flat is used to trace the fiber locations along the CCD. To combine the dome flats we median combine after running `pycosmic`. The flats are taken at two different exposure times to try to characterize the small and large fibers. We checked the individual dome flats to see if any images exceeded the linearity limit, which was the case for all long exposure (10/30 second) frames. To account for this, we cut out the small fibers in the 10 (30)-second flats and separately the large fibers in the 2 (5)-second flat for 2x2 (1x1) binning. Both dome flats are then divided by the exposure time so that the counts are per second. We median combined these frames in python without the use of PyRAF as it would not preserve the dimensions of our data as a result of separating the large and small fibers. We then merged the two combinations together to yield one master Domeflat.
8. **Combine Twilight Flats:** The Twilight flat is used to account for relative fiber-to-fiber throughput. We initially took two sets of twilight flats per night: those aimed at

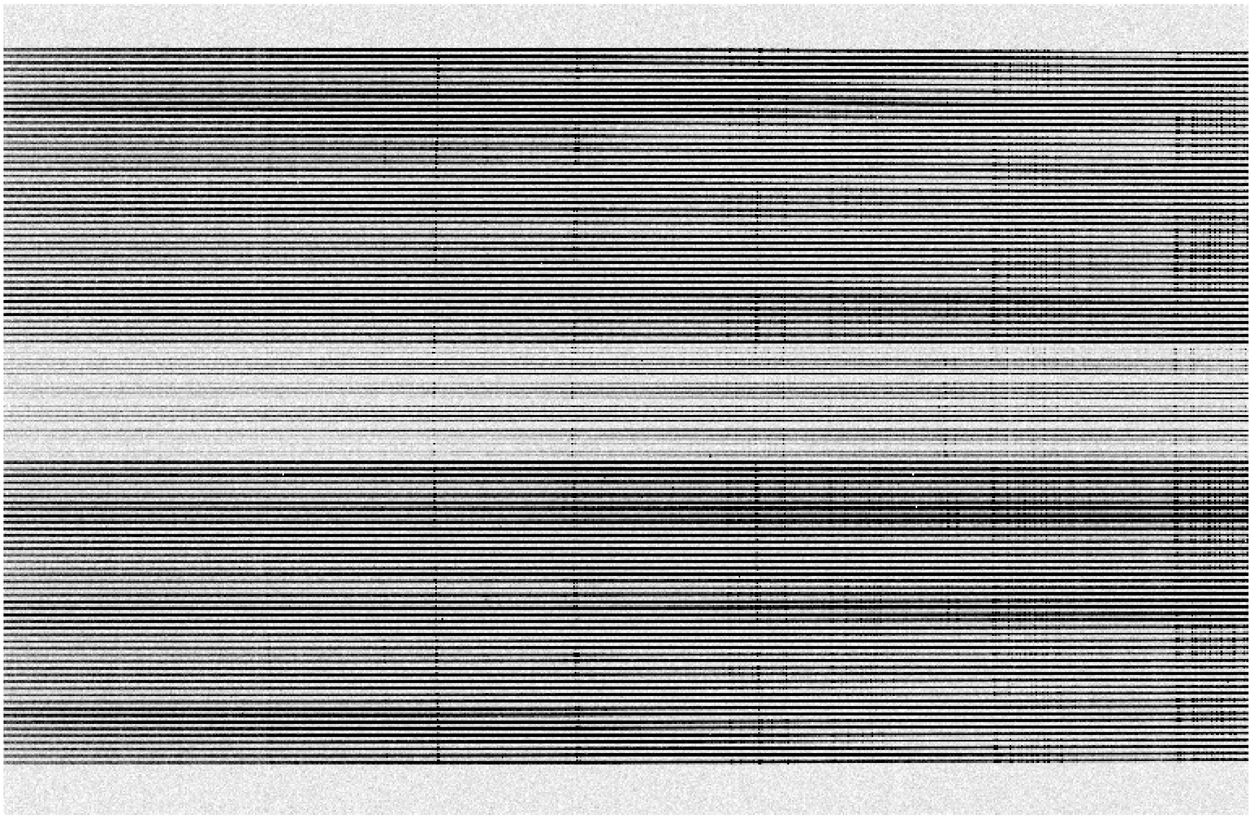

Figure 3.8 Raw object frame before 1D extraction of spectra for SN 2012et / CGCG 476-117. The thicker lines at the top and bottom correspond to the large fibers, while the thinner lines in the middle correspond to the small fibers. Wavelength increases to the right. Most of the structure that can be seen with the eye is from telluric lines; however, Hα plus the two [N II] lines are also obvious in some of the fibers including the small fibers in the middle.

getting sufficient flux in the large fibers (small fibers have low flux) and those aimed at getting sufficient flux in small fibers (large fibers are saturated). We tried to follow the same procedure to combine these as was done for the Domeflat; however, we found that this lead to unusual offsets between the large and small fibers. After much investigation, we determined that the large and small exposures were observed in different conditions because the night sky is changing so rapidly at twilight such that they contained two distinct sources. The Twilight flat could not correctly account for fiber to fiber variations. Instead, we median combined (in python) only the frames where the linearity limit was not exceeded for the large fibers. The result is a master Twilight flat with the small fibers have roughly 1/9th the flux of the large fibers which corresponds to the different physical sizes of the fibers.

9. **Extract Spectra:** In this step, we extract a 1-dimensional spectrum from 2-dimensional data. PyRAF has a built in function to extract IFS data called `noao.imred.hydra.dohydra`. This command was originally implemented for fiber spectra from Hydra and Nessie, which are mounted on the WIYN 3.5-m telescope. This function performs multiple steps: assigns fibers, traces apertures, flat field corrects, and wavelength calibration.

   The first step uses the `hexpak.iraf`[8] file to assign each spectrum a number and denote if it is a sky or object fiber. We use the master Domeflat to trace the apertures since it has a high signal to noise. The size of the aperture extends to the location where the counts have fallen to 5% of the peak value which allows for the large and small fibers to have different aperture sizes.

   The next step traces the fiber with a 50th (100th) order cubic spline for 2x2 (1x1) binning. The root mean square (RMS) of this fit is < 0.002 except for the one night with 1x1 binning that has 0.004 for large fibers and 0.002 for small fibers. After `dohydra` traces all 111 spectra, it combines all traces and fits the combination with a $\sim$35th order cubic spline. It then performs the flat field correction with this combined trace.

   Finally, we identified and marked emission lines from the comparison lamps using the

---

[8] `http://www.astro.wisc.edu/~mab/research/hexpak_gradpak/hexpak.iraf`

Copper Argon templates from the NOAO Spectral Atlas Central[9]. We marked a single fiber located in the small bundle, and the code assigned wavelengths to all other spectra according to this fiber. The header was modified to include the dispersion solution: CRVAL1 contains the first wavelength value (intercept), and CDELT1 is the step/slope. We extract the 1-dimensional spectra for all object frames and master Twilight flat.

10. **Fiber-to-Fiber Throughput:** This step determines the throughput of all the fibers relative to one fiber, typically the fiber that will be used for flux calibration with a standard star. The Twilight flat is used for this correction because it characterizes blue flux better than the Domeflat. Also, the light is coming in at the same angle (infinity) as the science observations.

    Using `onedspec.sarith`, we divide all the fibers by the fiber in which we observed the standard star. Since we are interested in the area around the location of the supernova, we tried to place the standard star on the same fibers that we used for the supernova locations. This step was done several times corresponding to the number of different fibers in which we observed a standard star. If we did not expose a standard star on the same fiber as the supernova, we used the fiber that was spatially closest. We did not use any of the small fibers for fiber-to-fiber throughput or calibration.

    The ratios will be noisy, so we then fit a 25th order spline function to the ratios to get smooth functions with `onedspec.sfit`, see Figure 3.9. Here we fit a smooth function because we are interested in the overall shape of the ratio and do not want to introduce large errors from edge effects. We only use wavelengths between 4618 Å and 7380 Å to reduce the number of outliers included. `onedspec.sarith` is used again to divide all of the fibers in the object files by the smoothed functions.

    See Section 3.5.1 for further discussion of caveats and consequences of using the Twilight flat for fiber-to-fiber throughput.

11. **Removing Sky Background:** Due to the variable responses from the different fibers to blue flux, we subtract the background sky from each object spectrum before flux calibration. We median combined the small and large sky fibers separately, and then subtracted them from the small and large object fibers, respectively. This is implemented

---

[9] http://iraf.noao.edu/specatlas/

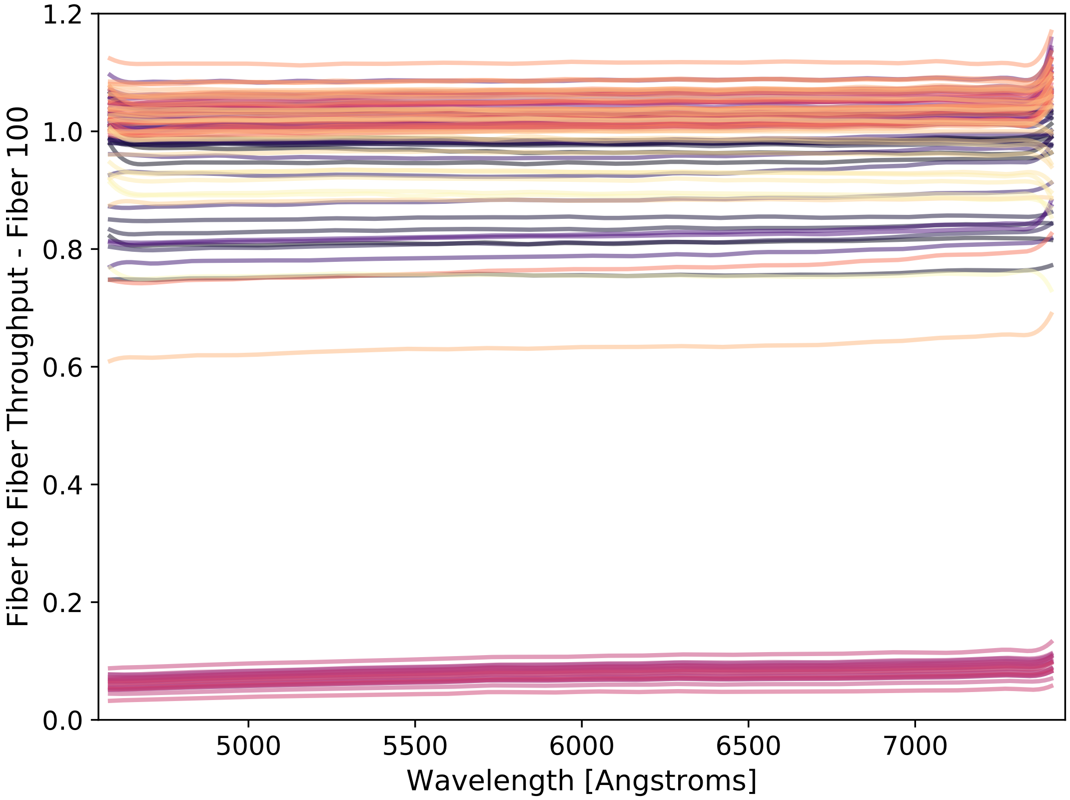

Figure 3.9 Example of the fiber to fiber throughput functions from Twilight flat relative to Fiber 100. When divided by a large fiber, the small fibers group around 0.1 and the large fibers group around 1. This is expected because the collecting area of small fibers is ∼1/9 that of the large fibers. In this example, the grouping is slightly less than 0.1 which is a product of their relationship to Fiber 100. If this plot was instead shown relative to Fiber 20, then the grouping would be centered around 0.1.

using our own Python code.

A few interesting things to note here: (a) The pointing for the host galaxy of SN 2013fj had a star in one of the small sky fibers, see Figure 3.6. For this object, only one small sky spectrum is subtracted from the small fibers instead of an averaged spectrum. (b) The Moon is a significant contributor of flux, especially in the blue, for the second half of 2015-11-30 and 2015-12-01 when the Moon is at 69% and 59% illumination, respectively. The sky fibers show contamination from the Moon before subtraction, but subtracting the sky spectra removed the effect. (c) Most spectra show residuals from telluric lines, see Section 3.5.2 for more in depth discussion.

12. **Flux Calibration** Standard star observations were used for flux calibration. Every night we observed two standard stars (BD+284211 and Hiltner 600) on at minimum two fibers: one large and one small. Though we observed each standard on the small center fiber, we did not use them for calibration. See Section 3.5.3 for more detail. Every night except the first night, we observed the standard stars on multiple large fibers corresponding to where we attempted to place the supernova explosion site, see Table 3.5 for a full list of fibers in which the standard stars were observed.

    To start calibration, we compare our observations of a standard star to its absolute star template using `onedspec.standard`. This function also corrects for the average atmospheric extinction at Kitt Peak and removes the instrumental response function. The output flux file is input to `onedspec.sensfunc` which will fit a sensitivity function using a 10th order cubic spline. Figure 3.10 shows resulting sensitivity functions for different fibers on one night using Hiltner 600 and a single fiber on the same night for BD+284211. The small fiber's sensitivity function is almost the same magnitude as the large fibers (within 10%).

    We repeat this process for all different fibers used to observe the standard stars. We then use `onedspec.calibrate` to calibrate science objects and standard star with the sensitivity function from the appropriate fiber. Tables 3.6 and 3.7 outlines which fiber we tried to place the location of the faded supernova on and which standard star and fiber were used for flux calibration. The final units are erg/cm^2/s/Å.

Table 3.5. HexPak Standard Star Observations

Date	Standard Star	Fiber
2015-11-16	BD+284211	20, 62
2015-11-16	Hiltner 600	20, 62
2015-11-17	BD+284211	62, 100
2015-11-17	Hiltner 600	20, 35, 62, 70, 85, 100
2015-11-30	BD+284211	35, 62
2015-11-30	Hiltner 600	12, 35, 38, 62, 72
2015-12-01	BD+284211	35, 62, 70, 77, 102
2015-12-01	Hiltner 600	35, 62, 70, 77, 102

13. **Combining Objects:** The sky subtracted, flux calibrated spectra are then median combined per pointing.

3.5.1 Caveats of Fiber to Fiber Throughput

The top panel of Figure 3.11 shows the spectrum from the Twilight flat for a large fiber that we commonly use for calibration purposes and so is used for fiber to fiber throughput. At the lowest and highest wavelengths, the counts cut off causing sharp turnovers. It is because of this that we do not fit the edges in Step 10 above.

The bottom panel shows a close up of the reddest part of the spectrum from 6800 to 7400 Å. We have marked the O_2 and H_2O bands that are prominent in this section. Around 7390 Å there is a water line which confuses the continuum flux because its location causes it to be unbounded on one side. Figure 3.9 shows the relative throughput functions are are fit from Step 10 above and they show a steep incline in that last 50 Å. The flux calibration sensitivity functions show this effect since sharp peaks continue to be prevalent as shown in Figure 3.10. Though the spectra continue until around 7407 Å, we suggest that everything beyond 7200–7300 Å should not be used. Removing these wavelengths do not interfere with

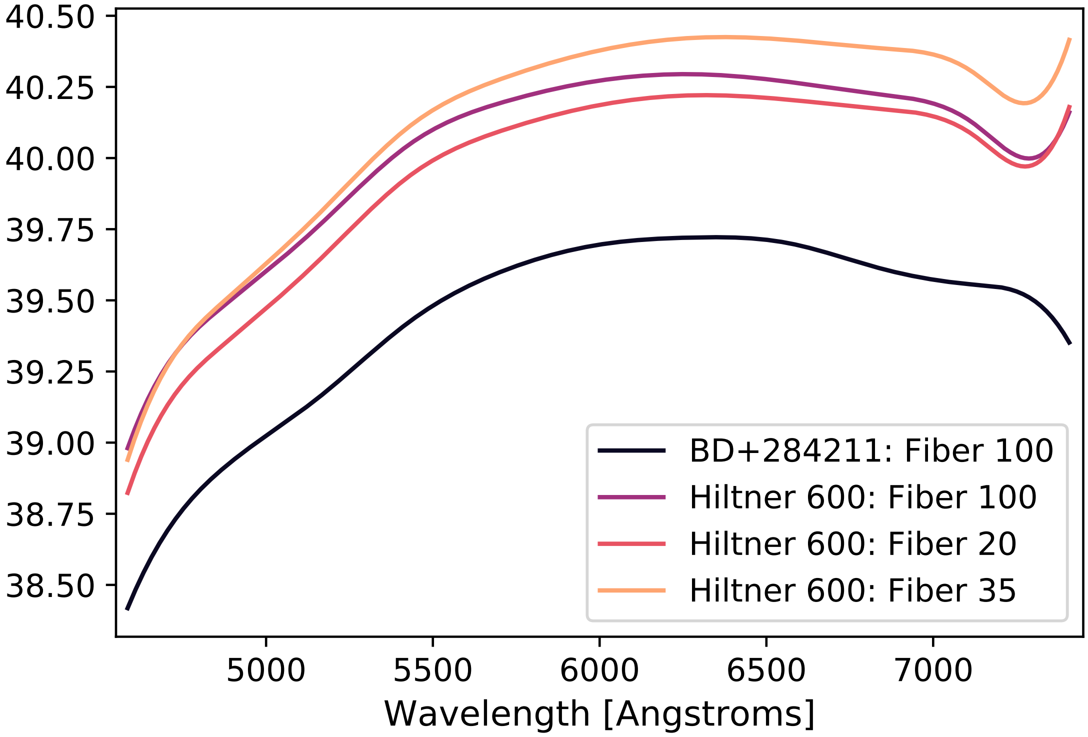

Figure 3.10 Several sensitivity functions from large and small fibers from Hiltner 600 observed on 2015-12-01. After ∼ 7200 Å, the sensitivity functions experience a downward or upward turn that causes a sharp feature in the calibrated spectra. We believe this is caused by a deep telluric line at the edge of our Twilight flats that is causing confusion in the shape of the sky continuum at those wavelengths, see Section 3.5.1.

Table 3.6. HexPak Targets: Fiber Observed versus Fiber Calibrated I

Date	SN Name	Star	Fiber	
			Observed	Calibrated
2015-11-30	ASASSN-15hg	Hiltner 600	62	35
	Host	Hiltner 600	35	35
2015-11-30	ASASSN-15ho	Hiltner 600	62	35
2015-11-17	LSQ12gef	BD+284211	85	100
2015-12-01	LSQ14aeg	Hiltner 600	20	35
2015-11-16	PS1-12bwh	Hiltner 600	62	20
2015-11-17	PS15mb	Hiltner 600	100	100
2015-11-16	PSN J07250042+2347030	Hiltner 600	62	20
	Host	Hiltner 600	28	20
2015-11-16	PSN J08593491+4555343	Hiltner 600	62	20
2015-12-01	PSN J10292799+2200468	Hiltner 600	5	102
2015-12-01	PTF12iiq	Hiltner 600	35	35
2015-11-17	PTF12ikt	BD+284211	70	100
2015-11-17	iPTF13ebh	Hiltner 600	20	20
2015-11-17	iPTF13dge	Hiltner 600	35	35
	Host	Hiltner 600	–	35
2015-12-01	iPTF13dkj	BD+284211	102	102
2015-11-17	iPTF14gdr	BD+284211	35	100
2015-11-17	SN 2011gy	Hiltner 600	85	85
2015-12-01	SN 2011hb	BD+284211	62	35
	Host	BD+284211	35	35
	Host-offset	BD+284211	–	35

Table 3.7. HexPak Targets: Fiber Observed versus Fiber Calibrated II

Date	SN Name	Star	Fiber	
			Observed	Calibrated
2015-11-16	SN 2011hk	BD+284211	62	20
2015-11-16	SN 2011hr	Hiltner 600	62	20
2015-12-01	SN 2011iu	Hiltner 600	35	35
2015-12-01	SN 2012cg	Hiltner 600	62	35
2015-11-16	SN 2012et	BD+284211	62	20
2015-11-17	SN 2012et	BD+284211	100	100
2015-11-30	SN 2012fm	Hiltner 600	12	12
2015-12-01	SN 2012gm	BD+284211	102	102
2015-11-30	SN 2013be	Hiltner 600	62	35
2015-12-01	SN 2013fj	BD+284211	70	70
2015-11-30	SN 2013fn	BD+284211	35	35
2015-11-30	SN 2013fw	BD+284211	62	35
	Host	BD+284211	35	35
2015-11-16	SN 2014aa	Hiltner 600	62	20
2015-11-16	SN 2014dm	BD+284211	62	20
	Host 1	BD+284211	20	20
	Host 2	BD+284211	–	20
2015-11-17	SNhunt206	Hiltner 600	Unknown[a]	85
2015-12-01	SNhunt263	Hiltner 600	77	77

[a] Original pointing had the supernova location on Fiber 85, but the telescope jumped when switching from pointing to object exposures.

our primary science goals as none of our galaxies have their H α lines redshifted to that area of the spectra. The galaxy with the highest redshift has the Hα line at 7022 Å.

3.5.2 Notes on Sky Subtraction

Currently, there are residuals in the spectra left over from poor sky subtraction as seen in Figure 3.12. Because the multi-fiber data fed into a single slit, the optical transfer function (essentially the point spread function (PSF)) varies over the different angles that each spectrum was dispersed through (Bershady et al., 2005). The size and shape of unresolved lines are different for each spectrum in the same frame. The left-hand panel in Figure 3.12 illustrates the different shapes and peaks of the [OI] line in the sky fibers and the resulting median-combined skyline that is subtracted from the rest of the fibers. The median combined line is also slightly broader than it should be to account for the changing shapes. The middle and rightmost panels show the residual effect from sky subtraction on sky and object fibers.

We examined the effect from the brightest sky line [OI]5577 and measured the number of counts in a sky fiber versus the counts in the object fiber. The residual counts from object fibers minus sky fibers are on the same order of the error in the counts defined as sqrt[$\sum(N_{\mathrm{sky}}/\mathrm{Gain} + N_{\mathrm{obj}}/\mathrm{Gain})$]. Therefore, the error from sky subtraction is reasonably within our expected error bars. Since this line causes the largest residual, we can assume all of the residuals are within the error bars and acceptable for this analysis.

To evaluate the error in wavelength calibration from this effect, we fit a Gaussian function using `astropy.modeling.fitting.LevMarLSQFitter` (Astropy Collaboration et al., 2013a) to the [OI]5577 line. We fit this function for every spectrum in every frame after fiber to fiber throughput correction. We varied the starting position around 5577 Å and took the median of the results. We then took the standard deviation per object of the peak of this line which results in an error in wavelength. The range in errors for all of the targets is 0.09–0.19 Å with an average of 0.12 Å which corresponds to an error in velocity measures of 5–10 km/s with an average of 7 km/s.

For our purposes of measuring Hα, we do not need to implement more sophisticated

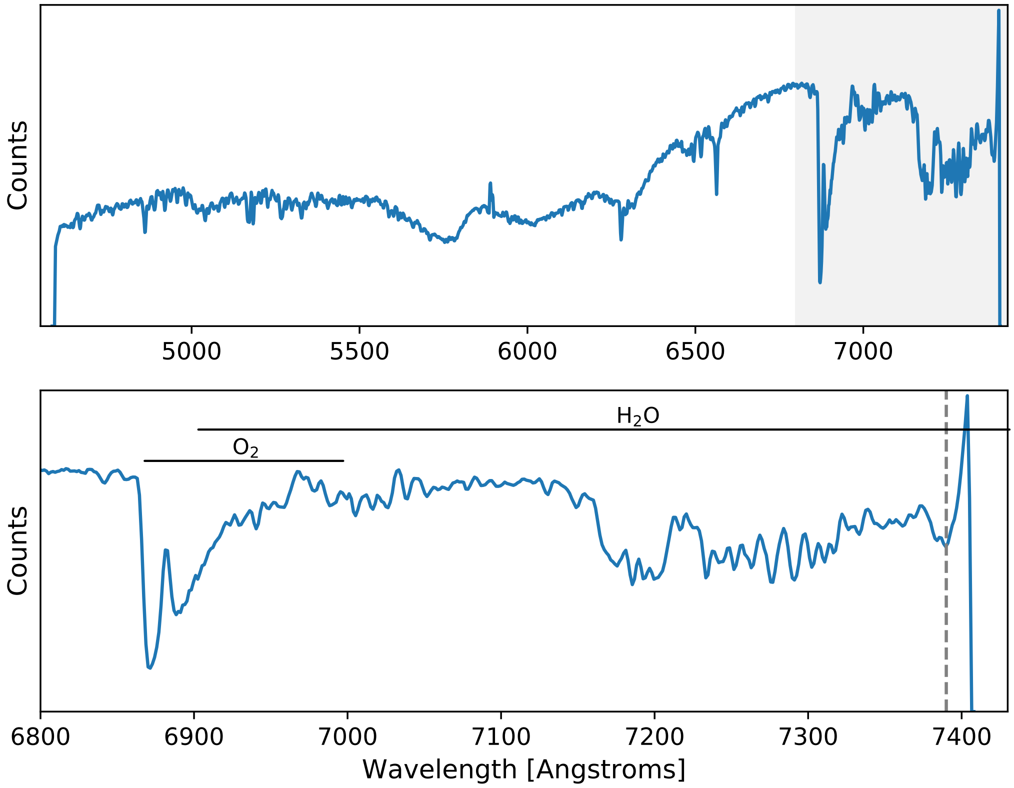

Figure 3.11 Master Twilight Flat of Fiber 35 from 2015-11-17. *Top:* Full spectrum in counts. The grey area is the zoomed in region in the plot below. *Bottom:* Zoom in on O_2 and H_2O bands that are difficult to subtract. The grey dashed line marks the water line that causes issues when fitting for fiber to fiber throughput.

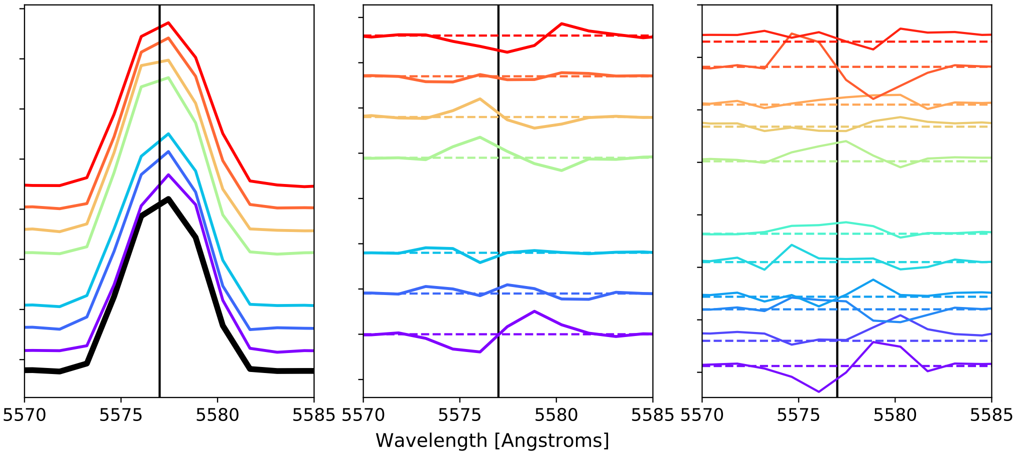

Figure 3.12 A zoom in of the [OI]5577 line. *Left:* The thick black line is the median of the large sky fibers which are the colored lines above it (plotted with some offset for clarity). *Middle:* The sky lines minus the median fit corresponding to the fibers shown in the left plot. *Right:* Object lines minus the median fit. In all three plots the color gets redder with increased fiber number. The dashed lines in the Middle and Right plots correspond to zero.

algorithms for sky subtraction as outlined in Bershady et al. (2005) but note that this is something that could be done in the future to improve the spectra.

Another error we see from sky subtraction is its inability to sufficiently remove the deep O_2 lines around 6870 Å. Figure 3.13 plots several spectra from two objects with different redshifts that show this poor subtraction. No Hα line falls into this wavelength range, so it is not pertinent to fix for our analysis, but the two sulfur lines (S II) at 6718 Å and 6733 Å are occasionally affected.

3.5.3 Notes on using Small or Large Fibers to Flux Calibrate

Both standard stars have a full width at half maximum greater than 1" on sky for all four nights of observation. The first two nights were notably affected since seeing hovering between 1.5" and 2.5" (possibly over 3") for the first two nights. Due to the poor seeing conditions, the small fibers gathered only $5-18\%$ of the counts that the large fibers collected.

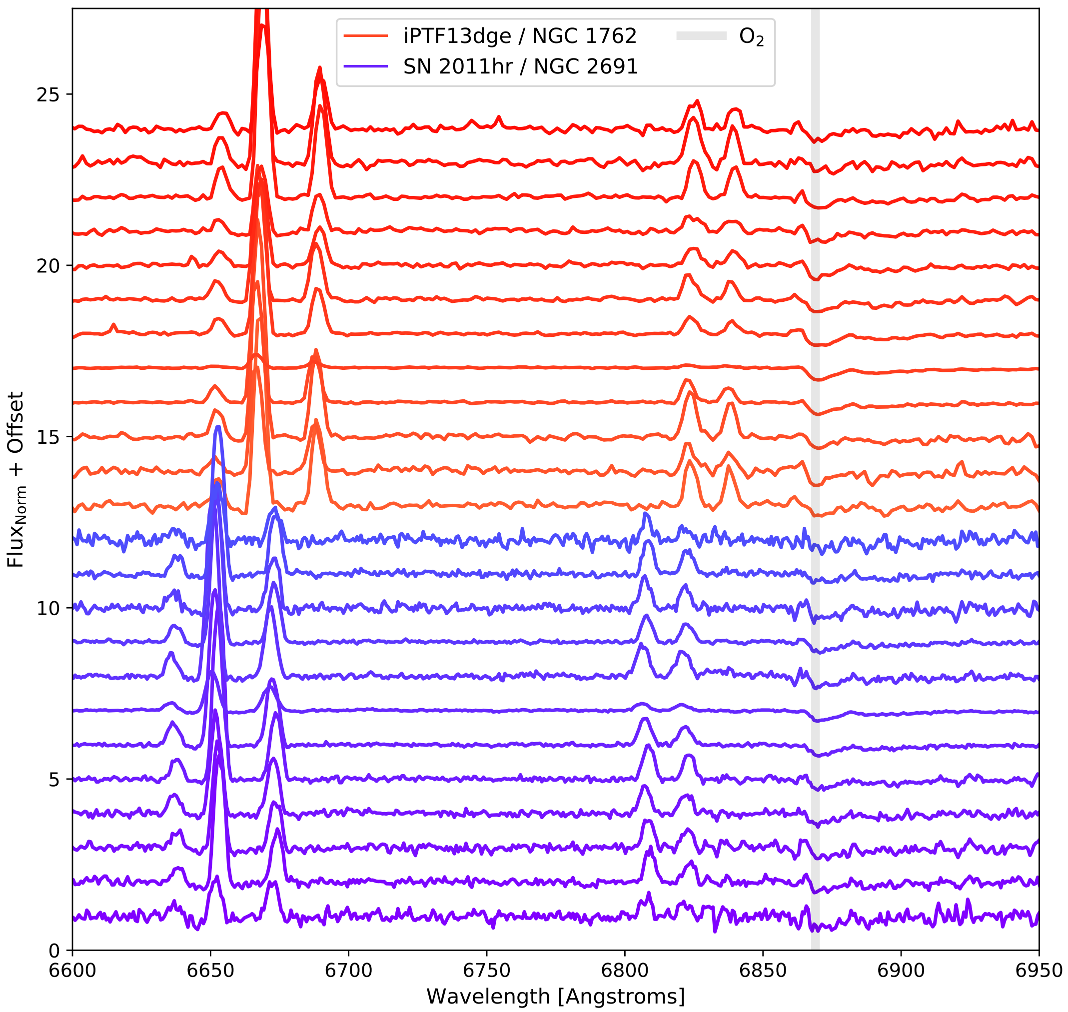

Figure 3.13 A zoom in of the O_2 B band region with the largest absorption line around 6870 Å marked in grey. The red lines are the fibers around the host galaxy of iPTF13dge (NGC 1762) and the purple lines are the fibers around the hosts galaxy of SN 2011hk (NGC 881). The flux is normalized and a constant offset is applied for clarity.

We chose to calibrate only with the large fibers. Though the large fibers are older than the small fibers, they have been more tested and have known properties. The large fibers should be fine to calibrate the small fibers since we are looking mostly at diffuse gas and not at stars, so the amount of light scattered into the fibers is roughly equal to the amount of light scattered out.

3.5.4 Error Estimation

To estimate the error in the flux calibration, we examined the results of calibrating a standard star observation with the same standard star observed on a different fiber. This method could not be performed for every standard star on every night since we did not always collect them on multiple large fibers. Figures 3.14 and 3.15 shows the results for the stars and nights where this analysis can be done. On the first night of the run, 2015-11-16, we observed the standard star on only one large fiber such that we cannot make an estimate of the flux error through this method. For 2015-11-17 and 2015-11-30, we observed BD+284211 on one fiber during the first half of the night, so we only calculate the calibration error for the second half of those two nights. The flux is calibrated to 10% for the second half of 2015-11-17, $\sim 8\%$ for the second half of 2015-11-30, and $\sim 9\%$ and $\sim 6\%$ for the first and second half of 2015-12-01, respectively. The flux is most likely calibrated to within $\sim 10\%$ for all objects, which is acceptable for our purposes.

Figure 3.16 shows how the error in calibration changes with wavelength. The errors increase with increasing wavelengths and can vary between short to long wavelengths by as much as 10% or as little as 3%

One way to improve the flux calibration would be to implement aperture corrections. Due to the finite size of the fibers on the sky, the amount of flux enclosed by each one is dependent on the point spread function (PSF) during a given exposure. A standard star observation can be used to estimate the PSF and determine how much energy the fiber enclosed. Unfortunately, to make these corrections on our science images, we would either need a standard star within the field of view or we would have needed to observed a nearby standard star before or after each scientific observation. We did not collect the necessary

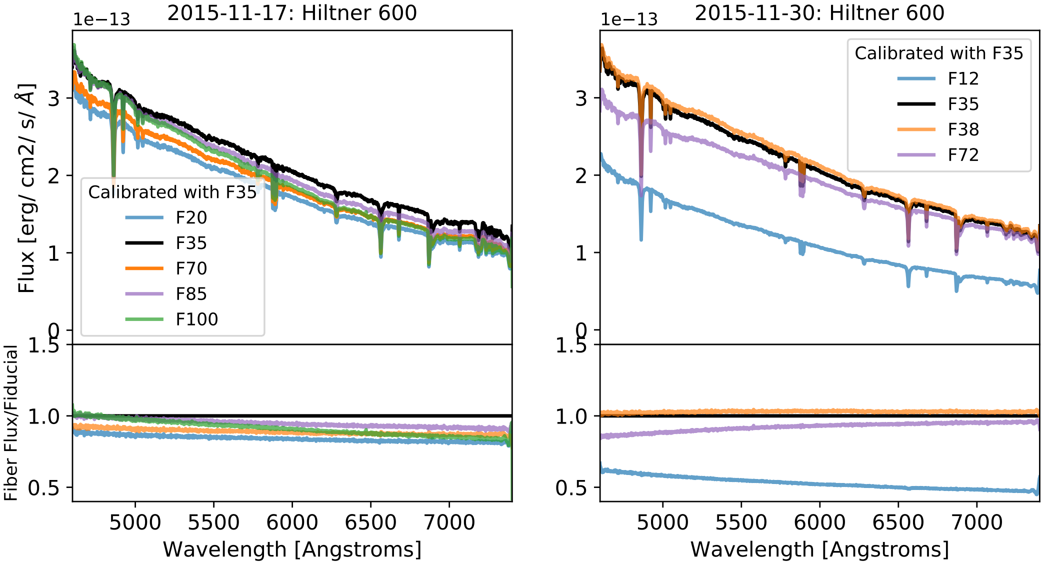

Figure 3.14 Comparison of standard stars observed on multiple fibers but calibrated with the same fiber. The top panel on all plots shows the resulting spectra. The black line always corresponds to the correctly calibrated spectrum. The bottom panel shows each spectrum dividing by the correctly calibrated spectrum or “fiducial” spectrum. All of the observations were calibrated with the sensitivity function derived from the observation of the star on Fiber 35. *Left:* On 2015-11-17, only Hiltner 600 was observed on multiple fibers and it was observed in the second half of the night. *Right:* On 2015-11-30, only Hiltner 600 was observed on multiple fibers and it was observed in the second half of the night.

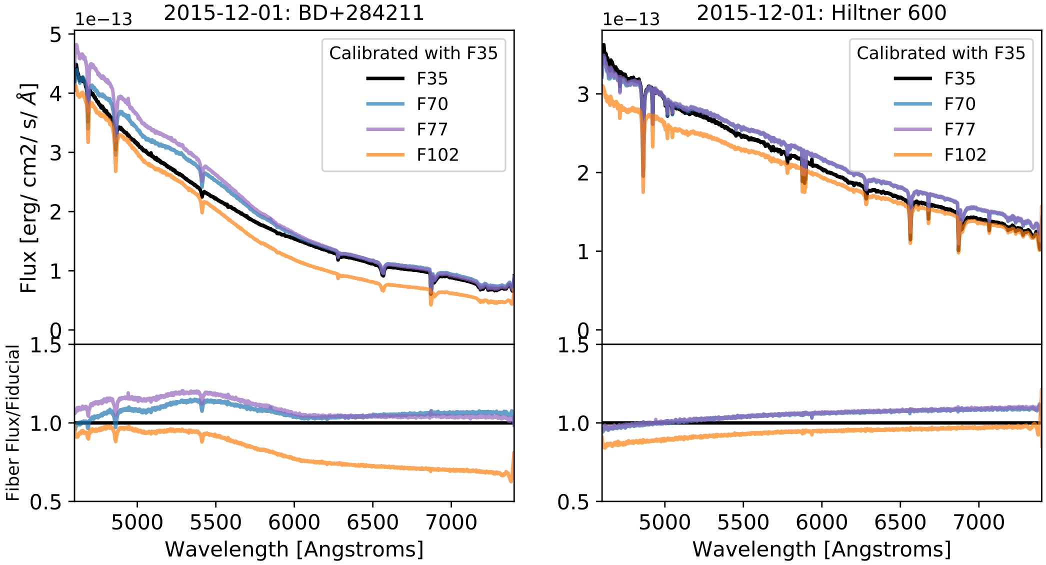

Figure 3.15 Comparison of standard stars observed on multiple fibers but calibrated with the same fiber. The top panel on all plots shows the resulting spectra. The black line always corresponds to the correctly calibrated spectrum. The bottom panel shows each spectrum dividing by the correctly calibrated spectrum or “fiducial” spectrum. All of the observations were calibrated with the sensitivity function derived from the observation of the star on Fiber 35. *Left:* 2015-12-01, BD+284211 was observed in the first half of the night. *Right:* 2015-12-01, Hiltner 600 was observed in the second half of the night.

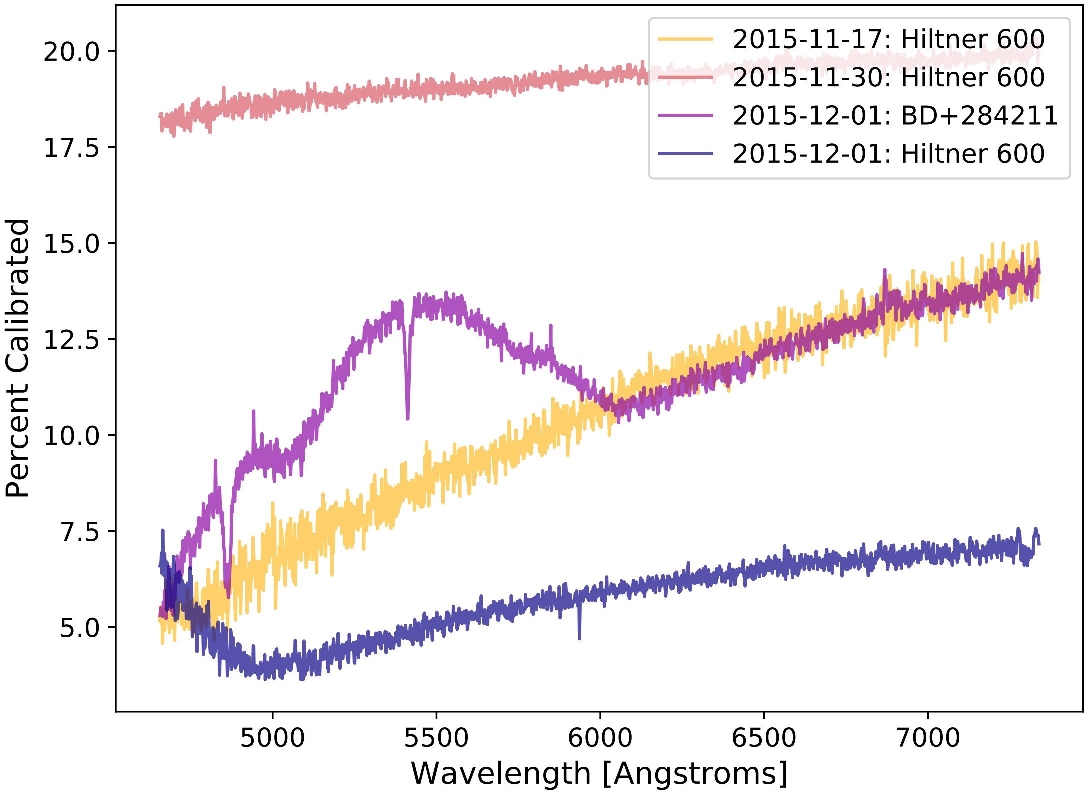

Figure 3.16 The average error in calibration from the bottom panels of Figures 3.14 and 3.15 for 4 standard stars observed over 3 nights.

data to make these corrections.

3.5.5 Comparison of Night to Night Calibration

The only object observed on multiple nights is SN 2012et / CGCG 476-117. We collected this target on the first night using 1x1 binning and again the next night using 2x2 binning. Figure 3.17 shows the comparison of the core of the galaxy for these two nights. The center of the galaxy was on a large fiber the first night but in the small fiber the second night. The lower panel is a zoom in of the Hα region. The 1" fibers exhibit a larger error because the individual collecting area is smaller causing a lower signal to noise. The spectra agree very well with each.

3.5.6 Comparison with SDSS

We compared the spectrum of the fiber on the bulge of NGC 2691, host galaxy of SN 2011hr, to the spectrum of the bulge taken with the Sloan Digital Sky Survey (SDSS) in Figure 3.18. The SDSS spectrum[10] was taken as a part of the SDSS Legacy Survey (Abazajian et al., 2009a) which surveyed the North Galactic Cap and three strips in the South Galactic Cap and used a 3" fiber. The spectrum from HexPak is uniformly more luminous than the one from SDSS, except in bluer wavelengths where the HexPak fibers are less reliable. They share the same basic shape, and the extra flux from HexPak could be from observing a slightly different area of the galaxy or from the lack of aperture corrections in absolute flux calibration. The difference in flux is 5% for $\sim$ 5800 Å to 7300 Å and 15% different at bluer wavelengths (4600–5800 Å).

3.5.7 Note on Spatial Resolution

The large and small fibers probe different spatial scales, and the physical sizes change with redshift. Seeing was 1.5-2.5", possibly up to 3", on 2015-11-16 and 2015-11-17, so the actual physical size probed on these two nights in the 1" small fibers is unknown as the light from

---

[10] Downloaded from the SDSS Object Explorer `http://skyserver.sdss.org/DR12/en/tools/explore/summary.aspx`

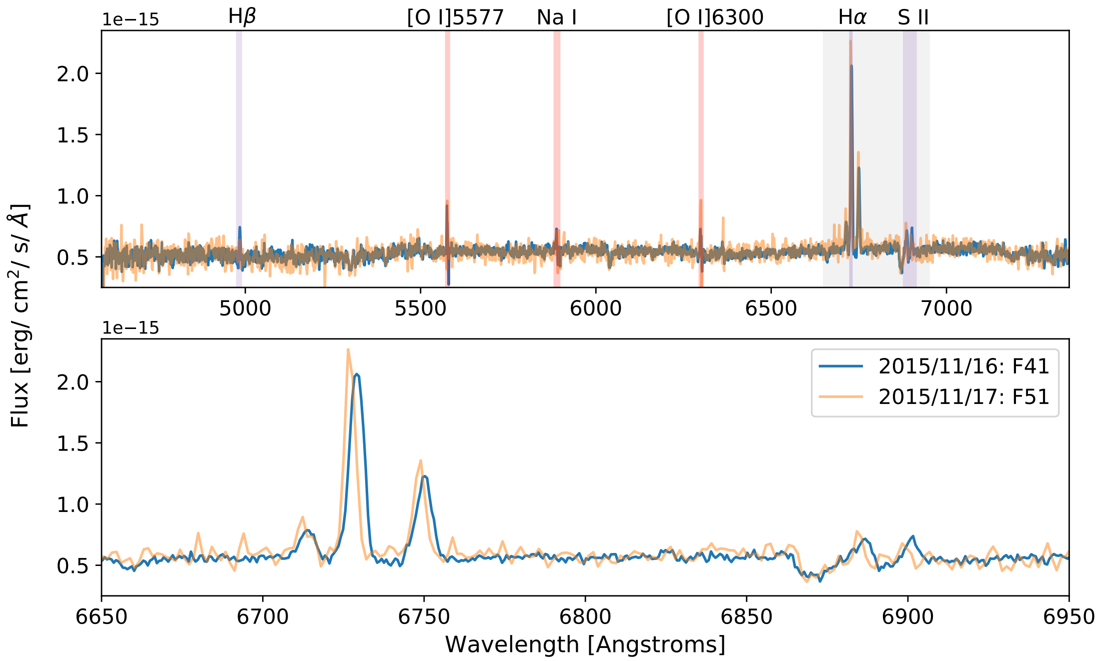

Figure 3.17 Galaxy: CGCG 476-117, Supernova: SN 2012et. Only object observed on two nights. The first night had 1x1 binning and the second night had 2x2 binning. On 2015-11-16, the core of the galaxy is on a large fiber, while 2015-11-17 was observed on a small fiber. *Top:* Full spectrum of the core of SN 2012et. Marked in purple are emission lines from the galaxy and marked in red are telluric lines that left residuals after subtraction. Telluric lines identified from Osterbrock et al. (1996). We did not mark the O_2 band that was discussed in Figure 3.13 because it is next to the S II lines on the left and cluttered the plot. *Bottom:* A zoom-in of the Hα region that is greyed out in the top plot.

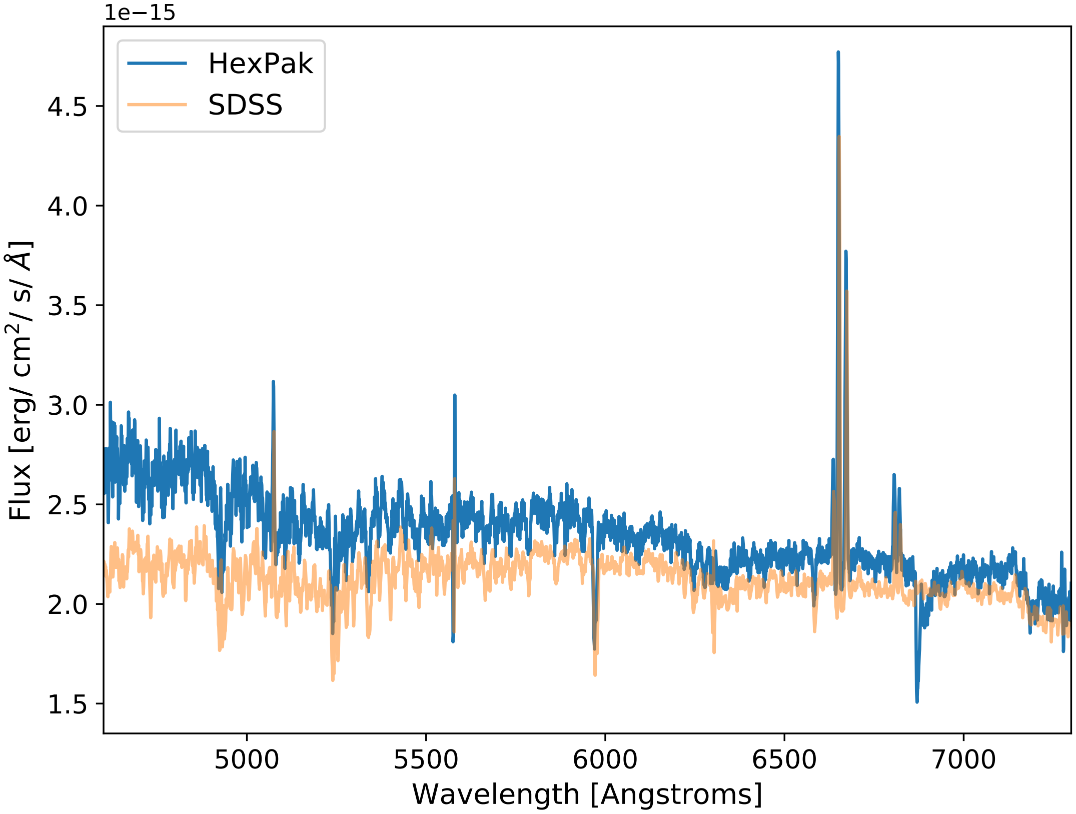

Figure 3.18 SN 2011hr: HexPak versus SDSS spectrum. We used the HexPak fiber closest to the center of the galaxy (Fiber 8). The poor telluric line removal is clear in the HexPak spectrum.

these regions was smeared out. On 2015-11-30 and 2015-12-01, since the seeing was closer to 1", the spatial scale of the small fibers is more accurate.

3.6 HEXPAK DATA RELEASE OF 32 SWEETSPOT HOST GALAXIES: RESULTS

3.6.1 r-band flux

We calculated the SDSS r-band flux using `onedspec.sbands`. The HexPak configuration that we used did not fully cover any other SDSS bands. We use the SDSS r-band flux maps to determine the actual pointing of our observations. Unfortunately, the Wifoe observations give us an idea of where to look for the host galaxy, but it is possible that when switching the mirrors for the pointing camera to HexPak that the locations shift a little. To determine the location of the host galaxy, we calculate weights of the x and y position of the fibers based on their r-band flux, and then we take the flux-weighted average of their x and y locations. We calculated the separation and the position angle of the supernova location relative to the host galaxy to determine the location of the faded supernova. If there was a bright star in the field, we masked associated fibers to not bias the fits.

3.6.2 Hα Measurements

Before measuring Hα, we account for extinction due to the Milky Way. We used the NASA/IPAC Infrared Science Archive[11] to get E(B-V) values from Schlafly & Finkbeiner (2011) assuming $R_V = 3.1$. We then use `PyAstronomy`[12] to deredden our spectra. We used the function `PyAstronomy.pyasl.unred`, which was converted from the IDL Astronomy User's Library[13] and uses the Fitzpatrick (1999) parameterization to correct for wavelength dependent Galactic extinction. In the current analysis, we do not correct for the dust extinction in the galaxies we are observing.

---

[11] `http://irsa.ipac.caltech.edu/applications/DUST/`

[12] `https://github.com/sczesla/PyAstronomy`

[13] `https://idlastro.gsfc.nasa.gov/`

We used `onedspec.continuum` to calculate the continuum flux with a first order Legendre polynomial (a line). We only used the area around Hα (without restframe corrections) which corresponds to the range of 6400 Å to 7100 Å with a gap of $\sim$ 70 Å. The location of Hα was based on previously recorded host galaxy redshifts; however, we estimated the redshifts for three host galaxies do not have redshifts previously recorded. One of these galaxies, 2MASXi J0909234-044327 the host galaxy of ASASSN-15ho, is significantly offset in redshift space by roughly 0.05 from its supernova, but the other two host galaxies exhibit redshifts close to the measured supernova redshift, see Appendix A.2 for more information. This wavelength range misses many of the sky lines that we could not subtract well including [OI], Na I, OH forests, and water bands. However, it includes the O_2 band at $\sim$6870 Å, but we adjusted the wavelength ranges to mask this line as well.

After normalizing the spectra, we fit for the Hα emission line by utilizing its location in reference to the nitrogen lines [N II]a and [N II]b. We used our own code written in python which utilizes `astropy.modeling.fitting.LevMarLSQFitter`. Assuming the emission lines are Gaussian, we create a three Gaussian model and constrain the relative locations of the peaks to match the relative positions between [N II]a, [N II]b, and Hα. We run the fitter at 5 initial guesses within 2 Å of the redshifted location of Hα and take the median results as our fits to the three emission lines. We then find all the wavelengths that are within 3 σ of the means for [N II] and within 2 σ for Hα to avoid getting [N II] flux and use the flux found in between them to measure equivalent width (EW) and Hα flux following the equations below:

$$\mathrm{EW} = \sum_{i=\lambda[-2\sigma]}^{i=\lambda[+2\sigma]} (\mathrm{F}_{\lambda,\mathrm{norm}}[i] - 1) * d\lambda, \tag{3.1}$$

$$\text{Total Flux} = \sum_{i=\lambda[-2\sigma]}^{i=\lambda[+2\sigma]} (\mathrm{F}_{\mathrm{continuum}}[i]) * (\mathrm{F}_{\lambda,\mathrm{norm}}[i] - 1). \tag{3.2}$$

Both of these values are affected by the expansion of the Universe, so in order to calculate the restframe values, the EW must be divided by $1 + z$ while the flux is multiplied by $1 + z$. Figure 3.19 shows the Hα line with the EW resulting from these fits. The restframe Hα EW maps are in Appendix A.3. Strong Hα lines blend with the surrounding [N II] lines which can cause the mixture model to overestimate the standard deviation which will cause

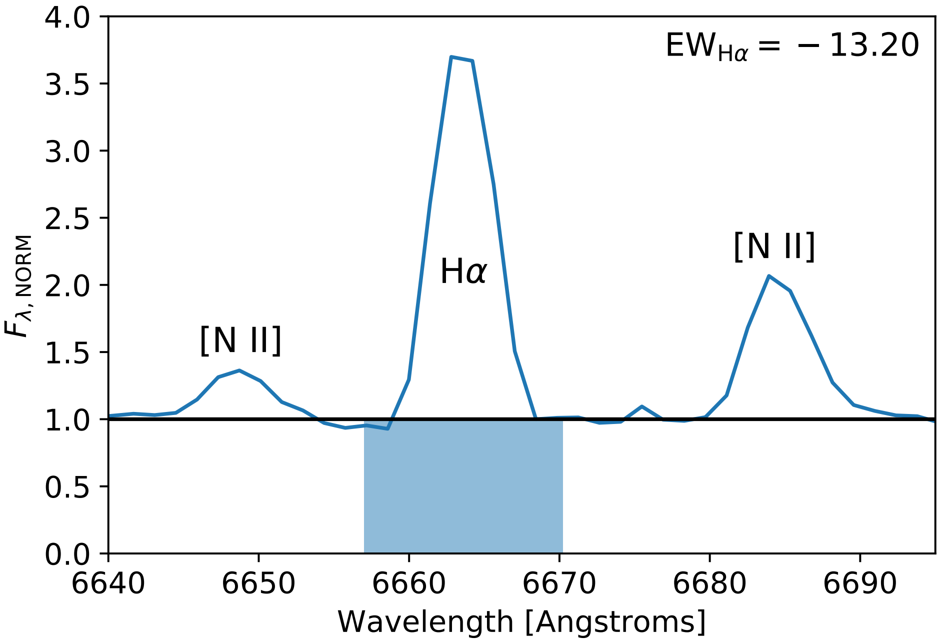

Figure 3.19 Example of the Hα emission line with the restframe EW shown in the blue shaded region. This is Fiber 103 for the first pointing of iPTF14dge / NGC 1762.

a significant overestimate in the EW and flux. However, these lines will not be plotted in our Hα EW maps as they do not meet the quality cut requiring the standard deviation to be below a reasonable threshold. We determine error on Hα by calculating the RMS or dispersion of the sky subtracted continuum in a range around the H-alpha line.

Using the observed position of Hα, the flux in Hα, plus redshift information, we calculate Hα velocity, luminosity, and surface brightness. All plots can be found in Figures 3.22 - 3.33. The colored, optical images in the left-most column come from Sloan Digital Sky Survey finder chart tool[14] or, if not in the SDSS foot print, from the Panoramic Survey Telescope and Rapid Response System (Pan-STARRS) image cutout service[15]. The host galaxies with Pan-STARRS cutouts are ASASSN-15ho, iPTF13dge, iPTF13ebh, SN 2011iu, SN 2013fn, SN 2013fw, and SN 2014dm. The maps that show r-band flux but no Hα surface brightness or velocity measurements are elliptical galaxies. If the galaxy had a low inclination, then

---

[14] `http://skyserver.sdss.org/DR12/en/tools/chart/image.aspx`
[15] `http://ps1images.stsci.edu/cgi-bin/ps1cutouts`

there are surface brightness measurements, but a blank velocity map. Following Rigault et al. (2013), the limit for a star forming region is $\log_{10}$ (Hα Surface Brightness) > 38.35 (which corresponds to ~ 1.22 x $10^{-3} M_{\odot}$ yr^{-1} kpc^{-2}). On these color maps, locally star forming regions correspond to the green and blue areas while yellow corresponds to locally passive regions.

3.6.3 Absorption at Hα

Hα flux is the result of bright stars ionizing the interstellar medium (ISM); however, there is an underlying absorption of Hα from the stellar population. Using a linear continuum around the Hα line will underestimate the ionized emission. A stellar population synthesis code that fits the continuum flux to different simple stellar population (SSP) models can account for the Hα absorption line so that it can be added back to the emitted flux. We use `STARLIGHT` (Cid Fernandes et al., 2005) to fit galaxy continuums. Figure 3.20 shows an example spectrum and fit continuum which illustrates the slight absorption line at Hα. Once the galaxy spectrum is fit, and the spectra are normalized, we can remeasure Hα. `STARLIGHT` will also return galaxy mass, age, and star formation rates where mass is dependent on absolute calibration of the spectra and the age and metallicity indicators rely on the shape of the continuum.

Figure 3.21 compares the EW per fiber from the two methods. The fiber that contains the core of the galaxy shows no Hα EW using the linear continuum method because the Gaussian mixture model fit failed to meet a quality cut. The Hα emission line is so strong that it blends with the surrounding [N II] lines causing the fitter to assign a standard deviation that encompasses the nitrogen lines. Using `STARLIGHT` to fit the continuum results in a larger EW measurements by on average 16 Å (median 10 Å) for this particular target. On average for all fibers, `STARLIGHT` returns an EW 2.2 time larger; however, if we look at the median, it is only 1.5 times larger.

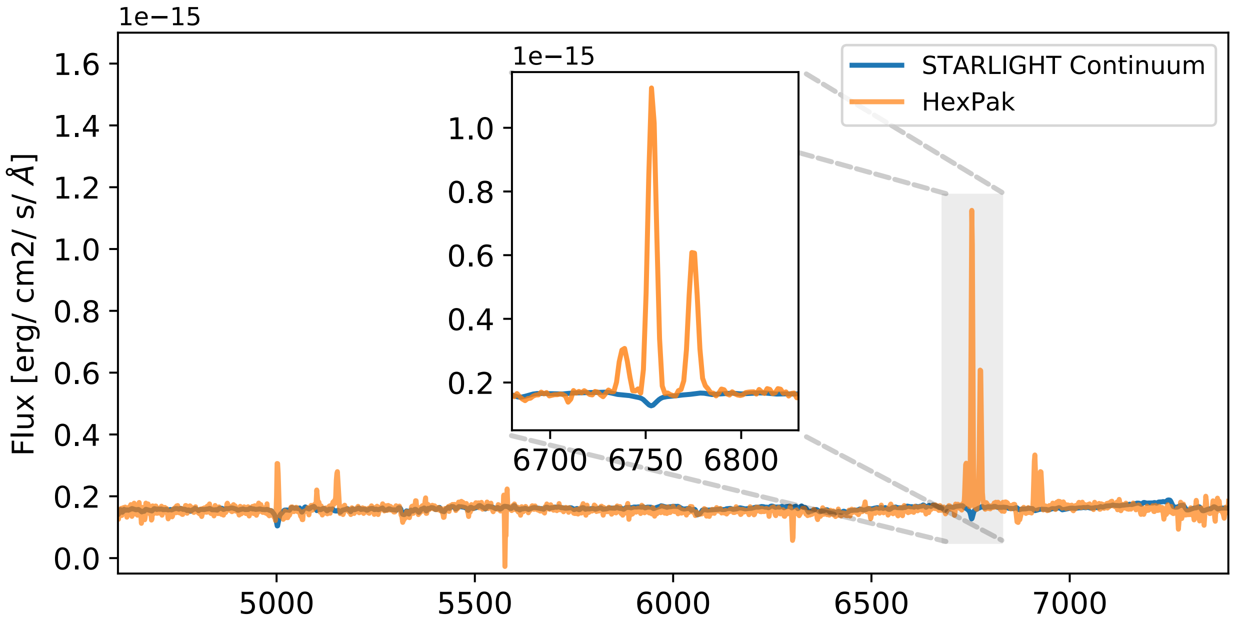

Figure 3.20 Comparing HexPak spectrum with the continuum fit from `STARLIGHT`. The Hα region is zoomed-in to get a closer look at the absorption. The spectrum is from SN 2011hb / NGC 7674 from the host only observation at fiber 28, which is next to the core of the galaxy.

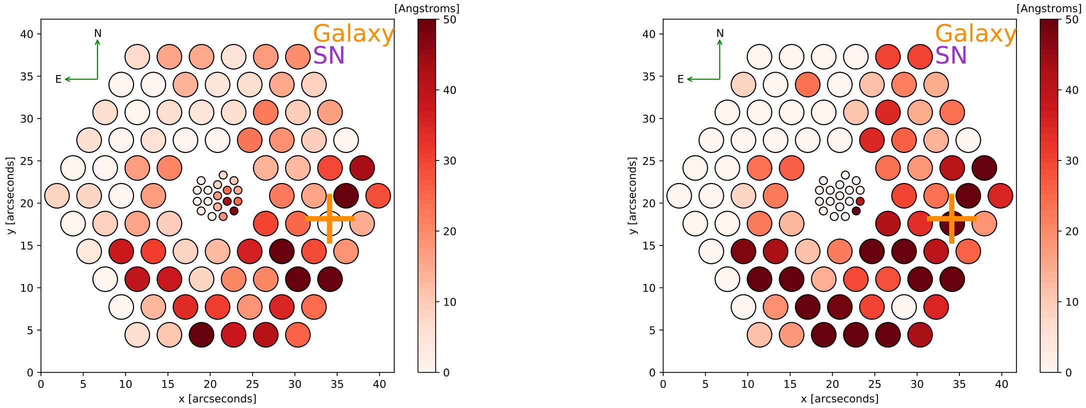

Figure 3.21 Maps of Hα EW for SN 2011hb / NGC 7674. *Left:* Hα EW from normalizing with a linear fit to the continuum around the Hα line. *Right:* Hα EW from normalizing by fitting for the underlying galaxy spectrum and accounting for absorption.

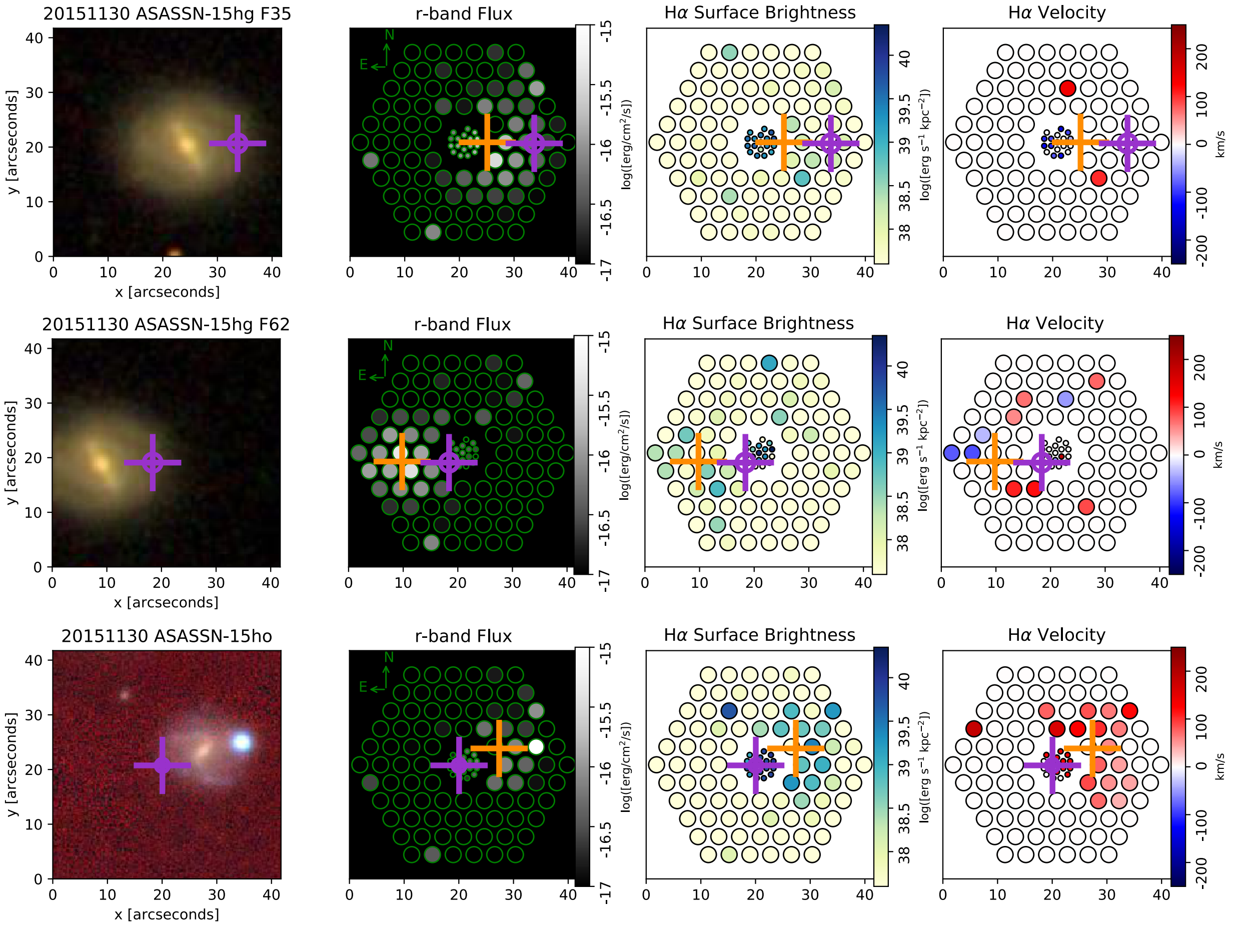

Figure 3.22 The orange cross indicates the location of the host galaxy and the purple cross is the location of the supernova. The purple circle occasionally visible in these plots indicates the 1 kpc radius circle around the SN location. The first panel is a colored image from SDSS/Pan-STARRS, the second panel is a recreated SDSS r-band flux map, the third panel is an Hα surface brightness map, and the fourth panel is an Hα velocity map. *First:* CGCG 063-098, host galaxy of ASASSN-15hg. This is the first of two pointings with the supernova explosion location around Fiber 35. *Second:* CGCG 063-098, host galaxy of ASASSN-15hg. This is the second of two pointings with the supernova explosion location around Fiber 62. *Third:* 2MASXi J0909234-044327, host galaxy of ASASSN-15ho.

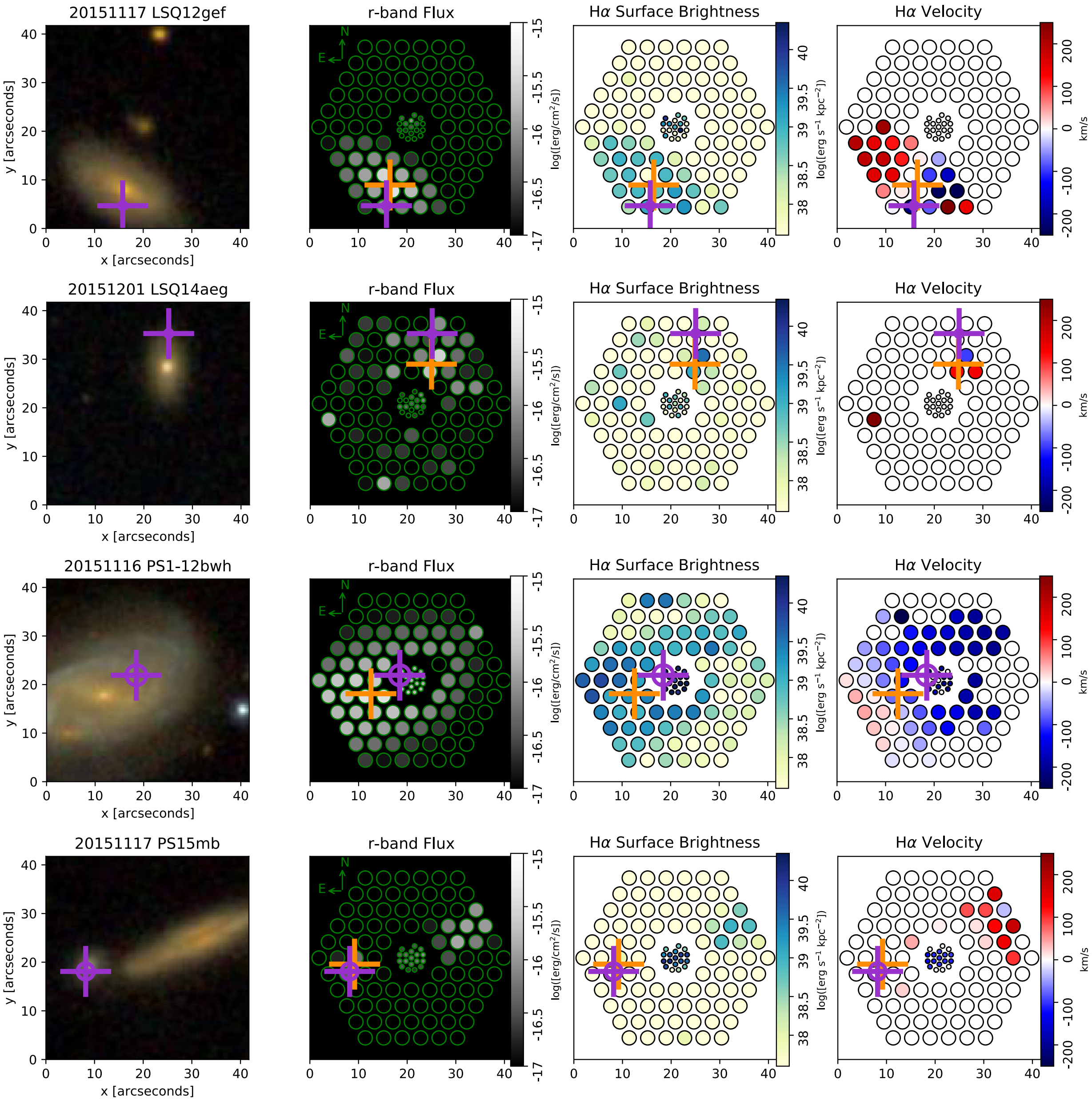

Figure 3.23 *First:* 2MASX J01403375+1830406, host galaxy of LSQ12gef. *Second:* 2MASX J10193682+1933131, host galaxy of LSQ14aeg. *Third:* CGCG 476-117, host galaxy of PS1-12bwh. *Forth:* SDSS J085940.13+151113.5, host galaxy of PS15mb.

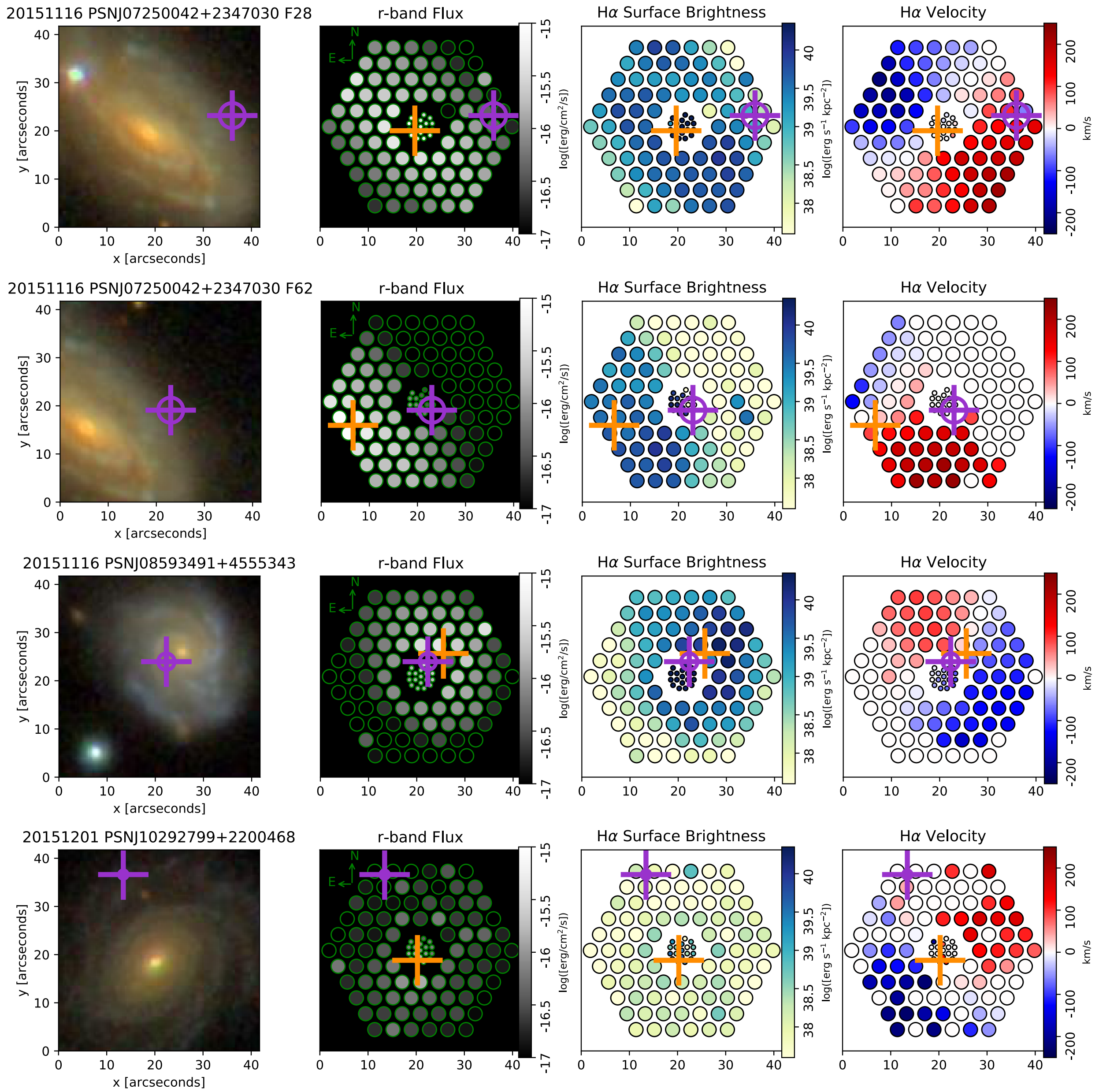

Figure 3.24 *First:* NGC 2370, host galaxy of PSN J07250042+2347030. This is the first of two pointings with the supernova explosion location around Fiber 28. *Second:* NGC 2370, host galaxy of PSN J07250042+2347030. This is the second of two pointings with the supernova explosion location around Fiber 62. *Third:* UGC 4709, host galaxy of PSN J08593491+4555343. *Forth:* UGC 5691, host galaxy of PSN J10292799+2200468.

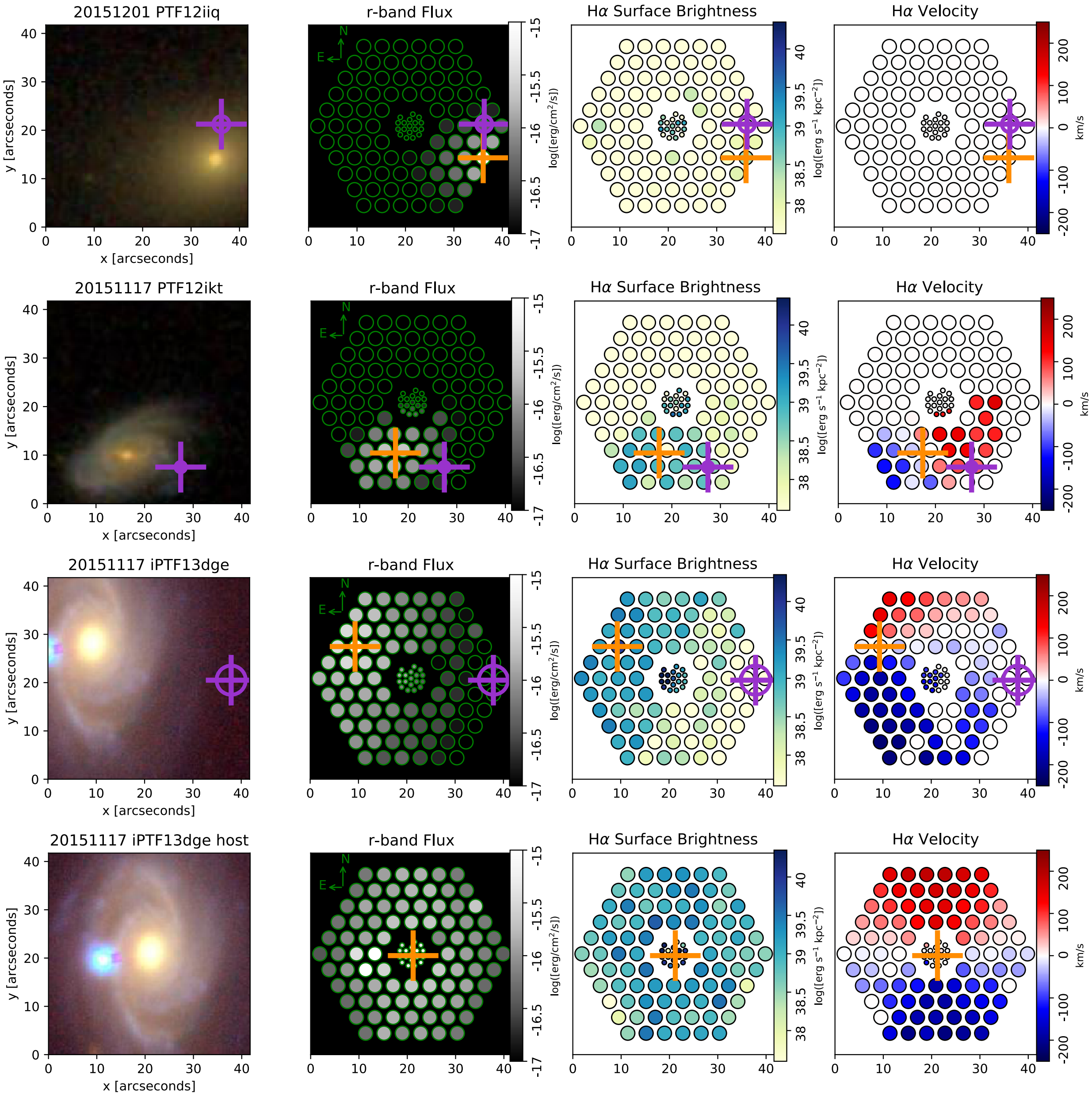

Figure 3.25 *First:* 2MASX J02500784-0016014, elliptical host galaxy for PTF12iiq. *Second:* 2MASX J01144386+0017100, host galaxy of PTF12ikt. *Third:* NGC 1762, host galaxy of iPTF13dge. This is the first of two pointings with the supernova explosion location around Fiber 35. *Fourth:* NGC 1762, host galaxy of iPTF13dge. This is the second of two pointings with the supernova explosion location off the fiber bundle.

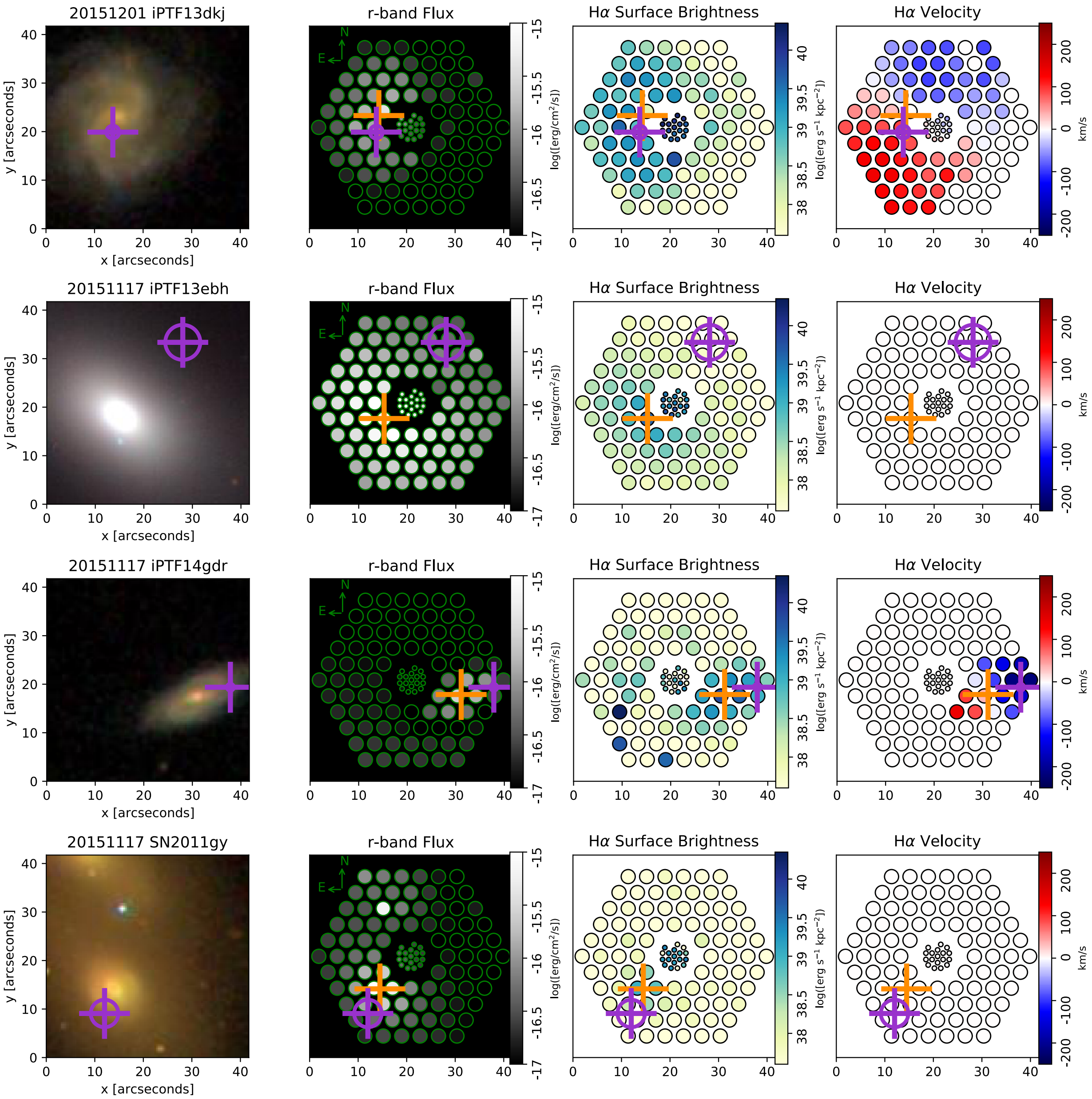

Figure 3.26 *First:* CGCG 454-00, host galaxy of iPTF13dkj. *Second:* NGC 890, host galaxy of iPTF13ebh. *Third:* 2MASX J00275880-0513014, host galaxy for iPTF14gdr. *Forth:* MCG +07-08-15, host galaxy of SN 2011gy.

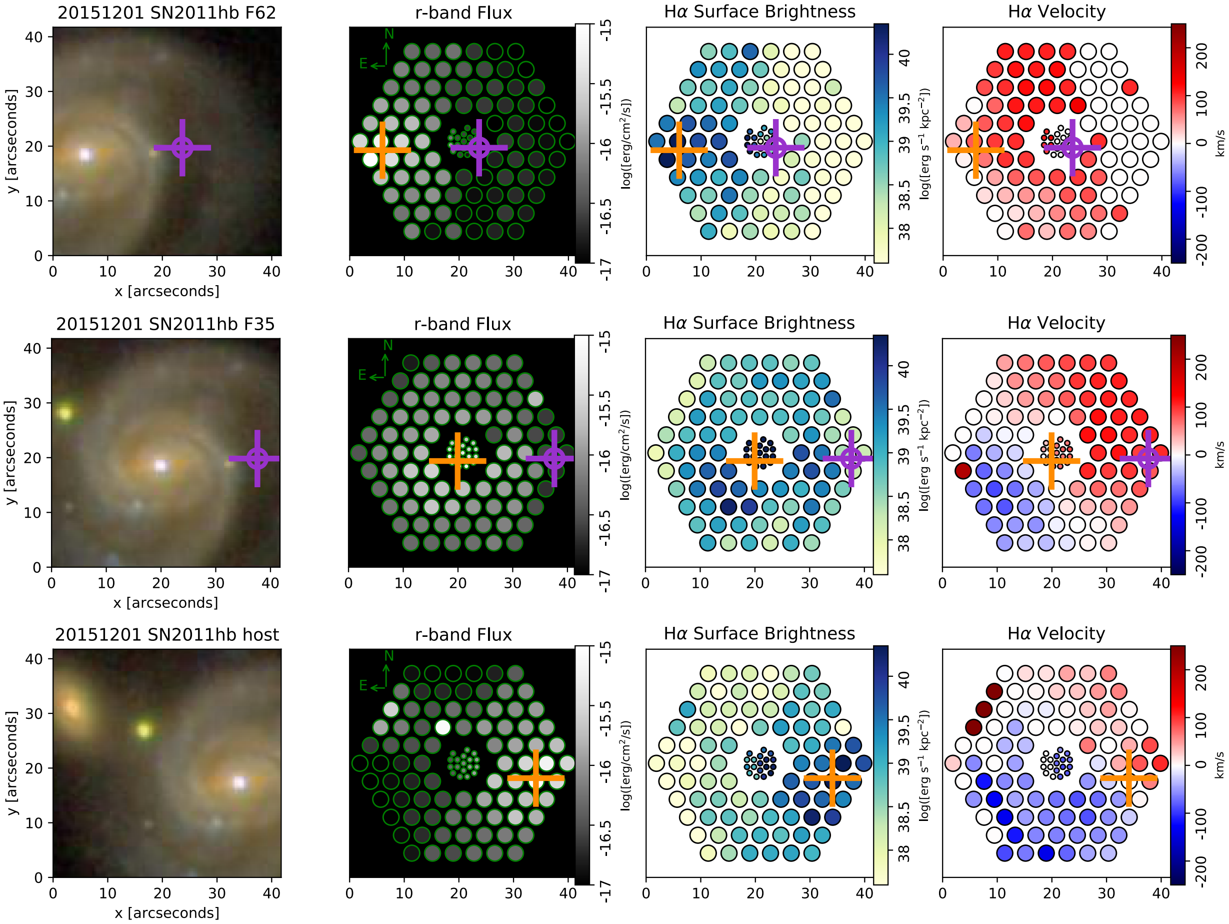

Figure 3.27 This shows all three pointings of NGC 7674, host galaxy of SN 2011hb. *First:* Supernova explosion location at Fiber 62. *Second:* Supernova explosion location at Fiber 35. *Third:* Supernova explosion location off the fiber bundle.

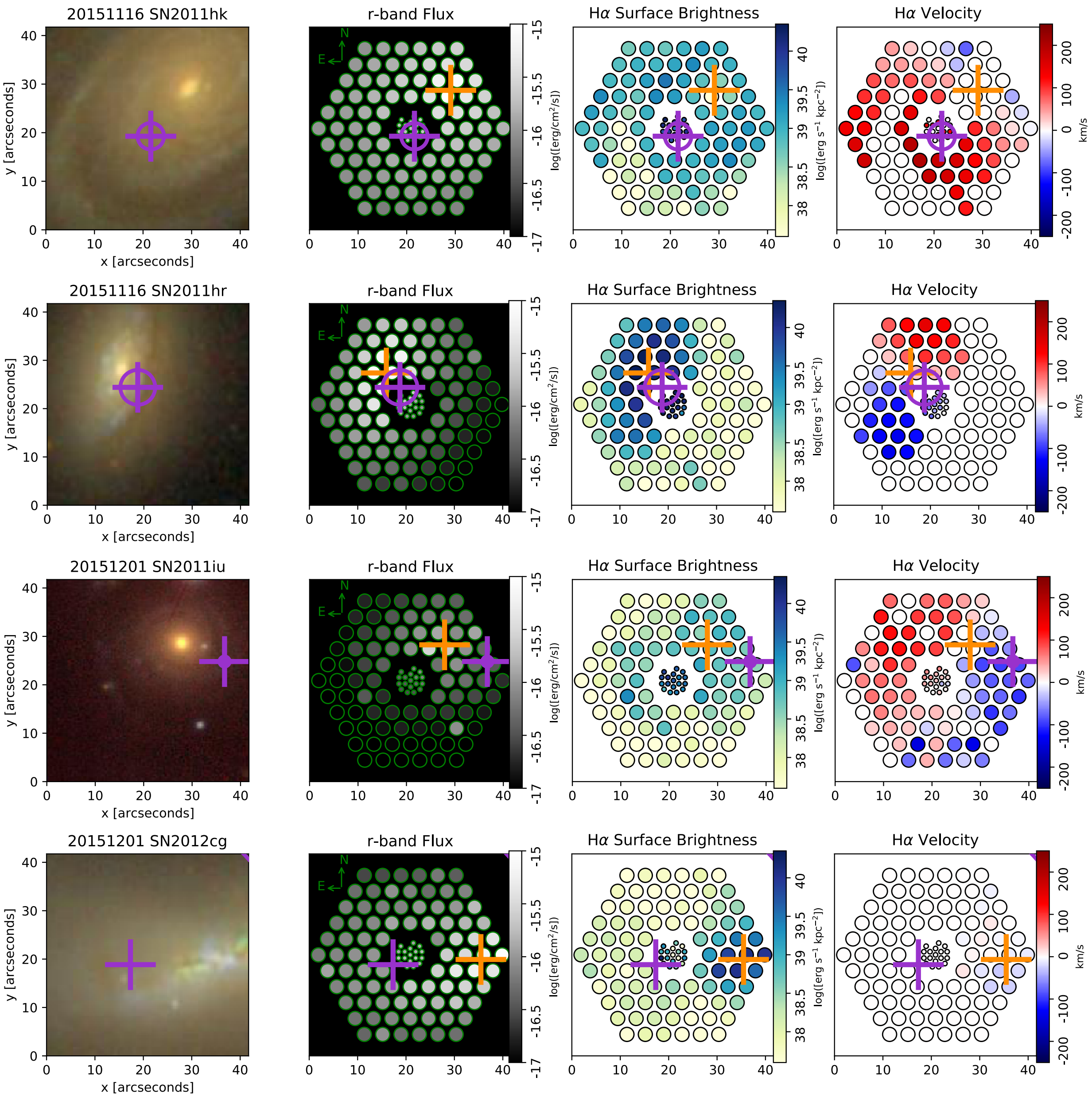

Figure 3.28 *First:* NGC 881, host galaxy of SN 2011hk. *Second:* NGC 2691, host galaxy of SN 2011hr. *Third:* UGC 12809, host galaxy of SN 2011iu. *Forth:* NGC 4424, host galaxy of SN 2012cg. In all other plots, the 1 kpc radius circle cannot be seen because it is too small. For this object, the circle is too large. Every fiber is within 1 kpc of the supernova and the edge of the circle can be seen in the top right hand corner.

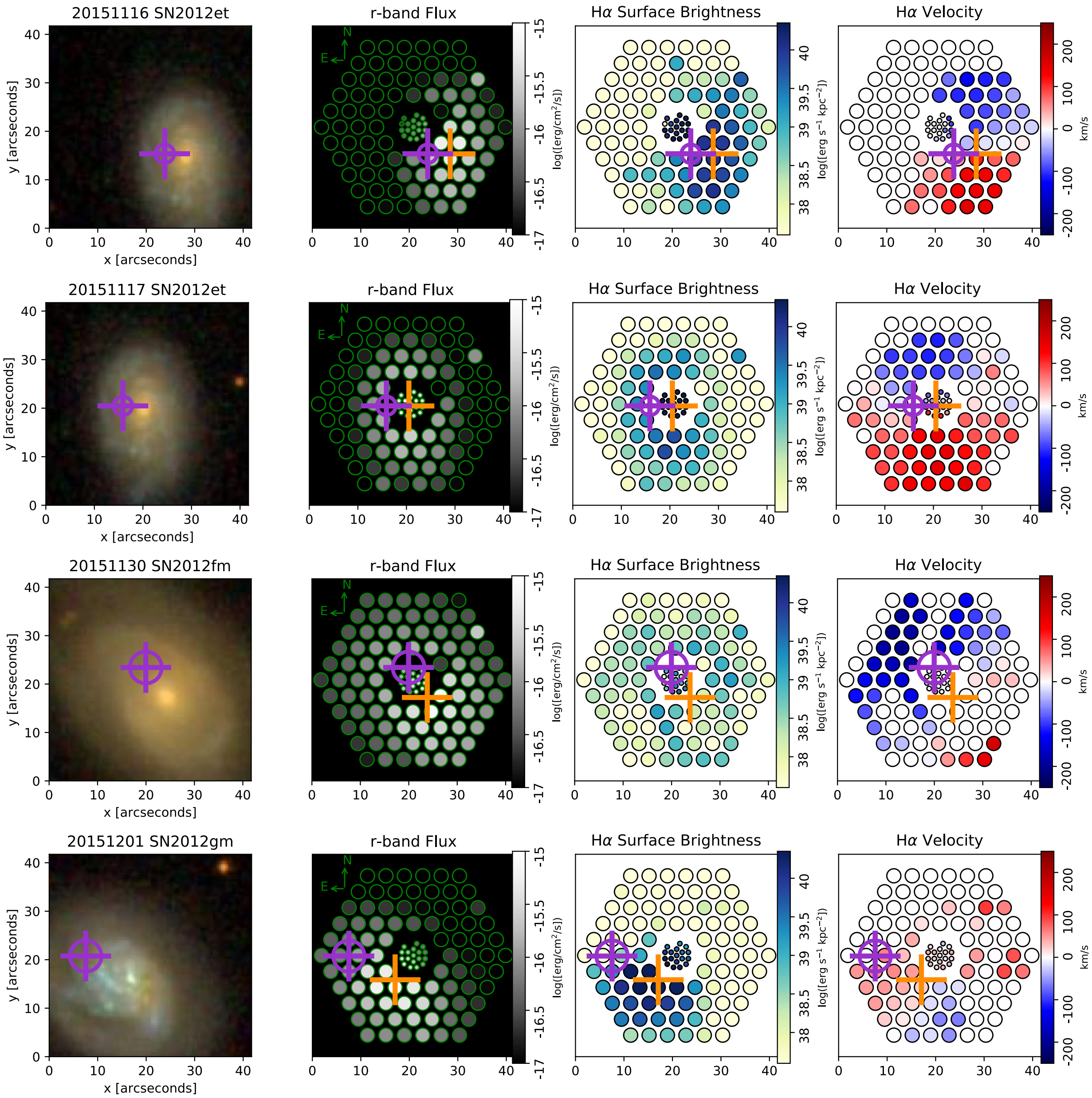

Figure 3.29 *First:* CGCG 476-117, host galaxy of SN 2012et, observed on 2015-11-16. *Second:* CGCG 476-117, host galaxy of SN 2012et, observed on 2015-11-17. *Third:* UGC 3528, host galaxy of SN 2012fm. *Forth:* NGC 7580, host galaxy of SN 2012gm.

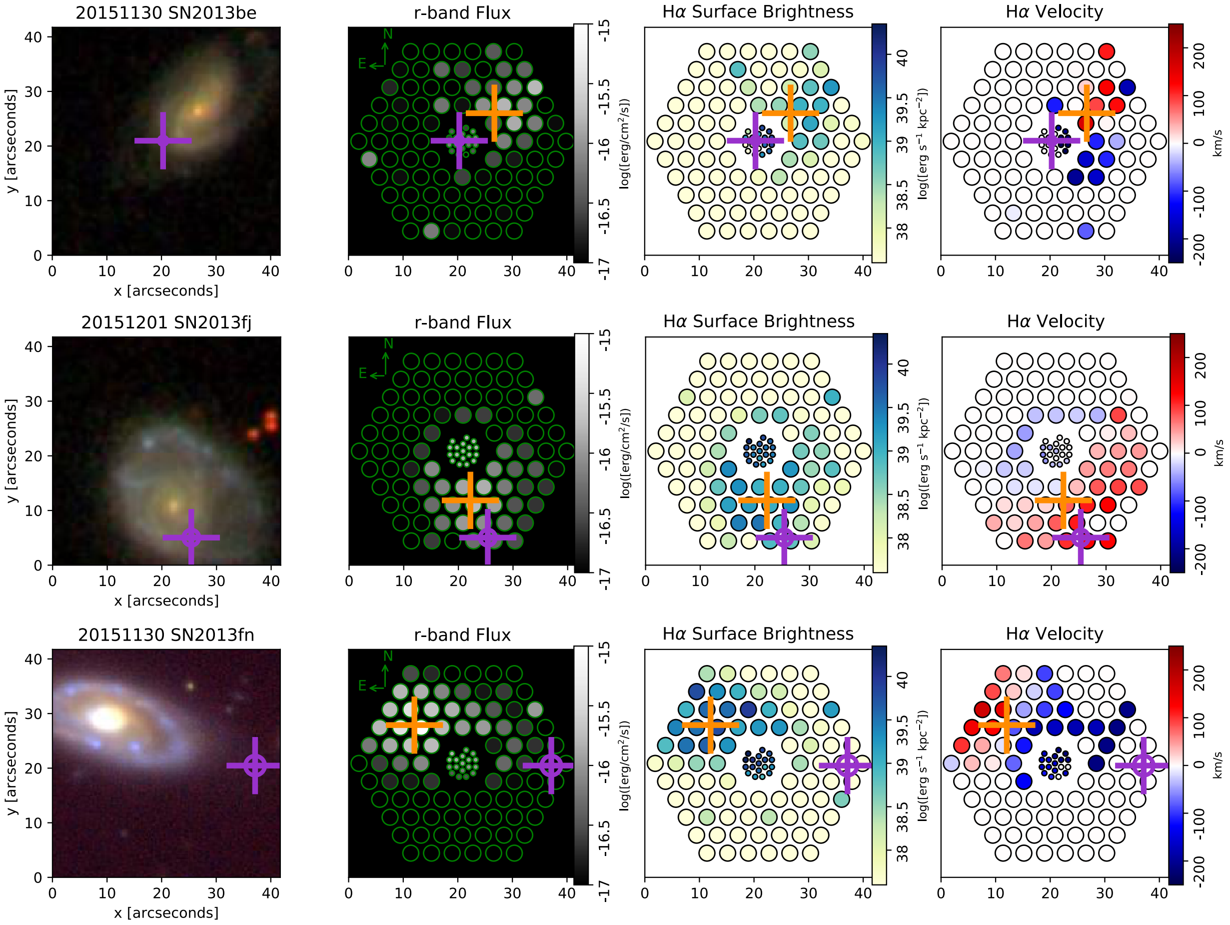

Figure 3.30 *First:* IC 3573, host galaxy of SN 2013be. *Second:* PGC 68419, host galaxy of SN 2013fj. *Third:* IC 1342, host galaxy of SN 2013fn.

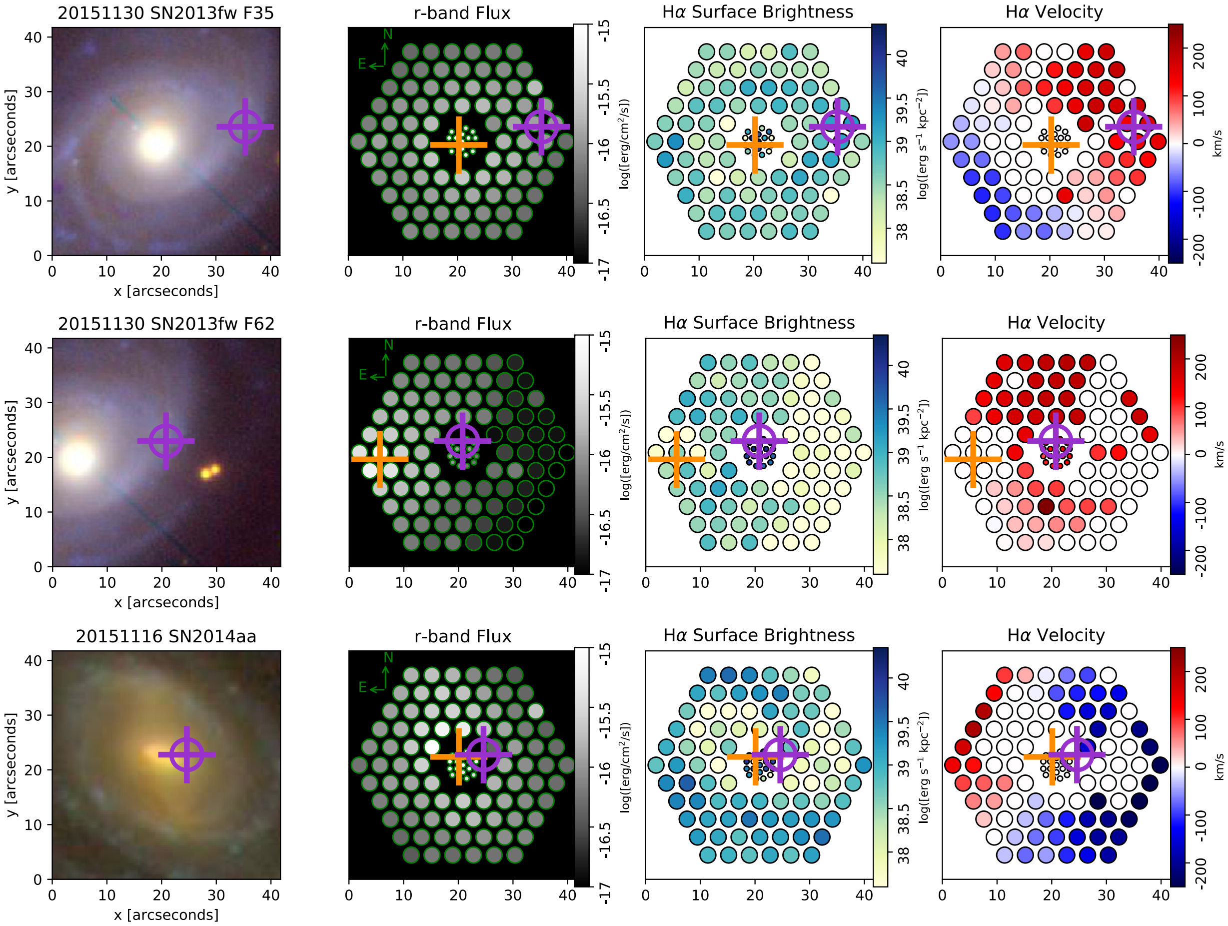

Figure 3.31 *First:* NGC 7042, host galaxy of SN 2013fw. This is the first of two pointings with the supernova explosion location around Fiber 35. *Second:* NGC 7042, host galaxy of SN 2013fw. This is the second of two pointings with the supernova explosion location around Fiber 62. *Third:* NGC 3861, host galaxy of SN 2014aa.

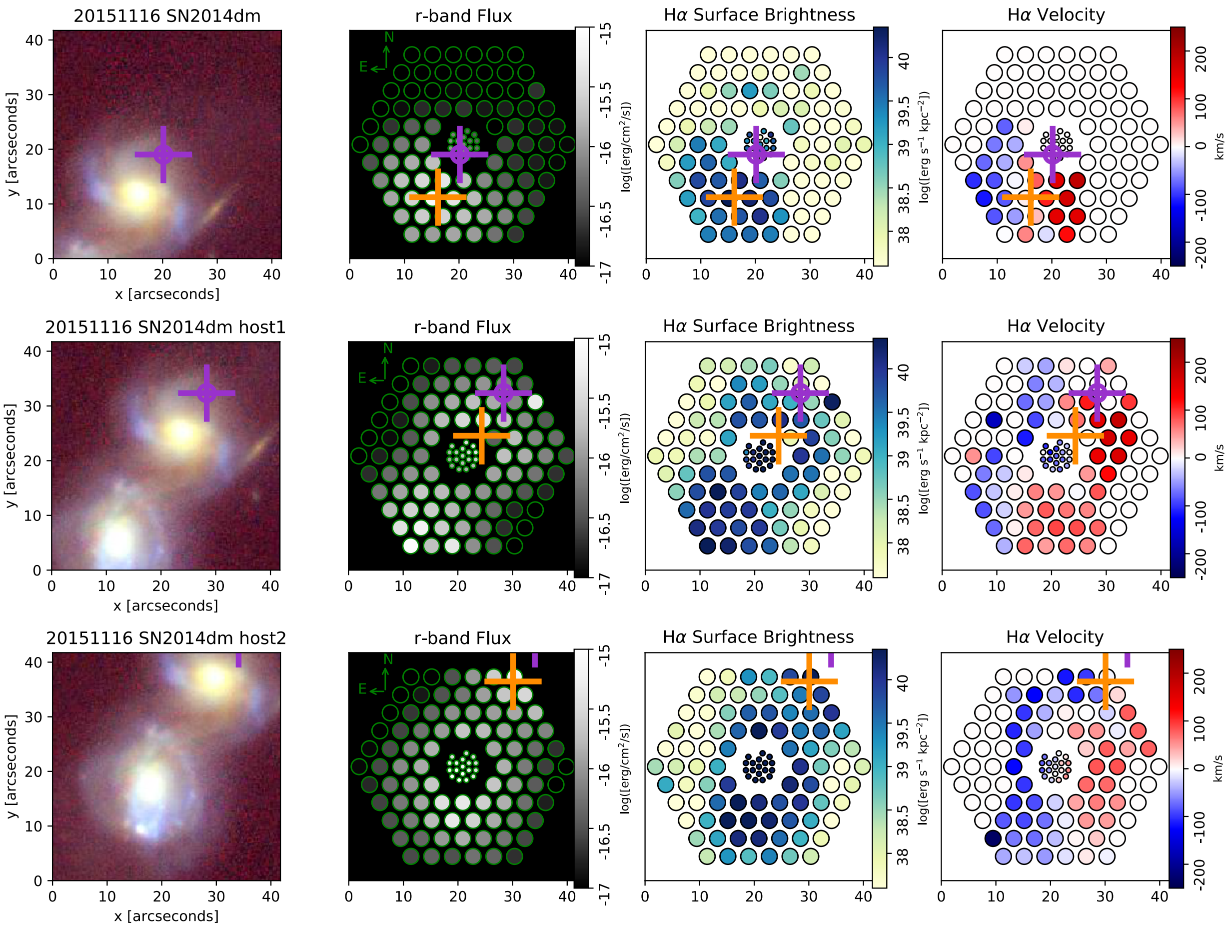

Figure 3.32 This shows all three pointings of NGC 1516A, host galaxy of SN 2014dm. *First:* Supernova explosion location at Fiber 62. *Second:* Supernova explosion location at Fiber 20. *Third:* Supernova explosion location off the fiber bundle.

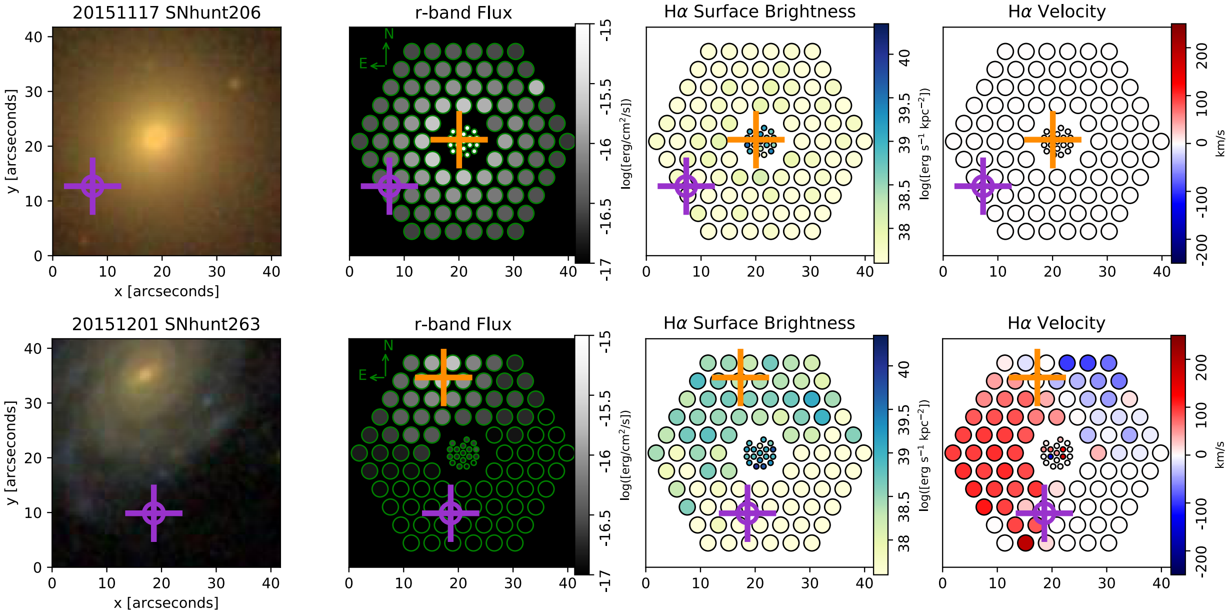

Figure 3.33 *First:* NGC 766, host galaxy of SNhunt206. *Second:* UGC 4798, host galaxy of SNhunt263.

3.7 CONCLUSION

The SweetSpot survey will provide a $\sim 50\%$ increase in the NIR lightcurve sample. SweetSpot will extend the H-band Hubble diagram out to $z \sim 0.08$, it will provide an interesting data set to study color evolution, and it will be a well-calibrated restframe data set that will be used to anchor high redshift surveys. The pilot data and DR1 are already public with DR2 and DR3 expected within the next two years.

Sections 3.4-3.6 will make up the basis for a paper on "HexPak Data Release of 32 SweetSpot Host Galaxies". We outlined the telescope configuration and target selection. We presented detailed steps of data reductions to go from raw data to sky subtracted and flux calibrated spectra. These spectra were then compared to standard star templates and SDSS spectra to test calibration. We then measured the Hα flux to determine surface brightness/star formation maps.

There are some caveats to this data and improvements that could be made: many spectra show increased flux in the blue that could cause confusion when fitting galaxy templates/stellar populations, but this could be improved with aperture corrections. The sky subtraction leaves residuals around strong and unresolved telluric lines which could be improved with a more sophisticated sky subtraction algorithm as presented in Bershady et al. (2004). However, our science is based on measuring Hα and is not affected by the problems affecting the telluric line subtraction.

Once SweetSpot DR2 becomes available, we will be able to use these spectra to probe correlations between the luminosity of NIR SNeIa and local galaxy properties.

3.8 ACKNOWLEDGEMENTS

Based on observations at Kitt Peak National Observatory, National Optical Astronomy Observatory, which is operated by the Association of Universities for Research in Astronomy (AURA) under a cooperative agreement with the National Science Foundation.

NOAO time on WIYN under two single-semester programs 2011B-0482 and2015B-0347 and one NOAO Survey program 2012B-0500 with W. Michael Wood-Vasey as the P.I for all three programs.

We thank the staff of KPNO and the WIYN telescope and engineering staff for their efforts that enabled these observations. We thank the WIYN Observing Assistants who have participated in our program: Karen Butler, Anthony Paat, Jennifer Power, Kristen Reetz, Amy Robertson, Malanka Riabokin, Christian Soto, David Summers, Doug Williams. Special thanks to Diane Harmer for scheduling the WIYN nights for the main SweetSpot survey and her invaluable help in setting up the WIYN Bench Spectrograph configuration and assisting us on initial HexPak observations.

We thank the Tohono O'odham Nation for leasing their mountain to allow for astronomical research.

We thank Eric Hooper and Matt Bershady for sharing their guide to HexPak data reductions and providing advice and feedback for the observations and data reductions.

We express our thanks to the hard-working groups who discover and provide rapid spectroscopic classification of SNeIa that have allowed our follow-up program to be viable. The

“Latest Supernovae” website[16] maintained by David Bishop was helpful in planning and executing these observations.

This research has made use of the NASA/IPAC Extragalactic Database (NED) which is operated by the Jet Propulsion Laboratory, California Institute of Technology, under contract with the National Aeronautics and Space Administration.

This publication makes use of data products from the Two Micron All Sky Survey, which is a joint project of the University of Massachusetts and the Infrared Processing and Analysis Center/California Institute of Technology, funded by the National Aeronautics and Space Administration and the National Science Foundation.

IRAF is distributed by the National Optical Astronomy Observatory, which is operated by the Association of Universities for Research in Astronomy (AURA) under a cooperative agreement with the National Science Foundation.

PyRAF is a product of the Space Telescope Science Institute, which is operated by AURA for NASA.

---

[16] `http://www.rochesterastronomy.org/supernova.html`

4.0 ARE TYPE IA SUPERNOVAE IN RESTFRAME H BRIGHTER IN MORE MASSIVE GALAXIES?

This chapter is a draft that will be submitted to the American Astronomical Society Journals. It is authored by Kara A. Ponder, W. Michael Wood-Vasey, Anja Weyant, Lluís Galbany, and Nathan Barton.

We analyze 147 Type Ia supernovae (SNeIa) from the literature that were observed in the H-band and find inconclusive evidence for a correlation between host galaxy mass. We confirm a host galaxy mass correlation with the distance modulus calculated from optical lightcurves fit with SNooPy. The host galaxy mass was estimated using photometry gathered from the Sloan Digital Sky Survey, Panoramic Survey Telescope and Rapid Response System, Galaxy Evolution Explorer, and Two Micron All Sky Survey. By comparing SN Ia residual brightnesses, we find that SNeIa in galaxies more massive than $> 10^{10.44} M_{\odot}$ are brighter than SNeIa in less massive galaxies by 0.16 ± 0.04 mag in the H band and 0.12 ± 0.03 mag at optical wavelengths. Our sample also shows a distinct outlier population with bright H-band residuals (≤ -0.5 mag) in massive, red galaxies in the smooth Hubble flow. Upon removing this outlier population, we find no correlation between H-band brightnesses and host galaxy mass.

4.1 INTRODUCTION

Since the late 1990s, Type Ia supernovae (SNeIa) have been used as standard candles to measure the expansion of the Universe (Riess et al., 1998; Perlmutter et al., 1999). Much work has gone into further standardizing optical SNeIa through lightcurve stretch (Phillips, 1993) and color (Riess et al., 1996; Tripp, 1998) as well as adding a correction from host galaxy correlations after lightcurve fitting (Betoule et al., 2014). However, there is evidence that lightcurves observed at near infrared (NIR) wavelengths ($1\ \mu m < \lambda < 2.5\ \mu m$) are more standard and require no or smaller corrections to their lightcurves to yield the same precision as optical lightcurves (Kasen, 2006; Folatelli et al., 2010; Kattner et al., 2012; Wood-Vasey et al., 2008; Barone-Nugent et al., 2012). We here compile one of the largest publicly available NIR data set to further test the standard nature of SNeIa by exploring different possible correlations between global host galaxy properties and NIR, specifically H-band, luminosity.

There is an extensive history of looking for correlations between the standardized optical luminosity of SNeIa and the properties of their host galaxies. Many papers have studied relationships with global host galaxy properties such as mass, metallicity, star formation rates, and age using galaxy photometry and galaxy photometry fit with stellar population synthesis codes (Sullivan et al., 2006; Gallagher et al., 2008; Kelly et al., 2010; Sullivan et al., 2010; Lampeitl et al., 2010; Gupta et al., 2011; D'Andrea et al., 2011; Hayden et al., 2013; Johansson et al., 2013; Childress et al., 2013a,b; Moreno-Raya et al., 2016; Campbell et al., 2016; Roman et al., 2017). These papers have found several correlations with host galaxy properties with the most significant one being host galaxy mass, though some interpret this as a result of the galaxy mass correlation with progenitor metallicity, progenitor age, or dust (Kelly et al., 2010; Hayden et al., 2013; Childress et al., 2013b). These analyses show that the standard brightness of SNeIa hosted in higher mass galaxies is brighter by $\sim$0.08 mag (Childress et al., 2013b) than the brightness of SNeIa hosted in galaxies with mass less than $10^{10} M_{\odot}$. The mass "step" was also implemented in one of the recent studies to produce cosmological constraints: the Joint Lightcurve Analysis (JLA; Betoule et al., 2014), where they independently measured a correlation with host galaxy mass and implemented a step function to account for it. Others have focused on local properties of host galaxies such as recent star formation rates within 1-5 kpc of the supernova position using spectroscopy or ultraviolet (UV) photometry (Rigault et al., 2013, 2015; Kelly et al., 2015). They find that the standard brightness of SNeIa in locally passive regions is $\sim$0.094 mag (Rigault et al., 2015) brighter than those in locally star forming regions. Furthermore, Kelly et al. (2015)

showed that SNeIa in locally star forming regions were more standard than those in non-star forming regions.

However, not every analysis suggests that there is a correlation with host galaxy properties. Kim et al. (2014) used an updated lightcurve analysis that is more flexible to intrinsic variations in SNeIa (introduced in Kim et al., 2013) and finds correlations with host galaxy mass, specific star formation rates, and metallicity to be consistent with zero. Jones et al. (2015) finds no host galaxy correlation with local star formation rates derived from UV photometry by using a larger sample size than previous studies and using different selection criteria. Scolnic et al. (2014) describes the systematics utilized in the Pan-STARRS Hubble diagram (Rest et al., 2014) and finds a correlation with host galaxy mass with a step size of 0.037 ± 0.032 mag, which is not a statistically significant trend. Instead of including the step function directly in the analysis, they add systematic uncertainty to allow the possibility that it might exist. We see much evidence to warrant continued exploration of this parameter space to understand whether we are searching for a real correlation or if we need to improve the analysis of SNeIa lightcurves.

All of the previous host galaxy analyses have examined correlations using only optical lightcurves. We here, for the first time, present similar studies using restframe NIR. Doing a similar analysis using NIR lightcurves will help shed light on physical mechanisms and color-dependent intrinsic dispersions.

SNeIa in the H-band have been shown to be standard to $0.15 - 0.2$ mag without lightcurve corrections (Folatelli et al., 2010; Kattner et al., 2012; Wood-Vasey et al., 2008; Barone-Nugent et al., 2012; Weyant et al., 2014) whereas optical lightcurves before brightness standardization have a scatter of ~ 0.8 mag (Hamuy et al., 1995). However, there are only ~ 279 NIR lightcurves publicly available compared to the over > 900 available for optically observed SNeIa.

The improved ability to determine standard distances, together with the reduced sensitivity to dust extinction, have motivated several recent projects to pursue larger samples of SNeIa observed in the restframe NIR: CSP-I, II (Contreras et al., 2010; Stritzinger et al., 2011; Kattner et al., 2012); CfA (Wood-Vasey et al., 2008; Friedman et al., 2015); RAISINS (Kirshner, 2012); and SweetSpot (Weyant et al., 2014, 2017).

To gather host galaxy properties, we utilized publicly available galaxy catalogs from Sloan Digital Sky Survey (SDSS), Panoramic Survey Telescope and Rapid Response System (Pan-STARRS), Galaxy Evolution Explorer (GALEX), and Two Micron All-Sky Survey (2MASS). From this, we can measure restframe colors and absolute magnitudes and estimate host galaxy mass.

We use SNooPy (Burns et al., 2011, 2014) for lightcurve fits as it is the most available fitter with NIR templates. We combine optical and NIR lightcurves to improve fits with the s_{BV} parameter from Burns et al. (2014). Using optical lightcurves only, we also test for a mass step with fits excluding NIR information. All previous analyses have explored host galaxy correlations with standardized brightnesses calculated from SALT2 (Guy et al., 2007) and/or MLCS2k2 (Jha et al., 2007) fitters (e.g., Kelly et al., 2010).

This chapter is organized as follows: Section 4.2 explains what supernovae we use and how we collected optical, UV, and NIR photometry of their host galaxies. Section 4.3details how we fit lightcurves and created the restframe H and optical Hubble diagrams. Section 4.4 goes through several host galaxy correlations and shows that less massive, blue spiral galaxies produce SNeIa that are dimmer than SNeIa found in more massive, red elliptical galaxies. Section 4.5 explores the statistical significance of these correlations with restframe H and optical distance moduli Hubble residuals. We find inconclusive evidence for correlations between H residuals and host galaxy properties, but we do confirm the host galaxy mass step with optical lightcurves. We conclude in Section 4.6.

4.2 SN IA LIGHTCURVES AND HOST GALAXY SAMPLE

4.2.1 SN Ia

We started with the compilation of literature SNeIa gathered in Weyant et al. (2014) and kept the naming scheme for different samples. SweetSpot had a first data release (Weyant et al., 2017) with 34 SNeIa that we are adding to this sample. Friedman et al. (2015) also presented 74 additional CfA SNeIa from their final data release and this will be the first analysis including these NIR lightcurves. We added 27 more SNeIa from miscellaneous sources to the full set that are nominally a part of the K+ sample (as defined in Weyant et al., 2014), but none are in the final lightcurve sample. We gathered host galaxy information for this full set of 279 SNeIa observed in the NIR, but only 147 lightcurves make it into the Hubble diagram and the correlations test (for more information see Section 4.3.1). Of these 279 SNeIa, 87 have optical photometry of their host galaxies to measure restframe $g-r$ color and 137 have sufficient host galaxy photometry to derive masses.

We used the Open Supernova Catalog[1] (OSC; Guillochon et al., 2017) to retrieve all lightcurve data. Several pull requests were made to the OSC in this process to correct and add information for several dozen SNeIa. 105 of the 147 SNeIa with NIR lightcurves used for the Hubble residual analysis also have optical lightcurves that we used for lightcurve fits and host galaxy correlations.

4.2.2 Host Galaxies

The host galaxy for all 279 SNeIa was identified from the IAU list of supernovae[2] and the NASA Extragalactic Database (NED)[3]. We used the heliocentric redshift for each galaxy recorded in NED. If NED did not have a spectroscopic redshift, we recorded the redshift from the respective supernova.

We are interested in exploring host magnitudes and colors relative to supernova brightness residuals. We obtained optical photometry from both the SDSS Data Release 13 (SDSS Collaboration et al., 2016) and the Pan-STARRS Data Release 1 (PS1; Chambers et al., 2016; Flewelling et al., 2016; Magnier et al., 2016) using their respective CasJobs[4] websites. From SDSS, we obtained the *ugriz* "modelMag" magnitudes, which are based on the best fit "de Vaucouleurs" or "Exponential" profile in the r-band. Though "cmodelMag" magnitudes give a more accurate description of the total flux in each filter, "modelMag" magnitudes are better for color studies because the flux is measured consistently across all filters (Stoughton et al., 2002). To replicate the "modelMag" procedure with PS1 data, we downloaded the de

---

[1] `https://sne.space/`

[2] `http://www.cbat.eps.harvard.edu/lists/Supernovae.html`

[3] `http://ned.ipac.caltech.edu/`

[4] `http://skyserver.sdss.org/CasJobs/`, `http://mastweb.stsci.edu/ps1casjobs/`

Vaucouleurs and Exponential profile fits with their associated reduced χ^2 values and used the best fit profile in the r-band for all $grizy$ magnitudes. SDSS always reported all five $ugriz$ magnitudes while PS1 does not always have all five $grizy$ magnitudes for all of our objects. If gri magnitudes were not available in PS1, we did not keep the host galaxy photometry as we could not calculate extinction coefficients (Tonry et al., 2012) or $g - r$ color. See Section 4.2.2.1 for a comparison of SDSS and PS1 photometry. Several host galaxies had photometry that we did not include because they did not meet quality cuts: for SDSS we require clean photometry (only objects from the Primary table, removed objects with deblending issues, cosmic rays, and other interpolation problems) and for PS1 we require several detections[5] in g and r as well as more than 95% of the pixels to be unmasked to consider the object real and (PSF mag - Kron mag) > 0.5 mag to ensure that the photometry was from a galaxy-like object and not a star.

We obtained GALEX GR6/GR7[6] (Bianchi et al., 2014) far ultraviolet (FUV/F) and near ultraviolet (NUV/N) information where available from the MAST data archive[7]. The magnitudes returned are the result of the elliptical aperture method "MAG_AUTO" in Source Extractor (Bertin & Arnouts, 1996). We also gathered JHK_s magnitudes from the 2MASS All-Sky Extended Source Catalog (XSC; Skrutskie et al., 2006) using the NASA/IPAC Infrared Science Archive (IRSA)[8]. We used the total magnitude calculated from the extrapolated radial surface brightness profile. 2MASS always reports JHK_s; however, GALEX often returns only FUV or NUV.

Figure 4.1 illustrates the wavelength coverage from these surveys by plotting the transmission functions per filter. 137 SNeIa of the subset of 147 lightcurves have host galaxy photometry available in at least one of these catalogs. Table 4.1 lists how many SNeIa host galaxies have photometry from the various surveys that are in our analysis. Figure 4.2 shows a histogram of how many SNeIa have photometry in each band ($griz$ in SDSS and PS1 are slightly different, but here we are treating them as approximately the same). Figures 4.3 and 4.4 show color postage stamps for galaxies used from SDSS and PS1, respectively.

---

[5] PS1 observed the same area of the sky on the same night with short intervals in between them to discover Near Earth Objects (NEOs) and once every 6 months in order to make parallax estimations.

[6] `http://galex.stsci.edu/GR6/`

[7] https://galex.stsci.edu/casjobs/

[8] `http://irsa.ipac.caltech.edu/frontpage/`

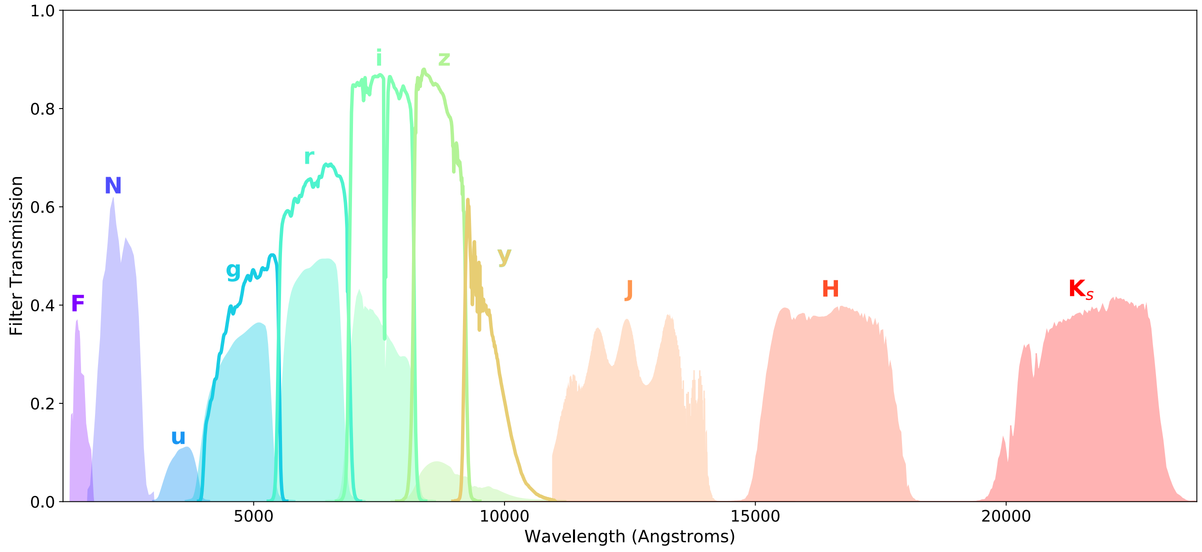

Figure 4.1 Detector, optics, filter, and atmospheric transmission functions for GALEX, SDSS, PS1, and 2MASS.

We use `kcorrect` from Blanton et al. (2003a); Blanton & Roweis (2007) to transform the photometry to the restframe and measure other physical parameters[9]. `kcorrect` fits galaxy spectral energy distributions from the UV to NIR and relies on Bruzual & Charlot (2003) stellar evolution synthesis code, so it can also return physical parameters such as stellar mass. Using the results from `kcorrect`, we then calculated restframe colors, absolute magnitudes, and host galaxy mass. The added UV plus NIR photometry help constrain the different models as many diverse galactic spectra overlap at optical wavelengths, but separate more cleanly at UV and NIR wavelengths. We combine optical photometry (either SDSS *ugriz* or PS1 *grizy*) plus GALEX and 2MASS for each host galaxy and only require that two filters in the set of $FNugrizyJHK_S$ be observed to derive K-corrections, restframe colors, and host galaxy mass. All magnitudes are converted to the AB magnitude system and extinction corrected before being input into `kcorrect`.

In our final sample, if a host galaxy was observed with both SDSS and PS1, we kept the SDSS observations since this survey contained u-band photometry that provides a better constraint on young stars and recent star formation. The redshift distribution of our final

---

[9] `kcorrect` does not return errors on the physical parameters.

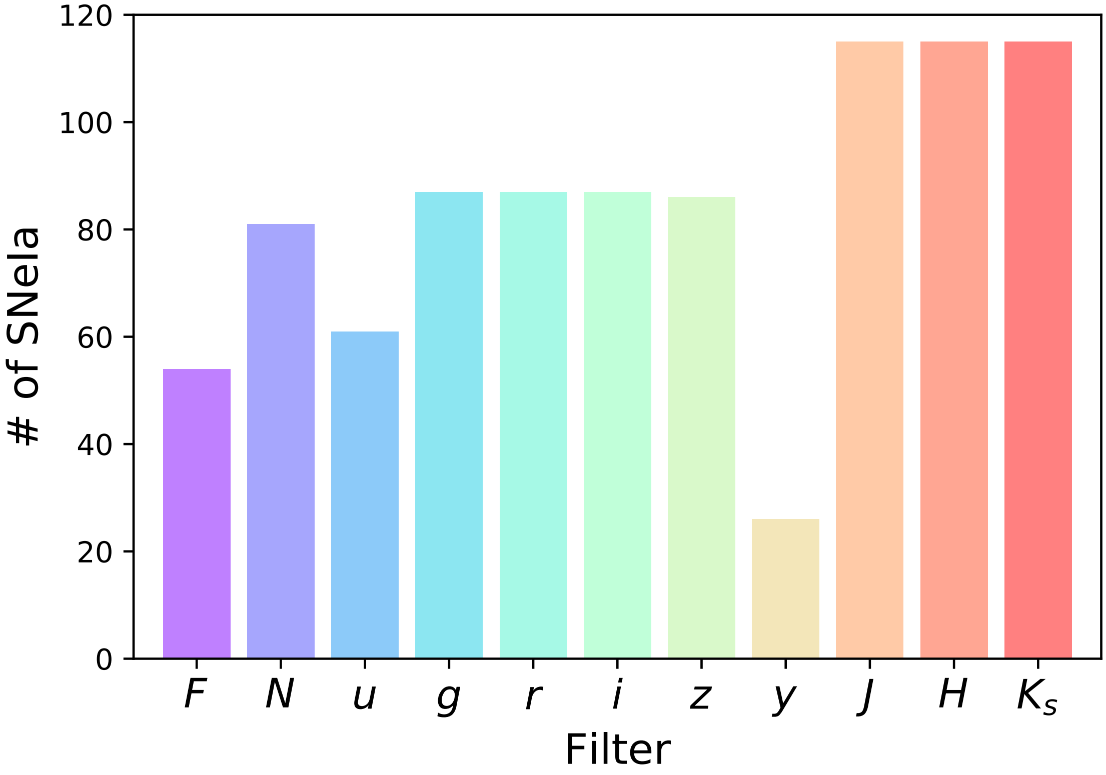

Figure 4.2 Histogram of number of SNe observed in each filter for the final sample of 147 SNeIa used in the Hubble residual analysis.

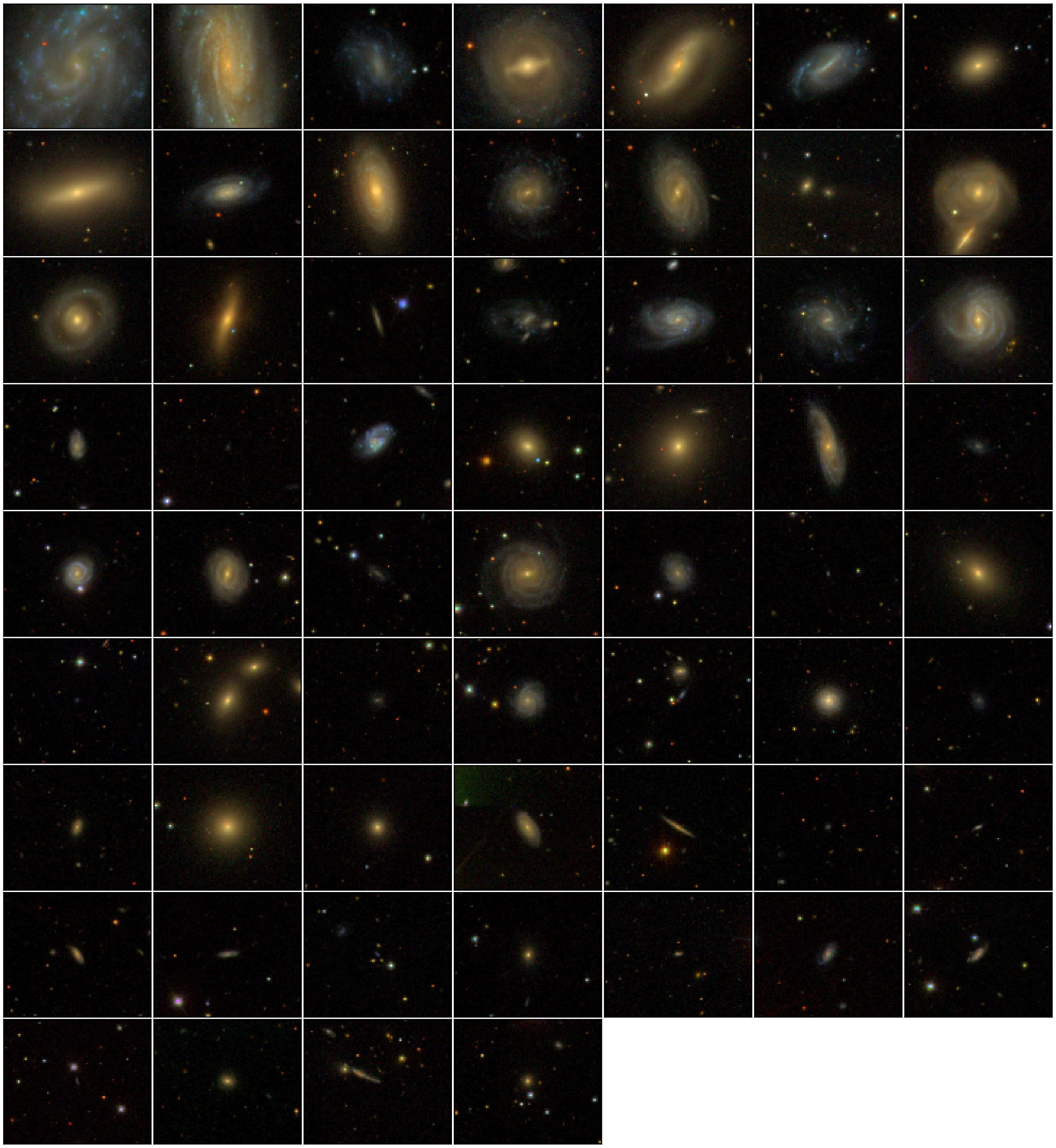

Figure 4.3 SDSS color postage stamps. The field of view is ∼2' by 2'. North is up and East is left.

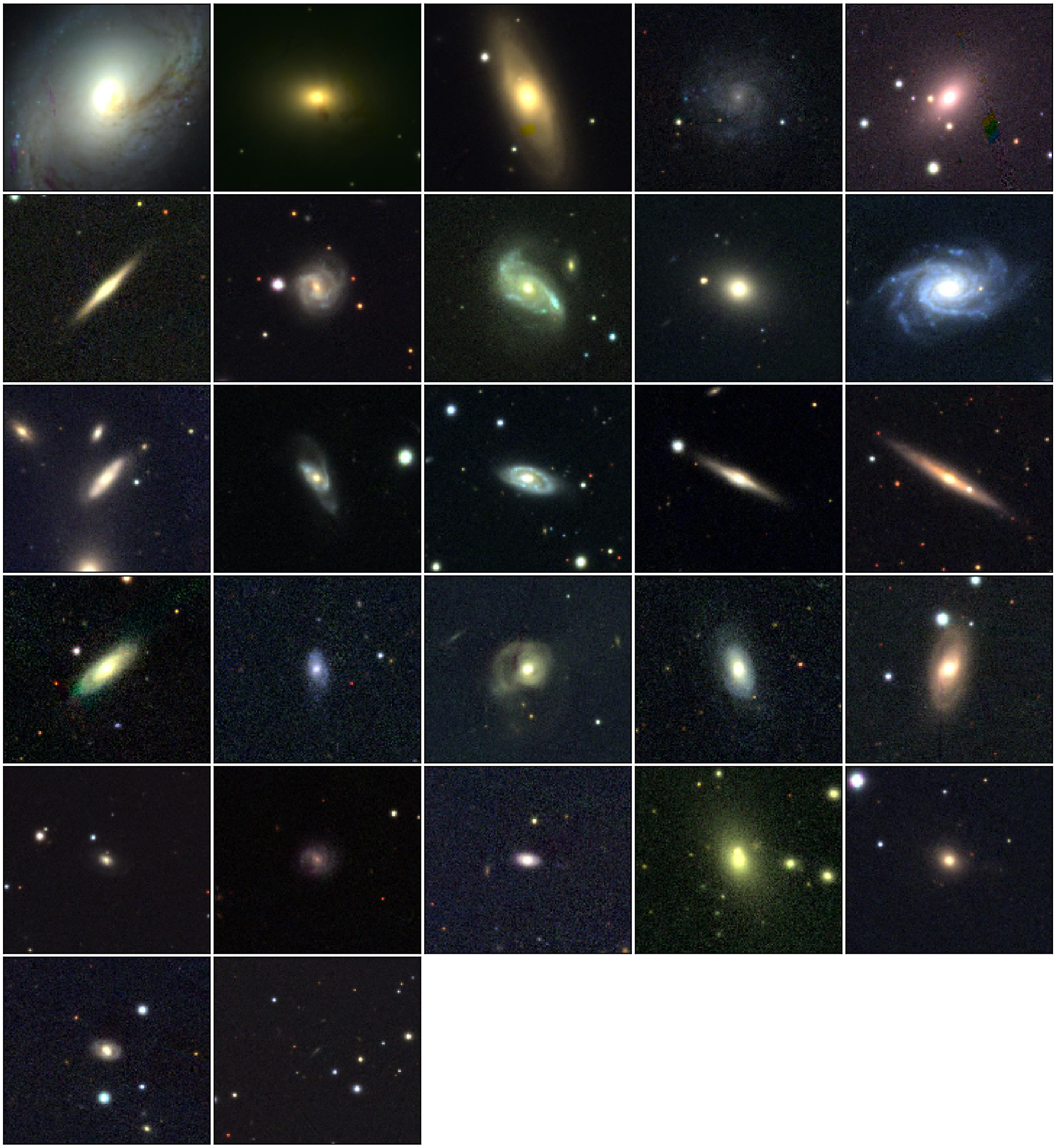

Figure 4.4 PS1 color postage stamps. The field of view is ∼2' by 2'. North is up and East is left. Host galaxies for (In order): SN1998bu, SN 2011B, SN 2005am, SN 2013cs, SN 2005al, SN 2009kk, SN 2009kq, SN 2005bo, SN 2006hb, SN 2009le, SN 2010cr, SN 2009D, SN 2013fn, SN 2006gj, SN 2006ev, SN 2006os, LSQ12fhs, SN 2008gp, SN 2005iq, SN 2007ba, SN 2010dw, SN 2010ho, SN 2006hx, LSQ13cmt, LSQ13cwp, SN 2005ag, PTF10ndc.

sample per survey is presented in Figure 4.5. We present the photometric data for all 279 SNeIa in Appendices B.1 and B.2.

4.2.2.1 Comparing SDSS and PS1 Photometry

67 host galaxies are found in both SDSS and PS1 surveys and are used here to examine differences between the two catalogs' photometry. Since we gathered host galaxy photometry for all 279 host galaxies, this sample of 67 contains SNeIa whose lightcurves are not used in the SNeIa brightness analysis below.

Both SDSS and PS1 fit de Vaucouleurs and Exponential surface brightness profiles to estimate flux. Figure 4.6 illustrates the differences in the galaxy profile fits between SDSS and PS1 for three host galaxies. The top row of Figure 4.6 shows NGC 5584, a low-redshift ($z = 0.005464$), well-resolved, face-on, spiral galaxy. The left hand side of the top row shows the r-band cutout from PS1 and the lines indicate the major axis that SDSS and PS1 derived from the profile fits. In this case, PS1 only returned an Exponential fit and listed the de Vaucouleurs fit as null. The right-hand side illustrates surface brightness profiles from SDSS and PS1 examining both de Vaucouleurs and Exponential fits to the galaxy on the right. The vertical lines correspond to the calculated effective radii, which is the radius that includes half of the total light. SDSS records this galaxy to be 2 magnitudes brighter than PS1, which is unsurprising since the effective radius from SDSS is over 4 times larger than effective radius from PS1. The effective radius from PS1 only includes the bulge while SDSS extends out amongst the spiral arms. The middle row of Figure 4.6 shows an edge-on spiral galaxy at $z = 0.049824$. In this case, SDSS and PS1 have nearly identical profiles and only differ in r-band magnitude by 0.08 mag. The bottom row of Figure 4.6 is an elliptical galaxy at $z = 0.027612$. Here the profiles are much different with PS1 again having a smaller effective radius than SDSS for both de Vaucouleurs and Exponential fits, which only encompass the core. Though these profiles are relatively different, SDSS is only 0.3 magnitudes brighter in the r-band.

SDSS systematically returns redder colors than PS1 by 0.05 mag (see the right panel in Figure 4.7). If we added the 0.05 mag offset to the uncertainty in the PS1 measurement, it would only increase the uncertainty by $< 1\%$. Because this error is so small, we do not

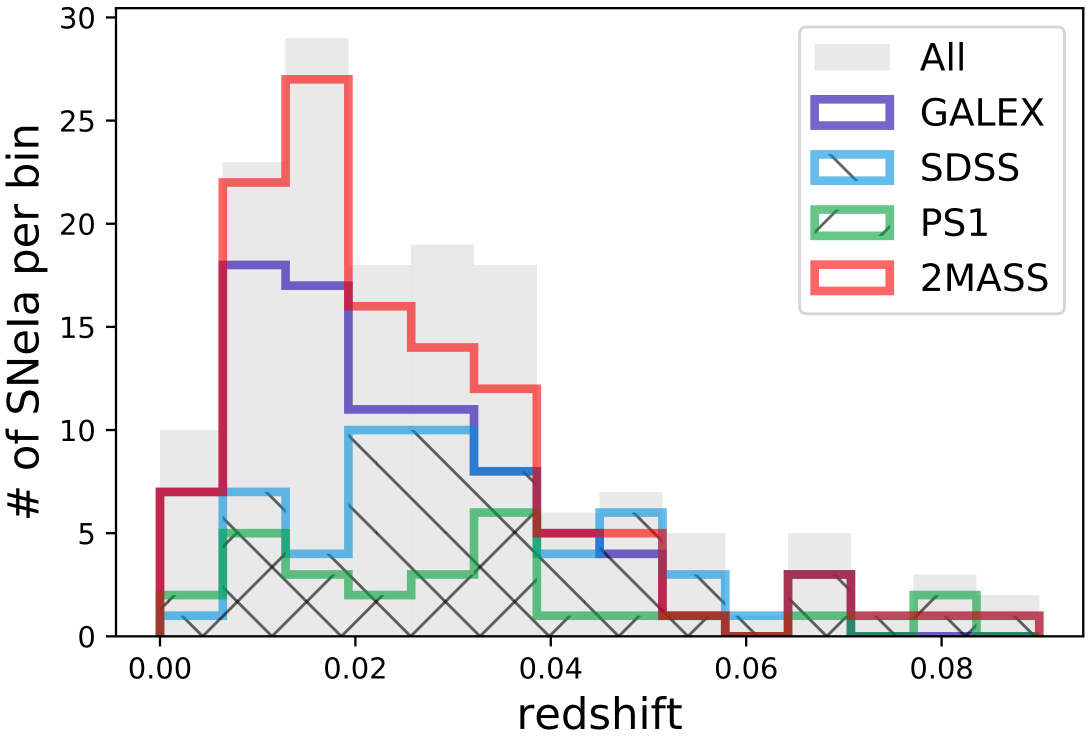

Figure 4.5 Distribution of redshifts for GALEX, SDSS, PS1, and 2MASS Surveys for the final sample of 147 SNeIa used in the Hubble residual analysis. The distribution of the full sample of SNeIa used in the Hubble residual analysis is in grey. Many of the host galaxies have photometry from more than one of these surveys such that the histogram with of all of the host galaxies is not a stack of the 4 other histograms, but a histogram of all unique galaxies between the 4 surveys.

Table 4.1. Number of Host Galaxies Observed per Survey.

Survey	GALEX	SDSS	PS1	2MASS	GALEX + Optical + 2MASS
GALEX	84				
SDSS	41	60			33
PS1	14	–	27		13
2MASS	75	42	24	115	

Note. — We have host galaxy photometry for 137 SNeIa out of 147 SNeIa with NIR lightcurves. Along the diagonals is the total number of galaxies with photometry from their respective survey. The off–diagonals are how many SNeIa host galaxies have photometry in both of the corresponding surveys.

factor it in.

The left plot of Figure 4.7 shows a comparison between the apparent magnitudes for the g and r bands from SDSS and PS1. Only four host galaxies show a discrepancy greater than 10%. Of these four, two are large spiral galaxies, one is a crowded field with two contaminating satellite galaxies, and one is a large elliptical for which PS1 underestimated the effective radius. In general, PS1 and SDSS photometry are in agreement; however, we are cautious with PS1 photometry for large, well-resolved galaxies and crowded fields. We can estimate the systematic errors on the PS1 photometry from this plot as well. The standard deviation of the distribution of the difference between the SDSS and PS1 photometry is ~ 0.4 mag. This additional uncertainty was not included in the `kcorrect` fits here, but will be included in future works.

There are 60 and 27 host galaxies that use SDSS and PS1 photometry, respectively. Examining Figure 4.4 we can see there are a few galaxies that may not be fit well by the PS1 algorithm. We reviewed the surface brightness profiles for the resolved spiral host galaxies of SN 2009le, SN 2009D, SN 2013fn, and SN 2010ho, but the effective radii seemed appropriate

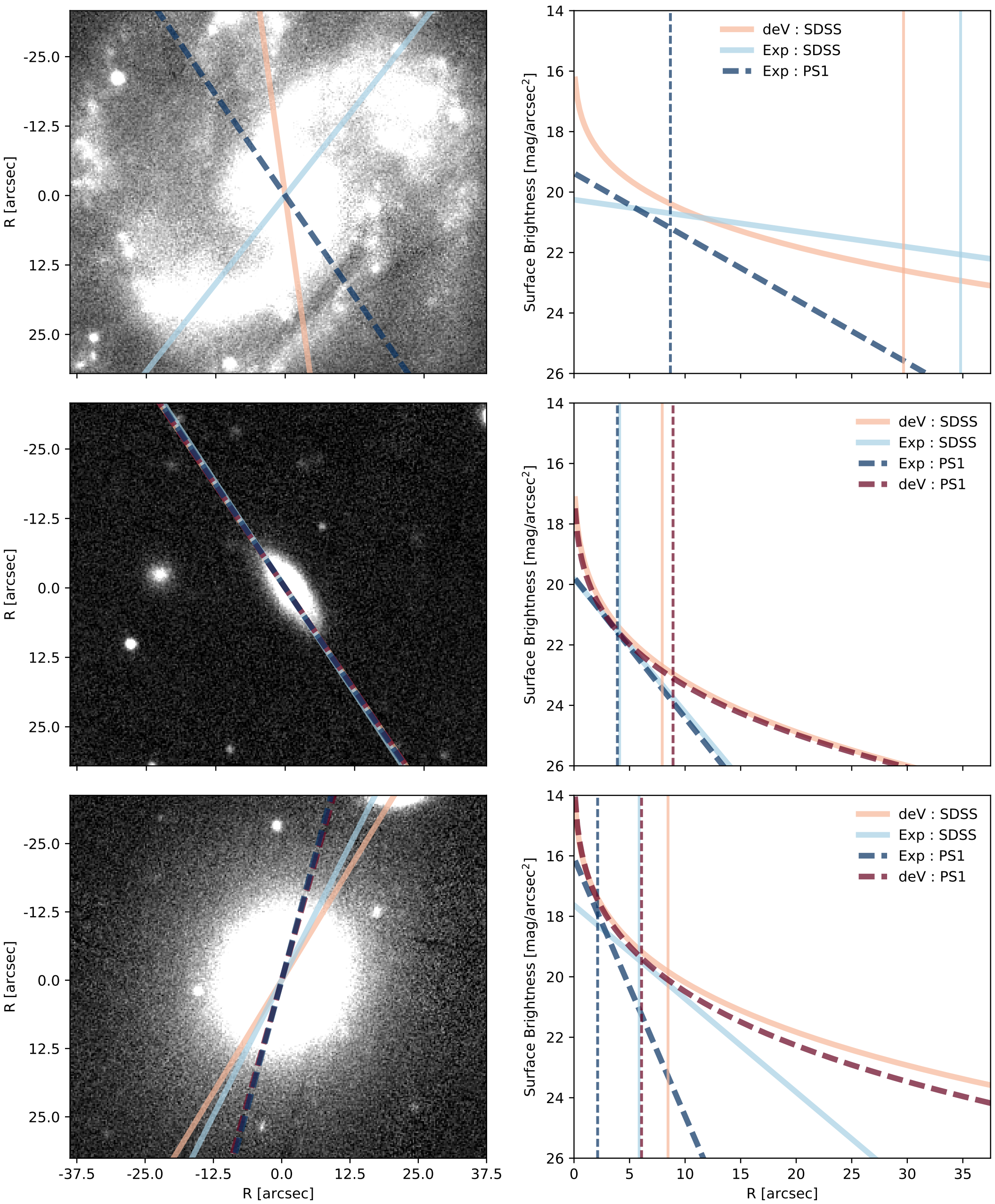

Figure 4.6 *Left:* r-band image from PS1. The lines indicate the derived major axis. *Right:* Surface Brightness Profiles calculated from either a de Vaucouleurs (deV) or Exponential (Exp) profile per survey. The vertical lines represent the effective radius calculated from each profile fit. The solid lines are fits from SDSS and the dashed lines are fits from PS1. The red lines are de Vaucouleurs fits and the blue lines are Exponential fits. *Top:* NGC 5584 / SN 2007af. PS1 did not return any de Vaucouleurs fits for this galaxy. *Middle:* SDSS J12837.60+011348.6 / SN 2006eq. *Bottom:* NGC 6343 / SN2013bs.

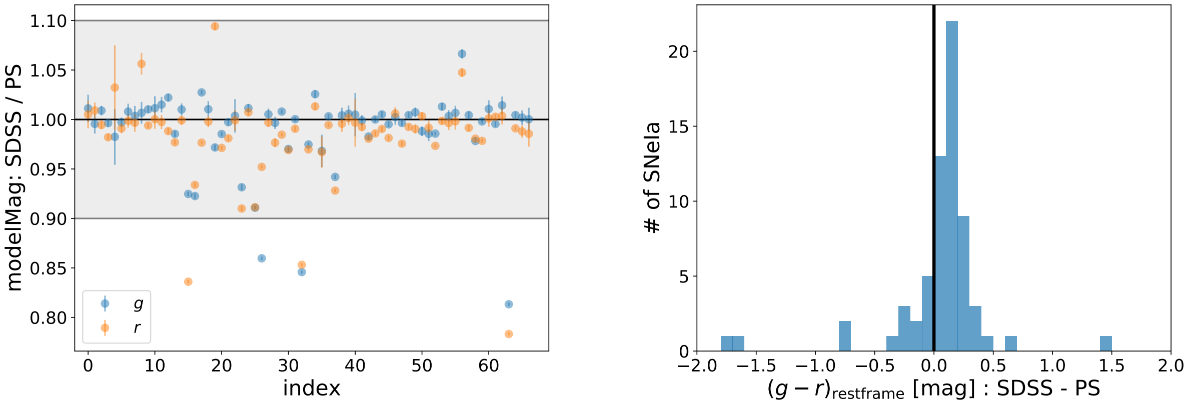

Figure 4.7 *Left:* Comparison of the catalog "modelMag" for g and r band observations. Errors assume no correlation between SDSS and PS1 photometry. The x-axis denotes the index in an array of matched host galaxies. The y-axis is the SDSS modelMag divided by the PS1 modelMag. The shaded region corresponds to differences within 10% between the two surveys. There are 4 outlier galaxies, but examining their fit profiles explains the differences: Index 17: Large, resolved, face-on spiral galaxy. The effective radius from is SDSS is around 20" but PS1 calculates it to be at 1", which causes the profiles in PS1 drop off much quicker than in SDSS excluding much of the flux. Index 28: Large elliptical galaxy where PS1 calculates the effective radius 10" closer to the core of the galaxy than SDSS. Index 34: This is the large spiral galaxy from Figure 4.6 Index 63: A crowded field with 2 satellite galaxies within the effective radius calculated from SDSS. *Right:* Histogram of restframe $(g-r)_{\rm SDSS} - (g-r)_{\rm PS1}$ showing that SDSS is redder than PS1 by 0.05 mag.

for each galaxy. However, the spiral host galaxies of SN 2009kq and SN 2005bo have very small effective radii and are probably underreporting their flux, and the host galaxy of SN 2008gp is a resolved spiral galaxy in a crowded field where the effective radius is too large. These three galaxies do not cause obvious outliers in the host galaxy properties shown below.

4.2.2.2 Live SNeIa in Host Galaxy Observations

If SDSS or PS1 observed a host galaxy when the respective SN Ia was live, the SN Ia could contaminate the measured flux. SDSS collected our host galaxies between 1999 and 2009 and PS1 started observations in 2010, so we only searched through the images of galaxies observed during the same time as these surveys. We only looked for SN Ia flux contamination from the SNeIa used in the Hubble residual analysis.

No SDSS observations occurred while the respective SN Ia was live with one possible exception: SN 2008gl was discovered on 2008-10-20 (Pignata et al., 2008) and SDSS observed its host galaxy UGC 881 on 2008-10-03. Friedman et al. (2015) reports a $\mathrm{T}_{B_{\max}}$ at 2008-10-29, so the SDSS observation was taken a few days before the SN Ia exploded. We confirmed this by examining the galaxy in all *ugriz* filters and found no additional flux at the SN Ia location.

We found two host galaxies in the PS1 sample with some contamination from an SN Ia as shown in Table 4.2. R_e is the effective radius reported by PS1, R_{SN} is the radial location of the supernova, and "SN/Host" is the ratio of the supernova to host galaxy flux. Both of these SNeIa have flux that is less than 1% of the host flux and are not a major contaminate. No other SNeIa were present in their host galaxy observation.

4.2.2.3 Comparing Optical Data Only to UV+Optical+NIR Data

The added UV plus NIR photometry help constrain the different models as many diverse galactic spectra overlap at optical wavelengths but show a clear difference at UV and NIR wavelengths.

The left panel of Figure 4.8 compares `kcorrect`–derived properties from optical only photometry versus optical plus UV, optical plus NIR, or optical plus both UV and NIR

Table 4.2. PS1 Galaxies with Host Contamination

SN	Galaxy	Galaxy Type	R_e (")	$R_{\rm SN}$ (")	Filter(s)	SN/Host[a]
SN 2013cs	ESO 576-17	Spiral	12.8	28.0	*grizy*	$< 0.1\%$
LSQ13cmt	ESO 541- G 013	Elliptical	14.9	30.0	*g*	$< 1.0\%$

[a] If more than one filter was contaminated, *r*-band was used to determine the amount of flux of the SN and Host.

photometry for 47 galaxies that had GALEX, optical (SDSS or PS1), and 2MASS photometry. Most high mass galaxies agree with the optical only measurements and even where they differ, all additional photometry agree on the mass. At masses $< 10^{10} M_\odot$, there are differences between the optical only and optical plus results with additional discrepancies between optical plus UV versus optical plus NIR in the derived mass. Adding UV and NIR wavelength coverage improves estimates of low mass galaxies.

Though we only use the inferred physical property of host galaxy mass from `kcorrect` for the residual analysis, we can examine a star formation rate indicator to illustrate how the fits change in different galaxy photometry. There are more variations in the calculated global recent Star Formation Rates (SFRs) from the Scalo *b*-parameter. In the right panel of Figure 4.8, we show the star formation rate within 300 million years divided by the average SFR. In the lower SFR areas, some galaxies have their rates drastically increased, and some have their rates drastically decreased.

There is no change to the *K*-correction values and so no change in restframe optical absolute magnitudes or colors by adding UV/NIR data.

4.2.2.4 Bias in Calculated Host Galaxy Mass

11 of our SNeIa overlapped with those used in the Kelly et al. (2010) analysis. We found that our host galaxy masses are consistently lower than those reported in Kelly et al. (2010). The difference in mass is within $1 - 3\ \sigma$ in mass (median difference of 0.36 dex), but `kcorrect` does not return any errors on the estimate so the values may be consistent within the error bars. One major outlier is the host galaxy of SN 2006ac, NGC 4619. We calculated the host galaxy mass at $10^{8.41} M_\odot$ while Kelly et al. (2010) derived a value at $10^{11.11+0.23/-0.25} M_\odot$. We

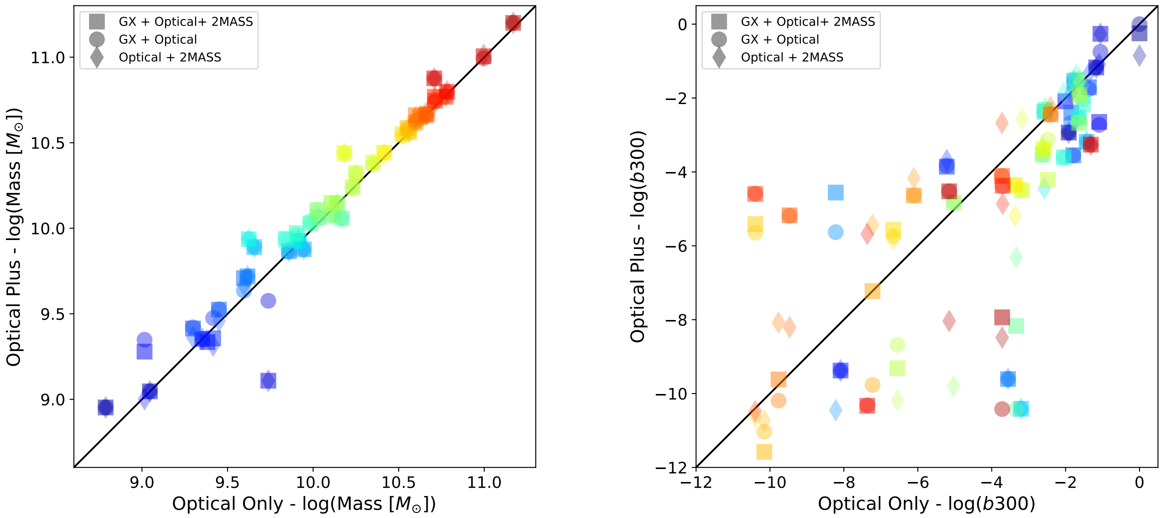

Figure 4.8 Comparison of derived quantities from `kcorrect` of 47 galaxies for when only optical data is used versus optical plus UV, optical plus NIR, or optical plus both UV and NIR photometry. In both plots, each color represents one galaxy and the three shapes represent how much photometry was included in `kcorrect`: squares for full GALEX, Optical, and 2MASS, circles for GALEX and Optical only, and diamonds for Optical plus 2MASS only. *Left:* Plot of the derived host galaxy masses. A blue to red color map was applied to give each host galaxy a different color, but the colors do not represent any quantity. Most high mass galaxies are in agreement with the optical only measurements; however, low mass galaxies have more variation and vary more depending on which photometry is used. *Right:* Comparison of derived host galaxy SFR within 300 million years compared to average SFR (Scalo b parameter). We have used the same color map as in the mass plot to the left in this plot. There is no correlation at lower recent star formation and a relative agreement at larger recent star formation with a preference to decrease the SFR.

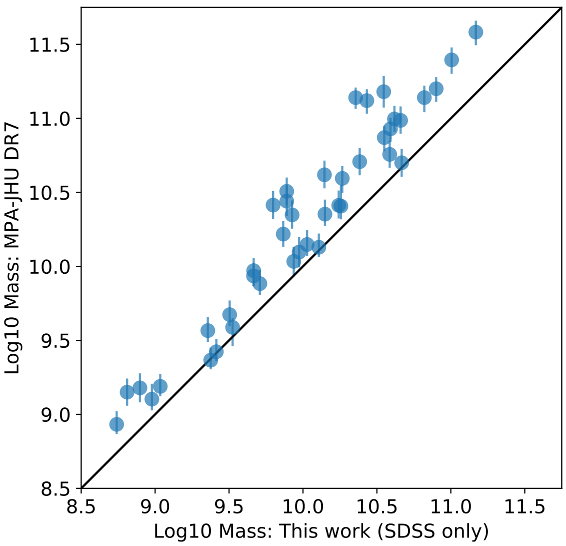

Figure 4.9 Comparison of `kcorrect`-derived host galaxy masses and the masses from the MPA-JHU sample originally presented in Kauffmann et al. (2003) with DR4 data and updated for DR7.

used photometry from $FNugrizJHK_S$ to fit the mass whereas Kelly et al. (2010) only used SDSS $ugriz$. If we use only SDSS magnitudes in `kcorrect`, we get an even more discrepant mass of $10^{7.3}M_\odot$. Following Kelly et al. (2010), we do not fit galaxies with a mass $< 10^{9.5}M_\odot$ so this object does not affect our results in Section 4.5.4; however, it is included in the high mass sample of Kelly et al. (2010).

We compared our `kcorrect`-derived masses to the photometric mass estimates from the MPA/JHU[10] originally presented in Kauffmann et al. (2003) for SDSS DR4 (Adelman-McCarthy et al., 2006a) and updated for SDSS DR7 (Abazajian et al., 2009b). Figure 4.9 plots the MPA/JHU DR7 masses versus our `kcorrect` masses and it is clear `kcorrect` systematically underestimates masses. This offset is linear, and the effect increases as mass increases. If smaller masses followed this trend, then smaller masses would be overestimated by `kcorrect`. Both Bernardi et al. (2010) and Moustakas et al. (2013) have previously seen this trend in which `kcorrect` produces lower masses for high mass galaxies and larger masses

---

[10] `http://home.strw.leidenuniv.nl/~jarle/SDSS/`

for low mass galaxies. We use the scatter seen in Figure 4.9 to estimate the error in `kcorrect` masses to be ~ 0.18 dex.

Kelly et al. (2010) compared their derived masses with Kauffmann et al. (2003) as well and found a mean bias of 0.033 dex with a dispersion of 0.15 dex, which is consistent with the Kauffmann et al. (2003) data. Therefore, our derived masses are systematically lower than those in Kelly et al. (2010).

4.3 HUBBLE DIAGRAM

We here present the NIR and optical Hubble diagram from the current global collection of literature data on SNeIa observed in restframe H.

4.3.1 Lightcurves

We used the SNooPy[11] fitter of Burns et al. (2011) to estimate maximum magnitudes in J, H, and K_s for the collected sample of supernovae. We also fit the optical lightcurves with the "EBV_model2". For both models, we use the parameterization based on the updated s_{BV} width parameter introduced in Burns et al. (2014).

We adopted the same approach as in Weyant et al. (2014) of fitting separately in each band using the "max_model" SNooPy model. Unlike in Weyant et al. (2014), where we held $\Delta m_{15} = 1.1$ fixed, we here fit for the width parameter, s_{BV}. We first fit with the reported time of maximum B-band light, $\mathrm{T}_{B_{\mathrm{max}}}$, from the original spectroscopic confirmation announcement (generally ATel or CBET). Where we had constraining lightcurve information in the optical or NIR that started before peak brightness, we generated an updated $\mathrm{T}_{B_{\mathrm{max}}}$ from a fit. We then recorded these updated $\mathrm{T}_{B_{\mathrm{max}}}$ values along with the original estimates for those not updated and ran the final fits with $\mathrm{T}_{B_{\mathrm{max}}}$ fixed.

We used the default SNooPy K-corrections using the Hsiao et al. (2007) spectral templates, but we did not warp the spectral templates to match the observed color ("man-

---

[11] Version 2.0, `https://github.com/obscode/snpy.git`

gle=False"). We do not apply any color-luminosity correction as we do not assume a relationship between the different filters in our "max_model" fitting.

We did not use lightcurves that were observed before 1990, had no known optical $T_{B_{\max}}$, or were known to be SN 1991bg-like or other peculiar types (although we include 91T-like events). We excluded from the Hubble residual analysis any SNeIa that had fewer than three lightcurve points in the H-band. After these quality cuts, we have a sample of 147 SNeIa.

4.3.2 Hubble Diagram

We compare our measured SN Ia apparent brightness to that predicted by a flat LCDM model ($H_0 = 72$ km/s/Mpc; $\Omega_M = 0.28$). For each set of SNooPy apparent magnitudes or distance moduli, we calculated the weighted best fit value of the absolute magnitude, after adding both an intrinsic dispersion of 0.08 mag and the equivalent magnitude uncertainty from a peculiar velocity of 300 km/s in quadrature to the reported uncertainty from SNooPy. These additions to the uncertainty were used in computing the weighted average, but are not included in the errors plotted on the residual plots or reported in Table B.3. While SNooPy "max_model" reports apparent brightness and "EBV_model2" returns distance modulus, the actual calculation of residuals follows the same process. The absolute magnitude is entirely degenerate with the chosen value for H_0. As we are here looking at residual relative brightness, the absolute brightness and value of H_0 are not directly relevant. This model was then subtracted from the data points to yield the residuals that were used to compare against properties of the host galaxies.

The results from these fits are tabulated in Table B22 and the resulting Hubble diagram is shown in Figure 4.10 with residuals shown in Figure 4.11. Figure 4.12 presents the histogram of Hubble residuals (i.e., the projection of the residual plot).

4.3.3 A Caveat on K-corrections

We note that the state of K-corrections in NIR SNeIa photometry remains in its beginning stages and we express concern that the K-corrections used here are not the final word. The two significant previously explicitly published K-corrections are those of Krisciunas et al.

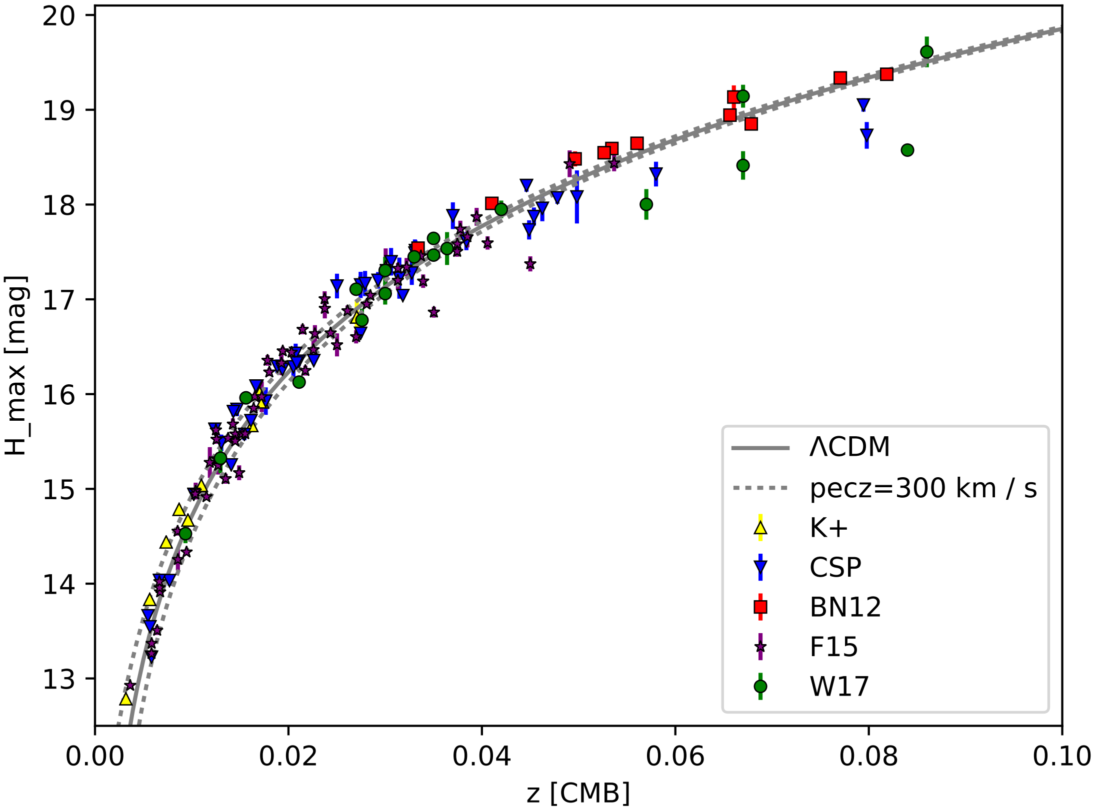

Figure 4.10 SN Ia H-band Hubble diagram for the sample considered in this paper. The grey line corresponds to ΛCDM cosmology. The points are coded in different shapes to indicate the source of the SNIa light-curve data (note that two SNeIa are in both "CSP" and "WV08").

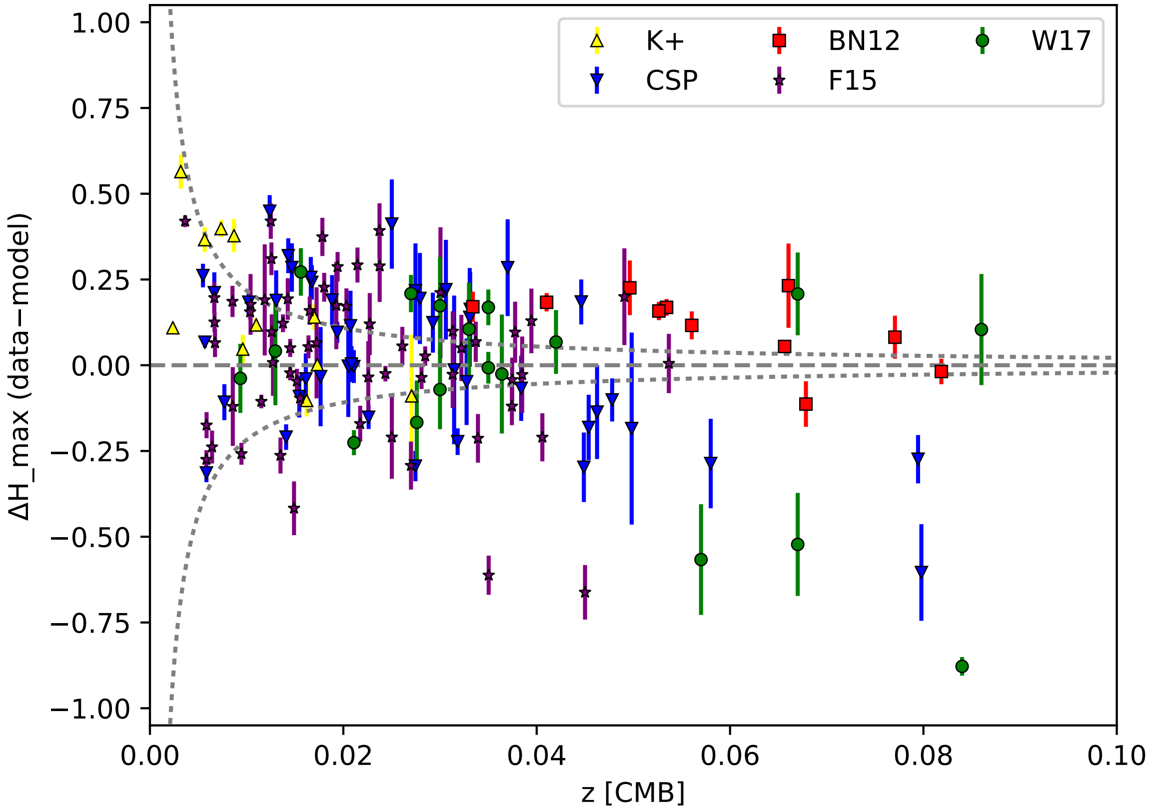

Figure 4.11 Hubble residuals from previous figure.

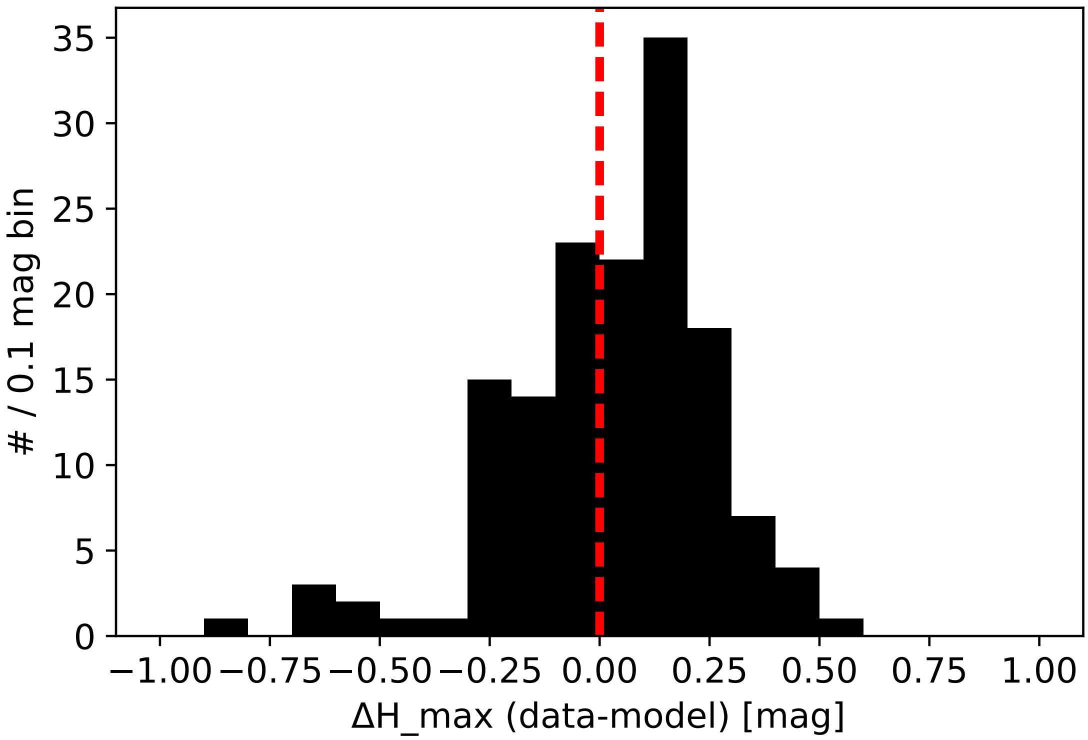

Figure 4.12 Histogram of Hubble residuals from previous 2 figures. The red line marks a residual of zero where the data completely agree with ΛCDM. This sample is slightly dimmer than expected for an unbiased sample.

(2004b) and Hsiao et al. (2007). The community has continued to gather NIR spectra, but these have not yet been compiled into a new set of spectral templates. Stanishev et al. (2015) presented their own K-correction methodology, but do not provide an updated set of spectral templates. If SNeIa were all the same in the NIR, then the excellent NIR spectral series on SN 2011fe (Hsiao et al., 2013) or SN 2014J (Marion et al., 2015) would provide sufficient data for good K-corrections. But while SNeIa NIR exhibit less scatter in the H-band than the optical, there is still clear evidence for some variation: single- vs. double-hump (e.g., the dromedarian SN 2005hk detailed in Phillips et al., 2007), bridge objects such as iPTF13ebh (Hsiao et al., 2015). We remain of the opinion that a new effort in K-corrections for SNeIa in the NIR would be a worthwhile endeavor with a clear benefit to the community.

One test that should be relatively insensitive to K-corrections would be to compare SNeIa brightness vs. host galaxy properties in small bins of redshift. I.e., to present the histograms in Figure 4.12 binned in redshift. To do so effectively, we estimate that one would require 500 SNeIa spread out between $0.01 < z < 0.1$. This estimate is based on resolving a 0.1 mag shift (that size seen in the optical) in each of 10 redshift bins from $0 < z < 0.1$. We currently see a standard deviation of ~ 0.2 mag. If this were the standard deviation in a given bin, 50 SNeIa in that bin would yield sensitivity of $0.2/\sqrt{50} \sim 0.03$ mag to resolve a 0.1 mag shift per bin.

4.4 ANALYSIS

We first explore correlations of restframe K-corrected $g - r$ color and other tracers of host galaxy morphology with the SN Ia Hubble diagram residuals. The largest trend seen with optical lightcurves is with host galaxy mass and using the mass estimates from `kcorrect`, we study host galaxy mass correlations. We then look at possible biases caused by the heterogeneous data set and briefly overview other correlations explored. Finally, we repeat the NIR correlations that were statistically significant with the sample of distance moduli derived from optical lightcurves. All correlations presented here are for the H-band unless otherwise noted.

4.4.1 $g - r$ Color

Figure 4.13 shows the $g - r$ restframe colors for our host galaxy sample, which exhibits the classic "green valley" in restframe $g - r$ color. Thus, we divide our host galaxy sample into two categories based on galaxy $g - r$ color: blue hosts, with $(g - r) < 0.6$ mag; and red hosts, with $(g - r) \geq 0.6$ mag. Figure 4.14 shows the Hubble residuals as a function of redshift with blue and red galaxies highlighted. Those with no indicator do not have optical host galaxy information. We see no clear trend in $g - r$ color versus redshift, though there is a population of bright SNeIa hosted in red galaxies at $z > 0.03$.

The subsample of host galaxies with optical photometry consists of 87 SNeIa with 40 SNeIa in blue galaxies and 47 SNeIa in red galaxies. The top plot in Figure 4.15 shows the Hubble residual versus $g - r$ and the bottom plot shows a histogram of the Hubble residuals grouped by color with the full sample included in grey for comparison. The red outliers in the smooth Hubble flow are in a small color range of $0.6 < g - r < 0.8$ mag and are consistent with the full sample.

We find that the measured un-weighted standard deviation of the whole sample is 0.2335 mag and the interquartile range (IQR) equivalent to 1 σ is 0.2120 mag. The IQR is more suited to this data set as it does not need to be symmetric and can reject outliers. The standard deviation (IQR) of SNeIa residuals in blue hosts is 0.1877 (0.1759) mag, while the standard deviation (IQR) of SNeIa residuals in red hosts is 0.2666 (0.2161) mag. The SNeIa in blues hosts produce a tighter scatter in their distribution. Table 4.3 shows the full details of the fits for the different populations including their peak residual magnitude, weighted peak residual magnitude, χ^2, χ^2/DoF, standard deviation, IQR, the standard error on the mean (SEM), and the intrinsic standard deviation that would result in a reduced $\chi^2 = 1$. SNeIa hosted in blue galaxies have lower standard deviation than SNeIa hosted in red galaxies, but the scatter in the red is dominated by the bright ($\Delta H_{\mathrm{max}} \leq -0.5$ mag) SNeIa in red galaxies at redshifts of $0.03 < z < 0.09$. Kelly et al. (2015) finds that SNeIa hosted in regions that are locally (within 5 kpc) NUV bright and star forming have a smaller intrinsic dispersion, which our results are consistent with as a blue color is a tracer for recent star formation.

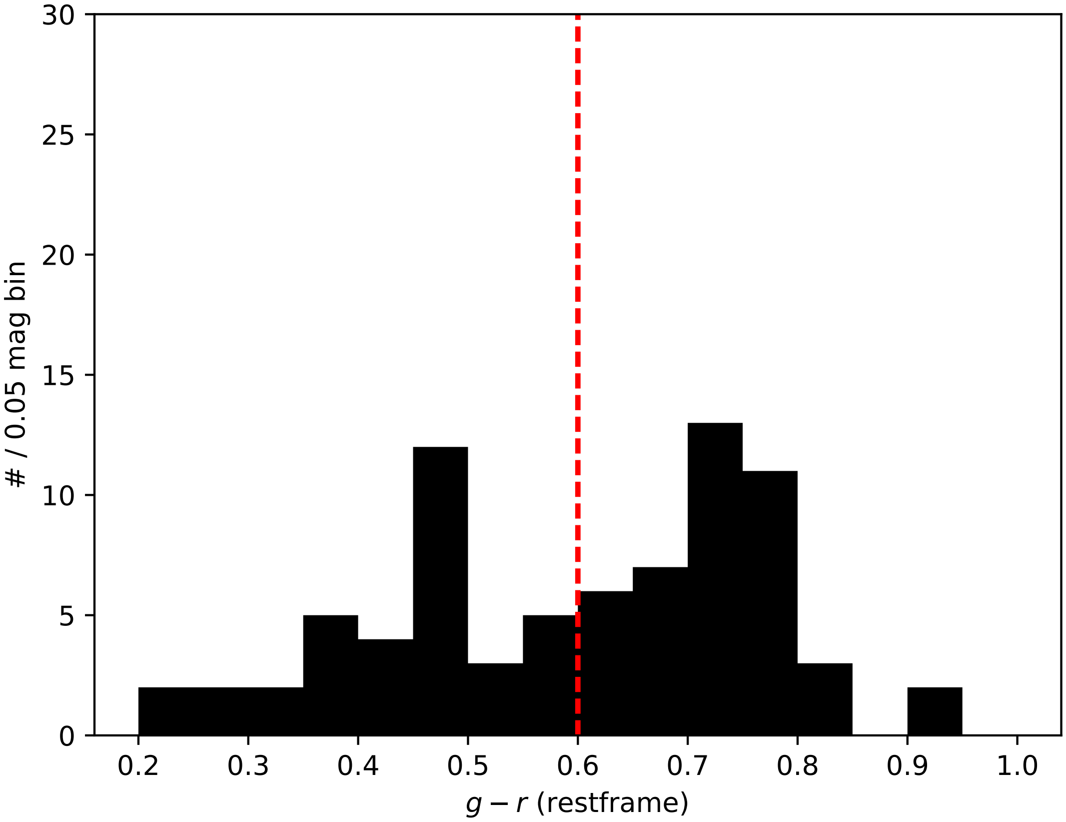

Figure 4.13 The restframe $g-r$ color distribution of the SNIa host galaxies. We have chosen $g-r=0.6$ mag as the division between "blue" and "red" galaxies.

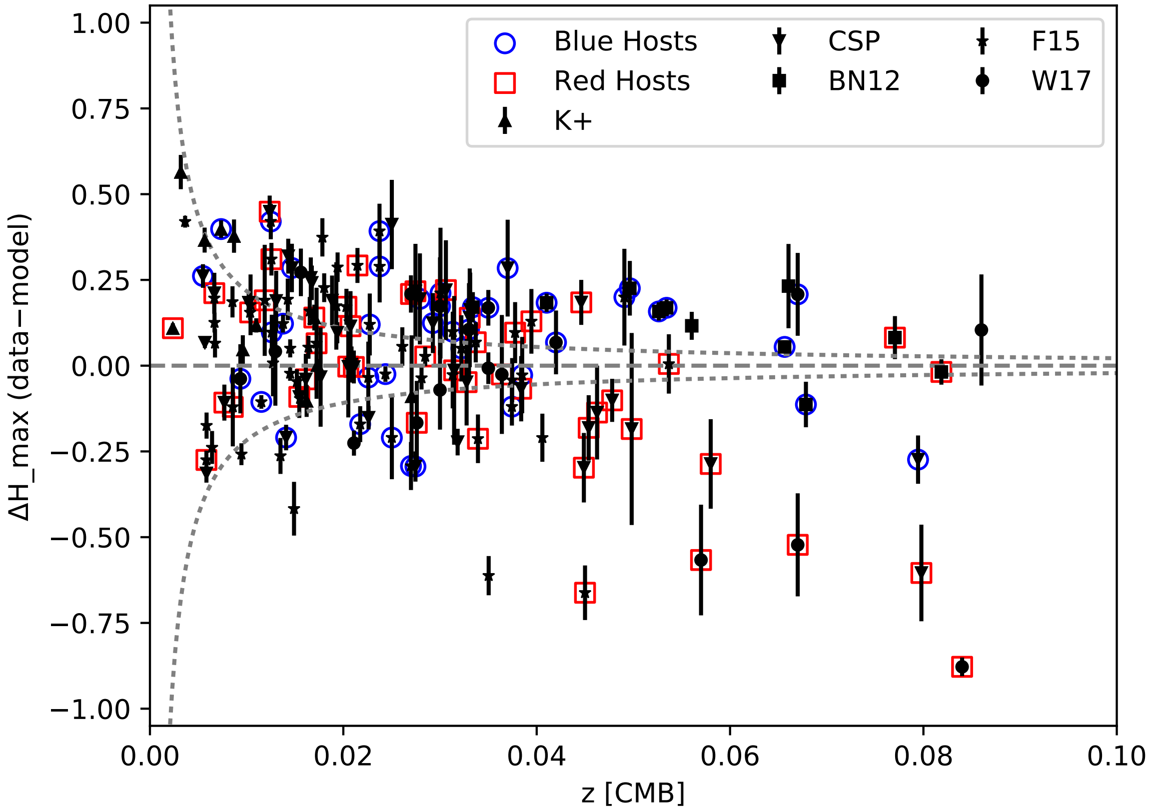

Figure 4.14 The residuals from the apparent H magnitude at maximum light (data−model) for the best-fit ΛCDM cosmology. The points are coded in different shapes to indicate the source of the SNIa light-curve data. Overlaid on the points are the classification of their host galaxy: blue circles are galaxies with $g - r < 0.6$ mag and red squares are galaxies with $g - r > 0.6$ mag.

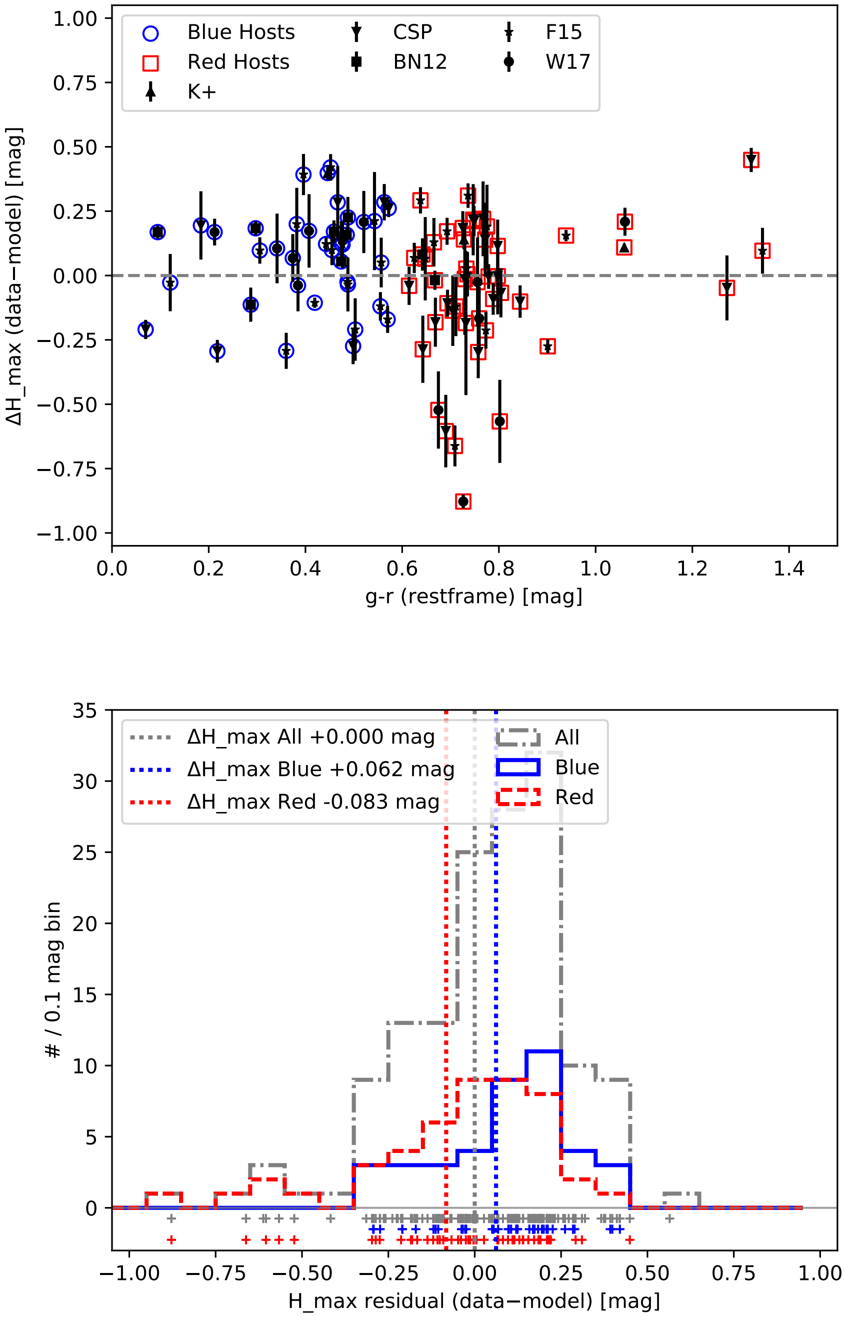

Figure 4.15 *Top:* SN Ia Hubble residuals vs. K-corrected host galaxy restframe $g - r$. *Bottom:* Histogram of Hubble residuals (data−model) for the 147 SNeIa of the full sample (grey dotted), the 40 SNeIa with host galaxies with restframe $g - r < 0.6$ mag (blue dotted), and the 47 SNeIa with host galaxies with restframe $g - r > 0.6$ mag (red dotted). Under the histograms, we show the actual distribution of the data points for the full, red, and blue samples.

The weighted average of the blue population is 0.0618 ± 0.0297 mag and the weighted average of the red population is -0.0826 ± 0.0389 mag. The difference between the peaks of these two distributions is 0.1458 ± 0.0489 mag, which is a $\sim 3\sigma$ detection of a separation between the populations. This shift is the same magnitude as the steps measured in optical distance modulii with respect to mass and star formation rates (Childress et al., 2013b; Rigault et al., 2013). The direction of the step also indicates that redder host galaxies host brighter SNeIa. This result is in agreement with the literature that says SNeIa exploding in massive, and presumably red, galaxies are brighter (Childress et al., 2013b). Figure 5 of Rigault et al. (2013) shows that in general a galaxy that is globally star forming can be locally star forming or passive, but a globally passive galaxy is usually locally passive. Rigault et al. (2013) shows that a subset of SNeIa that explode at locally passive regions are brighter than a SNeIa that explode in locally star forming environments. Assuming red galaxies are globally passive, our results agree.

If we remove the outlier population at $\Delta H_{\mathrm{max}} \leq -0.5$ mag, the difference in the weighted means of the populations decreases to 0.0363 ± 0.0397 mag, see Table 4.4. The correlations seen in the full sample is completely driven by the outlier population.

4.4.2 Morphology

We use two methods to separate galaxies based on their morphology: the inverse concentration index (Strateva et al., 2001; Shimasaku et al., 2001) and the ratio of the likelihoods for a de Vaucouleurs versus Exponential profile fit to the surface brightness. We chose to use the concentration index and likelihood functions instead of the Sérsic index (Sersic, 1968) because the Sérsic indices are not readily available from the SDSS catalogs. They have been calculated in some value added catalogs (VACs), but using the data from the regular survey allows us to measure morphology for all galaxies with optical data. Blanton et al. (2003b) shows that the concentration index traces the Sérsic index, and Lackner & Gunn (2012) illustrates that it is an even better indicator of the bulge-to-mass ratio than the Sérsic index.

Table 4.3. SN Sample Mean and Standard Deviations

Sample	SNeIa	residual mag	wgt residual mag	χ^2	χ^2/DoF	stddev mag	IQR (normal) mag	SEM mag	Implied σ_H^{int} mag	Notes
All	147	0.0323	0.0000	374.8	2.55	0.2335	0.2120	0.0192	0.1814	
Blue	40	0.0830	0.0618	74.2	1.86	0.1877	0.1759	0.0297	0.1498	$g-r$ <0.6 mag
Red	47	-0.0431	-0.0826	204.8	4.36	0.2666	0.2161	0.0389	0.2372	$g-r$ >0.6 mag
Light	61	0.0790	0.0693	96.2	1.58	0.1929	0.1753	0.0247	0.1370	$M < 10^{10} M_\odot$
Heavy	75	-0.0076	-0.0537	245.1	3.27	0.2458	0.2139	0.0284	0.2059	$M >= 10^{10} M_\odot$
Dim	51	0.0715	0.0683	86.9	1.70	0.1962	0.2213	0.0274	0.1437	$M_r >$ -21 mag
Bright	36	-0.0653	-0.1213	192.1	5.34	0.2756	0.1998	0.0459	0.2590	$M_r <=$ -21 mag
Hubble Flow	70	-0.0060	-0.0209	252.2	3.60	0.2341	0.2114	0.0280	0.2069	$z > 0.02$
Hubble Blue	28	0.0592	0.0499	59.4	2.12	0.1838	0.1783	0.0347	0.1575	$z > 0.02$, $g-r$ <0.6 mag
Hubble Red	30	-0.0770	-0.1034	176.0	5.87	0.2744	0.2152	0.0501	0.2637	$z > 0.02$, $g-r$ >0.6 mag
Hubble Light	30	0.0564	0.0599	60.3	2.01	0.1864	0.1708	0.0340	0.1548	$z > 0.02$, $M < 10^{10} M_\odot$
Hubble Heavy	38	-0.0610	-0.1029	189.5	4.99	0.2568	0.2059	0.0416	0.2415	$z > 0.02$, $M >= 10^{10} M_\odot$
Hubble Dim	28	0.0618	0.0699	61.5	2.20	0.1913	0.1759	0.0361	0.1639	$z > 0.02$, $M_r >$ -21 mag
Hubble Bright	30	-0.0794	-0.1318	174.0	5.80	0.2683	0.2059	0.0490	0.2593	$z > 0.02$, $M_r <=$ -21 mag
K+	11	0.1754	0.0755	7.0	0.63	0.2092	0.2578	0.0631	0.0000	
W17	18	-0.0640	-0.1306	132.6	7.37	0.3005	0.2190	0.0708	0.2874	
F15	62	0.0253	-0.0021	130.8	2.11	0.2231	0.2075	0.0283	0.1688	
CSP	45	0.0253	-0.0078	83.3	1.85	0.2233	0.2456	0.0333	0.1633	
BN12	11	0.1145	0.1049	21.2	1.93	0.1014	0.0806	0.0306	0.1306	

Table 4.4. SN Sample Mean and Std Deviations - Outliers Removed

Sample	SNeIa	residual mag	wgt residual mag	χ^2	χ^2/DoF	stddev mag	IQR (normal) mag	SEM mag	Implied σ_H^{int}	Notes
Blue	40	0.0830	0.0618	74.2	1.86	0.1877	0.1759	0.0297	0.1498	res<-0.5 mag, $g-r$ <0.6 mag
Red	42	0.0287	0.0255	44.8	1.07	0.1705	0.1854	0.0263	0.0889	res<-0.5 mag, $g-r$ >0.6 mag
Spiral CI Exp	35	0.0732	0.0684	54.5	1.56	0.1782	0.2085	0.0301	0.1288	res<-0.5 mag, CI> 0.4, Ratio LnL > 1.0
Elliptical CI DeV	28	0.0215	0.0005	31.2	1.11	0.1609	0.1769	0.0304	0.0929	res<-0.5 mag, CI< 0.4, Ratio LnL < 1.0
Spiral CI Blue	27	0.0999	0.0854	42.2	1.56	0.1599	0.1415	0.0308	0.1261	res<-0.5 mag, CI> 0.4, $g-r$ <0.6 mag
Elliptical CI Red	24	0.0146	0.0015	19.8	0.83	0.1449	0.1671	0.0296	0.0532	res<-0.5 mag, CI> 0.4, $g-r$ >0.6 mag
Spiral CI Exp Blue	25	0.0963	0.0797	39.2	1.57	0.1655	0.1724	0.0331	0.1272	res<-0.5 mag, CI> 0.4, Ratio LnL > 1.0, $g-r$ <0.6 mag
Elliptical CI DeV Red	22	0.0213	0.0127	19.0	0.86	0.1489	0.1646	0.0317	0.0586	res<-0.5 mag, CI> 0.4, Ratio LnL < 1.0 $g-r$ >0.6 mag
Light	61	0.0790	0.0693	96.2	1.58	0.1929	0.1753	0.0247	0.1370	res<-0.5 mag, $M < 10^{10} M_\odot$
Heavy	70	0.0380	0.0172	85.1	1.22	0.1801	0.1981	0.0215	0.1059	res<-0.5 mag, $M >= 10^{10} M_\odot$
Dim	51	0.0715	0.0683	86.9	1.70	0.1962	0.2213	0.0275	0.1437	res<-0.5 mag, $M_r >$ -21 mag
Bright	31	0.0285	0.0053	32.2	1.04	0.1497	0.1423	0.0268	0.0844	res<-0.5 mag, $M_r <=$ -21 mag

4.4.2.1 Inverse Concentration Index

The inverse concentration index is the radius that encompasses 50% of the total Petrosian flux divided by the radius that contains 90% of the total Petrosian flux. Small values indicate elliptical galaxies because ellipticals concentrate flux in the bulge but have a long tail of diffuse light such that R_{50} is small to encompass the bulge and R_{90} is higher to include the diffuse gas. On the other hand, spirals are not as bulge-dominated forcing the radius that encompasses 50% of the total flux to increase. We set the inverse concentration index cut off to be 0.4 (as is done in Galbany et al., 2012), and only compare measurements in r-band since the r-band is used to determine the surface brightness profile in all other filters for both SDSS and PS1.

4.4.2.2 Likelihood Ratio

The other indicator we use is the ratio of the likelihoods of the de Vaucouleurs versus Exponential profile fits. SDSS returns the log likelihood values of the de Vaucouleurs and Exponential fits in all 5 bands. PS1 returns the reduced χ^2 of de Vaucouleurs and Exponential fits in all bands reported. In both cases, a smaller ratio corresponds to de Vaucouleurs being the better fit profile to the data. We set this threshold at

$$\frac{\text{likelihood(deVaucouleurs)}}{\text{likelihood(Exponential)}} < 1.0 \tag{4.1}$$

for an elliptical galaxy and > 1.0 for a spiral galaxy.

4.4.2.3 Spirals versus Ellipticals

Figure 4.16 plots the log likelihood ratio versus inverse concentration index with a line denoting their respective thresholds and blue/red galaxies from the $g - r$ threshold are identified. Galaxies in PS1 that did not return a χ^2 measurement for both profiles are not included in this plot even though they are included in the inverse concentration index analysis below. The top right quadrant corresponds to spiral galaxies, and the bottom left quadrant contains ellipticals. The other two quadrants are not distinctly spirals or ellipticals but could be edge on spirals, lenticulars, or merging systems. Some of the hosts that are red in $g - r$ color are classified as spirals, while some blue hosts are classified as ellipticals.

Figure 4.17 shows the results from using the various cuts to find spiral versus elliptical galaxies. Starting with the sample of 87 host galaxies with optical photometry, we made cuts by inverse concentration index and the ratio of likelihoods. he standard deviation of spiral and elliptical galaxies is 0.1782 mag and 0.2634 mag, respectively. The two populations have a difference of 0.1203 ± 0.0561 mag such that ellipticals host brighter SNeIa than spirals. This analysis only includes 66 galaxies for two reasons: 1) PS1 did not always return a χ^2 for the de Vaucouleurs profile if it was a large, spiral galaxy; and 2) the cuts removed galaxies located in the top left and bottom right quadrants on Figure 4.16. We then cut by inverse concentration index and color, which yielded 55 host galaxies, and returned a difference of 0.2237 ± 0.0609 mag between the two populations again showing red ellipticals host SNeIa that are brighter in the H-band. Making an even more restrictive cut by inverse concentration index, the ratio of likelihoods, and color found difference of 0.2179 ± 0.0640 mag between the two populations and used only 50 host galaxies. These cuts correspond to $2.1, 3.7,$ and $3.4\ \sigma$ detections, respectively, of differences in the weighted means of the populations. See Table 4.5 for full details of weighted mean residuals, standard deviations, IQRs, SEMs, and implied intrinsic dispersions.

We note that the outlier population of bright SNeIa is associated with elliptical galaxies though only 3/4 out of 5 have host galaxy information that could be used in these analyses. If we remove the outlier population from the distributions, the significance of the separation in the means decreases to $< 2\ \sigma$ for all morphological indicators (Table 4.4).

Separating galaxies by morphology confirms that SNeIa that occur in blue, spiral galaxies have a lower standard deviation and are dimmer than those that occur in red, elliptical galaxies. Again, this result is driven by the outlier population.

4.4.3 Mass

Having collected UV, optical, or NIR data allows us to estimate stellar masses for 137 out of 147 host galaxies. Figure 4.18 shows the Hubble residuals separated by mass where the "light" population corresponds to galaxies with masses less than $10^{10}\ M_\odot$ and the "heavy" population corresponds to galaxies with masses greater than $10^{10}\ M_\odot$. The lighter galaxies

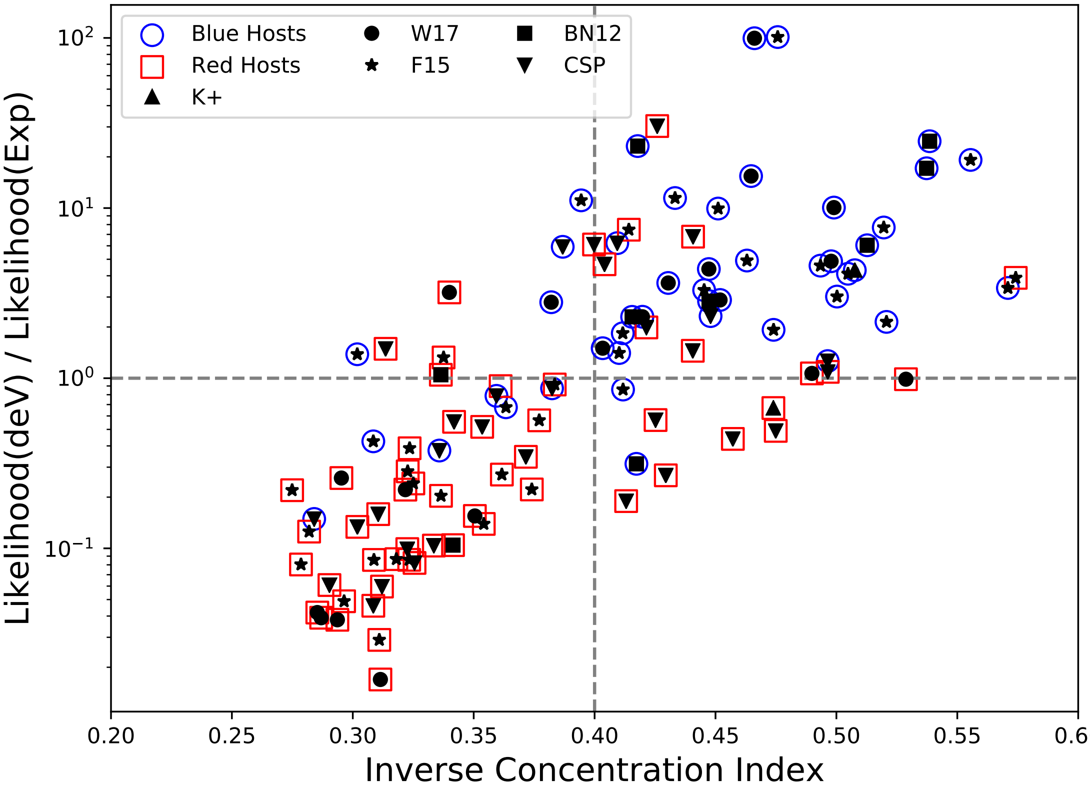

Figure 4.16 Log of the Likelihood Ratio versus Inverse concentration index color coded by restframe $g-r$ color. The dashed, grey lines indicate the thresholds for spiral versus elliptical galaxy for each indicator. The top right quadrant represents spiral galaxies and the bottom left quadrant represents elliptical galaxies.

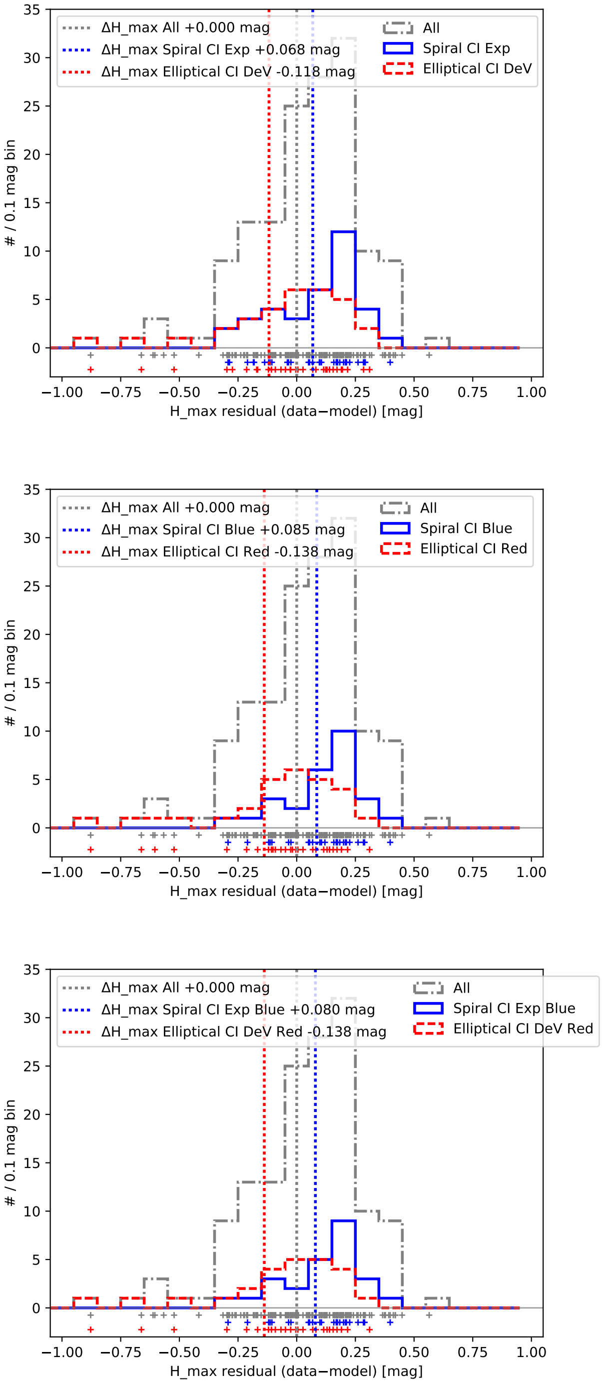

Figure 4.17 *Top:* Histogram of cuts in morphology separating Spiral and Ellipticals with Inverse concentration index and ratio of likelihoods. *Middle:* Histogram of cuts in morphology separating Spiral and Ellipticals with Inverse concentration index and a color cut based on $g - r$. *Bottom:* Histogram of cuts in morphology separating Spiral and Ellipticals with Inverse concentration index, the ratio of likelihoods, and a color cut based on $g - r$.

Table 4.5. SN Sample Mean and Standard Deviations - Comparing Color Cuts

Sample	SNeIa	residual mag	wgt residual mag	χ^2	χ^2/DoF	stddev mag	IQR (normal) mag	SEM mag	Implied σ_H^{int}	Notes
All	147	0.0323	0.0000	374.8	2.55	0.2335	0.2120	0.0192	0.1814	
Blue	40	0.0830	0.0618	74.2	1.86	0.1877	0.1759	0.0297	0.1498	$g-r$ <0.6 mag
Red	47	-0.0431	-0.0826	204.8	4.36	0.2666	0.2161	0.0389	0.2372	$g-r$ >0.6 mag
Spiral CI Exp	35	0.0732	0.0684	54.5	1.56	0.1782	0.2085	0.0301	0.1288	CI> 0.4, Ratio LnL > 1.0
Elliptical CI DeV	31	-0.0471	-0.1182	168.1	5.42	0.2634	0.2059	0.0473	0.2462	CI< 0.4, Ratio LnL < 1.0
Spiral CI Blue	27	0.0999	0.0854	42.2	1.56	0.1599	0.1415	0.0308	0.1261	CI> 0.4, $g-r$ <0.6 mag
Elliptical CI Red	28	-0.0828	-0.1383	170.2	6.08	0.2781	0.1857	0.0525	0.2686	CI> 0.4, $g-r$ >0.6 mag
Spiral CI Exp Blue	25	0.0963	0.0797	39.2	1.57	0.1655	0.1724	0.0331	0.1272	CI> 0.4, Ratio LnL > 1.0, $g-r$ <0.6 mag
Elliptical CI DeV Red	25	-0.0637	-0.1382	155.9	6.23	0.2742	0.1851	0.0548	0.2620	CI> 0.4, Ratio LnL < 1.0, $g-r$ >0.6 mag

mostly correspond to the bluer galaxies but not exclusively. They also have slightly smaller standard deviations (Table 4.3). The difference in average weighted residuals is 0.1230 ± 0.0376 mag with more massive galaxies hosting brighter SNeIa, which is a 3.2 σ detection and in agreement with the literature.

Here again, we see the same group of bright SNeIa clustered around a similar attribute – all of them correspond to high mass, red galaxies. When these SNeIa are removed from the sample, the separation between the peaks drops to 0.0521 ± 0.0327, a 1.59 σ significance (Table 4.4).

4.4.4 Per Sample

Figure 4.19 shows the residuals colored by SN lightcurve source (Sample). The difference in weighted mean residuals between the brightest (W17) and dimmest (BN12) samples is 0.24 mag (see Table 4.3). This difference is larger than any step size we see based on any feature. However, the brightest population comes from W17 which features 3 of the bright SNeIa in high mass and red galaxies with only 18 SNeIa in the sample. These 3 SNeIa also factor into the larger standard deviation and intrinsic dispersion seen in W17. The dimmest SN Ia sample BN12 also has the tightest standard deviation. We note that BN12 reported a small range in B-band stretch for their lightcurves indicating a data set lacking in intrinsic variation of SNeIa. 7 out of 9 BN12 SNeIa with host galaxy photometry are in blue galaxies, so based on the histogram fits shown above, we would expect them to be a little bit dimmer and have a smaller standard deviation.

The K+ "survey" is a collection of SNeIa from many different papers and is not a coherent set of data, unlike the other samples.

We see the outlier population comes from several surveys: 3 from W17, 2 from F15, and 1 from CSP. Since the outlier SNeIa are not from one survey, we must conclude that they may be consistent with a real second population of SNeIa.

Using SNeIa from different samples is not greatly biasing our results as they all appear to follow the same underlying distribution. The one exception is BN12, which shows little variation in host galaxy type and may contain an intrinsically different distribution of SNeIa.

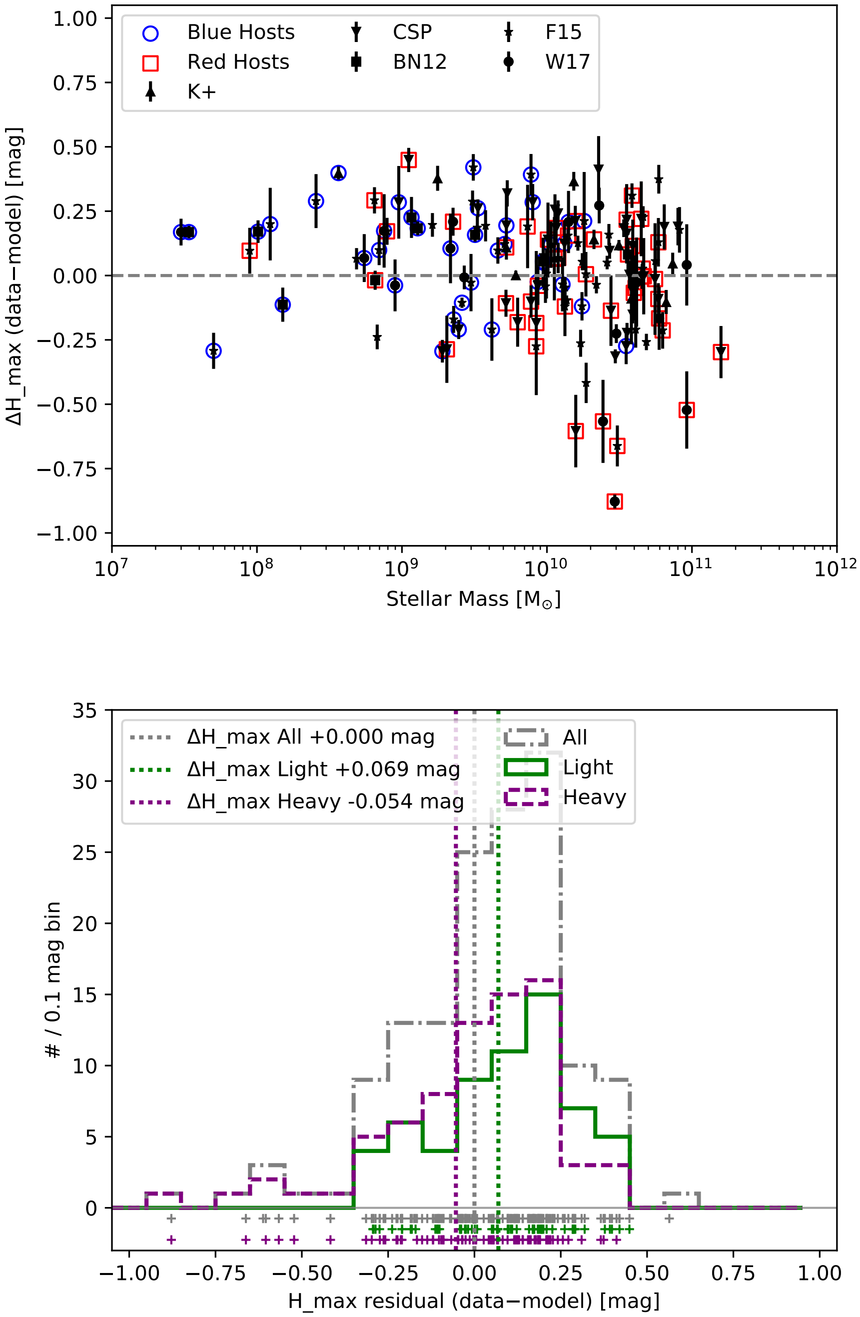

Figure 4.18 *Top:* SN Ia Hubble residuals vs host galaxy mass. Overlaid on the points are the classification of their host galaxy: blue circles are galaxies with $g - r < 0.6$ mag and red squares are galaxies with $g - r > 0.6$ mag. *Bottom:* Histogram of Hubble residuals (data−model) for the SNeIa of the full sample (grey dotted), the 61 SNeIa with host galaxies with $M < 10^{10} M_{\odot}$ (green dotted), and the 75 SNeIa with host galaxies with $M \geq 10^{10} M_{\odot}$ (purple dotted).

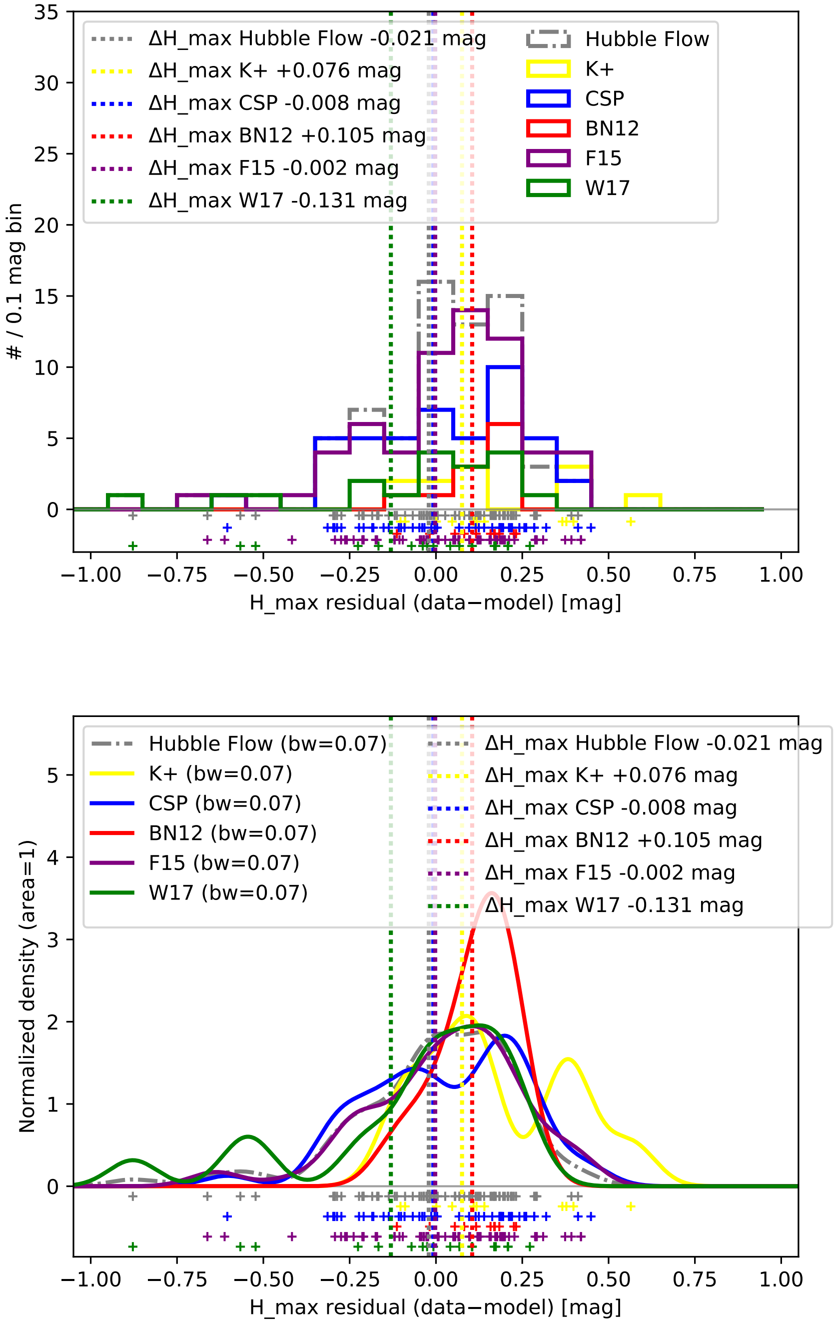

Figure 4.19 The H-band residuals from the best-fit ΛCDM cosmology for all Hubble flow SNeIa (grey dashed) and for each sample. *Left:* histogram with the offset for each sample listed; *Right:* kernel density estimation with a Gaussian kernel of bandwidth 0.07 mag. The individual points are shown below the $y = 0$ axis for ease of reference to the original data.

4.4.5 Other Possible Correlations

Other correlations that we tested are:

- **Absolute r-band Magnitude (M_r):** The absolute r-band magnitude shows a similar correlation as the $g - r$ color and host galaxy mass – see the "bright" and "dim" populations in Figure 4.20 and Table 4.3 with a threshold at -21.0 mag. This threshold was chosen to correspond with the typical brightness of a galaxy with mass $\sim 10^{10} M_\odot$ as seen in Figure 4.21. The outlier population is exclusively in bright galaxies. With the outliers, we report a correlation at 3.31 σ significance, but without the outliers, the correlation becomes 1.64 σ.
- **Smooth Hubble Flow:** We tested the effects of using SNe with $z > 0.02$ corresponding to the smooth Hubble Flow. This cut reduced our sample size by half and produced the same results as the full sample. Table 4.3 includes the results of using only Hubble flow SNeIa for three different host galaxy properties, and they are all labeled starting with "Hubble". The distributions of residuals of SNeIa with $z < 0.02$ in color, mass, and M_r are the same as the distributions of SNeIa residuals with $z > 0.02$. Therefore, we find no evidence for evolution with redshift. The one exception is the outlier group of SNeIa hosted in red, bright, high mass galaxies which only appear at $z > 0.03$, but there are so few of them it is unclear if this is a real trend or a coincidence of small sample size.
- **NUV colors:** By using $NUV - H$, we are picking out young, blue stars versus old, red stars, which should act as a tracer for recent star formation. Figure 4.22 shows the trends in SN Ia Hubble residuals versus $NUV - H$ color and the resulting histograms which are mostly identical in scatter with a negligible offset. $NUV - g$ exhibits the same distribution.
- **Distance from host galaxy:** We found no discernible correlation in projected distances of supernovae from their host galaxies, except for the outlier population which are all very separated from their host galaxy, see Figure 4.23

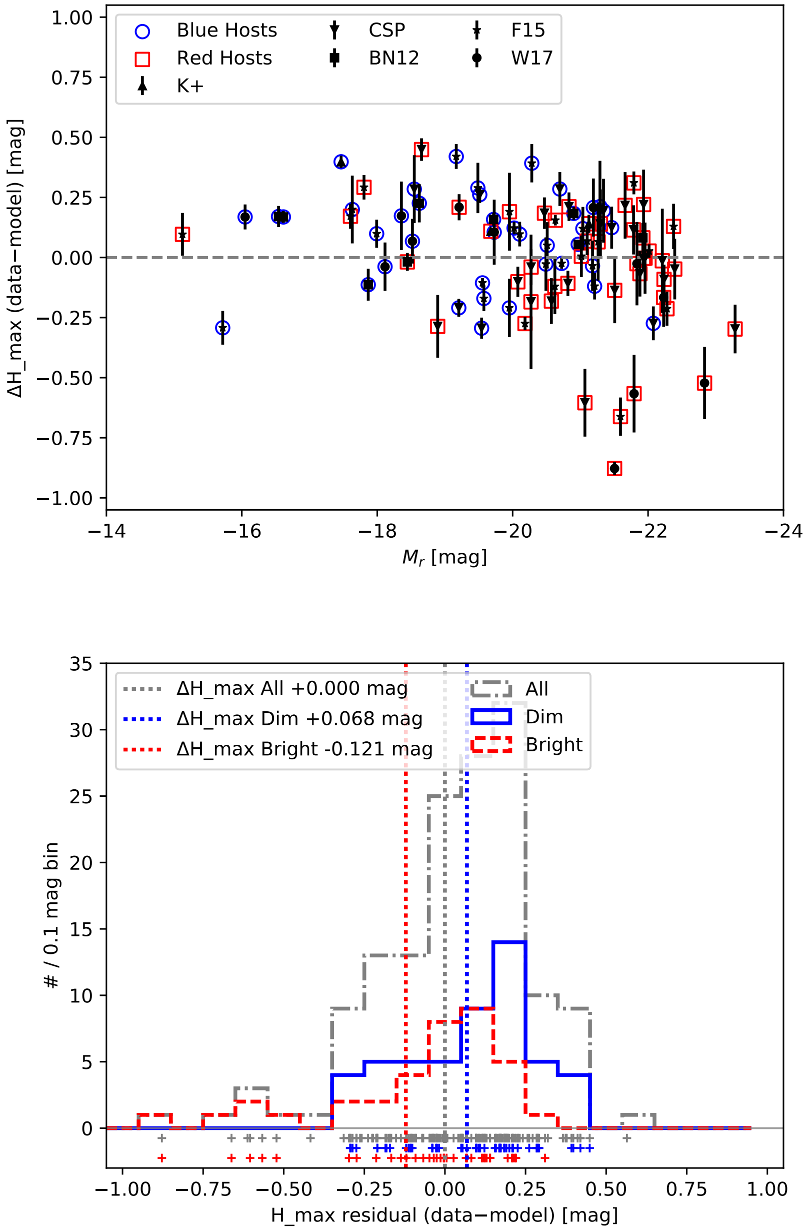

Figure 4.20 *Top:* SN Ia Hubble residuals vs restframe absolute r-band magnitude (M_r). The points are coded in different shapes to indicate the source of the SNIa light-curve data. Overlaid on the points are the classification of their host galaxy: blue circles are galaxies with $g-r < 0.6$ mag and red squares are galaxies with $g-r > 0.6$ mag. *Bottom:* Histogram of Hubble residuals (data−model) for the SNeIa of the full sample (grey dotted), the 51 SNeIa with host galaxies with restframe $M_r > -21$ mag (blue dotted), and the 36 SNeIa with host galaxies with restframe $M_r \leq -21$ mag (red dotted).

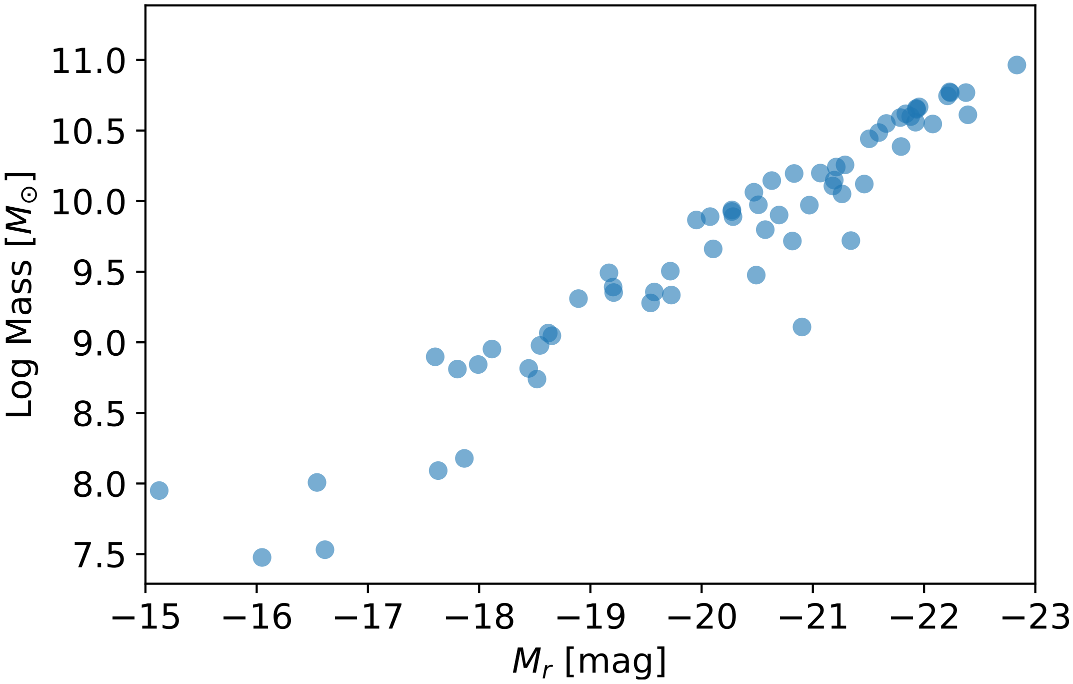

Figure 4.21 M_r versus log mass of host galaxy. The relationship is approximately linear.

4.4.6 Correlations with Corresponding Optical Lightcurves

Host galaxy correlations have been well studied in the optical wavelengths. To compare our results to these studies, we repeated the analysis with optical lightcurves of SNeIa observed in the H-band. The optical data set is only 105 SNeIa in total, 58 with optical host galaxy photometry, and 100 with host galaxy mass estimates. Figures 4.24, 4.25, and 4.26 show the distributions from $g - r$ restframe color, host galaxy mass, and M_r. Table 4.6 presents the resulting weighted residuals and standard deviations. All of the correlations result in $< 2\ \sigma$ detections of differences in the weighted means of the distributions.

In this histogram analysis, we found no statistically significant trends between restframe H or optical SNeIa brightnesses and host galaxy properties, but we do detect a distinct outlier population in the H-band.

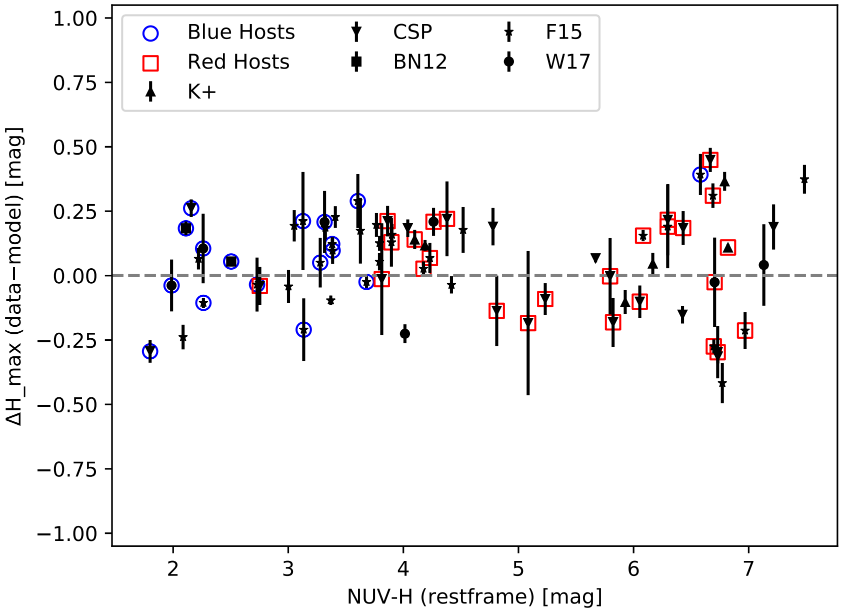

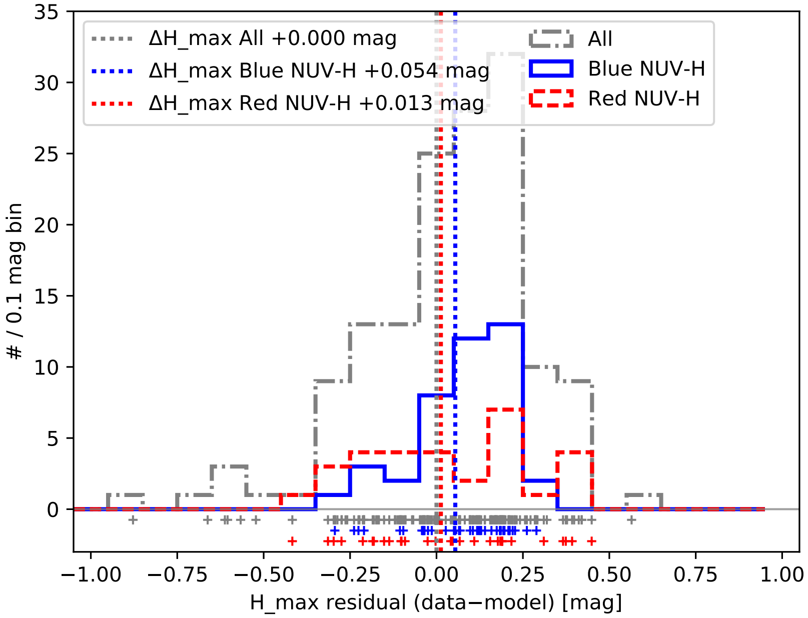

Figure 4.22 *Top:* SN Ia Hubble residuals vs $NUV - H$ color. *Bottom:* Histogram of Hubble residuals (data−model) for the SNeIa of the full sample (grey dotted), the 41 SNeIa with host galaxies with restframe $NUV - H < 4.5$ mag (blue dotted), and the 30 SNeIa with host galaxies with restframe $NUV - H > 4.5$ mag (red dotted).

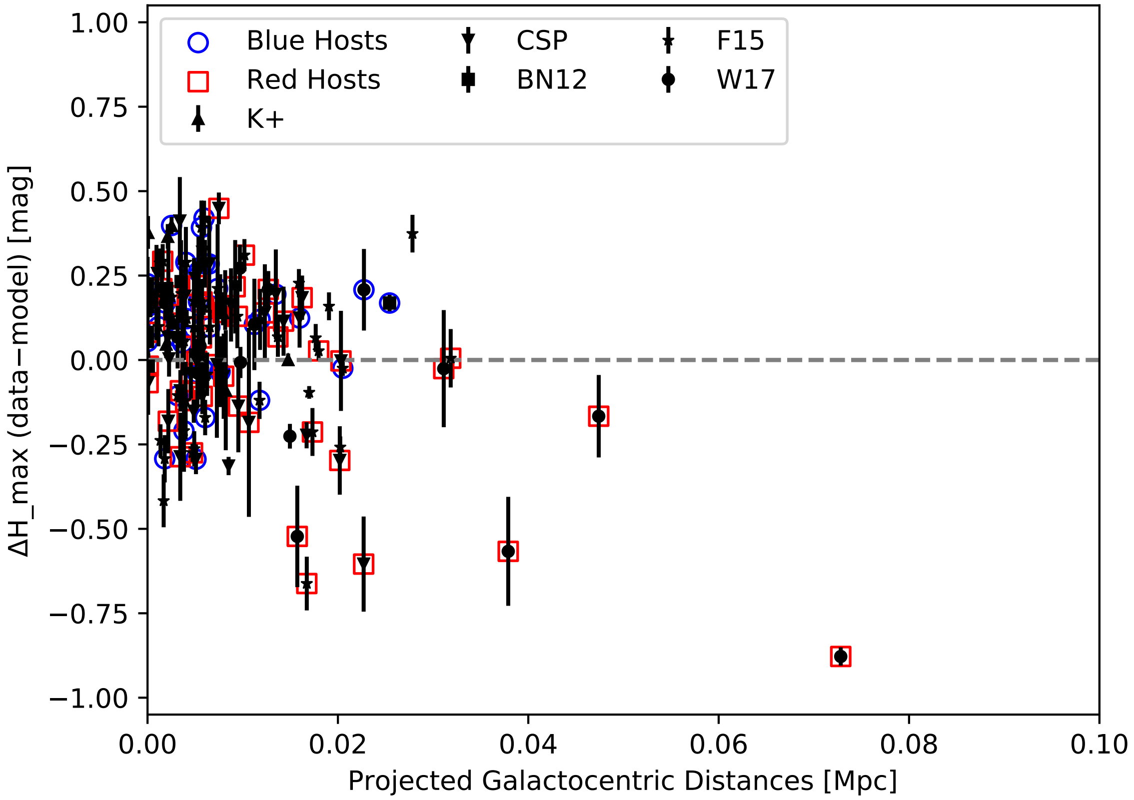

Figure 4.23 SN Ia Hubble residuals vs projected galactocentric distances. The points are coded in different shapes to indicate the source of the SNIa light-curve data. Overlaid on the points are the classification of their host galaxy: blue circles are galaxies with $g - r < 0.6$ mag and red squares are galaxies with $g - r > 0.6$ mag.

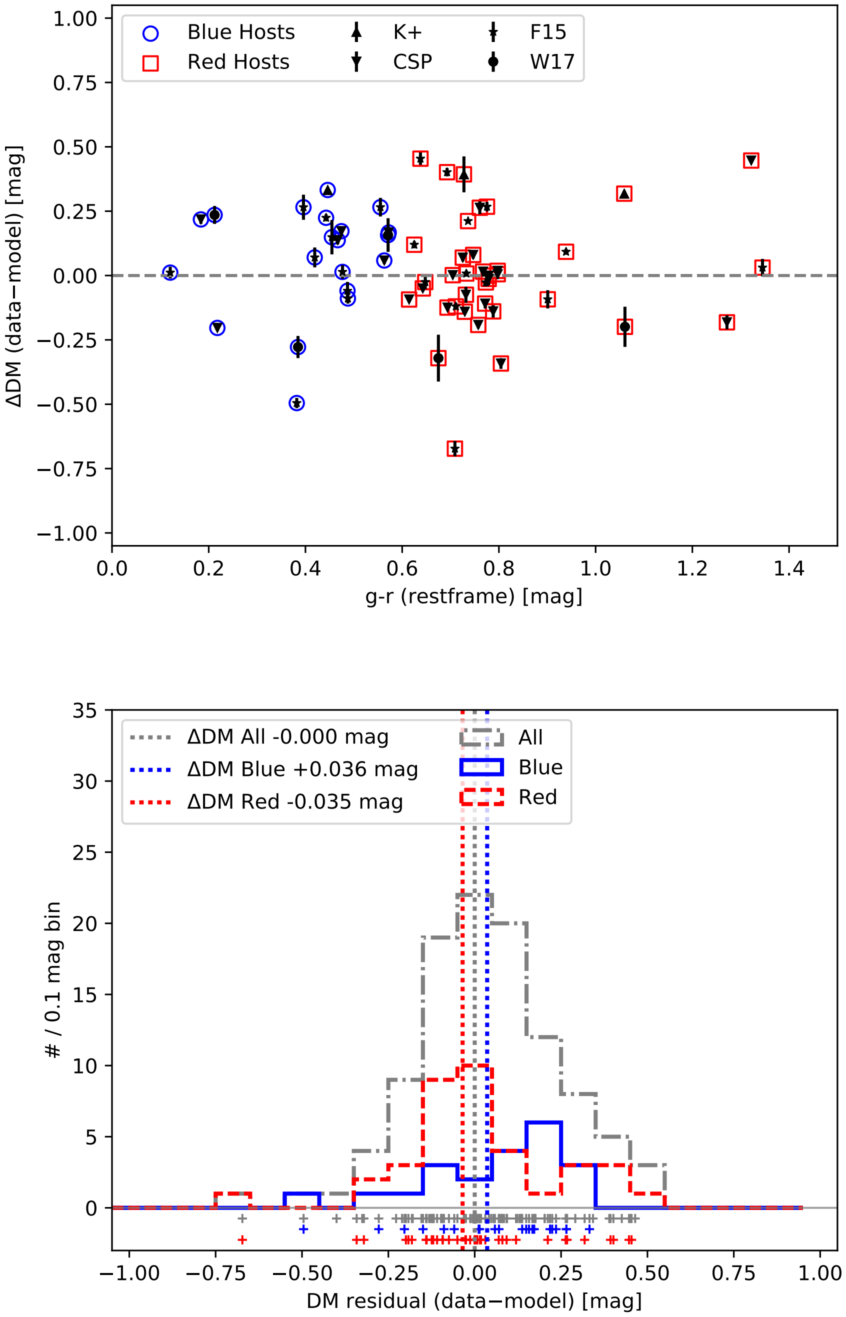

Figure 4.24 *Top:* SN Ia distance modulus residuals versus host galaxy color. Overlaid on the points are the classification of their host galaxy: blue circles are galaxies with $g - r < 0.6$ mag and red squares are galaxies with $g - r > 0.6$ mag. *Bottom:* Histogram of distance modulus residuals for the SNeIa of the full sample (grey dotted), the SNeIa with host galaxies with restframe $g - r < 0.6$ mag (blue dotted) and the SNeIa with host galaxies with restframe $g - r > 0.6$ mag (red dotted).

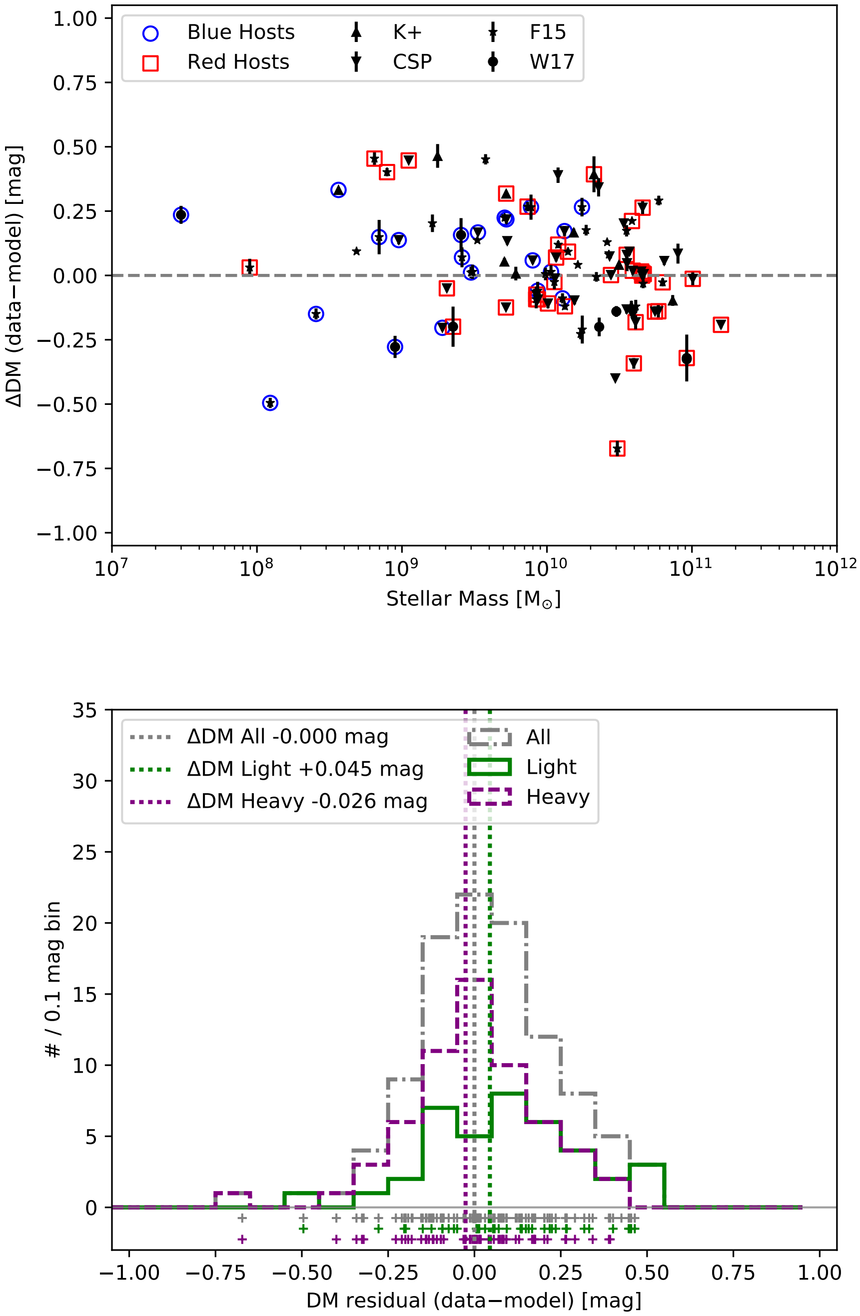

Figure 4.25 *Top:* SN Ia distance modulus residuals versus host galaxy mass. Overlaid on the points are the classification of their host galaxy: blue circles are galaxies with $g - r < 0.6$ mag and red squares are galaxies with $g - r > 0.6$ mag. *Bottom:* Histogram of distance modulus residuals for the SNeIa of the full sample (grey dotted), the SNeIa with host galaxies $M < 10^{10} M_\odot$ (green dotted) and the SNeIa with host galaxies with $M \geq 10^{10} M_\odot$ (purple dotted).

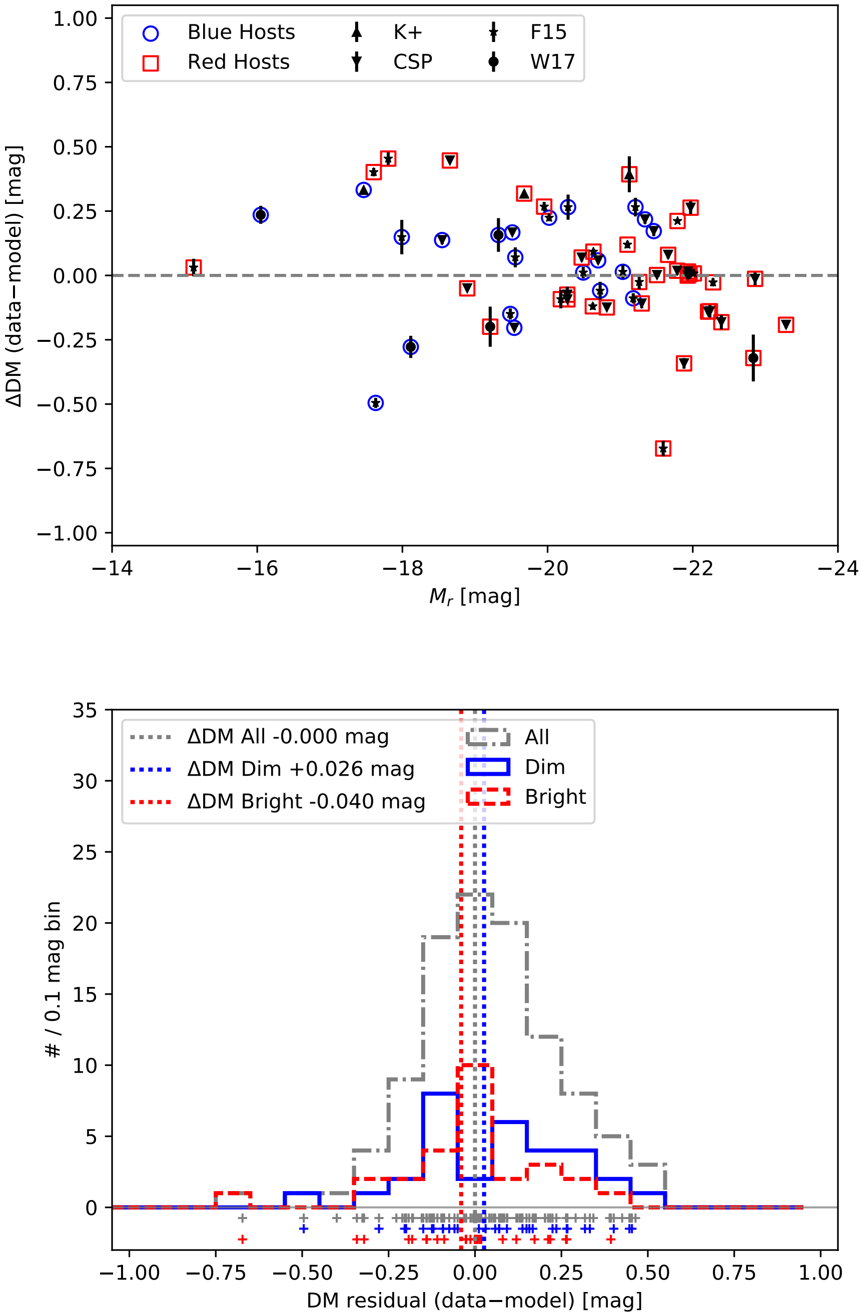

Figure 4.26 *Top:* SN Ia distance modulus residuals versus absolute r-band magnitude, M_r. Overlaid on the points are the classification of their host galaxy: blue circles are galaxies with $g-r < 0.6$ mag and red squares are galaxies with $g-r > 0.6$ mag. *Bottom:* Histogram of distance modulus residuals for the SNeIa of the full sample (grey dotted), the SNeIa with host galaxies $M_r > -21.0$ mag (blue dotted) and the SNeIa with host galaxies with $M_r \leq -21.0$ mag (red dotted).

Table 4.6. SN Sample Mean and Std Deviations - Optical SNeIa

Sample	SNeIa	residual mag	wgt residual mag	χ^2	χ^2/DoF	stddev mag	IQR (normal) mag	SEM mag	Implied σ_H^{int}	Notes
All	105	0.0333	-0.0000	243.0	2.31	0.2084	0.2046	0.0203	0.1611	
Blue	21	0.0573	0.0360	64.4	3.07	0.2030	0.2056	0.0442	0.1779	$g-r$ <0.6 mag
Red	37	0.0075	-0.0351	122.7	3.32	0.2285	0.1575	0.0376	0.1957	$g-r$ >0.6 mag
Light	39	0.0945	0.0447	98.2	2.52	0.2152	0.2109	0.0344	0.1792	$M <$ 1e+10 solMass
Heavy	60	-0.0088	-0.0257	140.9	2.35	0.1943	0.1600	0.0251	0.1578	$M >=$ 1e+10 solMass
Dim	31	0.0629	0.0263	84.1	2.71	0.2203	0.2391	0.0396	0.1807	$M_r >$ -21 mag
Bright	27	-0.0173	-0.0400	102.9	3.81	0.2136	0.1660	0.0411	0.1975	$M_r <=$ -21 mag

4.5 DISCUSSION

In the previous section, we compared the weighted mean residuals of SNeIa separated by different host galaxy properties. We found $\sim 3\,\sigma$ significant results supporting 0.12−0.15 mag shifts between $g-r$ color, mass, and M_r. Though these are in agreement with the results in the literature from optical studies, we showed that they are a result of a bright SN Ia population. However, by binning the data and analyzing a histogram, we are losing some information about the distributions. To further test the significance of these correlations, we follow the procedure done previously in the literature and fit different functions to the host galaxy properties versus the SN Ia Hubble diagram residuals. We here focus on the $H_{\rm max}$ and optical distance modulus residuals and show no results for J- or K_S-band.

4.5.1 Different Models to Fit

We fit 7 different models using `scipy.optimize.curve_fit` outlined below.

1. Constant function corresponding to a single population and no correlation.
2. Linear function where we fit for the slope and y-intercept.
3. Step function with a break corresponding to the thresholds used in the previous section ($g-r = 0.6$ mag, mass $= 10^{10} M_\odot$, $M_r = -21.0$ mag). We fit for the amplitude of the step and the location of the y-intercept.
4. Step function that fits for the location of the break as well as the amplitude and y-intercept.
5. “Modified” Logistic function: The Logistic function is constrained to be positive, so we added a constant offset to allow us to fit the negative residuals:

$$\text{Modified Logistic} = \frac{L}{1+e^{-k(x+x_0)}} + A. \tag{4.2}$$

   We fit for L, the maximum asymptote; k, the slope of the curve at midpoint; x_0 the location of the midpoint; and A, the constant offset corresponding to the minimum asymptote. We chose to fit sigmoid/Logistic functions to fit a smooth transition between two populations.

6. Modified Logistic function with x_0 set to the previous threshold values and fitting for L, k, and A.
7. Generalized Logistic function defined as:

$$\text{Generalized Logistic} = \frac{K - A}{(C + Qe^{-Bx})^{1/\nu}} + A. \tag{4.3}$$

   Here again we fit for A, the minimum asymptote; K, the maximum asymptote; C, a constant that is around 1; Q, similar to the y-intercept; B, the growth rate; and ν, which controls the location of the onset of the growth.

The error on the fitted model parameters corresponds to the diagonal elements of the resulting covariance matrix.

4.5.2 Information Criteria

After fitting the different functions to our data, we compare which model describes the data better using two different information criteria (ICs): the Akaike Information Criterion (AIC; Akaike, 1974) and the Bayesian/Schwartz Information Criterion (BIC; Schwarz, 1978). We use the updated AIC$_c$ (Sugiura, 1978) which is more suitable for smaller samples. The AIC$_C$ and BIC are defined as

$$\text{AIC}_c = \chi^2 + 2k + \frac{2k(k+1)}{N-k-1} \tag{4.4}$$

and

$$\text{BIC} = \chi^2 + k \ln N \tag{4.5}$$

where

$$\chi^2 = \sum_i^N \frac{(\text{data}_i - \text{model})^2}{\sigma_i^2}. \tag{4.6}$$

k is the number of parameters fit and N is the number of objects in the sample. For the fits below, σ corresponds to the model error on the residual from the SNooPy fits.

The better fitting model returns a lower value of the information criterion such that adding more parameters penalizes the results. However, AIC$_c$ and BIC cannot be used to determine the absolute best fit model; they can only establish which model the data favor compared to another model. We calculate ΔAIC$_c$ and ΔBIC relative to the constant model.

If the difference in IC is > 2, a constant model is preferred; > 5, a constant model is strongly preferred; < -2, the compared model is preferred; and < -5 the compared model is strongly preferred. When $0 < \mathrm{IC} < 2$, there is a preference for a constant model, but not a statistically significant one. Likewise, an IC between -2 and 0 shows a preference for the compared model, but it is not significant.

4.5.3 $g - r$ color

Using 86 SNeIa that have optical host galaxy photometry and H-band SN Ia photometry, we fit the seven different models to the restframe $g - r$ color versus the H_{max} residuals (ΔH_{max}). Similarly, we used the 56 SNeIa with corresponding lightcurves at optical wavelengths to fit the models to the restframe $g - r$ color versus the optical distance modulus residual (ΔDM). We removed the bluest galaxy in the ΔH_{max} sample with a color requirement of $g - r > 0$ mag. For the residual in the distance modulus, we removed one SN Ia located at $g - r \sim 1.3$ with $\Delta\mathrm{DM} > 0.4$ mag that had a small residual error and greatly influenced our fits.

We found that our data did not provide sufficient information to fit the location of the break in the step function using the built in SciPy function. To estimate the best site of the break, we fixed the position at a range of values between $0.0 < g - r < 1.5$ mag and fit for the step size and y-intercept. We then use the ICs to compare the model at each transition location versus the model with the step located at the original threshold of $g - r = 0.6$ mag and chose the break with the lowest IC. The top panels of Figure 4.27 show the results from doing this procedure for ΔH_{max} and ΔDM.

The top left panel is the result of fitting the H_{max} residuals and has a local minimum near our original threshold, but there is a global minimum at a much higher color of $g - r = 0.91$ mag. As seen in the bottom left panel of this figure, at $g - r \gtrsim 0.8$ mag there are very few data points which are driving this result. The top right panel finds the best fit location for the optical lightcurves, which favors a threshold around 0.6 mag. There is a large difference in y-axis for these two plots: ΔH_{max} varies between $-0.5 < \mathrm{IC} < 1.0$ while ΔDM varies between $0.0 < \mathrm{IC} < 18.0$. The ΔDM strongly prefers a particular location whereas ΔH_{max} cannot constrain the break well.

The bottom panels of Figure 4.27 show the models from the best fits: constant, linear, the best-fit step function, and the modified Logistic using the threshold value. Table 4.7 summarizes the best fit models using ICs and Table 4.8 outlines the significance in the slope of the linear function, the step size of the best-fit step function, and the step size of the step function with a break at the original threshold. The H_{max} residuals prefer a constant model with no correlations with host galaxy $g - r$ color. The distance modulus residuals prefer a constant model except for a step function at $g - r \sim 0.6$ mag; however, the step size is reported at 2.2 σ and is not a significant result.

For all host galaxy properties, the modified Logistic function with an unconstrained midpoint always placed the midpoint at values on the left of the x-axis and fit a straight line to the data. The generalized Logistic function responded similarly, but the ICs were so strongly against this model for every case, we do not include the fit on the plots.

We conclude that there is currently no significant trend between H-band lightcurves and host galaxy $g - r$ color. There is some evidence of a correlation with optical brightnesses because the ICs strongly preferred a step function over a constant model, but it is inconclusive because the detection of the amplitude was $< 3\ \sigma$.

4.5.4 Mass

Following Kelly et al. (2010), we chose to focus on the potential transition region by excluding all host galaxy with a stellar mass $< 10^{9.5}\ M_{\odot}$, which yields 101 NIR lightcurves and 78 optical lightcurves. Figure 4.28 shows the best-fit location for the break in the step function in the top two panels and different model fits in the bottom two panels. Both the H_{max} and DM residuals favor a mass step at $10^{10.44}\ M_{\odot}$, which is in between the typical number found at $10^{10}\ M_{\odot}$ (e.g., Sullivan et al., 2010; Lampeitl et al., 2010; Gupta et al., 2011; Childress et al., 2013b) and $10^{10.8}\ M_{\odot}$ found in Kelly et al. (2010). Again, the H_{max} residuals do not strongly prefer any break location over another, but the optical lightcurves do strongly favor a particular position.

Tables 4.9 and 4.10 outline the significance from these fits. We see in the ICs that

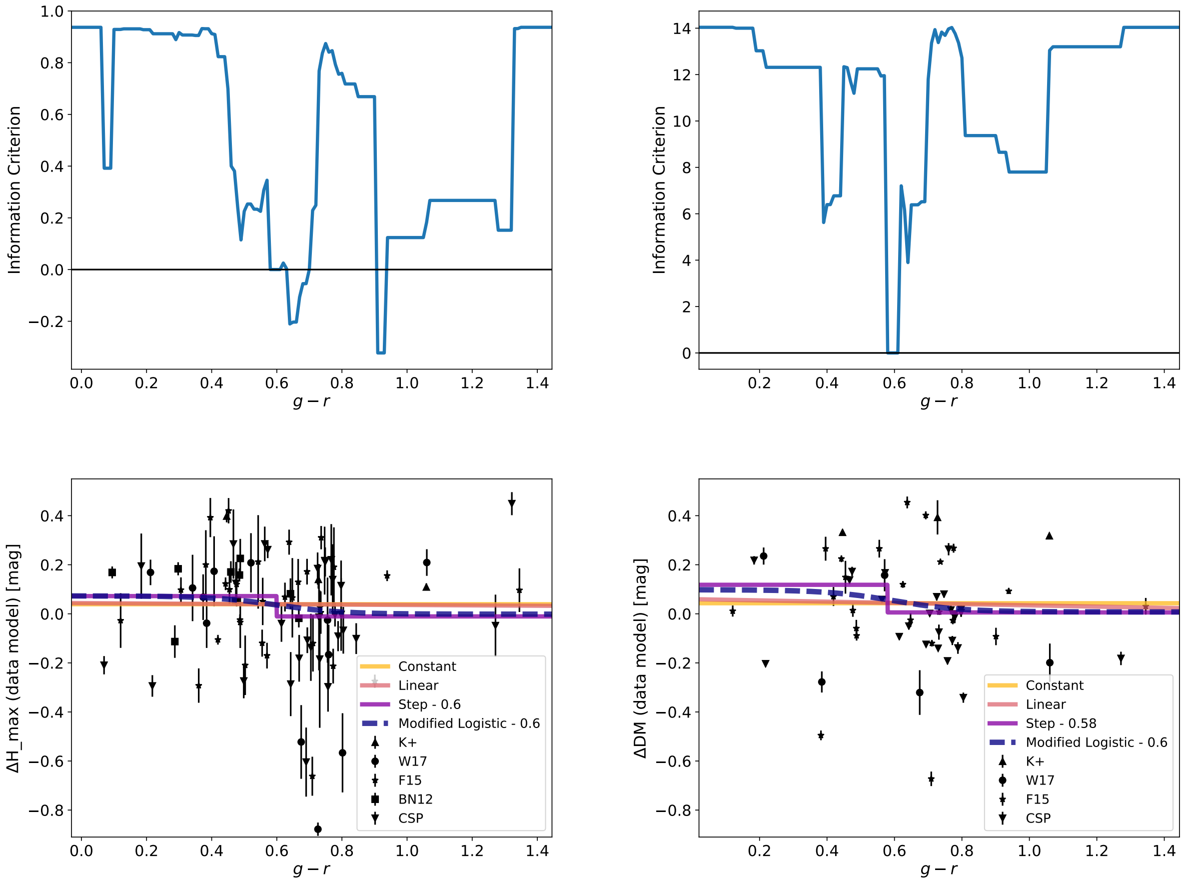

Figure 4.27 Correlations with Host galaxy $g-r$ color. *Top:* Best fit location of the step function threshold. *Bottom:* Various functions fit to the $g-r$ versus Hubble residuals. *Left:* Results form using the $H_{\rm max}$ Hubble residuals. *Right:* Results form using the distance modulus (DM)/optical lightcurve Hubble residuals.

Table 4.7. Information Criteria Results for Different Models - $g - r$

Residual	Fit	Δ AIC$_c$	Δ BIC
H_{max}	Constant	0.00	0.00
	Linear	2.44	4.793
	Step: 0.6	1.50	3.86
	Step: 0.91	1.18	3.53
	Modified Logistic	6.69	13.61
	Modified Logistic: 0.6	4.54	9.20
	Generalized Logistic	11.91	23.17
DM	Constant	0.00	0.00
	Linear	4.97	6.85
	Step: 0.6	-8.96	-7.09
	Step: 0.58	-8.96	-7.09
	Modified Logistic	8.64	14.00
	Modified Logistic: 0.6	7.33	11.00
	Generalized Logistic	26.22	34.69

Table 4.8. Significance of Linear and Step Function Fits - $g - r$

Residual	Fit	Constant	σ_{Constant}	Slope|Step	$\sigma_{\text{Slope\|Step}}$	Units
H_{max}	Constant	0.04	0.02			mag
	Linear	0.04	0.06	-0.01	0.09	mag/mag
	Step: 0.6	0.07	0.03	-0.08	0.05	mag
	Step: 0.91	0.02	0.03	+0.12	0.06	mag
DM	Constant	0.04	0.02			mag
	Linear	0.06	0.09	-0.03	0.09	mag/mag
	Step: 0.6	0.12	0.04	-0.11	0.05	mag
	Step: 0.58	0.12	0.04	-0.11	0.05	mag

H_{max} residuals prefer a constant model, but the results are inconclusive for the best-fit step function with the AIC very weakly preferring the step function and the BIC preferring the constant model. The slope of the linear function and the best-fit step size are both found at $> 3\sigma$ and appear to be significant correlations. However, the DM residuals *strongly* prefer a non-constant model with the most preferred model being the best-fit step function. The linear function and best-fit step function are found at a $> 3\sigma$ significance level and are detections. We report a step size of 0.10 ± 0.04 mag at 10^{10} $M_{\odot}$ which matches the results found previously in the literature. By using the updated best-fit location of $10^{10.44}$ $M_{\odot}$, this step size increases to 0.12 ± 0.04 mag, a more robust detection.

We confirm here, for the first time using the SNooPy fitter, a correlation between host galaxy mass and optical lightcurves in which more massive galaxies host SNeIa that are brighter by 0.12 mag. We found conflicting evidence for a correlation between host galaxy mass and H-band brightnesses. The ICs prefer a constant model, but we report a 4 σ detection of a 0.16 mag step at $10^{10.44}$ $M_{\odot}$.

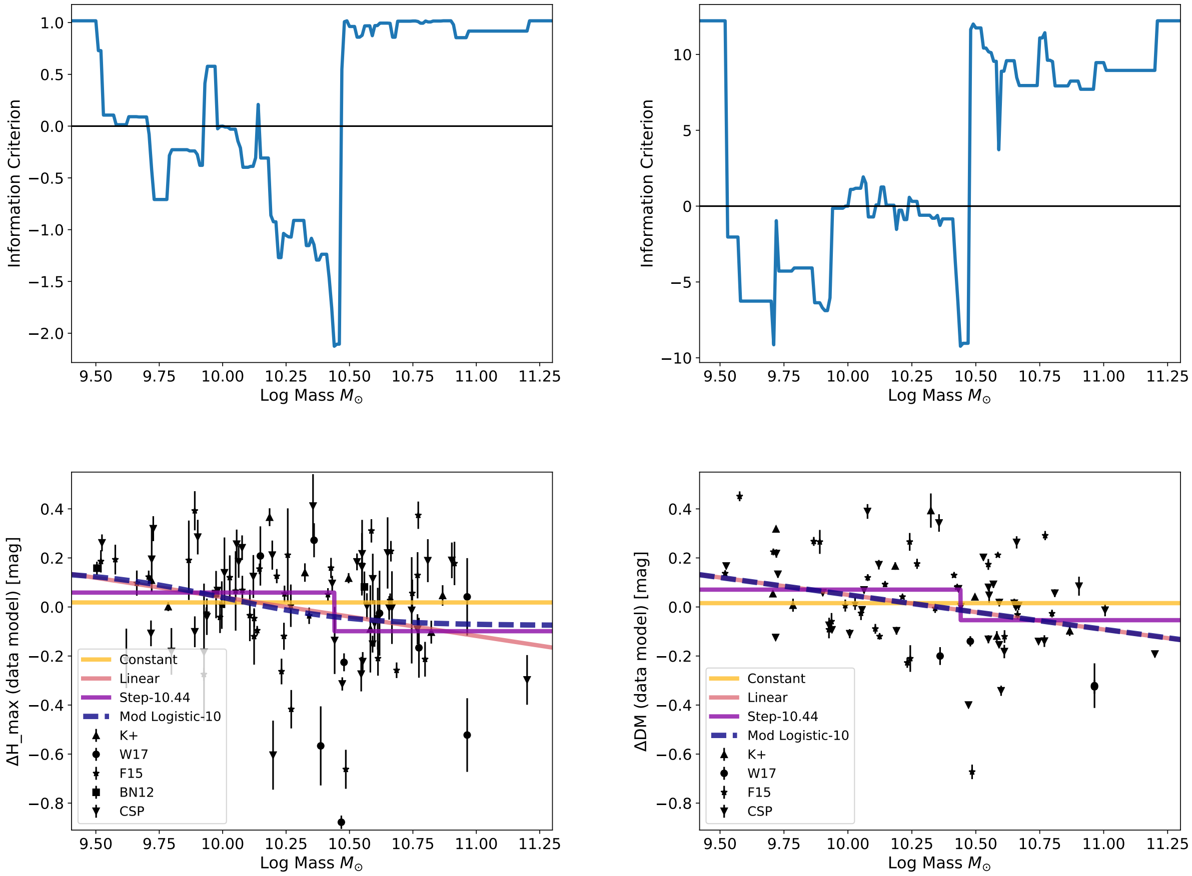

Figure 4.28 Correlations with host galaxy mass. *Top:* Best fit location of the step function threshold. *Bottom:* Various functions fit to the host galaxy mass versus Hubble residuals. *Left:* Results form using the $H_{\max}$ Hubble residuals. *Right:* Results form using the distance modulus (DM)/optical lightcurve Hubble residuals.

Table 4.9. Information Criteria Results for Different Models - Mass

Residual	Fit	Δ AIC$_c$	Δ BIC
$H_{\max}$	Constant	0.00	0.00
	Linear	0.36	2.89
	Step: 10	1.32	3.86
	Step: 10.44	-0.80	1.73
	Modified Logistic	7.18	14.65
	Modified Logistic - 10	2.58	7.60
	Generalized Logistic	10.48	22.70
DM	Constant	0.00	0.00
	Linear	-15.23	-12.98
	Step: 10	-7.89	-5.64
	Step: 10.44	-17.12	-14.88
	Modified Logistic	13.33	19.91
	Modified Logistic - 10	-11.04	-6.60
	Generalized Logistic	3.84	14.49

Table 4.10. Significance of Linear and Step Function Fits - Mass

Residual	Fit	Constant	$\sigma_{\mathrm{Constant}}$	Slope|Step	$\sigma_{\mathrm{Slope\|Step}}$	Units
H_{max}	Constant	0.02	0.02			mag
	Linear	1.62	0.56	-0.16	0.05	mag/log $M_{\odot}$
	Step: 10.0	0.06	0.03	-0.08	0.04	mag
	Step: 10.44	0.06	0.02	-0.16	0.04	mag
DM	Constant	0.02	0.02			mag
	Linear	1.46	0.46	-0.14	0.04	mag/log $M_{\odot}$
	Step: 10.0	0.09	0.03	-0.10	0.04	mag
	Step: 10.44	0.07	0.02	-0.12	0.04	mag

4.5.4.1 Effect of Mass Errors on Correlations

`kcorrect` does not return any errors, so could the correlation with host galaxy mass be an effect of unknown error bars? The photometry was chosen to return only high signal-to-noise detections of the galaxy, so there is a small, non-dominant error per object from the photometry. In Section 4.2.2.4, we showed `kcorrect` systematically underestimated the host galaxy masses; however, this error is a linear offset, and as such, it should not affect the significance of the correlations found in this section. We also reported a small scatter from the model fits of 0.18 dex, but this is too small to greatly impact the significance of our fits.

4.5.5 M_r

We used 87 H_{max} and 58 DM residuals to test correlations with the restframe, absolute r-band magnitude, M_r. Figure 4.29 shows the resulting best-fit break in the step function and the model fits to the data. Table 4.11 presents the ICs and shows inconclusive evidence for the H_{max} residuals. The model that most favors a correlation is the best-fit step function with a break at -21.5 mag. $\Delta\mathrm{AIC}_c$ prefers a non-constant model but not strongly, and

ΔBIC does not have a preference between the two models. The size of the best-fit step is a $\sim 3.4\sigma$ detection as seen in Table 4.12. For the linear function, both ΔAIC_c and ΔBIC do not favor either model, and the slope is significant to $\sim 2.5\sigma$. No model is apparently preferred; however, we report a strong detection of a step.

The distance modulus residuals show a large preference towards a break at -20.15 mag (see Table 4.11). The ICs exhibit a strong preference towards a non-constant model. The amplitude of the step with optical residuals is a 4σ detection (Table 4.12).

The results for the H-band again are inconclusive, but the optical SNeIa support a M_r correlation with brighter host galaxies hosting more luminous SNeIa.

4.5.6 Removing NIR Outlier Population

As noted in Section 4.4, there is a persistent outlier population of bright SNeIa hosted in red, high mass, bright galaxies. We excluded the outlier populations and repeated the ΔH_{max} fits versus host galaxy mass and M_r, but not $g-r$ since the correlation is already weak. For host galaxy mass, we find that the significance of the step size and slope drop to ~ 2.5 σ and the location of the step moved to $10^{9.73} M_\odot$. The data prefer the constant model in M_r for all fits, and all of the correlations are degraded with only the best-fit step function retaining a > 3 σ detection with a break at $M_r = -19.2$ mag. The location of the break is also shifted dimmer by about 2 magnitudes indicating the 5 bright SNeIa had a large effect on the M_r fits. We have inconclusive evidence for a shift at $M_r = -19.2$ mag. For any cosmological-based analysis with this data set, we suggest removing this outlier population, but it is unclear if this is a second population of SNeIa or a characteristic of this particular data set.

2 out of 5 SNeIa with host galaxy data were also present in the optical data set, and one of which is also an outlier in that sample with $\Delta\text{DM} \sim -0.6$ mag. We see a minimal change in the results for $g-r$ color: the ICs still strongly prefer a step function, but we only see a 2.0 *sigma* detection of the amplitude and the best fit location for the break stays the same. The correlation with mass for the linear model and step function at 10^{10} $M_\odot$ remain at the same amplitude and significance. However, the best-fit step function increased

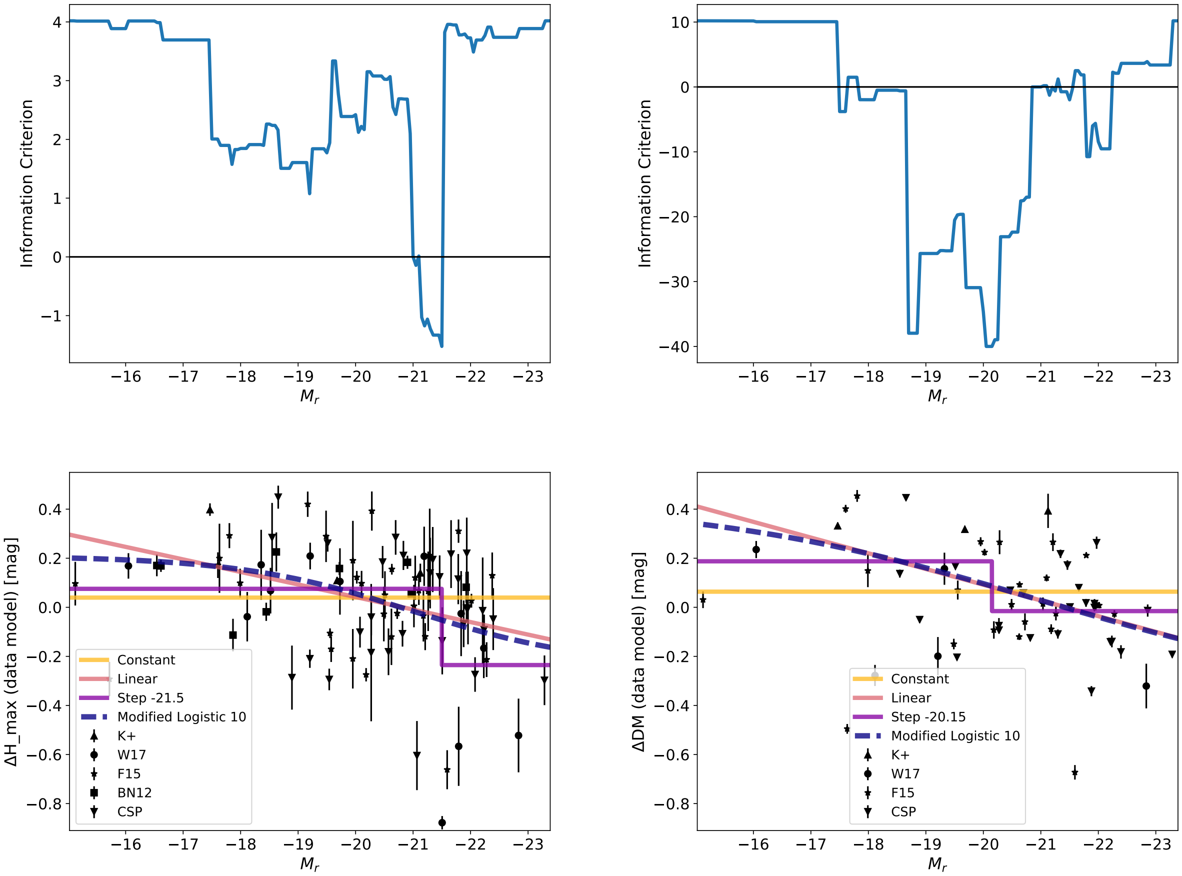

Figure 4.29 Correlations with host galaxy M_r. *Top:* Best fit location of the step function threshold. *Bottom:* Various functions fit to the M_r versus Hubble residuals. *Left:* Results form using the $H_{\max}$ Hubble residuals. *Right:* Results form using the distance modulus (DM)/optical lightcurve Hubble residuals.

Table 4.11. Information Criteria Results for Different Models - M_r

Residual	Fit	Δ AIC$_c$	Δ BIC
H_{max}	Constant	0.00	0.00
	Linear	-0.55	1.82
	Step: -21.0	-1.59	0.78
	Step: -21.5	-3.11	-0.74
	Modified Logistic	4.25	11.20
	Modified Logistic: - 21.0	1.63	6.32
	Generalized Logistic	9.86	21.19
DM	Constant	0.00	0.00
	Linear	-37.37	-35.44
	Step: -21.0	-4.53	-2.61
	Step: -20.15	-44.53	-42.62
	Modified Logistic	-33.81	-28.30
	Modified Logistic: -21.0	-32.66	-28.92
	Generalized Logistic	30.55	39.28

Table 4.12. Significance of Linear and Step Function Fits - M_r

Residual	Fit	Constant	$\sigma_{\mathrm{Constant}}$	Slope|Step	$\sigma_{\mathrm{Slope\|Step}}$	Units
H_{max}	Constant	0.04	0.02			mag
	Linear	1.06	0.32	-0.05	0.02	mag/mag
	Step: -21.0	0.15	0.06	-0.23	0.06	mag
	Step: -21.5	0.23	0.06	-0.31	0.07	mag
DM	Constant	0.06	0.03			mag
	Linear	1.37	0.33	-0.06	0.02	mag/mag
	Step: -21.0	0.01	0.04	-0.09	0.05	mag
	Step: -20.15	0.01	0.02	-0.20	0.05	mag

to 0.17 ± 0.05 mag, but the best-fit break is at the lower mass of $10^{9.73}$ $M_{\odot}$. Figure 4.28 illustrates that the original sample has this mass as a local minimum. The ICs were reduced very little and still strongly favored a non-constant model. In M_r, the slope detection became larger, and the two step function models remained the same, but the ICs still preferred a non-constant model for all fits. Removing the H-band outliers in the optical lightcurve data does not affect the results of the fits except for the best fit location of the mass cut and the slope of the M_r correlation.

4.5.7 SNeIa with Both H-band and Optical Lightcurves

We here explore the results from limiting the data set to only the SNeIa that have both H-band and optical lightcurves.

For restframe $g-r$ color, 53 SNeIa had H-band and optical lightcurves as well as optical galaxy photometry. The H_{max} residual show no significant correlation, but the slope and amplitude of the best-fit step function switch signs. The location of the best-fit step also decreases to 0.42 mag. Both of the ICs prefer a constant model. ΔDM shows the same trend as before with a slope $< 1\ \sigma$ and the best-fit step function approximately being 0.6 mag. Again the ICs only favor the color dependent step function, but the amplitude is a 2.2 σ detection.

74 SNeIa with host galaxy masses measured have both sets of lightcurves. The H-band brightness now favor a lower mass for the best-fit step function at $10^{9.73} M_{\odot}$ with a step of 0.11 ± 0.05 mag or 2.2 σ detection. The change in step location is a result of removing most of the outlier population of SNeIa. At $10^{10} M_{\odot}$, we calculate a $< 1\ \sigma$ detection with a step size of 0.01 mag and the slope is $< 1\ \sigma$ detection. As before, all the ICs favor a constant model. However, in the optical we get a 3 σ detection of the slope, a step size of 0.10 ± 0.04 mag (2.5 σ) for the break at $10^{10} M_{\odot}$, and 0.13 ± 0.04 mag (3.25 σ) for the best-fit at $10^{10.44}\ M_{\odot}$. The ICs very strongly favor a mass-dependent model. The same SNeIa that that show a mass dependence in optical wavelengths show no correlations in with the H-band brightness.

There are 55 SNeIa that have $\Delta H_{\max}$ and ΔDM with M_r measured. We see the same inconclusive evidence as above with $\Delta H_{\max}$ with 3 σ detection of the slope and a 4 σ detection of the best-fit step function of size 0.25 ± 0.06 mag located at $M_r = -19.5$. For the linear and the step function at the original threshold, the AIC and BIC disagree with neither model being preferred. The ICs only slightly prefer the best-fit step function over a constant model. ΔDM results are the same for the slope, the step function, and the best-fit step function. The break in the best-fit step function is the same as before at $M_r = -20.15$ mag. The ICs prefer a M_r dependent model with a linear or step function. This exercise yielded the same inconclusive evidence as before in the H-band and the same level of support for a correlation with the distance modulus from optical lightcurves.

In summary, there is no change in the analysis for $g - r$ color and M_r if we limit the SNeIa to those with both H-band and optical lightcurves. The evidence of a correlation between mass and the H-band decreases and now favors a constant model, but the optical SNeIa continue to support a step function.

4.5.8 Difference in Optical and NIR Error Bars

The error bars on the H-band residual are larger than those for the optical distance modulus for two main reasons. First, the model for NIR lightcurves is more uncertain than optical lightcurves, and that uncertainty gets transmitted to the residual error. Second, there are fewer lightcurve points that are used to fit the H_{max} model. This model only uses lightcurve points from the H-band, and typically NIR lightcurves are less sampled than optical lightcurves. Also, the EBV_model2 uses lightcurve points from all of the optical lightcurves instead of just one band.

We added in quadrature an additional scatter of 0.08 mag to approximate the intrinsic scatter and refit the models to the DM residuals. There is no detection in $g - r$ or M_r of a correlation since all ICs prefer a constant model and the slope/step detections drop below $\lesssim 2.2\sigma$. We continue to see some evidence for a host galaxy mass correlation with a $> 3\ \sigma$ detection for the best-fit step function that has a break at $10^{9.90} M_{\odot}$ and an amplitude of 0.18 ± 0.05. However, all of the information criteria now prefer a constant model, but it is not a strong preference (> 5) for the linear and step functions. The correlation with host galaxy mass in the optical is an inconclusive result with the increased error bars.

4.6 CONCLUSION

We have collected a data sample of 147 SNeIa with observations in the restframe H-band. 87 of these SNeIa were hosted in galaxies with optical photometry data available publicly from SDSS and PS1. 50 more hosts had observations in either GALEX or 2MASS or both allowing us to estimate masses for 137 host galaxies.

We explored many possible correlations between H_{max} residuals from the SNooPy fitter and host galaxy properties. All correlations with H-band brightnesses appear to be driven by an outlier population. However, the model fitting results for the host galaxy mass correlation are inconclusive; they are consistent with both a constant model and a model with a 0.1 mag step around $10^{10} - 10^{10.5} M_{\odot}$.

Using the optical lightcurves corresponding to the sample of NIR lightcurves, we have confirmed a host galaxy mass step of ~ 0.1 mag around $10^{10} M_{\odot}$. We have further shown that the correlation between host galaxy mass and optical brightnesses persists after removing the outlier population and after increasing the errors on the residuals. This work is the first time the mass correlation has been shown using SNooPy as all previous studies have used SALT2 and MLCS2k2. Showing this trend using a third lightcurve fitter provides further evidence of either a physical phenomenon or that there is some intrinsic property that is not well understood in optical wavelengths. There is also evidence for a correlation between the M_r of the host galaxy and optical brightnesses, but that is unsurprising since our galaxies show a linear relationship between the log of the galaxy mass and absolute brightness (Figure 4.21).

There is also an apparent outlier population of very bright SNeIa in the H-band located within the smooth Hubble flow ($0.03 < z < 0.09$). They explode with residual brightness ≥ -0.5 mag and are hosted in massive ($M > 10^{10} M_{\odot}$), bright ($M_r > -21.5$ mag), and red ($0.6 < g - r < 0.8$ mag), mostly elliptical galaxies. They are also very removed spatially from their host galaxies. We examined the postage stamps for the outlier galaxies and found that one was an irregular galaxy and a second one was an elliptical galaxy with a star close to its core, but the other 3 were consistent with red, elliptical galaxies. These appear to be a subpopulation that is driving up the standard deviation and derived intrinsic dispersion of SNeIa in massive, red galaxies. Rigault et al. (2013) shows two populations of SNeIa in the locally passive star forming regions which cluster around a $\Delta\mathrm{DM} \sim -0.2$ mag. With more NIR+optical lightcurves, we could determine the relationship between the NIR outliers at -0.5 mag to the optical population at -0.2 mag.

Host galaxy masses calculated by `kcorrect` are systematically underestimated with respect to Kauffmann et al. (2003) and Kelly et al. (2010). Our estimated masses thus suffer from this same systematic offset. However, since this offset is a linear transformation in mass, it does not affect the statistical significance of correlations with host galaxy mass.

If the cause of the host galaxy mass trend is dust, metallicity (Tremonti et al., 2004), or stellar population age, then we would expect to see no correlation in the NIR since SNeIa in the NIR are less sensitive to dust, progenitor metallicity (Kasen, 2006), and progenitor age[12]. As we find inconclusive evidence of a correlation, our results cannot distinguish between the possible drivers of the host galaxy mass correlation. Though we have highlighted these three properties, it is also possible that the step in host galaxy mass is due to differences in the nature of progenitor systems in different environments.

This analysis has concluded that SNeIa in the H-band currently show no convincing evidence of correlations with host galaxy properties except for a small outlier population. With more data from ground based studies imminent (CSP III and SweetSpot), we will be able to increase the sample size to test for the correlations again and to determine if there is a correlation or if the outlier population is persistent. Now is the time to examine these relationships in low redshift NIR lightcurve data to improve our NIR models in preparation for the ~ 2500 high redshift NIR SNeIa that will be observed by Wide-Field Infrared Survey Telescope (WFIRST; Spergel et al., 2015).

4.7 ACKNOWLEDGEMENTS

This research has made use of the NASA/IPAC Extragalactic Database (NED) which is operated by the Jet Propulsion Laboratory, California Institute of Technology, under contract with the National Aeronautics and Space Administration.

Funding for the Sloan Digital Sky Survey IV has been provided by the Alfred P. Sloan Foundation, the U.S. Department of Energy Office of Science, and the Participating Institutions. SDSS-IV acknowledges support and resources from the Center for High-Performance Computing at the University of Utah. The SDSS web site is www.sdss.org.

SDSS-IV is managed by the Astrophysical Research Consortium for the Participating Institutions of the SDSS Collaboration including the Brazilian Participation Group, the Carnegie Institution for Science, Carnegie Mellon University, the Chilean Participation Group, the French Participation Group, Harvard-Smithsonian Center for Astrophysics, In-

---

[12] Initial mass of ^{56}Ni is linked to progenitor age (Howell et al., 2009) and SNeIa in the NIR are less affected by ^{56}Ni mass (Kasen, 2006).

stituto de Astrofísica de Canarias, The Johns Hopkins University, Kavli Institute for the Physics and Mathematics of the Universe (IPMU) / University of Tokyo, Lawrence Berkeley National Laboratory, Leibniz Institut für Astrophysik Potsdam (AIP), Max-Planck-Institut für Astronomie (MPIA Heidelberg), Max-Planck-Institut für Astrophysik (MPA Garching), Max-Planck-Institut für Extraterrestrische Physik (MPE), National Astronomical Observatories of China, New Mexico State University, New York University, University of Notre Dame, Observatário Nacional / MCTI, The Ohio State University, Pennsylvania State University, Shanghai Astronomical Observatory, United Kingdom Participation Group, Universidad Nacional Autónoma de México, University of Arizona, University of Colorado Boulder, University of Oxford, University of Portsmouth, University of Utah, University of Virginia, University of Washington, University of Wisconsin, Vanderbilt University, and Yale University.

The Pan-STARRS1 Surveys (PS1) and the PS1 public science archive have been made possible through contributions by the Institute for Astronomy, the University of Hawaii, the Pan-STARRS Project Office, the Max-Planck Society and its participating institutes, the Max Planck Institute for Astronomy, Heidelberg and the Max Planck Institute for Extraterrestrial Physics, Garching, The Johns Hopkins University, Durham University, the University of Edinburgh, the Queen's University Belfast, the Harvard-Smithsonian Center for Astrophysics, the Las Cumbres Observatory Global Telescope Network Incorporated, the National Central University of Taiwan, the Space Telescope Science Institute, the National Aeronautics and Space Administration under Grant No. NNX08AR22G issued through the Planetary Science Division of the NASA Science Mission Directorate, the National Science Foundation Grant No. AST-1238877, the University of Maryland, Eotvos Lorand University (ELTE), the Los Alamos National Laboratory, and the Gordon and Betty Moore Foundation.

This publication makes use of data products from the Two Micron All Sky Survey, which is a joint project of the University of Massachusetts and the Infrared Processing and Analysis Center/California Institute of Technology, funded by the National Aeronautics and Space Administration and the National Science Foundation.

This research has made use of the NASA/ IPAC Infrared Science Archive, which is op-

erated by the Jet Propulsion Laboratory, California Institute of Technology, under contract with the National Aeronautics and Space Administration.

Some of the data presented in this paper were obtained from the Mikulski Archive for Space Telescopes (MAST). STScI is operated by the Association of Universities for Research in Astronomy, Inc., under NASA contract NAS5-26555. Support for MAST for non-HST data is provided by the NASA Office of Space Science via grant NNX09AF08G and by other grants and contracts.

Software Python[13], NumPy[14], SciPy[15], matplotlib (Hunter, 2007)[16], AstroPy (Astropy Collaboration et al., 2013b)[17], IDL[18].

---

[13] http://python.org

[14] http://www.numpy.org

[15] http://www.scipy.org

[16] http://matplotlib.org

[17] http://www.astropy.org

[18] http://www.harrisgeospatial.com/ProductsandSolutions/GeospatialProducts/IDL.aspx

5.0 DISSERTATION CONCLUSIONS

The path to understanding dark energy with SNeIa lies in a greater understanding of the limiting systematics. This dissertation presented steps toward this path through improved statistical techniques to account for complex formulations of systematics. I have spent over 80 calendar nights collecting data for SweetSpot, which will be crucial to understanding NIR SNeIa and enabling future surveys. The spectroscopic data that I have reduced will pave the way for future studies into local host galaxy correlations with any SNeIa observed in these galaxies. For the first time with NIR lightcurves, we showed that there are no significant global host galaxy correlations and NIR lightcurves may be less sensitive to the mechanism causing the trend in the optical.

Chapter 2 explored generalizing the likelihood function to account for multiple populations that evolve with redshift. We showed that even if there is no clear statistical evidence for multiple populations with smaller samples, cosmological parameters will still exhibit a significant bias. However, by using a more flexible likelihood function, we can remove the bias. If multiple populations do not exist, then we still return cosmological parameters with a minimal precision loss from fitting more degrees of freedom. This framework has many applications outside the example shown here. For instance, we already know there are subpopulations of SNeIa: super-luminous SN 1991T-like (Filippenko et al., 1992a; Phillips et al., 1992) and sub-luminous SN 1991bg-like (Filippenko et al., 1992b; Leibundgut et al., 1993). Cosmological analyses remove the peculiar SNeIa to have a more uniform sample, but if we instead approach it as multiple populations, the number of SNeIa used will increase and thus reduce statistical noise. Framing the problem in this way could help to understand the interplay between the different types of SNeIa. Any systematic that can be represented by a distribution can be included in this analysis and many systematics can be incorporated into one likelihood. One could include not only multiple populations, but also effects from using multiple surveys, a PDF representation of Malmquist bias, and the distributions from photometric redshifts all together in one likelihood. Photometric redshifts are particularly useful with the upcoming surveys as the sheer volume of SNeIa discoveries will make collecting spectroscopic redshifts for every SNeIa unattainable. Having such a complicated likelihood would need a Hierarchical Bayesian analysis, which marginalizes out different parameters in successive steps as opposed to fitting everything at one time. We have begun with this simple model, but the opportunities and applications are expansive. Large surveys such as LSST and WFIRST will be able to provide the volume of data needed to return precision dark energy constraints with these complex models.

The SweetSpot survey in Chapter 3 is vital for the advancement of NIR SNeIa cosmology. Weyant et al. (2014) showed that SNeIa continue to be excellent standard candles in the H-band. Our first data release with 74 SNeIa and 33 lightcurves is one of the largest contributions from a single survey. Once DR2 is released with the majority of our lightcurves including host galaxy subtractions, SweetSpot will be one of the largest surveys of NIR SNeIa. SweetSpot will increase the H and J band Hubble diagram out to $z \sim 0.08$, it will provide a useful data set to study color evolution, and it will be a major contributor to anchoring future high redshift surveys.

The spectra of 32 host galaxies is one of the first scientific studies with the HexPak IFU. As such, we provided an extremely detailed overview of data reductions. Though the spectra as presented here are adequate for our scientific goals, aperture corrections and more careful modeling of telluric lines would provide improvements. The scientific analysis resulting from these spectra must wait for the lightcurves from SweetSpot DR2 to become available. With these lightcurves, we will be able to conduct the first study to test for correlations between local host galaxy properties and NIR lightcurves.

In Chapter 4 we explored correlations with different global host galaxy properties. Using publicly available catalogs from SDSS, Pan-STARRS, 2MASS, and GALEX, we performed K-corrections on all photometry to transform the observer-frame magnitudes into the restframe magnitudes. With this data, we study a variety of properties such as color, morphology, mass, and absolute r-band magnitude. We showed that redder, more massive, elliptical galaxies host SNeIa that are brighter in the optical and NIR than SNeIa hosted in bluer, less massive, spiral galaxies. We have shown that this result in the NIR is driven by a small outlier population that is ~ 0.6 mag brighter than normal SNeIa. However, we cannot completely rule out a mass step of 0.1 mag around a host galaxy mass of $10^{10} M_{\odot}$ in the NIR. With or without this outlier population, optical SNeIa continue to show that they are ~ 0.1 mag brighter in massive galaxies, in good agreement with the previous literature. This work is also the first time SNooPY was used to fit lightcurves when examining host galaxy correlations. It is possible that every lightcurve fitter includes the same theoretical deficiency that cannot handle this effect, but it is also likely to be an astrophysical effect. The three currently proposed host galaxy properties that are correlated with mass and may provide a more physical interpretation to this effect are dust, progenitor metallicity, and progenitor age. NIR SNeIa are less sensitive to these three properties and are consistent with one or more of them as the underlying cause. We note that this step function could also be the result of different progenitor systems that occur in different environments. We have helped identify host galaxy correlations as a persistent systematic that must be explored further. In conjunction with the local galaxy properties, we plan to continue to search for an astrophysically motivated model to describe this effect.

It is important to pursue these studies to avoid significant biases in dark energy that would result from using improper models and likelihoods with the powerful data sets that will be produced by LSST and WFIRST. The goal of this dissertation is to enable the creation of these astrophysically motivated models that are causing the host galaxy correlation in SNeIa. These models can then be implemented into an entirely Hierarchical Bayesian framework that can be utilized by these large surveys to create a more precise and unbiased measurement of dark energy.

APPENDIX A

APPENDICES FROM CHAPTER 3

A.1 CITATIONS FOR SUPERNOVA AND HOST GALAXY INFORMATION USED FOR HEXPAK

Table A1 provides the references for the groups that discovered, classified, and determined the redshift for the SNeIa that were previously hosted in the galaxies observed with HexPak. We also include the references for host galaxy redshifts taken from NASA/IPAC Extragalactic Database (NED)[1].

---

[1] https://ned.ipac.caltech.edu/

Table A1. Citations for Host Galaxies Observed With HexPak

Name	Host Name	Discoverer[a]	Classifier[a]	z_{SN}[a]	z_{Host}[a]
ASASSN-15hg	CGCG 063-098	B15b	F15a	–	H12
ASASSN-15ho	2MASXi J0909234-044327	K15	F15b	F15b	This work
LSQ12gef	2MASX J01403375+1830406	CL12	CL12	CL12	This work
LSQ14aeg	2MASX J10193682+1933131	W14	W14	W14	SDSS6
PS1-12bwh	CGCG 205-021	Wr12	Wr12	Wr12	M96
PS15mb	SDSS J085940.13+151113.5	S15, B15a	No15	No15	Sa11
PSN J07250042+2347030	NGC 2370	BT12	BT12	–	dV91
PSN J08593491+4555343	UGC 4709	Ci15	O15	O15	SDSS3
PSN J10292799+2200468	UGC 5691	Ma14b, Fe14	Z14, Fe14	Fe14	SDSS6
PTF12iiq	2MASX J02500784-0016014	GY12	GY12	GY12	SDSS1
PTF12ikt	2MASX J01144386+0017100	GY12	GY12	–	D97
iPTF13dge	NGC 1762	C13b	C13b	–	T98
iPTF13dkj	CGCG 454-001	C13a	C13a	C13a	G93
iPTF13ebh	NGC 890	C13c	C13c	–	Wo06
iPTF14gdr	2MASX J00275880-0513014	Jo14	Jo14	Jo14	This work
SN 2011gy	MCG +07-08-15	J11	Ta11; Z11a	–	UZC
SN 2011hb	NGC 7674	Ho11	MB11a	–	Ni00
SN 2011hk	NGC 881	N11	MB11b	MB11b	Bo93
SN 2011hr	NGC 2691	Na11	Z11b	–	dV91
SN 2011iu	UGC 12809	Cox11	MB11c	MB11c	Bo93
SN 2012cg	NGC 4424	Ka12	Ce12; Mn12	–	Kt08
SN 2012et	CGCG 476-117	R12a	De12	–	SG08
SN 2012fm	UGC 3528	Be12	Za12	–	UZC
SN 2012gm	NGC 7580	R12b	O12	–	Ga05
SN 2013be	IC 3573	Zh13	Si13	–	SDSS4
SN 2013fj	PGC 68419	Cia13	ZT13	–	H99
SN 2013fn	IC 1342	Ho13	Mo13; MC13	–	T05
SN 2013fw	NGC 7042	J13	HL13	–	dV91
SN 2014aa	NGC 3861	A14	To14; BA14a	–	Co08
SN 2014dm	NGC 1516A	N14	Sh14; BA14b	BA14b	JS09
SNhunt206	NGC 766	Ke13	Ke13	Ke13	H99
SNhunt263	UGC 4798	Ma14a	ER14	ER14	dV91

[a] References for SN discovery, SN classifier, SN redshift and host galaxy redshift are: A14 Arbour et al. (2014), B15a Brimacombe et al. (2015b), B15b Brimacombe et al. (2015a), BA14a Blagorodnova et al. (2014a), BA14b Blagorodnova et al. (2014b), BT12 Buton et al. (2012), Be12 Belligoli et al. (2012), Bo93 Bottinelli et al. (1993), C13a Cao et al. (2013a), C13b Cao et al. (2013b), C13c Cao et al. (2013c), CL12 Cellier-Holzem et al. (2012), Ce12 Cenko et al. (2012),
Ci15 `http://www.cbat.eps.harvard.edu/unconf/followups/J08593491+4555343.html`,
Cia13 Ciabattari et al. (2013), Co08 Cortese et al. (2008), Cox11 Cox et al. (2011), D97 Dale et al. (1997), dV91 de Vaucouleurs et al. (1991), ER14 Elias-Rosa et al. (2014), F15a Falco et al. (2015a), F15b Falco et al. (2015b), Fe14 Ferretti et al. (2014), G93, Giovanelli & Haynes (1993), GY12 Gal-Yam et al. (2012), Ga05 Garland et al. (2005), H12 Huchra et al. (2012), H99 Huchra et al. (1999) HL13 Howell et al. (2013), Ho11 Howerton et al. (2011), Ho13 Howerton et al. (2013), J11 Jin & Gao (2011), J13 Jin et al. (2013), JS09 Jones et al. (2009), Jo14 Johansson et al. (2014), K15 Kiyota et al. (2015), Ka12 Kandrashoff et al. (2012), Ke13 Kankare et al. (2013), Kt08 Kent et al. (2008), M96 Marzke et al. (1996), MB11a Marion & Berlind (2011a), MB11b Marion & Berlind (2011b), MB11c Marion & Berlind (2011c), ML13 Milisavljevic (2013),
Ma14a `http://www.cbat.eps.harvard.edu/unconf/followups/J09084248+4448132.html`,
Ma14b `http://www.cbat.eps.harvard.edu/unconf/followups/J10292799+2200468.html`,
Mn12 Marion et al. (2012), Mo13 Mo et al. (2013), N11 Nakano (2011), N14 Nakano et al. (2014), Na11 Nayak et al. (2011), Ni00 Nishiura et al. (2000), No15 Noebauer et al. (2015), O12 Ochner et al. (2012), O15 Ochner et al. (2015), R12a Rich et al. (2012a), R12b Rich et al. (2012b), S15 Smith et al. (2015), SDSS1 Abazajian et al. (2003), SDSS3 Abazajian et al. (2005), SDSS4 Adelman-McCarthy et al. (2006b), SDSS6 Adelman-McCarthy et al. (2008), SG08 Saintonge et al. (2008), Sa11 Sánchez Almeida et al. (2011), Sh14 Shivvers & Filippenko (2014) Si13 Silverman et al. (2013), T98 Theureau et al. (1998), T05 Theureau et al. (2005), Ta11 Taubenberger et al. (2011), To14 G. et al. (2014), UZC Falco et al. (1999), W14 Walton et al. (2014), Wo06 Woods et al. (2006), Wr12 Wright et al. (2012), Z11a Zhang et al. (2011a), Z11b Zhang et al. (2011b), ZT13 Zanutta et al. (2013), Za12 Zaggia et al. (2012), Zh13 Zhang et al. (2013),

A.2 GALACTIC REDSHIFT ESTIMATIONS

We used the location of common emission lines (Hβ, [O III], Hα, [N II], S II) to estimate the redshift of three host galaxies. No previously recorded redshift was available for 2MASXi J0909234-044327, host galaxy of ASASSN-15ho. From our spectra we estimate the redshift to be 0.041. Figure A1 shows a range of spectra from the galaxy with the redshifted emission lines highlighted in grey. These lines correspond to a redshift of 0.041. This galaxy is a face on spiral galaxy, so its emission lines are not very affected by peculiar velocities.

The next two galaxies are spiral galaxies with some inclination, so the measurements are more affected by peculiar velocities, which makes it more difficult to estimate its redshift. We used the peculiar velocity plots presented in Figures 3.23 and 3.26, respectively, to help estimate the redshifts since the core should not be experiencing motion relative to its redshift. No previously recorded redshift was available for 2MASX J01403375+1830406, host galaxy of LSQ12gef. From our spectra we estimate the redshift to be 0.0648. Figure A2 shows a range of spectra from the galaxy with the redshifted emission lines highlighted in grey. These lines correspond to a redshift of $\sim$0.0648. The Hβ and [O III] lines are very faint in the calibrated spectra.

No previously recorded redshift was available for 2MASX J00275880-0513014, host galaxy of iPTF14gdr. From our spectra we estimate the redshift to be 0.0695. Figure A3 shows a range of spectra from the galaxy with the redshifted emission lines highlighted in grey. These lines correspond to a redshift of 0.0695.

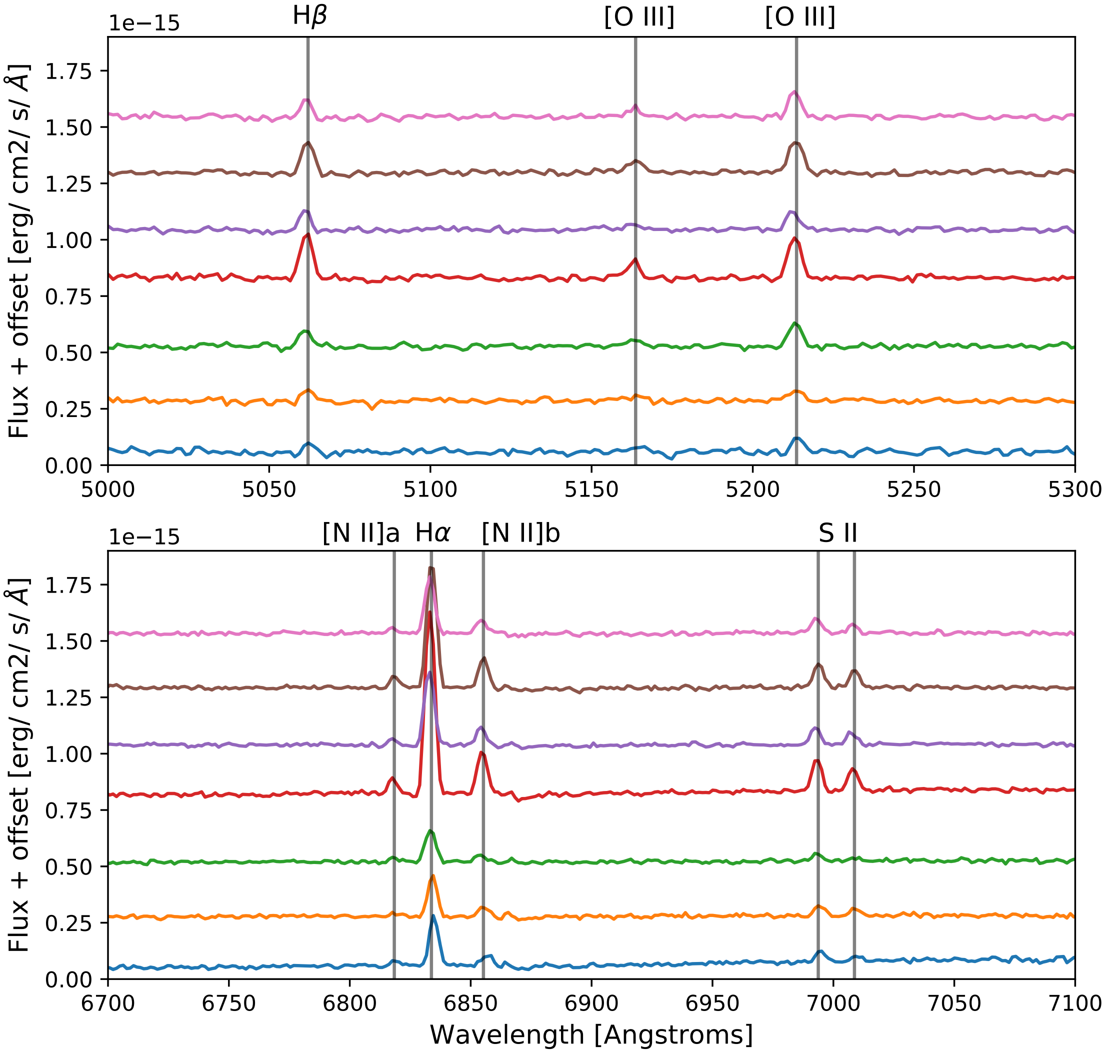

Figure A1 Spectra of 2MASXi J0909234-044327, host galaxy of ASASSN-15ho, with several emission lines denoted in grey. We have added a flux offset for each spectrum for clarity. The redshift is ~ 0.041.

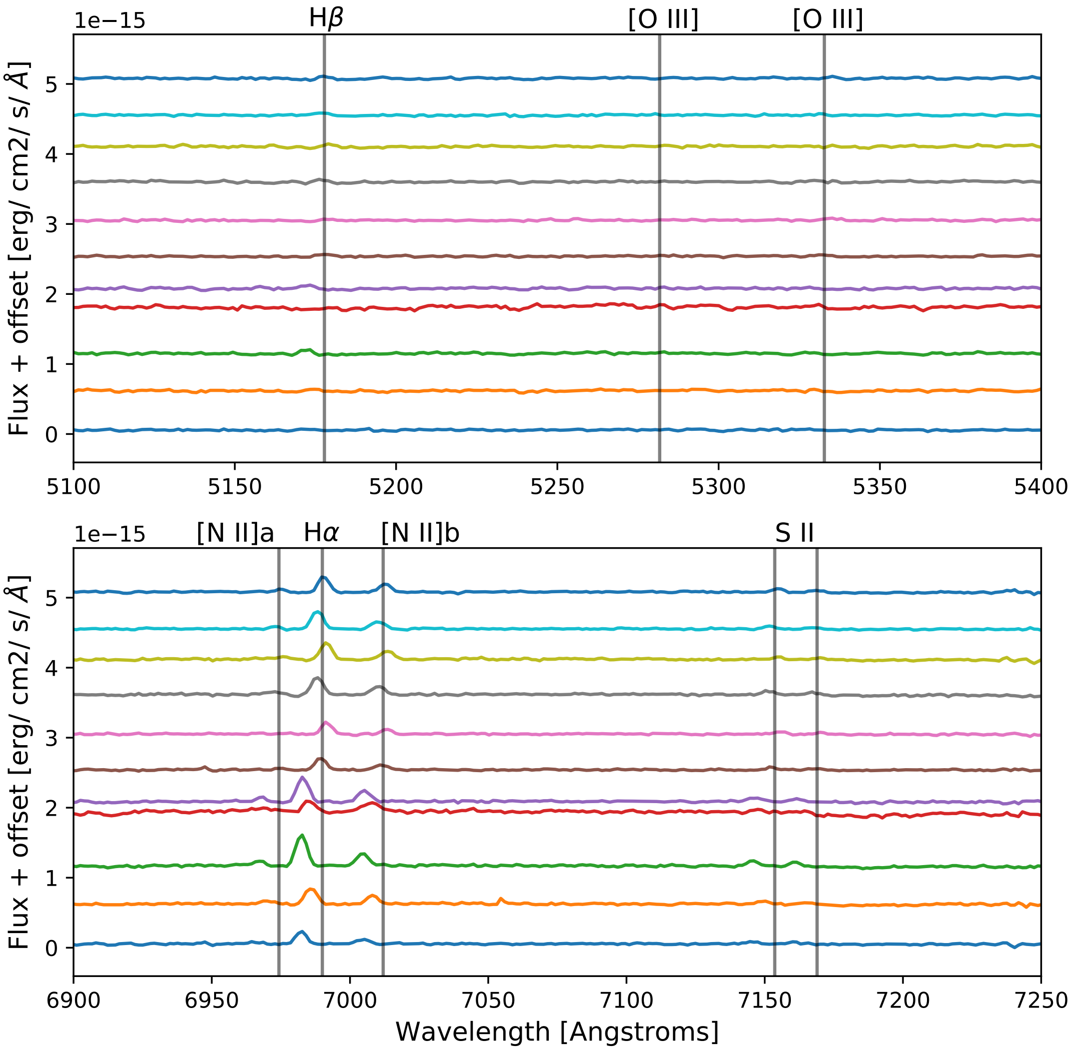

Figure A2 Spectra of 2MASX J01403375+1830406, host galaxy of LSQ12gef, with several emission lines denoted in grey. We have added a flux offset for each spectrum for clarity. The redshift is ~ 0.0648.

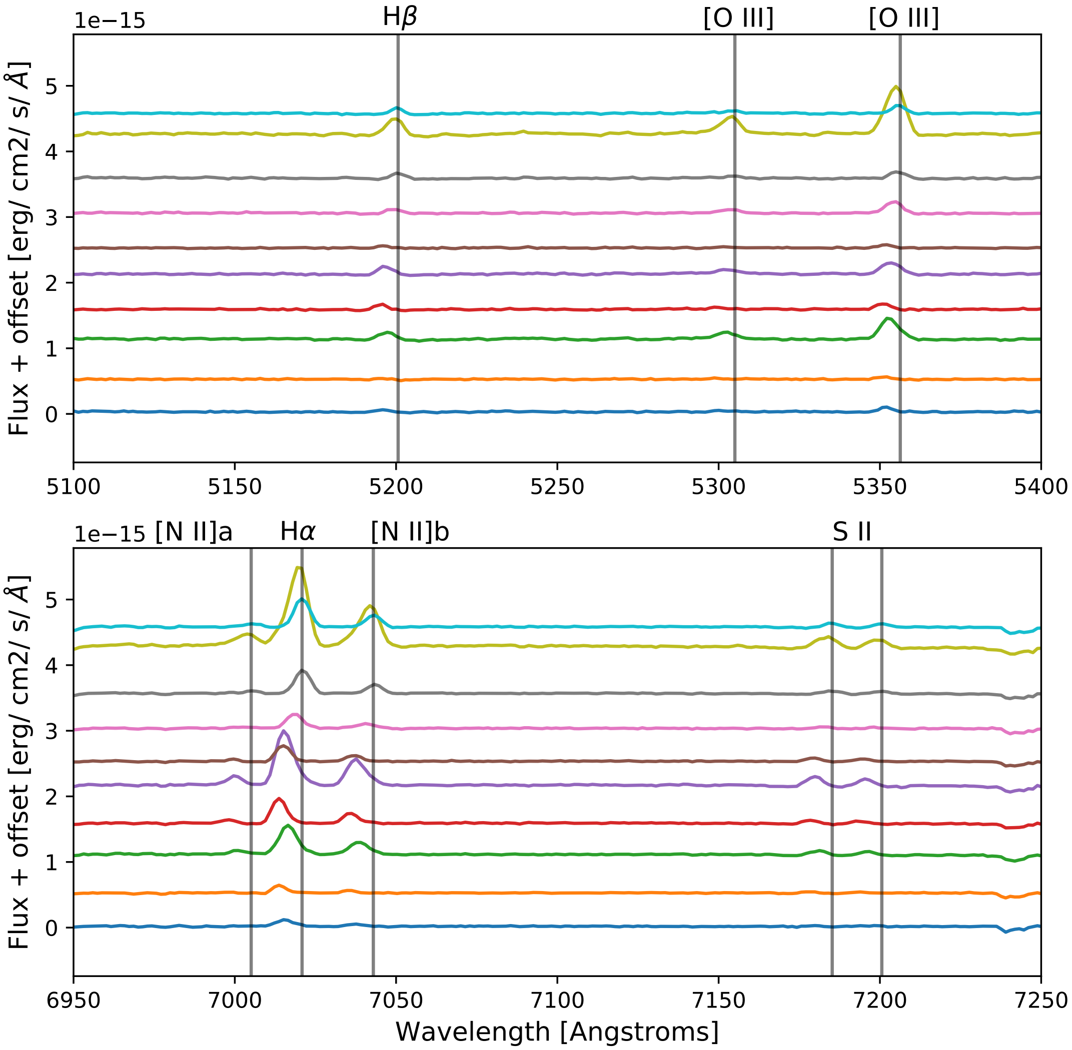

Figure A3 Spectra of MASX J00275880-0513014, host galaxy of iPTF14gdr, with several emission lines denoted in grey. We have added a flux offset for each spectrum for clarity. The redshift is ~ 0.0695.

A.3 Hα EQUIVALENT WIDTH MAPS

We here present the Hα Equivalent width maps for all 41 pointings of 32 host galaxies with HexPak.

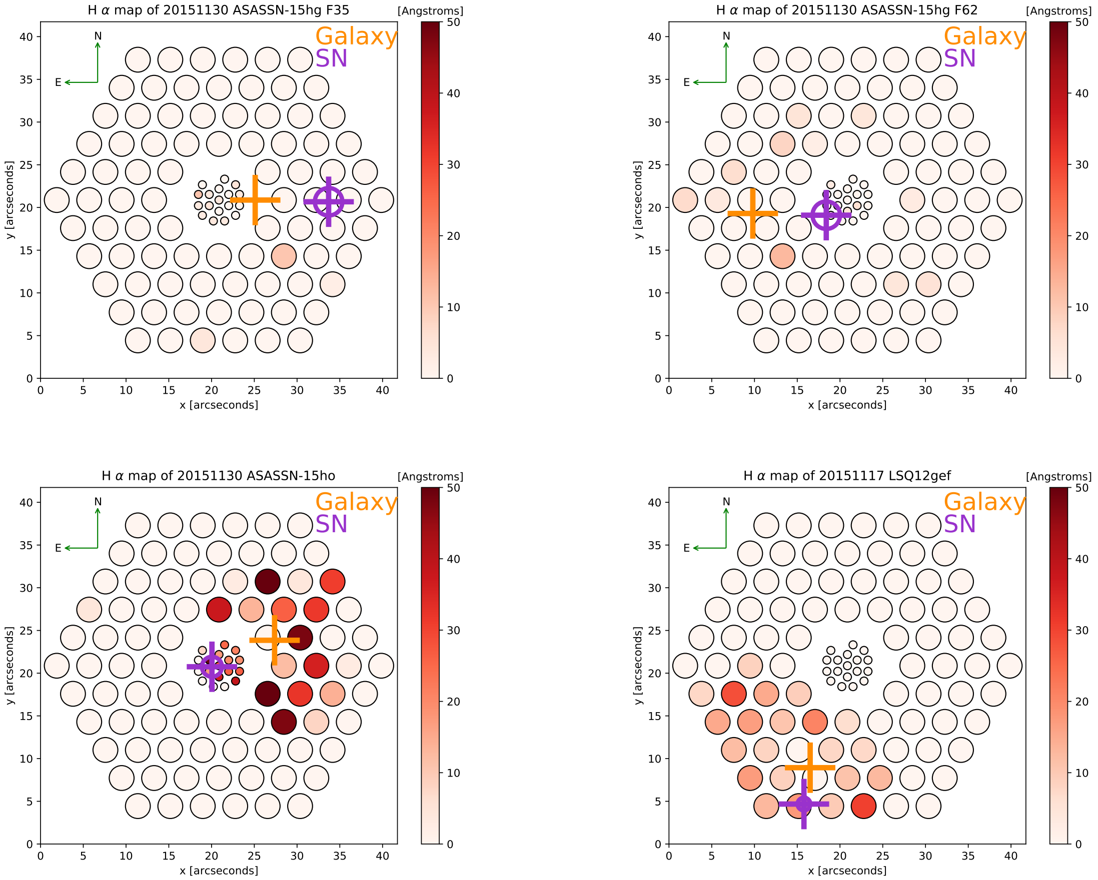

Figure A4 The orange cross indicates the location of the host galaxy and the purple cross is the location of the supernova. The purple circle occasionally visible in these plots indicates the 1 kpc radius circle around the SN location. Hα EW for: CGCG 063-098, host galaxy of ASASSN-15hg - Fiber 35; CGCG 063-098, host galaxy of ASASSN-15hg - Fiber 62; 2MASXi J0909234-044327, host galaxy of ASASSN-15ho; 2MASX J01403375+1830406, host galaxy of LSQ12gef.

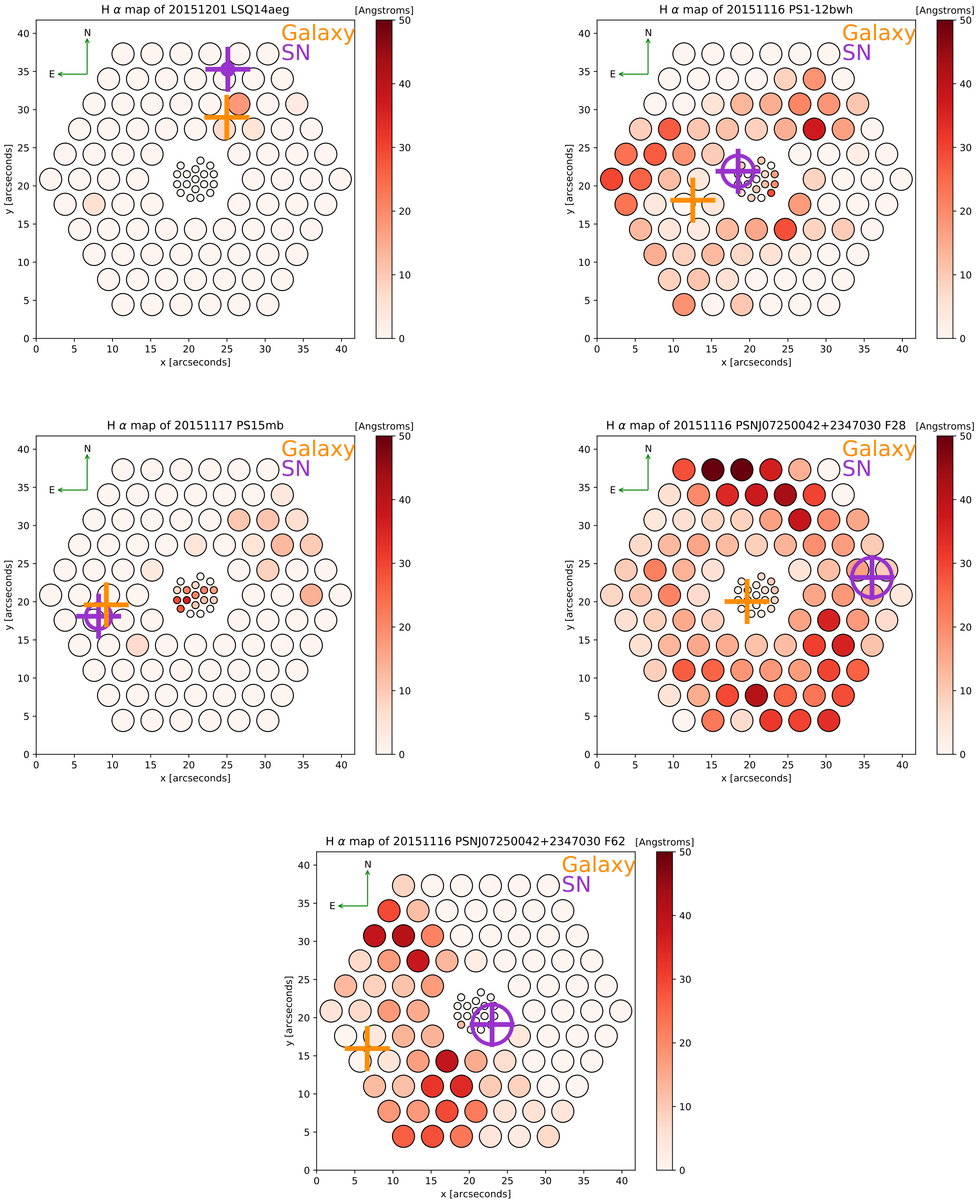

Figure A5 Hα EW for: 2MASX J10193682+1933131, host galaxy of LSQ14aeg; CGCG 205-021, host galaxy of PS1-12bwh; SDSS J085940.13+151113.5, host galaxy of PS15mb; NGC 2370, host galaxy of PSN J07250042+2347030 - Fiber 28; NGC 2370, host galaxy of PSN J07250042+2347030 - Fiber 62.

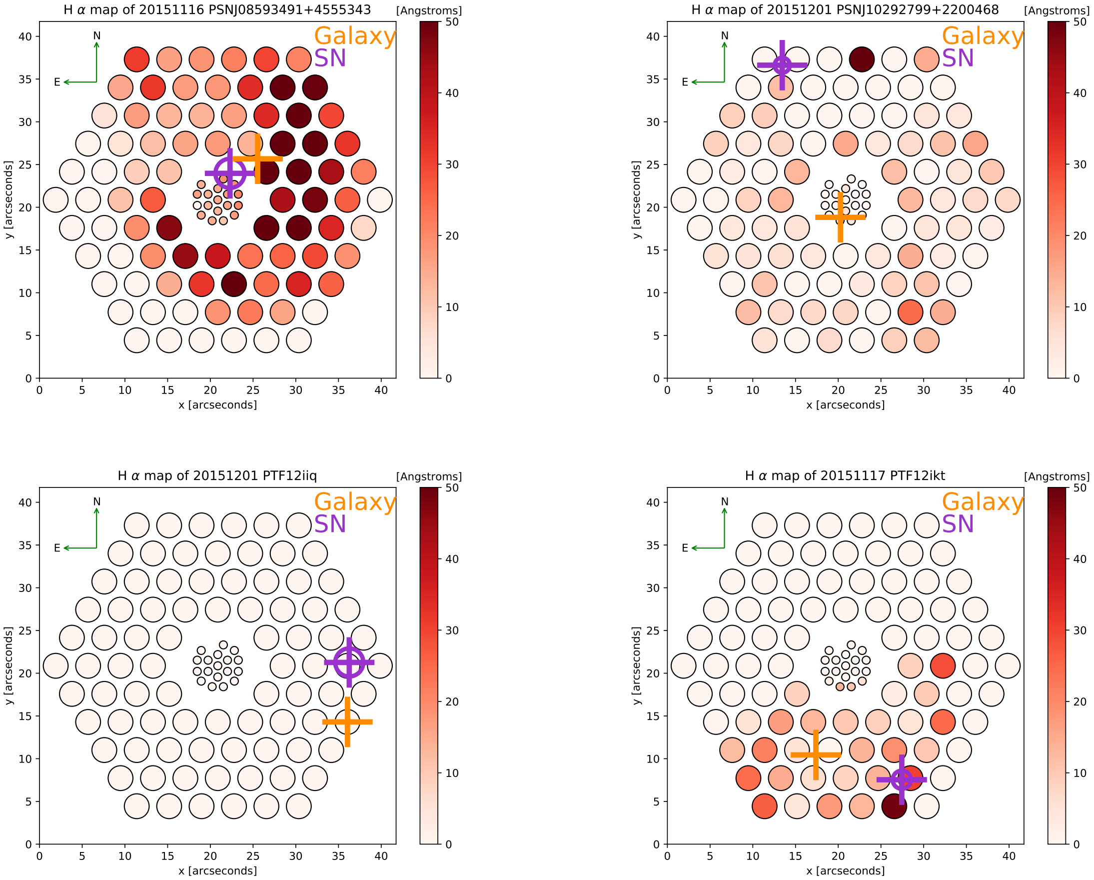

Figure A6 Hα EW for: UGC 4709, host galaxy of PSN J08593491+4555343; UGC 5691, host galaxy of PSN J10292799+2200468; 2MASX J02500784-0016014, host galaxy of PTF12iiq; 2MASX J01144386+0017100, host galaxy of PTF12ikt.

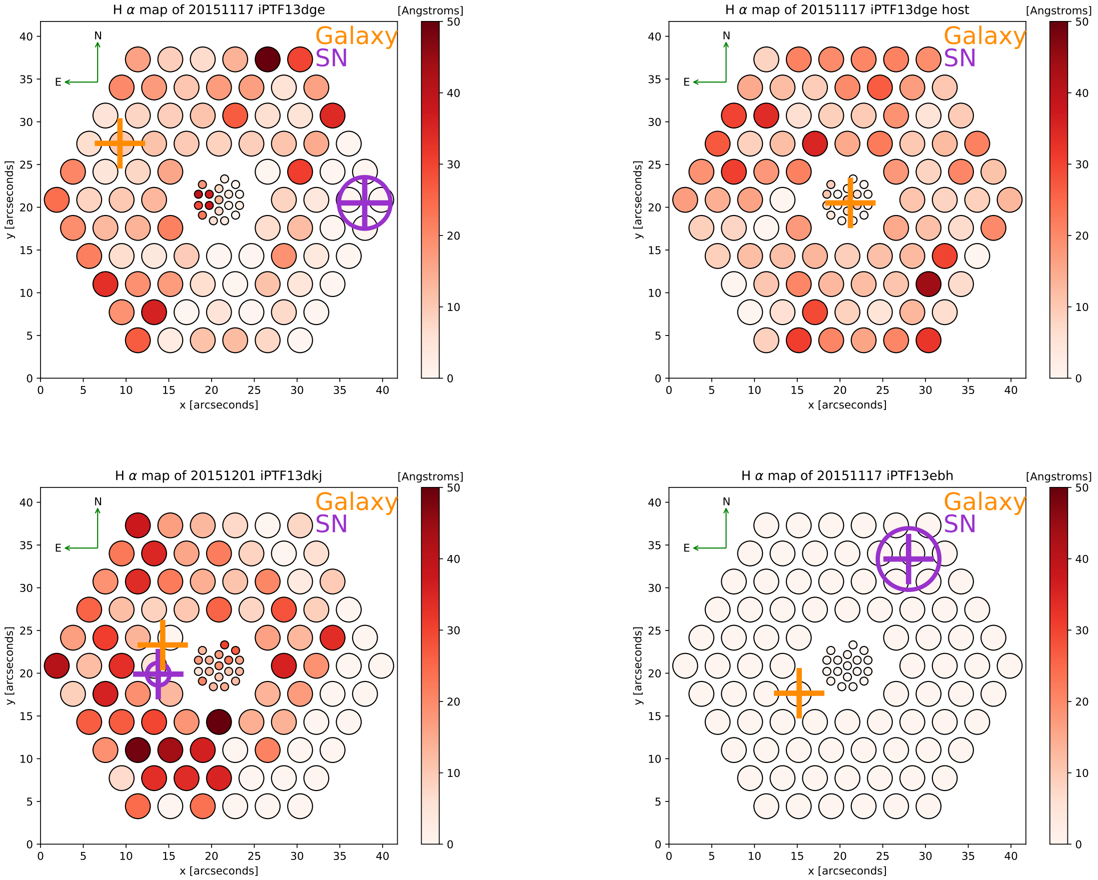

Figure A7 Hα EW for: NGC 1762, host galaxy of iPTF13dge - Fiber 35; NGC 1762, host galaxy of iPTF13dge - host only; CGCG 454-001, host galaxy of iPTF13dkj; NGC 890, host galaxy of iPTF13ebh.

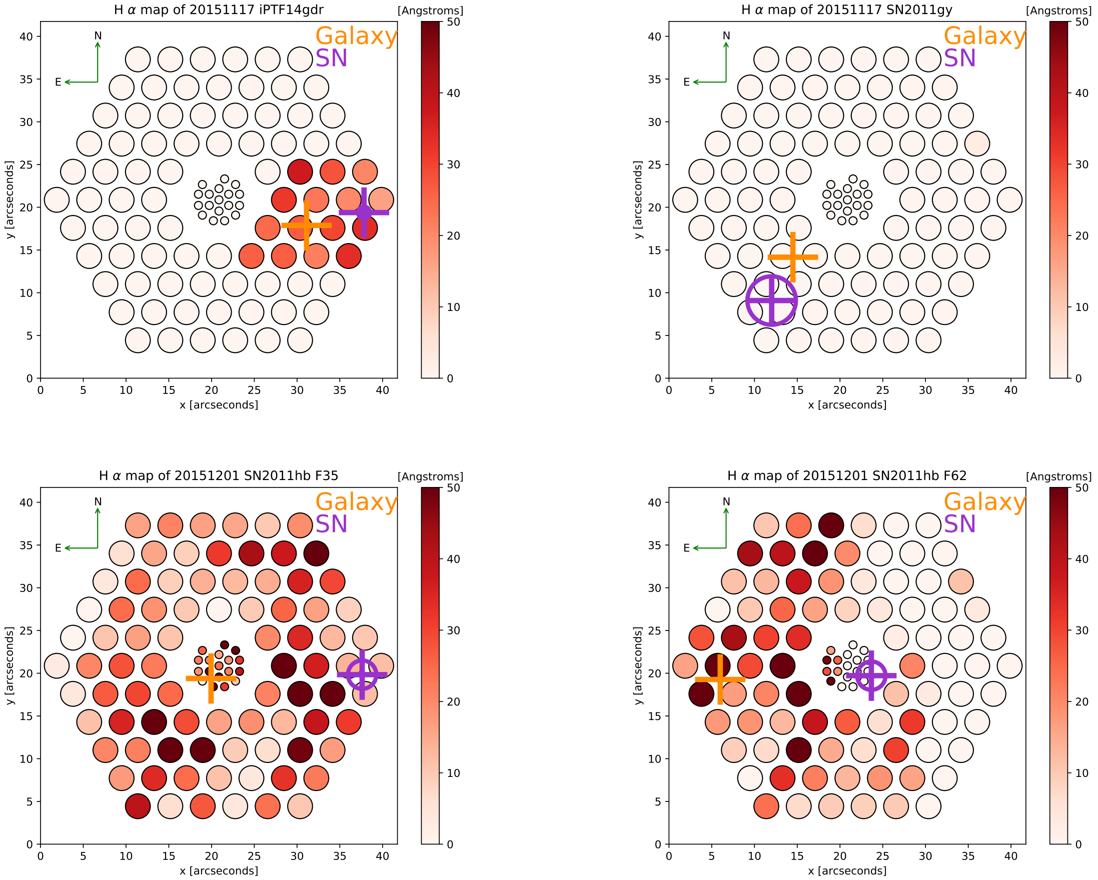

Figure A8 Hα EW for: 2MASX J00275880-0513014, host galaxy of iPTF14gdr; MCG +07-08-15, host galaxy of SN 2011gy; NGC 7674, host galaxy of SN 2011hb - Fiber 35; NGC 7674, host galaxy of SN 2011hb - Fiber 62.

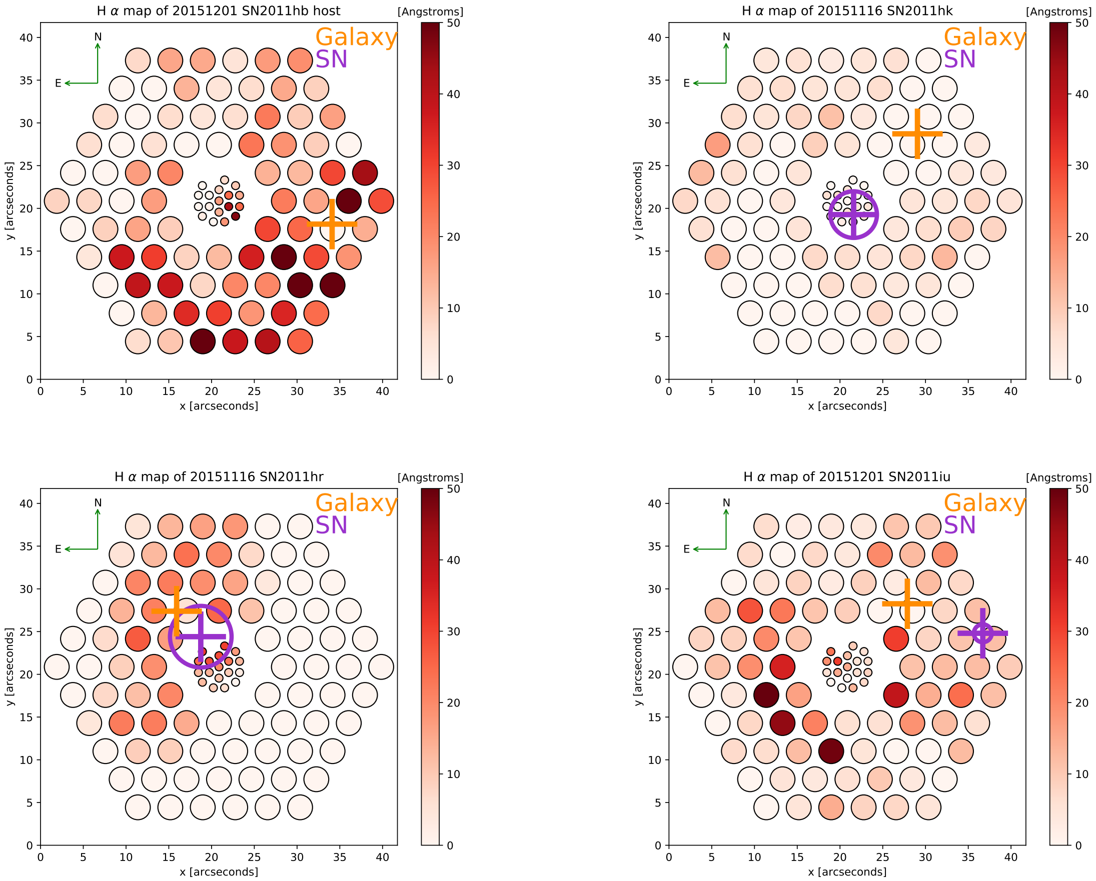

Figure A9 Hα EW for: NGC 7674, host galaxy of SN 2011hb - host only; NGC 881, host galaxy of SN 2011hk; NGC 2691, host galaxy of SN 2011hr; UGC 12809, host galaxy of SN 2011iu.

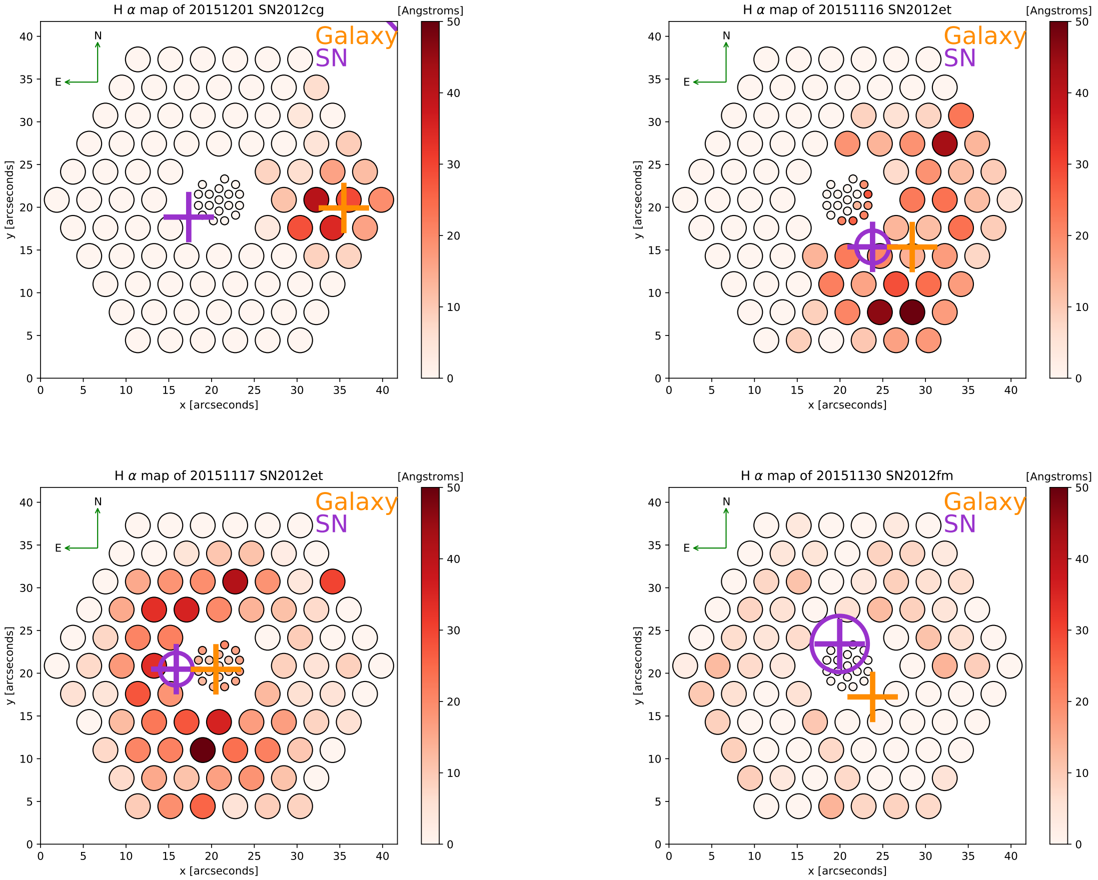

Figure A10 Hα EW for: NGC 4424, host galaxy of SN 2012cg; CGCG 476-117, host galaxy of SN 2012et - 2015-11-16; CGCG 476-117, host galaxy of SN 2012et - 2015-11-17; UGC 3528, host galaxy of SN 2012fm.

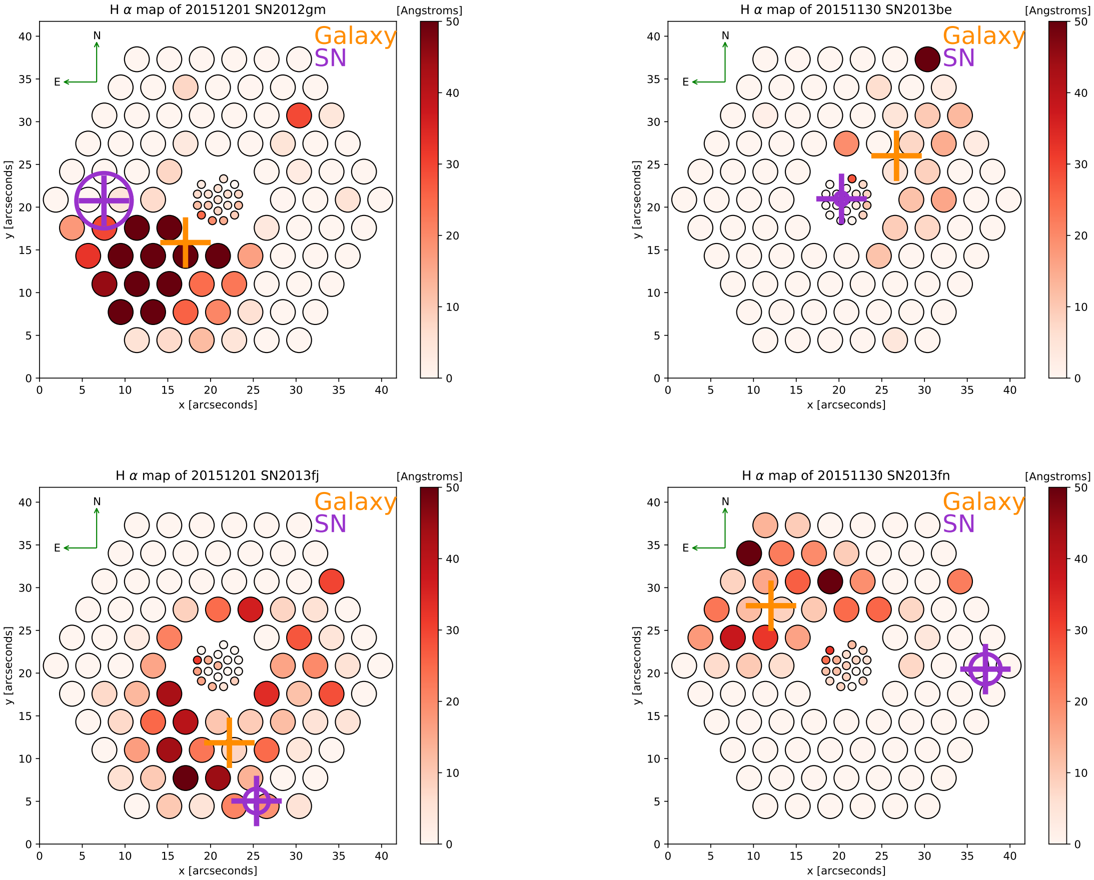

Figure A11 Hα EW for: NGC 7580, host galaxy of SN 2012gm; IC 3573, host galaxy of SN 2013be; PGC 68419, host galaxy of SN 2013fj; IC 1342, host galaxy of SN 2013fn.

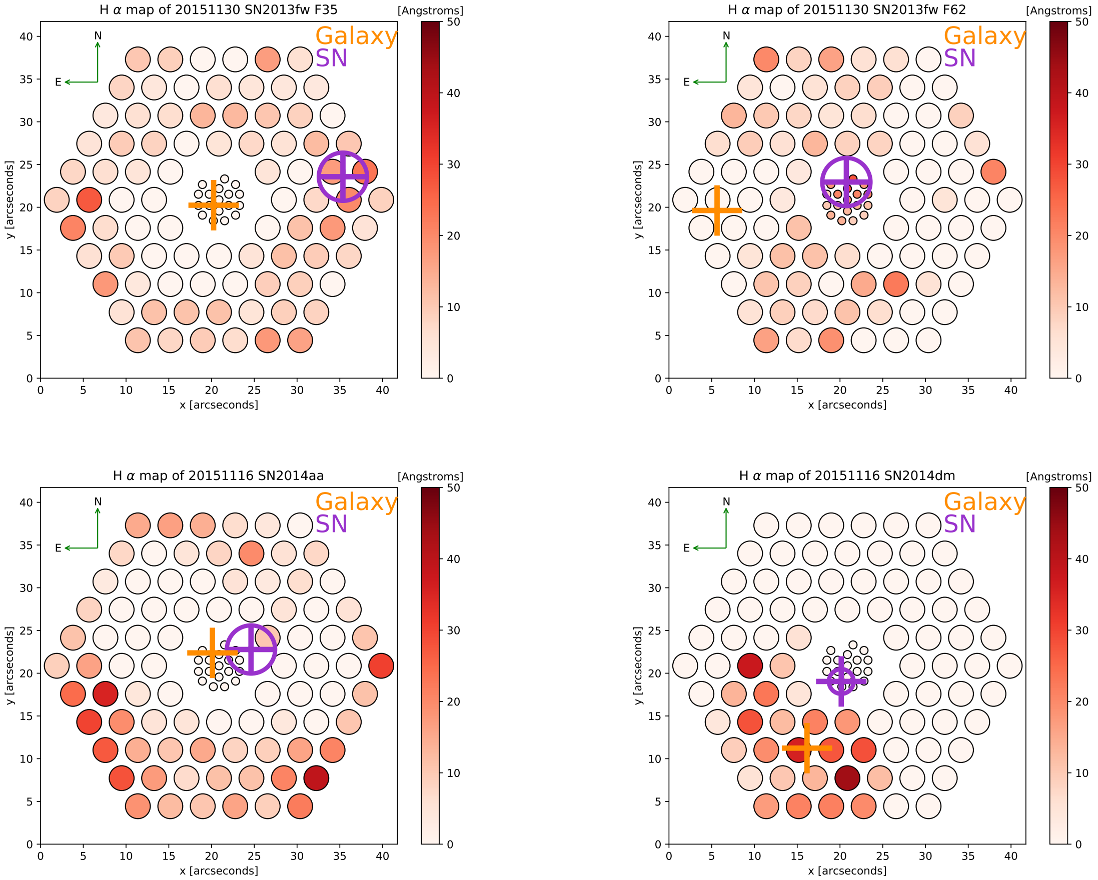

Figure A12 Hα EW for: NGC 7042, host galaxy of SN 2013fw - Fiber 35; NGC 7042, host galaxy of SN 2013fw - Fiber 62; NGC 3861, host galaxy of SN 2014aa; NGC 1516A, host galaxy of SN 2014dm - Fiber 62.

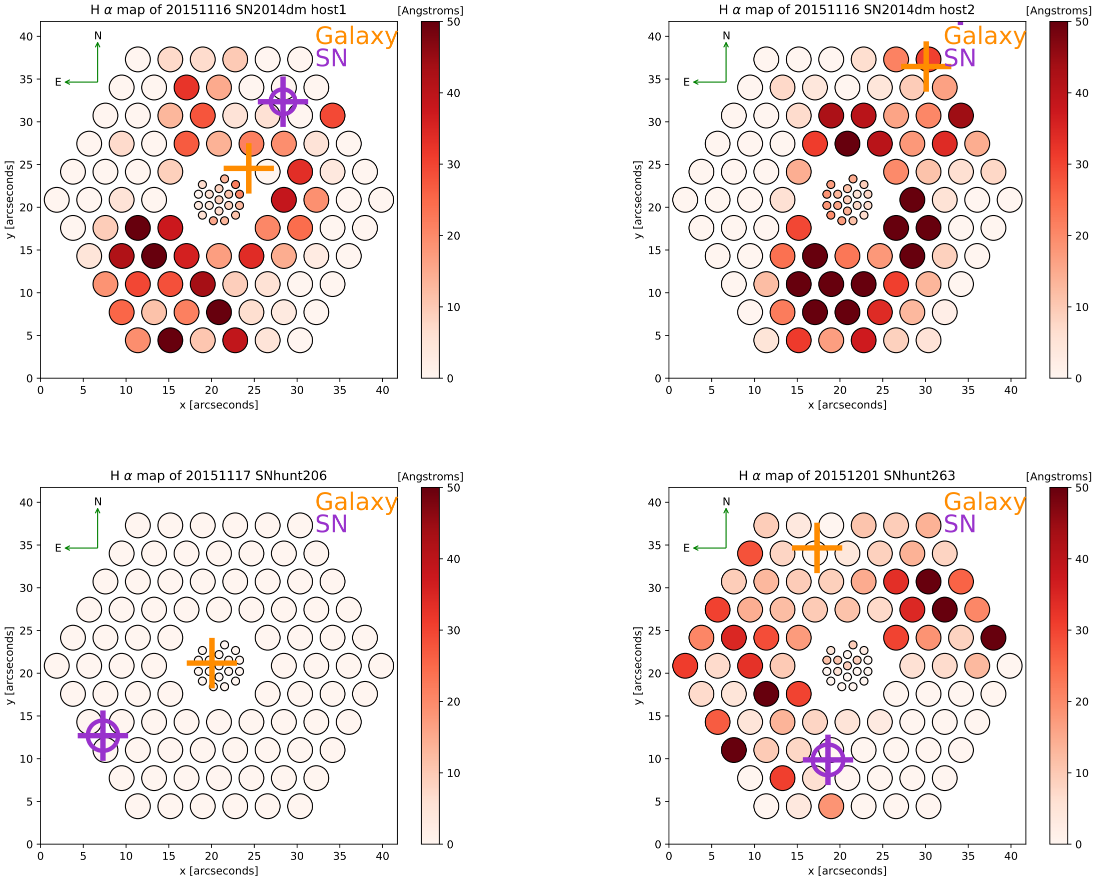

Figure A13 Hα EW for: NGC 1516A, host galaxy of SN 2014dm - Fiber 20; NGC 1516A, host galaxy of SN 2014dm - host only; NGC 766, host galaxy of SNhunt206; UGC 4798, host galaxy of SNhunt263.

APPENDIX B

APPENDICES FROM CHAPTER 4

B.1 HOST GALAXY PHOTOMETRY IN UV, OPTICAL, AND NIR

We here present all SNeIa with H-band photometry that we collected. We have identified the respective host galaxy and present the $FNugrizyJHK_S$ photometry downloaded from SDSS, PS1, GALEX, and 2MASS. All photometry is reported in units of magnitude and has been corrected for Milky Way extinction. The $g - r$ is in the restframe as is M_r. Mass is in units of Log $(M_*/M_\odot)$. The "LC" column denotes "Y" if the supernovae were used for the H-band lightcurve fits and included in the Hubble residual analysis.

Due to format constraints, we produced an "overflow" table with SNeIa/host galaxies whose names were too long to occupy a single line and fit on one page.

Table B1. Host Galaxy Photometry I

SN	Host Galaxy	F	N	u	g	r	i	z	y	J	H	K_s	$g-r$	M_r	Mass	LC
LSQ12fhs	2MASX J22522347-2036373	18.13	17.67	–	16.35	16.05	15.92	15.79	15.52	15.27	15.46	15.31	0.34	-19.73	9.33	Y
LSQ12fmx	2MASX J031252.93-001223.8	18.96	18.58	17.9	16.77	16.24	15.93	15.72	–	15.41	15.28	15.28	0.52	-21.19	10.15	Y
LSQ12fuk	None	–	–	–	–	–	–	–	–	–	–	–	–	–	–	N
LSQ12gef	SDSS J014033.71+183040.3	19.04	18.66	17.56	15.79	14.97	14.54	14.23	–	14.05	13.99	13.99	0.73	-22.38	10.82	N
LSQ13cmt	ESO 541- G 013	–	–	–	15.96	15.29	14.54	15.61	14.25	–	–	–	0.8	-21.79	10.39	Y
LSQ13cwp	2MASX J04035024-0239275	–	–	–	15.28	14.55	14.22	13.98	13.92	13.33	13.13	13.43	0.67	-22.83	10.96	Y
PS1-10w	CGCG 290-062	18.33	17.96	16.92	15.72	15.13	14.83	14.64	–	14.7	14.65	14.98	0.56	-20.51	9.97	Y
PS1-12bwh	Z 205-021	–	16.64	15.85	14.55	13.89	13.57	13.3	–	13.05	12.88	13.03	0.64	-21.09	10.26	N
PS1-13dkh	None	–	–	–	–	–	–	–	–	–	–	–	–	–	–	Y
PTF09dlc	SDSS J214630.02+062507.1	–	–	21.16	19.82	19.6	19.35	19.23	–	–	–	–	0.29	-17.87	8.18	Y
PTF10bjs	MCG +09-21-83	17.39	17.05	–	–	–	–	–	–	15.42	15.35	15.58	–	–	9.02	N
PTF10hdv	SDSS J120745.44+412928.7	–	–	21.01	20.27	20.34	20.2	20.6	–	–	–	–	0.09	-16.61	7.53	Y
PTF10icb	MCG +10-19-1	–	17.19	–	15.5	14.9	14.82	14.51	14.52	13.94	13.97	14.21	0.59	-17.88	8.51	N
PTF10ndc	SDSS J171949.85+284201.7	–	–	–	20.07	19.47	19.22	19.19	18.91	–	–	–	0.67	-18.45	8.82	Y
PTF10nlg	None	–	–	–	–	–	–	–	–	–	–	–	–	–	–	Y
PTF10wnm	SDSS J002203.68+270221.5	18.84	18.37	17.97	16.86	16.42	16.11	15.93	–	15.7	15.9	15.24	0.47	-20.97	9.97	Y
PTF10wof	SDSS J233241.42+152131.5	19.81	19.55	18.72	17.61	17.14	16.87	16.7	–	–	–	–	0.49	-19.72	9.5	Y
PTF10xyt	SDSS J231902.41+134726.2	–	–	19.54	18.54	18.06	17.8	17.64	–	–	–	–	0.49	-18.62	9.07	Y
PTF11moy	SDSS J170618.19+383218.5	–	–	22.35	21.27	20.87	20.71	21.07	–	–	–	–	0.43	-16.28	7.74	N
PTF11mty	SDSS J213405.07+102518.5	–	–	19.82	18.71	18.23	17.78	17.72	–	–	–	–	0.54	-19.59	9.39	N
PTF11owc	2MASX J091609.97+493732.0	–	–	18.07	16.1	15.2	14.83	14.55	–	13.96	13.62	13.9	0.77	-22.32	10.8	N
PTF11qmo	2MASX J10064866-0741124	18.34	–	–	15.96	15.32	15.03	14.98	14.72	14.12	14.1	13.95	0.62	-21.63	10.44	N
PTF11qpc	SDSS J122005.45+092418.3	–	19.31	19.32	17.94	17.45	17.16	17.07	–	–	–	–	0.49	-20.65	9.81	N
PTF11qri	LCRS B124431.1-060321	–	–	18.68	17.56	17.08	16.83	16.65	–	–	–	–	0.48	-19.86	9.53	N
PTF11qzq	2MASX J07192718+5413454	–	–	–	–	–	–	–	–	–	–	–	–	–	–	N
PTF12iiq	2MASX J02500784-0016014	–	–	16.81	15.01	14.21	13.86	13.56	–	13.46	13.17	13.44	0.75	-21.29	10.39	N
PTF12ikt	2MASX J01144386+0017100	18.65	18.21	17.43	16.06	15.36	15.0	14.72	–	14.43	14.24	14.46	0.66	-21.14	10.27	N
PTF13ayw	2MASX J15393305+3205382	–	19.95	17.43	15.56	14.71	14.35	14.09	–	13.64	13.72	13.71	0.75	-22.19	10.75	N
PTF13dad	None	–	–	–	–	–	–	–	–	–	–	–	–	–	–	Y
PTF13ddg	2MASX J004753.23+314848.1	–	–	19.33	17.32	16.44	16.06	15.78	–	15.47	15.4	15.54	0.73	-21.51	10.47	Y
SN 1972E	NGC 5253	–	–	–	–	–	–	–	–	9.92	9.87	10.12	–	–	8.66	N
SN 1980N	NGC 1316	–	13.95	–	–	–	–	–	–	7.34	7.25	7.43	–	–	11.31	N
SN 1981B	NGC 4536	–	–	14.69	12.66	11.61	11.11	10.74	–	9.39	9.26	9.36	1.04	-20.41	10.07	N
SN 1981D	NGC 1316	–	13.95	–	–	–	–	–	–	7.34	7.25	7.43	–	–	11.31	N
SN 1986G	NGC 5128	–	–	–	–	–	–	–	–	5.8	5.61	5.76	–	–	10.58	N
SN 1989B	NGC 3627	–	–	–	–	–	–	–	–	7.72	7.52	7.72	–	–	10.16	N
SN 1991T	NGC 4527	–	–	–	–	–	–	–	–	8.91	8.64	8.78	–	–	10.42	N
SN 1991bg	NGC 4374	16.58	14.63	–	10.98	10.34	9.96	9.79	9.57	8.0	7.84	8.06	0.64	-20.42	10.05	N
SN 1998bu	NGC 3368	–	14.78	–	11.87	10.81	10.5	10.23	9.92	8.13	7.95	8.16	1.06	-19.68	9.72	Y
SN 1999aa	NGC 2595	15.37	–	–	–	–	–	–	–	11.23	11.29	11.5	–	–	10.03	N

Table B2. Host Galaxy Photometry II

SN	Host Galaxy	F	N	u	g	r	i	z	y	J	H	K_s	$g-r$	M_r	Mass[a]	LC
SN 1999ac	NGC 6063	16.03	15.6	–	–	–	–	–	–	12.26	12.09	12.39	–	–	9.67	N
SN 1999cl	M88	–	–	–	–	–	–	–	–	–	–	–	–	–	–	Y
SN 1999cp	NGC 5468	–	–	–	–	–	–	–	–	11.82	11.71	12.24	–	–	9.71	N
SN 1999ee	IC 5179	15.18	14.53	–	–	–	–	–	–	10.55	10.33	10.47	–	–	10.5	Y
SN 1999ek	UGC 3329	–	–	–	–	–	–	–	–	12.53	12.43	12.09	–	–	9.79	Y
SN 1999gp	UGC 1993	–	–	–	–	–	–	–	–	12.45	12.19	12.53	–	–	10.58	Y
SN 2000E	NGC 6951	16.81	15.46	–	–	–	–	–	–	8.94	8.7	8.97	–	–	10.52	N
SN 2000bh	ESO 573-14	–	–	–	15.18	14.91	14.65	14.61	14.38	14.47	14.37	14.44	0.27	-20.02	9.75	N
SN 2000bk	NGC 4520	20.4	18.92	–	–	–	–	–	–	12.16	12.12	12.2	–	–	10.66	N
SN 2000ca	ESO 383-32	17.13	–	–	–	–	–	–	–	15.2	14.64	15.38	–	–	9.48	N
SN 2000ce	UGC 4195	16.76	16.11	15.28	13.83	13.08	12.71	12.42	–	12.15	12.02	12.19	0.73	-21.13	10.32	Y
SN 2000cx	NGC 524	18.28	16.18	–	–	–	–	–	–	8.98	8.78	8.99	–	–	10.89	N
SN 2001ba	MCG -05-28-1	17.39	16.19	–	–	–	–	–	–	12.36	12.09	12.37	–	–	10.64	N
SN 2001bt	IC 4830	–	15.48	–	–	–	–	–	–	10.87	10.66	10.81	–	–	10.71	N
SN 2001cn	IC 4758	–	15.72	–	–	–	–	–	–	12.31	12.18	12.25	–	–	10.14	N
SN 2001cz	NGC 4679	–	–	–	–	–	–	–	–	11.26	11.07	11.24	–	–	10.35	N
SN 2001el	NGC 1448	13.74	13.38	–	–	–	–	–	–	9.58	9.33	9.51	–	–	9.99	N
SN 2002bo	NGC 3190	18.02	15.95	–	–	–	–	–	–	9.4	9.15	9.3	–	–	10.19	Y
SN 2002cv	NGC 3190	18.02	15.95	–	–	–	–	–	–	9.4	9.15	9.3	–	–	10.19	N
SN 2002dj	NGC 5018	–	15.58	–	–	–	–	–	–	9.51	9.38	9.56	–	–	10.87	Y
SN 2002fk	NGC 1309	13.75	13.27	–	14.7	12.65	12.43	12.24	–	10.94	10.75	10.94	2.05	-19.74	9.64	N
SN 2003cg	NGC 3169	–	–	–	12.7	7.39	8.63	8.53	9.08	9.14	8.94	9.12	5.31	-23.79	10.05	N
SN 2003du	UGC 9391	–	15.97	16.68	15.12	14.67	14.58	14.57	–	–	–	–	0.45	-17.47	8.56	Y
SN 2003gs	NGC 936	16.96	–	–	12.19	11.41	11.03	10.87	10.74	8.72	8.51	8.75	0.78	-20.09	9.88	N
SN 2003hv	NGC 1201	18.36	16.42	–	–	–	–	–	–	9.45	9.27	9.52	–	–	10.43	N
SN 2004S	MCG -05-16-21	–	–	–	–	–	–	–	–	12.72	12.6	12.79	–	–	9.25	Y
SN 2004ef	UGC 12158	–	16.41	15.82	14.19	13.43	13.08	12.83	–	12.82	12.62	12.71	0.73	-22.21	10.75	Y
SN 2004eo	NGC 6928	18.53	16.39	–	–	–	–	–	–	10.64	10.41	10.56	–	–	10.82	Y
SN 2004ey	UGC 11816	16.04	15.61	15.76	14.48	13.86	13.56	13.39	–	13.04	12.87	13.26	0.61	-20.27	9.94	Y
SN 2004gs	MCG +03-22-20	20.05	19.18	16.29	14.49	13.7	13.31	13.02	–	13.01	12.76	12.88	0.75	-21.66	10.55	Y
SN 2004gu	FGC 175A	21.27	20.83	19.1	17.37	16.49	16.04	15.64	–	15.02	14.77	14.86	0.84	-20.08	9.89	Y
SN 2005A	NGC 958	15.92	15.27	–	–	–	–	–	–	10.76	10.48	10.64	–	–	10.9	Y
SN 2005M	NGC 2930	15.86	15.58	16.3	15.75	15.6	15.53	15.44	–	13.86	13.82	13.83	0.22	-19.54	9.28	Y
SN 2005ag	2MASX J14564322+0919361	–	–	–	16.3	15.72	15.72	15.11	15.29	14.51	14.34	14.25	0.5	-22.08	10.55	Y
SN 2005al	NGC 5304	19.56	17.8	–	16.26	14.93	14.51	14.68	14.57	11.31	11.11	11.35	1.32	-18.65	9.05	Y
SN 2005am	NGC 2811	–	–	–	12.48	11.79	11.71	11.48	11.32	9.81	9.6	9.81	0.69	-20.82	9.72	Y
SN 2005ao	NGC 6462	17.34	16.61	16.06	14.45	13.76	13.42	13.12	–	12.93	12.72	12.86	0.67	-22.38	10.77	Y
SN 2005bl	NGC 4070	–	18.52	15.17	13.34	12.5	12.13	11.9	–	11.62	11.39	11.59	0.79	-22.56	10.9	N
SN 2005bo	NGC 4708	15.98	–	–	14.71	14.64	14.04	–	13.63	12.04	11.89	11.98	0.07	-19.2	9.39	Y
SN 2005cf	MCG -01-39-3	15.91	15.07	–	–	–	–	–	–	12.92	12.83	13.12	–	–	8.69	Y

Table B3. Host Galaxy Photometry III

SN	Host Galaxy	F	N	u	g	r	i	z	y	J	H	K_s	$g-r$	M_r	Mass[a]	LC
SN 2005el	NGC 1819	–	–	–	–	–	–	–	–	11.14	10.88	11.05	–	–	10.42	Y
SN 2005eq	MCG -01-9-6	17.1	16.63	15.65	14.24	13.47	13.09	12.75	–	12.63	12.46	12.63	0.73	-22.01	10.66	Y
SN 2005eu	NSF J022743.32+281037.6	–	–	–	–	–	–	–	–	–	–	–	–	–	–	Y
SN 2005hc	MCG +00-6-3	–	18.56	17.42	15.79	15.03	14.68	14.42	–	13.87	13.76	13.83	0.7	-21.51	10.44	Y
SN 2005hj	SDSS J012648.45-011417.3	–	–	20.15	18.82	18.15	17.8	17.54	–	–	–	–	0.64	-18.89	9.31	Y
SN 2005hk	UGC 272	16.45	16.14	16.31	14.84	14.38	14.18	14.09	–	15.08	14.1	14.83	0.46	-19.32	9.38	N
SN 2005iq	MCG -03-1-8	17.51	17.33	–	15.37	14.76	14.48	14.21	13.92	13.38	13.15	13.59	0.63	-21.1	10.08	Y
SN 2005kc	NGC 7311	–	15.77	14.44	12.61	11.8	11.42	11.15	–	10.77	10.53	10.75	0.79	-22.24	10.77	Y
SN 2005ke	NGC 1371	17.77	16.35	–	12.83	12.21	11.94	11.94	11.43	9.45	9.29	9.47	0.62	-19.34	9.48	N
SN 2005ki	NGC 3332	–	–	–	–	–	–	–	–	11.25	11.1	11.22	–	–	10.43	Y
SN 2005ku	SDSS J225942.66-000048.8	19.1	18.56	17.88	16.74	16.29	16.03	15.85	–	15.32	15.29	15.5	0.48	-20.24	9.67	N
SN 2005ls	MCG +07-7-1	16.42	15.75	15.37	14.46	13.94	13.72	13.52	–	13.1	13.08	13.19	0.51	-20.83	10.05	N
SN 2005na	UGC 3634	–	–	–	–	–	–	–	–	11.94	11.68	11.91	–	–	10.75	Y
SN 2006D	MCG -01-33-34	15.88	15.49	–	–	–	–	–	–	12.34	12.16	12.33	–	–	9.52	Y
SN 2006E	NGC 5338	–	–	14.79	13.43	12.85	12.59	12.4	–	12.11	11.96	12.22	0.58	-17.43	8.7	N
SN 2006N	MCG +11-8-12	–	18.61	–	–	–	–	–	–	11.93	11.76	11.96	–	–	10.27	Y
SN 2006X	NGC 4321	–	–	–	–	–	–	–	–	–	–	–	–	–	–	Y
SN 2006ac	NGC 4619	15.67	15.21	15.67	14.88	15.5	15.75	23.02	–	11.72	11.59	11.73	-0.54	-19.49	8.41	Y
SN 2006ax	NGC 3663	15.99	15.31	–	–	–	–	–	–	11.61	11.39	11.73	–	–	10.43	Y
SN 2006bd	UGC 6609	20.57	18.61	16.02	14.05	13.25	12.87	12.57	–	12.28	11.99	12.16	0.76	-21.97	10.66	N
SN 2006bh	NGC 7329	–	14.53	–	–	–	–	–	–	10.69	10.49	10.72	–	–	10.53	Y
SN 2006br	NGC 5185	–	–	–	–	–	–	–	–	12.09	11.94	12.08	–	–	10.36	Y
SN 2006bt	CGCG 108-013	–	–	16.02	14.14	13.37	13.0	12.74	–	12.42	12.24	12.43	0.72	-22.35	10.82	N
SN 2006cp	UGC 7357	16.7	–	15.4	14.33	13.85	13.65	13.5	–	13.99	13.7	13.98	0.48	-21.04	10.03	Y
SN 2006cz	MCG -01-38-2	–	16.28	–	–	–	–	–	–	12.73	12.51	12.56	–	–	10.86	N
SN 2006ej	NGC 191	–	16.98	15.47	13.56	12.73	12.33	12.05	–	11.43	11.14	11.41	0.8	-21.96	10.67	Y
SN 2006eq	SDSS J12837.60+011348.6	20.97	20.1	18.78	17.24	16.47	16.06	15.76	–	15.55	14.98	15.19	0.73	-20.27	9.93	Y
SN 2006et	NGC 232	–	18.12	–	–	–	–	–	–	11.93	11.64	11.72	–	–	10.59	Y
SN 2006ev	UGC 11758	–	–	–	14.46	14.0	13.95	13.38	13.44	12.33	12.07	12.15	0.47	-21.46	10.12	Y
SN 2006gj	UGC 2650	–	–	–	14.24	14.06	14.22	13.55	13.91	12.83	12.74	12.88	0.18	-21.34	9.72	Y
SN 2006gr	UGC 12071	–	–	15.88	14.55	13.81	13.41	13.12	–	–	–	–	0.72	-22.09	10.64	N
SN 2006gt	2MASX J00561810-0137327	–	22.04	18.53	16.8	16.0	15.63	15.34	–	15.45	15.32	15.34	0.73	-20.47	10.06	Y
SN 2006hb	MCG -04-12-34	–	–	–	13.91	13.37	13.31	12.82	12.62	12.09	11.91	12.11	0.56	-20.7	9.9	Y
SN 2006hx	PGC 73820	–	20.22	–	16.6	15.94	15.6	15.4	15.23	14.8	14.36	14.59	0.67	-20.57	9.8	Y
SN 2006is	ESO 486- G 049	–	–	–	–	–	–	–	–	–	–	–	–	–	–	Y
SN 2006kf	UGC 2829	–	–	15.5	13.68	12.87	12.48	12.19	–	11.84	11.63	11.83	0.78	-21.93	10.66	Y
SN 2006le	UGC 3218	15.2	14.18	–	–	–	–	–	–	10.92	10.74	10.95	–	–	10.66	Y
SN 2006lf	UGC 3108	–	–	–	–	–	–	–	–	11.08	10.95	11.13	–	–	10.23	Y
SN 2006lu	2MASX J09151727-2536001	18.84	18.52	–	–	–	–	–	–	14.91	14.76	14.99	–	–	10.19	N
SN 2006mq	ESO 494-G26	–	–	–	–	–	–	–	–	9.51	9.41	9.61	–	–	9.58	N

Table B4.   Host Galaxy Photometry IV

SN	Host Galaxy	F	N	u	g	r	i	z	y	J	H	K_s	$g-r$	M_r	Mass[a]	LC
SN 2006mr	NGC 1316	–	13.95	–	–	–	–	–	–	7.34	7.25	7.43	–	–	11.31	N
SN 2006ob	UGC 1333	18.5	17.94	17.07	15.13	14.28	13.86	13.56	–	13.15	12.92	13.3	0.78	-22.86	11.01	N
SN 2006os	UGC 2384	–	–	–	14.74	13.42	13.88	12.64	12.58	12.61	12.41	12.49	1.27	-22.39	10.61	Y
SN 2006ot	ESO 544-G31	–	20.2	–	14.6	13.75	13.9	13.54	13.39	12.68	12.56	12.69	0.87	-23.13	10.88	N
SN 2007A	NGC 105	–	–	–	–	–	–	–	–	–	–	–	–	–	–	Y
SN 2007N	MCG -01-33-12	17.52	16.86	15.41	13.83	13.12	12.78	12.51	–	12.47	12.37	12.55	0.69	-20.56	10.09	N
SN 2007S	UGC 5378	16.83	16.33	15.69	14.27	13.83	13.51	13.28	–	13.06	12.95	13.18	0.44	-20.02	9.71	Y
SN 2007af	NGC 5584	–	13.57	14.07	12.86	12.28	11.97	12.2	–	11.72	11.42	11.79	0.57	-19.51	9.52	Y
SN 2007ai	MCG -04-38-4	–	–	–	–	–	–	–	–	12.38	12.16	12.27	–	–	10.55	Y
SN 2007as	ESO 18-G18	–	–	–	–	–	–	–	–	12.62	12.39	12.83	–	–	10.08	Y
SN 2007ax	NGC 2577	–	–	–	–	–	–	–	–	10.88	10.7	10.89	–	–	9.78	N
SN 2007ba	UGC 9798	19.34	18.62	–	15.12	14.25	13.97	13.64	13.55	–	–	–	0.8	-21.88	10.6	Y
SN 2007bc	UGC 6332	–	–	15.61	13.79	12.95	12.58	12.32	–	12.06	11.79	11.96	0.8	-21.79	10.59	Y
SN 2007bd	UGC 4455	17.47	17.12	16.32	14.51	13.7	13.32	13.01	–	12.98	12.73	12.76	0.77	-21.93	10.65	Y
SN 2007bm	NGC 3672	–	13.79	13.47	12.0	11.25	10.86	10.63	–	10.08	9.93	10.11	0.75	-20.83	10.2	Y
SN 2007ca	MCG -02-34-61	–	16.32	–	–	–	–	–	–	13.4	13.27	13.41	–	–	9.58	Y
SN 2007co	MCG +05-43-16	–	–	–	–	–	–	–	–	13.06	12.9	13.15	–	–	10.21	N
SN 2007cq	2MASX J22144070+0504435	18.14	17.73	16.99	15.81	15.32	15.09	14.89	–	14.72	14.6	14.68	0.5	-19.95	9.62	Y
SN 2007fb	UGC 12859	–	17.26	–	15.01	14.41	13.56	13.46	13.65	12.7	12.52	12.79	0.59	-20.01	9.71	N
SN 2007hx	SDSS J020626.74-005400.4	–	–	19.11	17.54	16.79	16.39	16.08	–	–	–	–	0.69	-21.07	10.2	Y
SN 2007if	J011051.37+152739	–	–	–	–	–	–	–	–	–	–	–	–	–	–	N
SN 2007jg	SDSS J032950.83+000316.0	19.64	19.37	18.99	17.95	17.52	17.33	17.33	–	–	–	–	0.47	-18.55	8.98	Y
SN 2007jh	CGCG 391-014	–	–	16.56	14.8	13.96	13.57	13.3	–	13.0	12.75	12.88	0.76	-22.29	10.8	N
SN 2007le	NGC 7721	–	14.04	–	–	–	–	–	–	10.41	10.25	10.52	–	–	10.21	Y
SN 2007nq	UGC 595	20.76	19.48	15.77	14.04	13.2	12.82	12.48	–	12.54	12.41	12.39	0.76	-23.29	11.2	Y
SN 2007on	NGC 1404	–	15.2	–	–	–	–	–	–	8.67	8.47	8.67	–	–	10.47	Y
SN 2007qe	NSF J235412.09+272432.3	19.93	19.54	18.71	17.51	16.98	16.74	16.63	–	–	–	–	0.51	-17.66	8.78	N
SN 2007rx	BATC J234012.05+272512.23	–	–	–	–	–	–	–	–	–	–	–	–	–	–	N
SN 2007sr	NGC 4038	–	–	–	–	–	–	–	–	–	–	–	–	–	–	Y
SN 2008A	NGC 634	18.27	17.29	–	14.4	13.64	13.14	12.99	12.7	11.63	11.4	11.57	0.74	-20.58	10.14	N
SN 2008C	UGC 3611	–	–	–	–	–	–	–	–	12.38	12.13	12.3	–	–	10.06	Y
SN 2008R	NGC 1200	18.91	17.51	–	–	–	–	–	–	10.43	10.21	10.41	–	–	10.81	Y
SN 2008Z	SDSS J094315.36+361709.2	–	–	18.9	17.6	16.97	16.63	16.36	–	–	–	–	0.64	-17.8	8.81	Y
SN 2008ae	IC 577	16.78	16.3	15.98	14.82	14.3	13.91	13.72	–	13.34	13.2	13.36	0.54	-21.29	10.26	Y
SN 2008af	UGC 9640	–	18.72	15.61	13.7	12.85	12.48	12.22	–	11.85	11.68	11.86	0.8	-22.97	11.06	N
SN 2008bc	KK 1524	–	–	–	–	–	–	–	–	13.14	12.93	13.19	–	–	9.73	Y
SN 2008bq	ESO 308-G25	–	–	–	–	–	–	–	–	12.39	12.27	12.42	–	–	10.55	Y
SN 2008fp	ESO 428-G14	–	16.04	–	–	–	–	–	–	10.57	10.36	10.57	–	–	9.98	Y
SN 2008fr	SDSS J011149.19+143826.5	–	–	20.6	19.4	19.09	18.92	19.11	–	–	–	–	0.38	-17.63	8.09	Y
SN 2008fv	NGC 3147	14.31	13.67	–	–	–	–	–	–	9.26	9.14	9.25	–	–	10.91	Y

Table B5. Host Galaxy Photometry V

SN	Host Galaxy	F	N	u	g	r	i	z	y	J	H	K_s	$g-r$	M_r	Mass[a]	LC
SN 2008fx	2MASX J02113233+2353074	–	–	18.75	16.93	16.1	15.73	15.42	–	15.26	14.75	14.91	0.74	-21.02	10.27	Y
SN 2008gb	UGC 2427	–	16.99	–	–	–	–	–	–	14.06	13.95	14.09	–	–	9.99	Y
SN 2008gl	UGC 881	21.15	19.63	16.28	14.4	13.57	13.17	12.88	–	12.55	12.43	12.54	0.77	-22.28	10.8	Y
SN 2008gp	MCG +00-9-74	–	–	–	15.27	14.49	14.32	14.26	14.19	12.8	12.72	12.82	0.77	-21.3	10.01	Y
SN 2008ha	UGC 12682	15.58	15.15	–	–	–	–	–	–	–	–	–	–	–	8.95	N
SN 2008hm	2MFGC 02845	–	–	–	–	–	–	–	–	13.52	13.34	13.39	–	–	9.49	Y
SN 2008hs	NGC 910	–	18.41	–	–	–	–	–	–	11.03	10.81	11.04	–	–	10.77	Y
SN 2008hv	NGC 2765	19.78	17.62	14.33	12.59	11.83	11.53	11.19	–	11.05	10.86	11.06	0.74	-21.79	10.59	Y
SN 2008hy	IC 334	19.43	–	–	–	–	–	–	–	9.48	9.24	9.5	–	–	10.69	Y
SN 2008ia	ESO 125-6	–	–	–	–	–	–	–	–	11.71	11.52	11.74	–	–	10.57	Y
SN 2008s1	UGC 8472	–	18.29	16.05	14.39	13.64	13.28	12.99	–	12.3	12.05	12.49	0.73	-21.25	10.32	N
SN 2009D	MCG -03-10-52	16.96	16.55	–	14.89	14.41	14.35	14.26	14.07	13.12	12.89	13.06	0.49	-20.72	9.94	Y
SN 2009F	NGC 1725	–	–	–	–	–	–	–	–	11.19	11.0	11.21	–	–	10.26	N
SN 2009Y	NGC 5728	–	–	–	–	–	–	–	–	10.02	9.83	9.99	–	–	10.37	N
SN 2009ad	UGC 3236	–	17.35	–	–	–	–	–	–	13.18	12.93	13.1	–	–	10.34	Y
SN 2009al	NGC 3425	20.18	18.29	15.85	13.99	13.17	12.78	12.54	–	12.28	12.04	12.37	0.78	-21.71	10.56	N
SN 2009an	NGC 4332	–	16.98	15.04	13.27	12.32	11.86	11.51	–	11.15	10.89	11.08	0.94	-20.63	10.15	Y
SN 2009bv	MCG +06-29-39	–	–	16.62	15.38	14.79	14.5	14.28	–	14.15	13.96	14.2	0.55	-21.21	10.24	Y
SN 2009dc	UGC 10064	–	18.86	–	–	–	–	–	–	12.44	12.24	12.49	–	–	10.41	N
SN 2009do	NGC 4537	–	–	–	–	–	–	–	–	12.63	12.4	12.47	–	–	10.61	Y
SN 2009ds	NGC 3905	–	15.24	–	–	–	–	–	–	11.83	11.62	11.72	–	–	10.55	Y
SN 2009fv	NGC 6173	19.66	18.19	–	–	–	–	–	–	11.16	10.99	11.21	–	–	11.17	N
SN 2009fw	ESO 597-6	–	19.39	–	–	–	–	–	–	11.8	11.38	11.66	–	–	10.86	N
SN 2009ig	NGC 1015	–	–	14.61	12.94	12.21	11.85	11.61	–	11.23	11.05	11.19	0.71	-20.62	10.12	Y
SN 2009im	NGC 1355	–	–	–	–	–	–	–	–	11.81	11.64	11.84	–	–	10.0	Y
SN 2009jr	IC 1320	15.93	15.47	–	–	–	–	–	–	12.52	12.31	12.51	–	–	10.0	N
SN 2009kk	2MFGC 03182	–	–	–	14.97	14.5	14.21	14.03	13.86	13.43	13.22	13.5	0.45	-19.17	9.49	Y
SN 2009kq	MCG +05-21-1	16.49	15.95	–	13.65	13.35	13.23	13.22	13.0	12.69	12.58	12.72	0.31	-20.1	9.66	Y
SN 2009le	ESO 478-6	–	–	–	13.75	13.12	13.16	12.79	12.52	11.46	11.27	11.43	0.65	-21.26	10.05	Y
SN 2009lf	2MASX J02014081+151952	–	–	17.39	15.67	14.89	14.54	14.27	–	14.34	14.04	14.21	0.71	-21.59	10.49	Y
SN 2009na	UGC 5884	16.13	15.68	15.19	14.08	13.6	13.39	13.24	–	13.12	12.96	12.92	0.49	-21.18	10.11	Y
SN 2010Y	NGC 3392	20.02	18.67	15.95	14.15	13.35	12.96	12.68	–	12.47	12.33	12.59	0.78	-19.95	9.87	Y
SN 2010ae	ESO 162- G 017	–	–	–	–	–	–	–	–	11.73	11.61	11.86	–	–	8.89	N
SN 2010ag	UGC 10679	18.77	18.05	16.95	15.34	14.55	14.15	13.86	–	13.35	13.19	13.37	0.75	-21.29	10.38	N
SN 2010ai	SDSS J125925.04+275948.2	–	21.76	19.63	17.58	16.86	16.51	16.29	–	–	–	–	0.69	-17.6	8.9	Y
SN 2010cr	NGC 5177	–	19.59	–	14.93	14.53	14.28	14.17	13.93	13.48	13.03	13.19	0.4	-20.28	9.89	Y
SN 2010dl	IC 1391	21.93	19.93	17.13	15.36	14.58	14.22	13.98	–	13.95	13.8	14.17	0.73	-20.98	10.27	N
SN 2010dm	SDSS J121133.31+471628.6	–	–	20.78	19.62	19.19	19.05	18.91	–	–	–	–	0.46	-16.54	8.01	Y
SN 2010dw	2MASX J15224062-0555214	–	–	–	15.69	15.57	15.22	15.33	15.16	14.52	14.36	14.57	0.12	-20.49	9.48	Y
SN 2010ew	CGCG 173-018	17.67	–	–	–	–	–	–	–	14.35	14.17	14.47	–	–	9.66	N

Table B6. Host Galaxy Photometry VI

SN	Host Galaxy	F	N	u	g	r	i	z	y	J	H	K_s	$g-r$	M_r	Mass[a]	LC
SN 2010ex	CGCG 475-019	17.59	17.02	16.36	15.33	14.88	14.7	14.53	–	14.42	14.35	14.61	0.46	-20.07	9.62	N
SN 2010gn	SDSS J171750.05+405252.5	–	20.06	19.15	18.1	17.62	17.38	17.38	–	–	–	–	0.45	-17.99	8.84	Y
SN 2010gy	A022712-0432	–	23.21	–	–	–	–	–	–	–	–	–	–	–	5.5	Y
SN 2010ho	PGC 1361264	18.4	18.08	15.96	15.68	15.26	15.35	15.29	–	15.35	15.94	15.59	0.3	-20.9	9.11	Y
SN 2010hs	2MASX J02253767+2445579	–	–	18.06	16.55	15.81	15.46	15.21	–	15.01	14.64	15.25	0.64	-21.92	10.56	Y
SN 2010iw	UGC 4570	17.72	–	17.56	15.81	15.25	15.09	14.95	–	16.02	16.12	16.35	0.57	-19.58	9.36	Y
SN 2010ju	UGC 3341	–	–	–	–	–	–	–	–	11.79	11.58	11.72	–	–	10.12	Y
SN 2010jv	NGC 2379	–	–	–	14.26	13.65	13.39	13.13	13.04	12.41	12.19	12.42	0.61	-20.13	9.56	N
SN 2010kg	NGC 1633	16.33	15.71	–	–	–	–	–	–	12.07	11.9	12.14	–	–	10.24	Y
SN 2011B	NGC 2655	17.42	15.28	–	12.18	11.27	10.91	10.87	10.5	8.77	8.56	8.79	0.9	-20.18	9.93	Y
SN 2011K	CSS J044530.38-072054.7	–	–	–	–	–	–	–	–	–	–	–	–	–	–	Y
SN 2011aa	UGC 3906	–	–	–	–	–	–	–	–	–	–	–	–	–	–	N
SN 2011ae	MCG -03-30-19	15.42	15.14	–	–	–	–	–	–	13.29	13.05	13.83	–	–	8.83	Y
SN 2011ao	IC 2973	15.94	15.58	15.09	14.13	13.71	13.54	13.39	–	13.54	13.31	13.58	0.42	-19.55	9.41	Y
SN 2011at	MCG -02-24-27	16.46	15.92	–	–	–	–	–	–	12.49	12.15	12.46	–	–	9.21	Y
SN 2011by	NGC 3972	–	15.24	14.41	13.08	12.38	12.02	11.84	–	11.44	11.21	11.48	0.7	-17.99	9.06	N
SN 2011de	UGC 10018	–	16.6	–	15.03	14.13	13.77	13.59	13.59	12.86	12.67	12.78	0.87	-21.36	10.31	N
SN 2011df	NGC 6801	–	15.21	–	–	–	–	–	–	12.02	11.83	12.21	–	–	10.14	Y
SN 2011fe	M101	–	–	–	–	–	–	–	–	7.42	7.19	7.36	–	–	9.27	N
SN 2011fs	UGC 11975	16.65	15.8	–	–	–	–	–	–	11.9	11.76	11.88	–	–	10.48	Y
SN 2011gf	SDSS J211222.69-074913.9	18.14	17.79	17.91	16.84	16.53	16.35	16.24	–	–	–	–	0.38	-18.89	8.94	N
SN 2011gy	UGC 02756	–	–	–	–	–	–	–	–	11.76	11.55	11.42	–	–	10.13	N
SN 2011ha	2MASX J035740.51+101013.0	–	–	–	17.46	16.72	16.38	16.17	16.13	15.99	15.13	15.37	0.7	-21.47	10.39	N
SN 2011hb	NGC 7674	15.79	15.33	14.66	13.53	13.02	12.73	12.44	–	11.79	11.58	11.62	0.55	-22.5	10.57	N
SN 2011hk	NGC 0881	16.71	15.88	–	–	–	–	–	–	11.19	11.04	11.21	–	–	10.7	N
SN 2011ho	NGC 3847	–	–	15.46	13.63	12.81	12.42	12.17	–	11.85	11.66	11.82	0.77	-22.89	11.04	N
SN 2011hr	NGC 2691	17.58	16.76	–	–	–	–	–	–	12.18	11.93	12.12	–	–	10.04	N
SN 2011io	2MASX J23024668+0848186	–	20.89	18.18	16.22	15.34	14.93	14.61	–	14.17	13.95	14.23	0.81	-20.88	10.24	N
SN 2011iu	UGC 12809	–	16.0	–	–	–	–	–	–	12.77	12.75	12.64	–	–	10.55	N
SN 2011iy	NGC 4984	16.39	15.11	–	12.63	11.79	11.43	11.2	11.03	9.59	9.38	9.58	0.84	-19.47	9.42	N
SN 2011jh	NGC 4682	–	15.09	–	–	–	–	–	–	11.47	11.18	11.44	–	–	9.93	N
SN 2012Z	NGC 1309	13.75	13.27	–	14.7	12.65	12.43	12.24	–	10.94	10.75	10.94	2.05	-19.74	9.64	N
SN 2012bh	UGC 7228	–	17.13	–	14.8	14.35	14.11	13.92	13.69	13.06	12.78	12.96	0.45	-20.82	9.92	N
SN 2012bm	UGC 8189	18.84	18.12	22.89	21.16	19.88	19.36	18.93	–	13.02	12.63	12.69	1.34	-15.3	7.93	N
SN 2012bo	NGC 4726	–	18.25	–	15.27	14.65	14.29	14.01	13.8	13.31	13.18	13.26	0.62	-20.54	9.88	N
SN 2012bp	SDSS J161812.44+362902.6	–	18.88	18.12	16.98	16.57	16.4	16.3	–	–	–	–	0.44	-18.89	9.03	N
SN 2012cg	NGC 4424	16.32	15.17	13.76	12.39	11.84	11.55	11.42	–	10.76	10.65	10.94	0.54	-17.08	8.56	N
SN 2012dn	ESO 462-G16	–	14.76	–	–	–	–	–	–	12.43	12.14	12.48	–	–	9.78	N
SN 2012em	CGCG 453-001	–	19.83	16.43	14.58	13.75	13.37	13.08	–	12.83	12.73	12.91	0.76	-22.35	10.82	N
SN 2012et	Z 476-117	17.55	17.01	15.96	14.57	13.88	13.53	13.22	–	13.12	12.98	13.18	0.66	-21.27	10.36	N

Table B7. Host Galaxy Photometry VII

SN	Host Galaxy	F	N	u	g	r	i	z	y	J	H	K_s	$g-r$	M_r	Mass^a	LC
SN 2012fb	SDSS J015051.24+330823.0	–	–	18.52	17.4	16.97	16.76	16.58	–	–	–	–	0.46	-19.15	9.14	N
SN 2012fk	2MASX J023052.08+222832.6	–	–	–	–	–	–	–	–	15.02	14.75	14.67	–	–	9.43	Y
SN 2012fm	UGC 3528	17.95	17.25	15.51	13.73	12.93	12.55	12.3	–	11.96	11.82	11.97	0.77	-21.02	10.29	N
SN 2012fr	NGC 1365	–	–	–	–	–	–	–	–	8.26	8.12	8.22	–	–	10.44	N
SN 2012gm	NGC 7580	16.38	15.81	15.18	14.31	13.83	13.68	13.47	–	12.73	12.61	12.76	0.49	-20.16	9.57	N
SN 2012go	PGC 214858	–	–	17.45	15.95	15.2	14.78	14.38	–	14.21	13.99	14.03	0.71	-20.37	10.0	N
SN 2013ar	2MASX J083745.57+492840.0	–	18.59	17.77	16.59	16.17	15.86	15.7	–	15.59	15.2	15.27	0.48	-20.7	9.79	N
SN 2013be	IC 3573	19.23	18.5	17.53	16.08	15.38	15.01	14.75	–	14.47	14.14	14.46	0.66	-22.01	10.58	N
SN 2013bo	SDSS J131729.23+424429.6	–	–	21.1	20.29	20.03	19.9	19.91	–	–	–	–	0.32	-15.96	7.63	N
SN 2013bq	SDSS J130408.44+435407.3	–	–	20.6	19.5	19.22	19.06	18.98	–	–	–	–	0.31	-17.92	8.23	N
SN 2013bs	NGC 6343	–	–	15.78	13.95	13.14	12.76	12.52	–	12.11	11.91	12.07	0.76	-22.23	10.77	Y
SN 2013bt	PGC 51271	–	19.86	16.85	14.99	14.17	13.75	13.48	–	13.19	12.93	13.23	0.76	-21.84	10.62	Y
SN 2013cb	SDSS J113501.95+160712.2	–	–	19.48	17.81	17.42	17.18	17.08	–	–	–	–	0.46	-19.55	9.15	N
SN 2013ck	SDSS J152429.19+483252.7	–	–	22.66	21.3	21.08	21.08	21.16	–	–	–	–	0.28	-15.61	7.24	N
SN 2013cs	ESO 576-17	–	16.05	–	15.21	14.83	14.66	14.54	14.23	14.57	14.07	14.14	0.38	-18.12	8.95	Y
SN 2013cv	SDSS J162243.02+185733.8	–	–	21.86	20.05	19.93	19.74	19.44	–	–	–	–	0.21	-16.05	7.48	Y
SN 2013da	2MASX J13453653-0719350	17.05	16.54	–	14.81	14.49	14.34	14.19	14.04	13.31	13.2	13.29	0.32	-20.59	9.59	N
SN 2013dy	NGC 7250	14.54	–	–	–	–	–	–	–	11.99	11.9	12.06	–	–	8.74	N
SN 2013fj	PGC 68419	17.3	16.94	16.55	15.24	14.7	14.4	14.22	–	13.81	13.53	14.04	0.56	-21.15	10.17	N
SN 2013fn	IC 1342	17.48	16.8	–	17.26	16.16	16.47	15.03	15.41	12.54	12.33	12.43	1.06	-19.21	9.35	Y
SN 2013fw	NGC 7042	–	15.29	–	–	–	–	–	–	11.19	10.96	11.2	–	–	10.72	N
SN 2015H	NGC 3464	14.96	14.54	14.95	13.29	12.51	12.12	11.84	–	11.25	11.03	11.3	0.77	-21.11	10.3	N
SNhunt175	NGC 5910	–	–	15.81	13.89	13.03	12.6	12.31	–	11.75	11.4	11.67	0.8	-23.25	11.19	N
SNhunt206	NGC 0766	–	–	15.36	13.42	12.59	12.17	11.84	–	11.56	11.31	11.59	0.79	-22.74	10.99	N
iPTF13dge	NGC 1762	–	–	–	–	–	–	–	–	11.33	11.15	11.34	–	–	10.36	Y
iPTF13dkj	Z 454-001	–	–	16.3	14.95	14.37	14.1	13.85	–	13.62	13.39	13.81	0.58	-21.64	10.38	N
iPTF13dkl	SDSS J234457.63+032337.9	19.8	19.37	18.75	17.47	16.93	16.65	16.4	–	–	–	–	0.57	-19.32	9.41	N
iPTF13dkx	SDSS J012052.56+032023.0	19.32	19.01	18.52	17.6	17.21	17.03	16.88	–	–	–	–	0.41	-18.36	8.88	Y
iPTF13ebh	NGC 890	–	17.06	–	–	–	–	–	–	10.06	9.84	10.07	–	–	10.96	Y

Table B8. Host Galaxy Photometry VIII - Overflow

SN	Galaxy	F	N	u	g	r	i	z	y	J	H	K_s	$g-r$	M_r	Mass[a]	LC
CSS121006:232854+085452 SDSS J232854.54+085452.3	Below	–	–	–	–	–	–	–	–	–	–	–	–	–	–	N
CSS121009:011101-172841 2MASX J01105973-1728527	Below	–	20.77	–	16.61	15.85	15.36	15.17	14.97	14.19	13.77	13.87	0.79	-21.03	10.06	N
CSS121114:090202+101800 SDSS J090202.19+101759.7	Below	19.59	19.35	18.77	17.87	17.57	17.37	17.24	–	–	–	–	0.37	-18.52	8.74	Y
CSS130218:092354+385837 SDSS J092355.83+385819.1	Below	–	20.51	19.92	18.22	17.48	17.13	16.91	–	–	–	–	0.68	-19.57	9.65	N
CSS130317:082848+293031 SDSS J082847+293022.6	Below	–	–	–	16.28	15.43	15.17	14.91	15.03	14.75	14.07	14.46	0.8	-22.35	10.6	N
LSQ13crf GALEXASC J031050.32+012521.1	Below	18.08	17.9	–	–	–	–	–	–	–	–	–	–	–	9.42	N
PSN J07250042+2347030 NGC 2370	Below	–	16.46	15.82	13.98	13.1	12.66	12.27	–	11.89	11.66	11.79	0.85	-21.37	10.44	N
SN 2005ch APMUKS(BJ) B141934.25+021314.0	Below	21.19	21.27	22.17	19.95	19.65	19.38	19.54	–	–	–	–	0.36	-15.72	7.7	Y
SNF20080522-000 SDSS J133647.59+050833.0	Below	–	19.36	18.59	17.45	16.95	16.65	16.54	–	–	–	–	0.53	-19.58	9.48	N
SNF20080522-011 SDSS J151959.16+045411.2	Below	–	–	24.41	22.41	21.01	20.48	20.28	–	–	–	–	1.35	-15.12	7.95	Y

Note. — This table contains SNeIa with names too long to fit in the tables in alphabetical order. All host galaxy names are in lines below the SN name. The column name "Host Galaxy" also had to be shortened to galaxy and is only kept for symmetry with the other tables.

B.2 ERROR IN HOST GALAXY PHOTOMETRY IN UV, OPTICAL, AND NIR

These tables provide the given photometric errors for the photometry listed in the tables above. All PS1 errors appear to be zero here, but they are reported as $10^3 - 10^{-5}$ mag in the catalogs and do not show up when rounding to two significant digits. All units are in magnitudes. The SNeIa are in the same order as the tables above.

Due to format constraints, we produced an "overflow" table with SNeIa/host galaxies whose names were too long to occupy a single line and fit on one page.

Table B9. Error in Host Galaxy Photometry I

Name	Host Galaxy	F_{err}	N_{err}	u_{err}	g_{err}	r_{err}	i_{err}	z_{err}	y_{err}	J_{err}	H_{err}	$K_{S,err}$	LC
LSQ12fhs	2MASX J22522347-2036373	0.07	0.04	–	0.00	0.00	0.00	0.00	0.00	0.12	0.2	0.23	Y
LSQ12fmx	2MASX J031252.93-001223.8	0.05	0.03	0.02	0.00	0.00	0.00	0.01	–	0.11	0.18	0.16	Y
LSQ12fuk	None	–	–	–	–	–	–	–	–	–	–	–	N
LSQ12gef	SDSS J014033.71+183040.3	0.12	0.09	0.04	0.00	0.00	0.00	0.01	–	0.04	0.08	0.06	N
LSQ13cmt	ESO 541- G 013	–	–	–	0.00	0.00	0.00	0.00	0.00	–	–	–	Y
LSQ13cwp	2MASX J04035024-0239275	–	–	–	0.00	0.00	0.00	0.00	0.00	0.04	0.07	0.04	Y
PS1-10w	CGCG 290-062	0.06	0.04	0.02	0.00	0.00	0.00	0.01	–	0.09	0.18	0.14	Y
PS1-12bwh	Z 205-021	–	0.01	0.01	0.00	0.00	0.00	0.00	–	0.04	0.05	0.05	N
PS1-13dkh	None	–	–	–	–	–	–	–	–	–	–	–	Y
PTF09dlc	SDSS J214630.02+062507.1	–	–	0.23	0.03	0.04	0.04	0.11	–	–	–	–	Y
PTF10bjs	MCG +09-21-83	0.06	0.02	–	–	–	–	–	–	0.12	0.22	0.18	N
PTF10hdv	SDSS J120745.44+412928.7	–	–	0.11	0.03	0.04	0.05	0.24	–	–	–	–	Y
PTF10icb	MCG +10-19-1	–	0.01	–	0.00	0.00	0.00	0.00	0.00	0.05	0.1	0.09	N
PTF10ndc	SDSS J171949.85+284201.7	–	–	–	0.00	0.00	0.00	0.00	0.00	–	–	–	Y
PTF10nlg	None	–	–	–	–	–	–	–	–	–	–	–	Y
PTF10wnm	SDSS J002203.68+270221.5	0.09	0.05	0.03	0.00	0.01	0.01	0.01	–	0.15	0.18	0.15	Y
PTF10wof	SDSS J233241.42+152131.5	0.07	0.03	0.04	0.01	0.01	0.01	0.02	–	–	–	–	Y
PTF10xyt	SDSS J231902.41+134726.2	–	–	0.05	0.01	0.01	0.01	0.02	–	–	–	–	Y
PTF11moy	SDSS J170618.19+383218.5	–	–	0.39	0.07	0.07	0.1	0.43	–	–	–	–	N
PTF11mty	SDSS J213405.07+102518.5	–	–	0.07	0.01	0.01	0.01	0.03	–	–	–	–	N
PTF11owc	2MASX J091609.97+493732.0	–	–	0.03	0.00	0.00	0.00	0.01	–	0.05	0.07	0.06	N
PTF11qmo	2MASX J10064866-0741124	0.05	–	–	0.00	0.00	0.00	0.00	0.00	0.06	0.1	0.09	N
PTF11qpc	SDSS J122005.45+092418.3	–	0.07	0.08	0.01	0.01	0.01	0.03	–	–	–	–	N
PTF11qri	LCRS B124431.1-060321	–	–	0.08	0.01	0.01	0.01	0.02	–	–	–	–	N
PTF11qzq	2MASX J07192718+5413454	–	–	–	–	–	–	–	–	–	–	–	N
PTF12iiq	2MASX J02500784-0016014	–	–	0.02	0.00	0.00	0.00	0.00	–	0.05	0.09	0.06	N
PTF12ikt	2MASX J01144386+0017100	0.02	0.01	0.02	0.00	0.00	0.00	0.01	–	0.06	0.12	0.08	N
PTF13ayw	2MASX J15393305+3205382	–	0.25	0.02	0.00	0.00	0.00	0.00	–	0.04	0.07	0.07	N
PTF13dad	None	–	–	–	–	–	–	–	–	–	–	–	Y
PTF13ddg	2MASX J004753.23+314848.1	–	–	0.07	0.01	0.00	0.00	0.01	–	0.09	0.15	0.13	Y
SN 1972E	NGC 5253	–	–	–	–	–	–	–	–	0.01	0.03	0.02	N
SN 1980N	NGC 1316	–	0.01	–	–	–	–	–	–	0.02	0.02	0.02	N
SN 1981B	NGC 4536	–	–	0.01	0.00	0.00	0.00	0.00	–	0.02	0.03	0.03	N
SN 1981D	NGC 1316	–	0.01	–	–	–	–	–	–	0.02	0.02	0.02	N
SN 1986G	NGC 5128	–	–	–	–	–	–	–	–	0.02	0.02	0.02	N
SN 1989B	NGC 3627	–	–	–	–	–	–	–	–	0.02	0.02	0.02	N
SN 1991T	NGC 4527	–	–	–	–	–	–	–	–	0.02	0.02	0.02	N
SN 1991bg	NGC 4374	0.05	0.01	–	0.00	0.00	0.00	0.00	0.00	0.02	0.02	0.02	N
SN 1998bu	NGC 3368	–	0.00	–	0.00	0.00	0.00	0.00	0.00	0.02	0.02	0.02	Y
SN 1999aa	NGC 2595	0.01	–	–	–	–	–	–	–	0.03	0.05	0.04	N

Table B10. Error in Host Galaxy Photometry II

Name	Host Galaxy	F_{err}	N_{err}	u_{err}	g_{err}	r_{err}	i_{err}	z_{err}	y_{err}	J_{err}	H_{err}	$K_{S,err}$	LC
SN 1999ac	NGC 6063	0.01	0.01	–	–	–	–	–	–	0.04	0.08	0.05	N
SN 1999cl	M88	–	–	–	–	–	–	–	–	–	–	–	Y
SN 1999cp	NGC 5468	–	–	–	–	–	–	–	–	0.02	0.06	0.03	N
SN 1999ee	IC 5179	0.02	0.01	–	–	–	–	–	–	0.01	0.02	0.01	Y
SN 1999ek	UGC 3329	–	–	–	–	–	–	–	–	0.07	0.07	0.08	Y
SN 1999gp	UGC 1993	–	–	–	–	–	–	–	–	0.02	0.05	0.03	Y
SN 2000E	NGC 6951	0.07	0.02	–	–	–	–	–	–	0.02	0.03	0.02	N
SN 2000bh	ESO 573-14	–	–	–	0.00	0.00	0.00	0.00	0.00	0.07	0.12	0.09	N
SN 2000bk	NGC 4520	0.08	0.02	–	–	–	–	–	–	0.03	0.04	0.03	N
SN 2000ca	ESO 383-32	0.07	–	–	–	–	–	–	–	0.17	0.28	0.09	N
SN 2000ce	UGC 4195	0.05	0.02	0.01	0.00	0.00	0.00	0.00	–	0.03	0.04	0.03	Y
SN 2000cx	NGC 524	0.09	0.03	–	–	–	–	–	–	0.01	0.01	0.01	N
SN 2001ba	MCG -05-28-1	0.1	0.04	–	–	–	–	–	–	0.03	0.05	0.03	N
SN 2001bt	IC 4830	–	0.02	–	–	–	–	–	–	0.02	0.03	0.03	N
SN 2001cn	IC 4758	–	0.02	–	–	–	–	–	–	0.04	0.06	0.06	N
SN 2001cz	NGC 4679	–	–	–	–	–	–	–	–	0.02	0.03	0.02	N
SN 2001el	NGC 1448	0.01	0.00	–	–	–	–	–	–	0.02	0.03	0.02	N
SN 2002bo	NGC 3190	0.08	0.02	–	–	–	–	–	–	0.02	0.02	0.02	Y
SN 2002cv	NGC 3190	0.08	0.02	–	–	–	–	–	–	0.02	0.02	0.02	N
SN 2002dj	NGC 5018	–	0.01	–	–	–	–	–	–	0.01	0.01	0.01	Y
SN 2002fk	NGC 1309	0.01	0.01	–	0.00	0.00	0.00	0.00	–	0.02	0.03	0.02	N
SN 2003cg	NGC 3169	–	–	–	0.00	0.00	0.00	0.00	0.00	0.02	0.02	0.02	N
SN 2003du	UGC 9391	–	0.01	0.02	0.00	0.00	0.00	0.02	–	–	–	–	Y
SN 2003gs	NGC 936	0.01	–	–	0.00	0.00	0.00	0.00	0.00	0.02	0.03	0.02	N
SN 2003hv	NGC 1201	0.08	0.02	–	–	–	–	–	–	0.01	0.02	0.01	N
SN 2004S	MCG -05-16-21	–	–	–	–	–	–	–	–	0.03	0.06	0.04	Y
SN 2004ef	UGC 12158	–	0.01	0.02	0.00	0.00	0.00	0.00	–	0.05	0.09	0.06	Y
SN 2004eo	NGC 6928	0.15	0.04	–	–	–	–	–	–	0.02	0.03	0.03	Y
SN 2004ey	UGC 11816	0.01	0.01	0.02	0.00	0.00	0.00	0.01	–	0.06	0.12	0.08	Y
SN 2004gs	MCG +03-22-20	0.09	0.04	0.01	0.00	0.00	0.00	0.00	–	0.03	0.05	0.04	Y
SN 2004gu	FGC 175A	0.06	0.09	0.08	0.01	0.01	0.01	0.01	–	0.11	0.16	0.11	Y
SN 2005A	NGC 958	0.01	0.00	–	–	–	–	–	–	0.01	0.02	0.01	Y
SN 2005M	NGC 2930	0.02	0.01	0.01	0.00	0.00	0.00	0.01	–	0.06	0.09	0.09	Y
SN 2005ag	2MASX J14564322+0919361	–	–	–	0.00	0.00	0.00	0.00	0.00	0.09	0.11	0.11	Y
SN 2005al	NGC 5304	0.06	0.01	–	0.00	0.00	0.00	0.00	0.00	0.02	0.03	0.03	Y
SN 2005am	NGC 2811	–	–	–	0.00	0.00	0.00	0.00	0.00	0.01	0.01	0.01	Y
SN 2005ao	NGC 6462	0.08	0.04	0.01	0.00	0.00	0.00	0.00	–	0.03	0.04	0.03	Y
SN 2005bl	NGC 4070	–	0.12	0.01	0.00	0.00	0.00	0.00	–	0.02	0.03	0.02	N
SN 2005bo	NGC 4708	0.04	–	–	0.00	0.00	0.00	–	0.00	0.03	0.05	0.04	Y
SN 2005cf	MCG -01-39-3	0.01	0.00	–	–	–	–	–	–	0.04	0.07	0.05	Y

Table B11. Error in Host Galaxy Photometry III

Name	Host Galaxy	F_{err}	N_{err}	u_{err}	g_{err}	r_{err}	i_{err}	z_{err}	y_{err}	J_{err}	H_{err}	$K_{S,err}$	LC
SN 2005el	NGC 1819	–	–	–	–	–	–	–	–	0.02	0.03	0.03	Y
SN 2005eq	MCG -01-9-6	0.02	0.01	0.01	0.00	0.00	0.00	0.00	–	0.04	0.06	0.04	Y
SN 2005eu	NSF J022743.32+281037.6	–	–	–	–	–	–	–	–	–	–	–	Y
SN 2005hc	MCG +00-6-3	–	0.01	0.02	0.00	0.00	0.00	0.01	–	0.07	0.11	0.08	Y
SN 2005hj	SDSS J012648.45-011417.3	–	–	0.07	0.02	0.01	0.01	0.03	–	–	–	–	Y
SN 2005hk	UGC 272	0.02	0.01	0.01	0.00	0.00	0.00	0.01	–	0.15	0.2	0.09	N
SN 2005iq	MCG -03-1-8	0.07	0.05	–	0.00	0.00	0.00	0.00	0.00	0.03	0.06	0.04	Y
SN 2005kc	NGC 7311	–	0.01	0.00	0.00	0.00	0.00	0.00	–	0.01	0.01	0.01	Y
SN 2005ke	NGC 1371	0.06	0.02	–	0.00	0.00	0.00	0.00	0.00	0.02	0.04	0.03	N
SN 2005ki	NGC 3332	–	–	–	–	–	–	–	–	0.02	0.04	0.03	Y
SN 2005ku	SDSS J225942.66-000048.8	0.02	0.01	0.02	0.00	0.00	0.00	0.01	–	0.08	0.16	0.14	N
SN 2005ls	MCG +07-7-1	0.05	0.03	0.01	0.00	0.00	0.00	0.00	–	0.04	0.06	0.06	N
SN 2005na	UGC 3634	–	–	–	–	–	–	–	–	0.02	0.04	0.03	Y
SN 2006D	MCG -01-33-34	0.03	0.01	–	–	–	–	–	–	0.03	0.05	0.03	Y
SN 2006E	NGC 5338	–	–	0.01	0.00	0.00	0.00	0.00	–	0.05	0.1	0.06	N
SN 2006N	MCG +11-8-12	–	0.03	–	–	–	–	–	–	0.01	0.02	0.02	Y
SN 2006X	NGC 4321	–	–	–	–	–	–	–	–	–	–	–	Y
SN 2006ac	NGC 4619	0.02	0.01	0.02	0.00	0.01	0.02	16.96	–	0.02	0.03	0.03	Y
SN 2006ax	NGC 3663	0.04	0.01	–	–	–	–	–	–	0.04	0.07	0.04	Y
SN 2006bd	UGC 6609	0.09	0.03	0.01	0.00	0.00	0.00	0.00	–	0.03	0.05	0.03	N
SN 2006bh	NGC 7329	–	0.00	–	–	–	–	–	–	0.02	0.03	0.02	Y
SN 2006br	NGC 5185	–	–	–	–	–	–	–	–	0.02	0.04	0.03	Y
SN 2006bt	CGCG 108-013	–	–	0.01	0.00	0.00	0.00	0.00	–	0.03	0.05	0.03	N
SN 2006cp	UGC 7357	0.05	–	0.01	0.00	0.00	0.00	0.01	–	0.06	0.09	0.07	Y
SN 2006cz	MCG -01-38-2	–	0.02	–	–	–	–	–	–	0.07	0.1	0.08	N
SN 2006ej	NGC 191	–	0.04	0.01	0.00	0.00	0.00	0.00	–	0.02	0.04	0.03	Y
SN 2006eq	SDSS J12837.60+011348.6	0.08	0.05	0.05	0.01	0.00	0.00	0.01	–	0.13	0.16	0.13	Y
SN 2006et	NGC 232	–	0.07	–	–	–	–	–	–	0.02	0.02	0.02	Y
SN 2006ev	UGC 11758	–	–	–	0.00	0.00	0.00	0.00	0.00	0.02	0.03	0.03	Y
SN 2006gj	UGC 2650	–	–	–	0.00	0.00	0.00	0.00	0.00	0.04	0.06	0.06	Y
SN 2006gr	UGC 12071	–	–	0.02	0.00	0.00	0.00	0.00	–	–	–	–	N
SN 2006gt	2MASX J00561810-0137327	–	0.16	0.06	0.01	0.00	0.00	0.01	–	0.12	0.21	0.17	Y
SN 2006hb	MCG -04-12-34	–	–	–	0.00	0.00	0.00	0.00	0.00	0.03	0.05	0.03	Y
SN 2006hx	PGC 73820	–	0.05	–	0.00	0.00	0.00	0.00	0.00	0.08	0.1	0.09	Y
SN 2006is	ESO 486- G 049	–	–	–	–	–	–	–	–	–	–	–	Y
SN 2006kf	UGC 2829	–	–	0.01	0.00	0.00	0.00	0.00	–	0.02	0.03	0.03	Y
SN 2006le	UGC 3218	0.11	0.04	–	–	–	–	–	–	0.02	0.02	0.02	Y
SN 2006lf	UGC 3108	–	–	–	–	–	–	–	–	0.04	0.03	0.03	Y
SN 2006lu	2MASX J09151727-2536001	0.19	0.11	–	–	–	–	–	–	0.12	0.19	0.15	N
SN 2006mq	ESO 494-G26	–	–	–	–	–	–	–	–	0.03	0.04	0.03	N

Table B12. Error in Host Galaxy Photometry IV

Name	Host Galaxy	F_{err}	N_{err}	u_{err}	g_{err}	r_{err}	i_{err}	z_{err}	y_{err}	J_{err}	H_{err}	$K_{S,err}$	LC
SN 2006mr	NGC 1316	–	0.01	–	–	–	–	–	–	0.02	0.02	0.02	N
SN 2006ob	UGC 1333	0.02	0.02	0.02	0.00	0.00	0.00	0.00	–	0.03	0.06	0.05	N
SN 2006os	UGC 2384	–	–	–	0.00	0.00	0.00	0.00	0.00	0.03	0.04	0.04	Y
SN 2006ot	ESO 544-G31	–	0.2	–	0.00	0.00	0.00	0.00	0.00	0.03	0.05	0.04	N
SN 2007A	NGC 105	–	–	–	–	–	–	–	–	–	–	–	Y
SN 2007N	MCG -01-33-12	0.08	0.03	0.01	0.00	0.00	0.00	0.00	–	0.04	0.08	0.05	N
SN 2007S	UGC 5378	0.03	0.01	0.01	0.00	0.00	0.00	0.00	–	0.04	0.07	0.05	Y
SN 2007af	NGC 5584	–	0.01	0.01	0.00	0.00	0.00	0.00	–	0.02	0.07	0.02	Y
SN 2007ai	MCG -04-38-4	–	–	–	–	–	–	–	–	0.04	0.06	0.04	Y
SN 2007as	ESO 18-G18	–	–	–	–	–	–	–	–	0.03	0.06	0.04	Y
SN 2007ax	NGC 2577	–	–	–	–	–	–	–	–	0.01	0.02	0.01	N
SN 2007ba	UGC 9798	0.04	0.02	–	0.00	0.00	0.00	0.00	0.00	–	–	–	Y
SN 2007bc	UGC 6332	–	–	0.01	0.00	0.00	0.00	0.00	–	0.03	0.04	0.03	Y
SN 2007bd	UGC 4455	0.07	0.04	0.01	0.00	0.00	0.00	0.00	–	0.06	0.08	0.07	Y
SN 2007bm	NGC 3672	–	0.01	0.00	0.00	0.00	0.00	0.00	–	0.01	0.01	0.01	Y
SN 2007ca	MCG -02-34-61	–	0.03	–	–	–	–	–	–	0.04	0.08	0.05	Y
SN 2007co	MCG +05-43-16	–	–	–	–	–	–	–	–	0.04	0.07	0.04	N
SN 2007cq	2MASX J22144070+0504435	0.06	0.04	0.02	0.00	0.00	0.00	0.01	–	0.1	0.16	0.16	Y
SN 2007fb	UGC 12859	–	0.04	–	0.00	0.00	0.00	0.00	0.00	0.03	0.05	0.04	N
SN 2007hx	SDSS J020626.74-005400.4	–	–	0.08	0.01	0.01	0.01	0.02	–	–	–	–	Y
SN 2007if	J011051.37+152739	–	–	–	–	–	–	–	–	–	–	–	N
SN 2007jg	SDSS J032950.83+000316.0	0.07	0.04	0.1	0.02	0.02	0.02	0.07	–	–	–	–	Y
SN 2007jh	CGCG 391-014	–	–	0.01	0.00	0.00	0.00	0.00	–	0.04	0.06	0.04	N
SN 2007le	NGC 7721	–	0.00	–	–	–	–	–	–	0.02	0.03	0.02	Y
SN 2007nq	UGC 595	0.07	0.04	0.02	0.00	0.00	0.00	0.00	–	0.04	0.06	0.04	Y
SN 2007on	NGC 1404	–	0.00	–	–	–	–	–	–	0.02	0.02	0.02	Y
SN 2007qe	NSF J235412.09+272432.3	0.07	0.04	0.07	0.01	0.01	0.01	0.03	–	–	–	–	N
SN 2007rx	BATC J234012.05+272512.23	–	–	–	–	–	–	–	–	–	–	–	N
SN 2007sr	NGC 4038	–	–	–	–	–	–	–	–	–	–	–	Y
SN 2008A	NGC 634	0.08	0.04	–	0.00	0.00	0.00	0.00	0.00	0.01	0.02	0.01	N
SN 2008C	UGC 3611	–	–	–	–	–	–	–	–	0.03	0.03	0.03	Y
SN 2008R	NGC 1200	0.12	0.06	–	–	–	–	–	–	0.02	0.03	0.02	Y
SN 2008Z	SDSS J094315.36+361709.2	–	–	0.05	0.01	0.01	0.01	0.02	–	–	–	–	Y
SN 2008ae	IC 577	0.04	0.02	0.01	0.00	0.00	0.00	0.00	–	0.05	0.09	0.06	Y
SN 2008af	UGC 9640	–	0.04	0.01	0.00	0.00	0.00	0.00	–	0.02	0.04	0.03	N
SN 2008bc	KK 1524	–	–	–	–	–	–	–	–	0.05	0.07	0.04	Y
SN 2008bq	ESO 308-G25	–	–	–	–	–	–	–	–	0.04	0.06	0.04	Y
SN 2008fp	ESO 428-G14	–	0.07	–	–	–	–	–	–	0.01	0.02	0.01	Y
SN 2008fr	SDSS J011149.19+143826.5	–	–	0.14	0.02	0.02	0.03	0.12	–	–	–	–	Y
SN 2008fv	NGC 3147	0.00	0.00	–	–	–	–	–	–	0.01	0.02	0.02	Y

Table B13. Error in Host Galaxy Photometry V

Name	Host Galaxy	F_{err}	N_{err}	u_{err}	g_{err}	r_{err}	i_{err}	z_{err}	y_{err}	J_{err}	H_{err}	$K_{S,err}$	LC
SN 2008fx	2MASX J02113233+2353074	–	–	0.05	0.01	0.00	0.00	0.01	–	0.11	0.14	0.09	Y
SN 2008gb	UGC 2427	–	0.13	–	–	–	–	–	–	0.06	0.09	0.08	Y
SN 2008gl	UGC 881	0.09	0.05	0.01	0.00	0.00	0.00	0.00	–	0.04	0.06	0.05	Y
SN 2008gp	MCG +00-9-74	–	–	–	0.00	0.00	0.00	0.00	0.00	0.04	0.06	0.06	Y
SN 2008ha	UGC 12682	0.03	0.01	–	–	–	–	–	–	–	–	–	N
SN 2008hm	2MFGC 02845	–	–	–	–	–	–	–	–	0.05	0.06	0.06	Y
SN 2008hs	NGC 910	–	0.11	–	–	–	–	–	–	0.02	0.03	0.02	Y
SN 2008hv	NGC 2765	0.07	0.02	0.00	0.00	0.00	0.00	0.00	–	0.02	0.03	0.02	Y
SN 2008hy	IC 334	0.16	–	–	–	–	–	–	–	0.01	0.02	0.02	Y
SN 2008ia	ESO 125-6	–	–	–	–	–	–	–	–	0.02	0.04	0.03	Y
SN 2008s1	UGC 8472	–	0.02	0.01	0.00	0.00	0.00	0.00	–	0.04	0.07	0.04	N
SN 2009D	MCG -03-10-52	0.04	0.02	–	0.00	0.00	0.00	0.00	0.00	0.05	0.07	0.05	Y
SN 2009F	NGC 1725	–	–	–	–	–	–	–	–	0.01	0.02	0.02	N
SN 2009Y	NGC 5728	–	–	–	–	–	–	–	–	0.02	0.03	0.02	N
SN 2009ad	UGC 3236	–	0.08	–	–	–	–	–	–	0.04	0.05	0.05	Y
SN 2009al	NGC 3425	0.1	0.02	0.01	0.00	0.00	0.00	0.00	–	0.02	0.04	0.03	N
SN 2009an	NGC 4332	–	0.01	0.01	0.00	0.00	0.00	0.00	–	0.02	0.02	0.02	Y
SN 2009bv	MCG +06-29-39	–	–	0.01	0.00	0.00	0.00	0.01	–	0.06	0.1	0.07	Y
SN 2009dc	UGC 10064	–	0.14	–	–	–	–	–	–	0.02	0.03	0.03	N
SN 2009do	NGC 4537	–	–	–	–	–	–	–	–	0.05	0.05	0.05	Y
SN 2009ds	NGC 3905	–	0.01	–	–	–	–	–	–	0.04	0.07	0.04	Y
SN 2009fv	NGC 6173	0.02	0.00	–	–	–	–	–	–	0.02	0.03	0.02	N
SN 2009fw	ESO 597-6	–	0.17	–	–	–	–	–	–	0.03	0.04	0.03	N
SN 2009ig	NGC 1015	–	–	0.01	0.00	0.00	0.00	0.00	–	0.02	0.03	0.02	Y
SN 2009im	NGC 1355	–	–	–	–	–	–	–	–	0.02	0.03	0.02	Y
SN 2009jr	IC 1320	0.04	0.02	–	–	–	–	–	–	0.03	0.04	0.04	N
SN 2009kk	2MFGC 03182	–	–	–	0.00	0.00	0.00	0.00	0.00	0.04	0.06	0.04	Y
SN 2009kq	MCG +05-21-1	0.01	0.01	–	0.00	0.00	0.00	0.00	0.00	0.03	0.04	0.04	Y
SN 2009le	ESO 478-6	–	–	–	0.00	0.00	0.00	0.00	0.00	0.01	0.02	0.02	Y
SN 2009lf	2MASX J02014081+151952	–	–	0.02	0.00	0.00	0.00	0.00	–	0.07	0.12	0.07	Y
SN 2009na	UGC 5884	0.03	0.01	0.01	0.00	0.00	0.00	0.00	–	0.05	0.07	0.07	Y
SN 2010Y	NGC 3392	0.06	0.02	0.01	0.00	0.00	0.00	0.00	–	0.02	0.04	0.03	Y
SN 2010ae	ESO 162- G 017	–	–	–	–	–	–	–	–	0.03	0.04	0.03	N
SN 2010ag	UGC 10679	0.1	0.06	0.01	0.00	0.00	0.00	0.00	–	0.03	0.05	0.04	N
SN 2010ai	SDSS J125925.04+275948.2	–	0.17	0.1	0.01	0.01	0.01	0.02	–	–	–	–	Y
SN 2010cr	NGC 5177	–	0.2	–	0.00	0.00	0.00	0.00	0.00	0.06	0.08	0.06	Y
SN 2010dl	IC 1391	0.2	0.05	0.02	0.00	0.00	0.00	0.00	–	0.04	0.09	0.07	N
SN 2010dm	SDSS J121133.31+471628.6	–	–	0.12	0.02	0.02	0.02	0.08	–	–	–	–	Y
SN 2010dw	2MASX J15224062-0555214	–	–	–	0.00	0.00	0.00	0.00	0.00	0.06	0.13	0.07	Y
SN 2010ew	CGCG 173-018	0.14	–	–	–	–	–	–	–	0.07	0.12	0.07	N

Table B14. Error in Host Galaxy Photometry VI

Name	Host Galaxy	F_{err}	N_{err}	u_{err}	g_{err}	r_{err}	i_{err}	z_{err}	y_{err}	J_{err}	H_{err}	$K_{S,err}$	LC
SN 2010ex	CGCG 475-019	0.06	0.03	0.01	0.00	0.00	0.00	0.01	–	0.06	0.11	0.09	N
SN 2010gn	SDSS J171750.05+405252.5	–	0.11	0.11	0.02	0.02	0.02	0.07	–	–	–	–	Y
SN 2010gy	A022712-0432	–	0.2	–	–	–	–	–	–	–	–	–	Y
SN 2010ho	PGC 1361264	0.07	0.04	0.00	0.00	0.00	0.00	0.00	–	0.15	0.29	0.00	Y
SN 2010hs	2MASX J02253767+2445579	–	–	0.04	0.00	0.00	0.00	0.01	–	0.07	0.16	0.07	Y
SN 2010iw	UGC 4570	0.05	–	0.05	0.01	0.01	0.01	0.02	–	0.12	0.29	0.2	Y
SN 2010ju	UGC 3341	–	–	–	–	–	–	–	–	0.05	0.06	0.04	Y
SN 2010jv	NGC 2379	–	–	–	0.00	0.00	0.00	0.00	0.00	0.02	0.04	0.03	N
SN 2010kg	NGC 1633	0.08	0.04	–	–	–	–	–	–	0.02	0.04	0.03	Y
SN 2011B	NGC 2655	0.07	0.02	–	0.00	0.00	0.00	0.00	0.00	0.02	0.03	0.02	Y
SN 2011K	CSS J044530.38-072054.7	–	–	–	–	–	–	–	–	–	–	–	Y
SN 2011aa	UGC 3906	–	–	–	–	–	–	–	–	–	–	–	N
SN 2011ae	MCG -03-30-19	0.03	0.02	–	–	–	–	–	–	0.06	0.13	0.04	Y
SN 2011ao	IC 2973	0.03	0.02	0.01	0.00	0.00	0.00	0.01	–	0.05	0.08	0.07	Y
SN 2011at	MCG -02-24-27	0.03	0.02	–	–	–	–	–	–	0.05	0.1	0.04	Y
SN 2011by	NGC 3972	–	0.00	0.01	0.00	0.00	0.00	0.00	–	0.01	0.02	0.01	N
SN 2011de	UGC 10018	–	0.01	–	0.00	0.00	0.00	0.00	0.00	0.05	0.06	0.05	N
SN 2011df	NGC 6801	–	0.02	–	–	–	–	–	–	0.04	0.05	0.04	Y
SN 2011fe	M101	–	–	–	–	–	–	–	–	0.03	0.05	0.04	N
SN 2011fs	UGC 11975	0.06	0.02	–	–	–	–	–	–	0.02	0.04	0.03	Y
SN 2011gf	SDSS J211222.69-074913.9	0.02	0.02	0.04	0.01	0.01	0.01	0.02	–	–	–	–	N
SN 2011gy	UGC 02756	–	–	–	–	–	–	–	–	0.01	0.04	0.13	N
SN 2011ha	2MASX J035740.51+101013.0	–	–	–	0.00	0.00	0.00	0.00	0.00	0.16	0.13	0.11	N
SN 2011hb	NGC 7674	0.02	0.01	0.01	0.00	0.00	0.00	0.00	–	0.03	0.04	0.05	N
SN 2011hk	NGC 0881	0.07	0.03	–	–	–	–	–	–	0.02	0.04	0.03	N
SN 2011ho	NGC 3847	–	–	0.01	0.00	0.00	0.00	0.00	–	0.02	0.03	0.03	N
SN 2011hr	NGC 2691	0.06	0.03	–	–	–	–	–	–	0.02	0.03	0.03	N
SN 2011io	2MASX J23024668+0848186	–	0.27	0.03	0.00	0.00	0.00	0.00	–	0.04	0.06	0.05	N
SN 2011iu	UGC 12809	–	0.05	–	–	–	–	–	–	0.08	0.1	0.1	N
SN 2011iy	NGC 4984	0.05	0.01	–	0.00	0.00	0.00	0.00	0.00	0.01	0.02	0.01	N
SN 2011jh	NGC 4682	–	0.01	–	–	–	–	–	–	0.01	0.02	0.02	N
SN 2012Z	NGC 1309	0.01	0.01	–	0.00	0.00	0.00	0.00	–	0.02	0.03	0.02	N
SN 2012bh	UGC 7228	–	0.00	–	0.00	0.00	0.00	0.00	0.00	0.04	0.05	0.04	N
SN 2012bm	UGC 8189	0.04	0.01	0.41	0.05	0.02	0.02	0.04	–	0.04	0.04	0.04	N
SN 2012bo	NGC 4726	–	0.05	–	0.00	0.00	0.00	0.00	0.00	0.04	0.06	0.05	N
SN 2012bp	SDSS J161812.44+362902.6	–	0.02	0.03	0.01	0.01	0.01	0.03	–	–	–	–	N
SN 2012cg	NGC 4424	0.01	0.00	0.00	0.00	0.00	0.00	0.00	–	0.02	0.04	0.03	N
SN 2012dn	ESO 462-G16	–	0.01	–	–	–	–	–	–	0.04	0.07	0.05	N
SN 2012em	CGCG 453-001	–	0.14	0.01	0.00	0.00	0.00	0.00	–	0.03	0.05	0.04	N
SN 2012et	Z 476-117	0.06	0.03	0.01	0.00	0.00	0.00	0.00	–	0.04	0.05	0.05	N

Table B15. Error in Host Galaxy Photometry VII

Name	Host Galaxy	F_{err}	N_{err}	u_{err}	g_{err}	r_{err}	i_{err}	z_{err}	y_{err}	J_{err}	H_{err}	$K_{S,err}$	LC
SN 2012fb	SDSS J015051.24+330823.0	–	–	0.05	0.01	0.01	0.01	0.03	–	–	–	–	N
SN 2012fk	2MASX J023052.08+222832.6	–	–	–	–	–	–	–	–	0.05	0.1	0.06	Y
SN 2012fm	UGC 3528	0.06	0.03	0.01	0.00	0.00	0.00	0.00	–	0.02	0.04	0.03	N
SN 2012fr	NGC 1365	–	–	–	–	–	–	–	–	0.03	0.04	0.03	N
SN 2012gm	NGC 7580	0.03	0.01	0.01	0.00	0.00	0.00	0.00	–	0.03	0.05	0.04	N
SN 2012go	PGC 214858	–	–	0.03	0.00	0.00	0.00	0.01	–	0.04	0.07	0.04	N
SN 2013ar	2MASX J083745.57+492840.0	–	0.02	0.02	0.00	0.00	0.00	0.01	–	0.12	0.14	0.12	N
SN 2013be	IC 3573	0.06	0.01	0.02	0.00	0.00	0.00	0.01	–	0.08	0.13	0.08	N
SN 2013bo	SDSS J131729.23+424429.6	–	–	0.16	0.03	0.03	0.05	0.15	–	–	–	–	N
SN 2013bq	SDSS J130408.44+435407.3	–	–	0.09	0.02	0.02	0.02	0.05	–	–	–	–	N
SN 2013bs	NGC 6343	–	–	0.01	0.00	0.00	0.00	0.00	–	0.03	0.04	0.04	Y
SN 2013bt	PGC 51271	–	0.06	0.01	0.00	0.00	0.00	0.00	–	0.03	0.05	0.04	Y
SN 2013cb	SDSS J113501.95+160712.2	–	–	0.08	0.01	0.01	0.01	0.03	–	–	–	–	N
SN 2013ck	SDSS J152429.19+483252.7	–	–	0.61	0.08	0.09	0.15	0.56	–	–	–	–	N
SN 2013cs	ESO 576-17	–	0.04	–	0.00	0.00	0.00	0.00	0.00	0.12	0.15	0.12	Y
SN 2013cv	SDSS J162243.02+185733.8	–	–	0.39	0.04	0.04	0.05	0.16	–	–	–	–	Y
SN 2013da	2MASX J13453653-0719350	0.05	0.03	–	0.00	0.00	0.00	0.00	0.00	0.04	0.06	0.04	N
SN 2013dy	NGC 7250	0.02	–	–	–	–	–	–	–	0.03	0.05	0.04	N
SN 2013fj	PGC 68419	0.06	0.03	0.02	0.00	0.00	0.00	0.01	–	0.06	0.13	0.05	N
SN 2013fn	IC 1342	0.05	0.02	–	0.00	0.00	0.00	0.00	0.00	0.02	0.03	0.03	Y
SN 2013fw	NGC 7042	–	0.02	–	–	–	–	–	–	0.02	0.03	0.02	N
SN 2015H	NGC 3464	0.02	0.01	0.01	0.00	0.00	0.00	0.00	–	0.03	0.05	0.03	N
SNhunt175	NGC 5910	–	–	0.01	0.00	0.00	0.00	0.00	–	0.03	0.04	0.02	N
SNhunt206	NGC 0766	–	–	0.01	0.00	0.00	0.00	0.00	–	0.02	0.04	0.03	N
iPTF13dge	NGC 1762	–	–	–	–	–	–	–	–	0.03	0.04	0.03	Y
iPTF13dkj	Z 454-001	–	–	0.02	0.00	0.00	0.00	0.00	–	0.05	0.1	0.05	N
iPTF13dkl	SDSS J234457.63+032337.9	0.1	0.07	0.06	0.01	0.01	0.01	0.02	–	–	–	–	N
iPTF13dkx	SDSS J012052.56+032023.0	0.02	0.02	0.06	0.01	0.01	0.02	0.04	–	–	–	–	Y
iPTF13ebh	NGC 890	–	0.08	–	–	–	–	–	–	0.01	0.02	0.01	Y

Table B16. Error in Host Galaxy Photometry VIII - Overflow

Name	Host Galaxy	F_{err}	N_{err}	u_{err}	g_{err}	r_{err}	i_{err}	z_{err}	y_{err}	J_{err}	H_{err}	$K_{S,err}$	LC
CSS121006:232854+085452 SDSS J232854.54+085452.3	Below	–	–	–	–	–	–	–	–	–	–	–	N
CSS121009:011101-172841 2MASX J01105973-1728527	Below	–	0.23	–	0.00	0.00	0.00	0.00	0.00	0.06	0.08	0.06	N
CSS121114:090202+101800 SDSS J090202.19+101759.7	Below	0.04	0.03	0.05	0.01	0.01	0.01	0.04	–	–	–	–	Y
CSS130218:092354+385837 SDSS J092355.83+385819.1	Below	–	0.17	0.08	0.01	0.01	0.01	0.02	–	–	–	–	N
CSS130317:082848+293031 SDSS J082847+293022.6	Below	–	–	–	0.00	0.00	0.00	0.00	0.00	0.08	0.1	0.06	N
LSQ13crf GALEXASC J031050.32+012521.1	Below	0.09	0.06	–	–	–	–	–	–	–	–	–	N
PSN J07250042+2347030 NGC 2370	Below	–	0.02	0.01	0.00	0.00	0.00	0.00	–	0.02	0.03	0.02	N
SN 2005ch APMUKS(BJ) B141934.25+021314.0	Below	0.13	0.12	0.78	0.04	0.05	0.06	0.29	–	–	–	–	Y
SNF20080522-000 SDSS SDSS J133647.59+050833.0	Below	–	0.05	0.05	0.01	0.01	0.01	0.03	–	–	–	–	N
SNF20080522-011 SDSS J151959.16+045411.2	Below	–	–	1.13	0.14	0.06	0.05	0.18	–	–	–	–	Y

Note. — This table contains SNeIa with names too long to fit in the tables in alphabetical order. All host galaxy names are in lines below the SN name. The column name “Host Galaxy” also had to be shortened to galaxy and is only kept for symmetry with the other tables.

B.3 *H*-BAND AND OPTICAL LIGHTCURVE FITS

We here include all of the lightcurve fits from *H*-band "max_model" and optical "EBV_model2" distance modulus (DM) from SNooPy. Included is Name, time of *B*-band maximum, error on time of *B*-band maximum, redshift, error in redshift, apparent magnitude in *H*-band at maximum, error in apparent magnitude in *H*-band at maximum, number of *H*-band observations, *H*-band stretch parameter, error on *H*-band stretch parameter, optical DM at maximum, error in optical DM at maximum, number of optical observations, optical DM stretch parameter, error on optical DM stretch parameter, Reference code (paper it was presented in), Sample (sample code given by W14 and updated here).

The sample names are used for the divisions in the analysis. Some SNe Ia were observed by multiple projects, but we assign each SNe Ia to a single sample to quote dispersions and distributions in the analysis. Due to format constraints, 2 SNeIa have the references codes as a footnote and we produced an "overflow" table with SNeIa whose names were too long to occupy a single line and fit on one page.

Reference codes: J99: Jha et al. (1999); H00: Hernandez et al. (2000); K00: Krisciunas et al. (2000); K04a: Krisciunas et al. (2004a); K04b: Krisciunas et al. (2004b); Ph06: Phillips et al. (2006); Pa07a: Pastorello et al. (2007b); Pa07b: Pastorello et al. (2007a); St07: Stanishev et al. (2007); F15: Wood-Vasey et al. (2008); C10: Contreras et al. (2010); S11: Stritzinger et al. (2011); BN12: Barone-Nugent et al. (2012); W14: Weyant et al. (2014); F15: Friedman et al. (2015); W17: Weyant et al. (2017).

Table B17. SN H-band “max_model” and Optical “EBV_model2” DM fits I

Name	$t_{\rm max}$ MJD	$t^{\rm err}_{\rm max}$ MJD	$z_{\rm cmb}$	$z^{\rm err}_{\rm cmb}$	$H_{\rm max}$ mag	$H^{\rm err}_{\rm max}$ mag	N_H	st$_H$	st$^{\rm err}_H$	DM mag	DM$^{\rm err}$ mag	$N_{\rm DM}$	st$_{\rm DM}$	st$^{\rm err}_{\rm DM}$	Ref.	Samp.
LSQ12fhs	56206.0	0.07	0.0329	0.0003	17.4483	0.1352	4.0	0.9181	0.0476						W17	W17
LSQ12fmx	56227.0	0.46	0.0669	0.0006	19.1430	0.1207	4.0	0.8803	0.0499						W17	W17
LSQ13cmt	56582.0	0.0	0.0569	0.0005	18.0018	0.1613	3.0	0.6844	0.2002						W17	W17
LSQ13cwp	56606.0	0.07	0.0669	0.0006	18.4127	0.1502	3.0	0.9107	0.0481	37.0528	0.0910	17.0	1.0031	0.0597	W17	W17
PS1-10w	55248.0	0.0	0.0322	0.0001	17.3397	0.0964	10.0	0.9146	0.0127						F15	F15
PS1-13dkh	56572.0	0.07	0.0300	0.0003	17.0604	0.1156	3.0	0.9379	0.0414	34.9733	1.4070	12.0	1.4570	2.7834	W17	W17
PTF09dlc	55073.0	0.0	0.0678	0.0001	18.8505	0.0663	4.0	0.7482	0.0490						BN12	BN12
PTF10hdv	55344.0	0.0	0.0534	0.0001	18.5913	0.0243	4.0	1.0687	0.0634						BN12	BN12
PTF10ndc	55390.0	0.0	0.0818	0.0001	19.3746	0.0370	4.0	1.0867	0.0678						BN12	BN12
PTF10nlg	55391.0	0.0	0.0560	0.0001	18.6462	0.0407	5.0	1.1070	0.0832						BN12	BN12
PTF10wnm	55477.0	0.0	0.0656	0.0001	18.9434	0.0103	4.0	0.9826	0.0327						BN12	BN12
PTF10wof	55474.0	0.0	0.0526	0.0001	18.5467	0.0265	4.0	1.0045	0.0517						BN12	BN12
PTF10xyt	55493.0	0.0	0.0496	0.0001	18.4819	0.0796	4.0	1.5246	0.5405						BN12	BN12
PTF11moy	55824.0	0.07	0.0600	0.0001	19.3100	0.01	1.0	0.955	0.0						W17	W17
PTF11qmo	55894.0	0.46	0.0564	0.0001	18.3449	0.0730	2.0	1.1738	0.0743						W17	W17
PTF11qri	55897.0	0.46	0.0550	0.0001	19.2177	0.3422	2.0	1.3501	0.2912						W17	W17
PTF13dad	56547.0	0.07	0.0859	0.0008	19.6105	0.1619	3.0	1.1738	0.1253						W17	W17
PTF13ddg	56545.0	0.07	0.0840	0.0008	18.5744	0.0271	3.0	0.7048	0.0077						W17	W17
SN 1998bu	50952.0	0.0	0.0023	6.6712e-05	11.6807	0.0142	19.0	0.9772	0.0030	30.3281	0.0113	382.0	0.9670	0.0051	[a]	K+
SN 1999ac	51250.0	0.0	0.0100	3.3356e-05	14.5874	0.0301	29.0	0.9819	0.0077						Ph06	K+
SN 1999cl	51342.0	0.0	0.0031	0.0002	12.7855	0.0499	5.0	0.9332	0.0100	31.0854	0.0175	175.0	0.9219	0.0111	K00	K+
SN 1999cp	51363.0	0.0	0.0097	4.6698e-05	14.7526	0.0675	2.0	1.0000	0.0088	33.1389	0.0131	117.0	0.9911	0.0085	K00	K+
SN 1999ee	51469.0	0.0	0.0109	5.0034e-05	15.0371	0.0207	33.0	1.1175	0.0056	33.3996	0.0069	625.0	1.1171	0.0058	K04a	K+
SN 1999ek	51481.0	0.0	0.0173	3.3356e-05	15.9178	0.0180	15.0	0.9732	0.0297	34.3625	0.0265	56.0	0.9481	0.0142	K04b	K+
SN 1999gp	51550.0	0.07	0.0270	6.0041e-05	16.8131	0.1778	3.0	1.2425	0.0109	35.2225	0.0201	150.0	1.1282	0.0221	K01	K+
SN 2000ce	51667.0	0.46	0.0170	5.0034e-05	16.0167	0.0375	5.0	1.0406	0.0328	34.7082	0.0697	43.0	1.0968	0.0509	K01	K+
SN 2002bo	52356.0	0.0	0.0056	6.6712ed-05	13.8340	0.0363	14.0	0.9555	0.0071	32.0734	0.0152	374.0	0.9521	0.0081	K04b	K+
SN 2002dj	52450.0	0.0	0.0096	7.3384e-05	14.6713	0.0417	21.0	0.9449	0.0126	32.9657	0.0209	166.0	0.9441	0.0152	P08	K+
SN 2003du	52766.0	0.0	0.0073	4.6698e-05	14.4399	0.0254	6.0	1.0180	0.0049	32.8125	0.0095	279.0	1.0158	0.0058	St07	K+
SN 2004S	53038.0	0.46	0.0086	5.3370e-05	14.7843	0.0485	17.0	1.1890	0.0281	33.3096	0.0460	120.0	1.1110	0.0396	K07	K+
SN 2004ef	53263.0	0.46	0.0314	6.3377e-05	17.2232	0.2167	4.0	0.8972	0.0090	35.5348	0.0091	393.0	0.8446	0.0044	C10	CSP
SN 2004eo	53278.0	0.0	0.0162	5.6705e-05	15.6685	0.0466	19.0	0.8720	0.0039						Pa07b	K+
SN 2004ey	53303.0	0.0	0.0161	5.6705e-05	15.7196	0.0742	9.0	1.1158	0.0168	34.1049	0.0085	269.0	1.0421	0.0059	C10	CSP
SN 2004gs	53355.0	0.0	0.0274	0.0001	17.1519	0.1383	10.0	0.7105	0.0099	35.4537	0.0138	356.0	0.6294	0.0096	C10	CSP
SN 2004gu	53361.0	0.0	0.0478	0.0002	18.0707	0.0627	7.0	1.2606	0.0203						C10	CSP
SN 2005A	53379.0	0.0	0.0188	4.0027e-05	16.2924	0.0727	10.0	0.9823	0.0090	34.6258	0.0387	196.0	1.1079	0.0295	C10	CSP
SN 2005M	53405.0	0.0	0.0274	0.0001	16.6410	0.0439	14.0	1.2396	0.0077	35.1701	0.0118	476.0	1.2205	0.0077	C10	CSP

[a] J99,H00

Table B18. SN H-band “max_model” and Optical “EBV_model2” DM fits II

Name	$t_{\rm max}$ MJD	$t_{\rm max}^{\rm err}$ MJD	$z_{\rm cmb}$	$z_{\rm cmb}^{\rm err}$	$H_{\rm max}$ mag	$H_{\rm max}^{\rm err}$ mag	N_H	${\rm st}_H$	${\rm st}_H^{\rm err}$	DM mag	DM$^{\rm err}$ mag	$N_{\rm DM}$	${\rm st}_{\rm DM}$	${\rm st}_{\rm DM}^{\rm err}$	Ref.	Samp.
SN 2005ag	53413.0	0.0	0.0794	0.0001	19.0504	0.0704	9.0	1.1482	0.0115						C10	CSP
SN 2005al	53430.0	0.0	0.0123	6.3377e-05	15.6297	0.0469	8.0	0.8789	0.0026	34.0660	0.0080	239.0	0.8699	0.0028	C10	CSP
SN 2005am	53436.0	0.0	0.0076	0.0001	14.0327	0.0524	6.0	0.7722	0.0031	32.4545	0.0067	483.0	0.7524	0.0030	C10	CSP
SN 2005ao	53439.0	0.07	0.0394	0.0004	17.8706	0.0942	8.0	1.1168	0.2262	36.2422	0.4569	27.0	1.1156	0.2127	F15	F15
SN 2005bl	53482.0	0.0	0.0245	9.6733e-05	16.9904	0.1299	13.0	0.3643	0.0074						T08,F15	F15
SN 2005bo	53479.0	0.07	0.0140	7.3384e-05	15.2530	0.0372	16.0	0.8569	0.0033						C10	CSP
SN 2005cf	53533.0	0.0	0.0067	3.6692e-05	13.9124	0.0413	17.0	1.0699	0.0101	32.3793	0.0089	401.0	0.9978	0.0052	F15	F15
SN 2005ch	53535.0	0.46	0.0269	0.0050	16.6048	0.0700	11.0	0.9456	0.0494						F15	F15
SN 2005el	53646.0	0.0	0.0145	2.6685e-05	15.5781	0.0262	49.0	0.8761	0.0036	34.0955	0.0102	550.0	0.8685	0.0043	F15	F15
SN 2005eq	53653.0	0.0	0.0284	8.3391e-05	17.0417	0.0282	43.0	1.2827	0.0049	35.4613	0.0121	454.0	1.1354	0.0099	F15	F15
SN 2005eu	53659.0	0.0	0.0350	4.6698e-05	16.8640	0.0571	23.0	1.1125	0.0328						F15	F15
SN 2005hc	53666.0	0.0	0.0462	0.0001	17.9606	0.1367	9.0	1.2025	0.0061	36.5373	0.0094	504.0	1.1328	0.0079	C10	CSP
SN 2005hj	53674.0	0.0	0.0580	0.0001	18.3212	0.1305	10.0	1.1995	0.0081	36.9962	0.0121	247.0	1.1935	0.0089	S11	CSP
SN 2005hk	53685.0	0.0	0.0128	7.0048e-05	15.5329	0.1023	25.0	0.5216	0.0153						F15	F15
SN 2005iq	53687.0	0.0	0.0336	0.0001	17.4578	0.0587	20.0	0.9017	0.0052	35.9478	0.0138	207.0	0.8989	0.0068	F15	F15
SN 2005kc	53697.0	0.0	0.0154	5.6705e-05	15.5746	0.0613	8.0	0.9219	0.0124	33.9650	0.0238	131.0	0.9084	0.0137	C10	CSP
SN 2005ki	53705.0	0.0	0.0193	6.3377e-05	16.2603	0.0308	10.0	0.8363	0.0032	34.6771	0.0083	356.0	0.8263	0.0038	C10	CSP
SN 2005ku	53693.0	0.0	0.0454	0.0001	16.9037	0.3118	4.0	1.4995	0.0426						S11	CSP
SN 2005ls	53714.0	0.0	0.0214	0.0001	15.6531	0.0406	19.0	1.1313	0.0239						F15	F15
SN 2005na	53740.0	0.46	0.0261	8.6726e-05	16.8786	0.0560	16.0	0.9727	0.0176						F15	F15
SN 2006D	53756.0	0.0	0.0085	6.0041e-05	14.5528	0.0454	37.0	0.8927	0.0059	32.9421	0.0102	485.0	0.8611	0.0044	F15	F15
SN 2006N	53760.0	0.46	0.0149	9.0062e-05	15.1699	0.0783	12.0	0.7930	0.0203	34.2015	0.0207	114.0	0.7763	0.0086	F15	F15
SN 2006X	53786.0	0.0	0.0036	6.6712e-05	12.9262	0.0171	75.0	0.9721	0.0046	30.9580	0.0197	686.0	0.9345	0.0088	F15	F15
SN 2006ac	53781.0	0.46	0.0237	5.6705e-05	16.9036	0.1047	15.0	0.8886	0.0216	34.9034	0.0214	164.0	0.8712	0.0082	F15	F15
SN 2006ax	53826.0	0.0	0.0165	6.6712e-05	15.9733	0.0412	31.0	1.0905	0.0144	34.3339	0.0086	342.0	0.9998	0.0049	F15	F15
SN 2006bd	53822.0	0.46	0.0280	0.0001	17.2754	0.1173	2.0	0.3455	0.0284	35.6815	0.0249	56.0	0.3633	0.0117	S11	CSP
SN 2006bh	53833.0	0.0	0.0102	3.3356e-05	14.9423	0.0343	10.0	0.8347	0.0039	33.3994	0.0107	176.0	0.8238	0.0055	C10	CSP
SN 2006br	53849.0	0.46	0.0250	0.0001	17.1400	0.1301	5.0	0.9463	0.0343	35.5096	0.0356	60.0	0.9503	0.0242	S11	CSP
SN 2006bt	53858.0	0.0	0.0510	0.0001	16.7983	0.1248	5.0	1.1890	0.0116						S11	CSP
SN 2006cp	53897.0	0.46	0.0227	4.6698e-05	16.6372	0.0902	5.0	1.0469	0.0136	34.9697	0.0261	93.0	1.0287	0.0175	F15	F15
SN 2006cz	53908.0	0.0	0.0420	0.0002	17.8479	0.6363	2.0	1.1291	0.2625						F15	F15
SN 2006ej	53974.0	0.0	0.0205	0.0001	16.2874	0.1481	3.0	0.9023	0.0221	34.7339	0.0180	225.0	0.8725	0.0072	S11	CSP
SN 2006eq	53976.0	0.0	0.0498	8.0055e-05	18.0802	0.2799	8.0	0.6725	0.0307	36.6288	0.0307	190.0	0.6616	0.0157	C10	CSP
SN 2006et	53993.0	0.0	0.0226	0.0001	16.3537	0.0342	13.0	1.2116	0.0068	34.7897	0.0092	205.0	1.1890	0.0061	S11	CSP
SN 2006ev	53987.0	0.46	0.0292	6.0041e-05	17.2001	0.0874	8.0	0.8995	0.0208	35.6868	0.0194	106.0	0.8982	0.0080	S11	CSP
SN 2006gj	53999.0	0.0	0.0279	3.0020e-05	17.1665	0.1327	4.0	0.7179	0.0102	35.6284	0.0171	153.0	0.6404	0.0109	S11	CSP
SN 2006gr	54012.0	0.0	0.0351	7.3384e-05	16.9195	0.1602	5.0	1.1575	0.0209						F15	F15
SN 2006gt	54003.0	0.0	0.0446	7.6719e-05	18.2010	0.0655	6.0	0.5747	0.0089	36.5246	0.0149	108.0	0.5669	0.0080	C10	CSP
SN 2006hb	54004.0	0.46	0.0146	0.0001	15.8386	0.0705	9.0	0.6430	0.0193	34.0507	0.0130	270.0	0.6524	0.0067	S11	CSP

Table B19. SN H-band “max_model” and Optical “EBV_model2” DM fits III

Name	$t_{\rm max}$ MJD	$t_{\rm max}^{\rm err}$ MJD	$z_{\rm cmb}$	$z_{\rm cmb}^{\rm err}$	$H_{\rm max}$ mag	$H_{\rm max}^{\rm err}$ mag	N_H	st_H	$\mathrm{st}_H^{\rm err}$	DM mag	$\mathrm{DM}^{\rm err}$ mag	$N_{\rm DM}$	$\mathrm{st}_{\rm DM}$	$\mathrm{st}_{\rm DM}^{\rm err}$	Ref.	Samp.
SN 2006hx	54021.0	0.0	0.0453	0.0001	17.8734	0.0952	5.0	0.9821	0.0159						S11	CSP
SN 2006is	54009.0	0.46	0.0313	0.0001	17.1997	0.0977	7.0	1.1370	0.0336	35.5371	0.0338	206.0	1.1315	0.0223	F15,S11	F15
SN 2006kf	54041.0	0.0	0.0210	0.0001	16.3471	0.0479	11.0	0.7512	0.0038	34.7890	0.0112	194.0	0.7082	0.0061	S11	CSP
SN 2006le	54047.0	0.0	0.0180	4.0027e-05	16.2320	0.0419	36.0	1.1122	0.0140	34.4116	0.0179	287.0	1.1150	0.0148	F15	F15
SN 2006lf	54044.0	0.0	0.0135	3.3356e-05	15.1070	0.0524	41.0	0.8730	0.0117	33.5812	0.0206	224.0	0.8377	0.0091	F15	F15
SN 2006lu	54036.0	0.46	0.0534	0.0001	17.7429	0.1334	2.0	0.9964	0.0200	36.7625	0.0158	131.0	0.9932	0.0066	S11	CSP
SN 2006ob	54062.0	0.0	0.0590	0.0001	18.4568	0.3370	5.0	0.6479	0.0211	37.0734	0.0248	163.0	0.6744	0.0143	S11	CSP
SN 2006os	54063.0	0.46	0.0327	0.0001	17.2782	0.1262	5.0	0.9506	0.0230	35.5830	0.0273	114.0	0.9371	0.0112	S11	CSP
SN 2006ot	54069.0	0.0	0.0525	0.0001	18.0250	0.2529	7.0	0.6832	0.0316	36.3697	0.0551	130.0	0.6625	0.0366	S11	CSP
SN 2007A	54112.0	0.0	0.0176	0.0001	15.9258	0.1447	3.0	1.1163	0.0229	34.4750	0.0278	74.0	1.0897	0.0249	S11	CSP
SN 2007S	54143.0	0.0	0.0137	6.3377e-05	15.5345	0.0258	45.0	1.2760	0.0077	34.0749	0.0135	432.0	1.2539	0.0084	S11,F15	F15
SN 2007af	54173.0	0.0	0.0054	0.0001	13.6614	0.0344	24.0	1.0859	0.0097	32.0056	0.0052	976.0	0.9391	0.0025	S11	CSP
SN 2007ai	54173.0	0.0	0.0318	0.0001	17.0396	0.0387	6.0	1.2204	0.0067	35.7486	0.0310	132.0	1.1293	0.0246	S11	CSP
SN 2007as	54180.0	0.46	0.0167	0.0004	16.0841	0.0503	10.0	0.9424	0.0193	34.6706	0.0299	141.0	0.9336	0.0124	S11	CSP
SN 2007ba	54197.0	0.0	0.0383	0.0001	17.6135	0.0951	8.0	0.5515	0.0089	35.7775	0.0206	134.0	0.5675	0.0107	S11	CSP
SN 2007bc	54199.0	0.0	0.0207	0.0001	16.4296	0.1022	6.0	0.9250	0.0072	34.7716	0.0158	183.0	0.8957	0.0064	S11	CSP
SN 2007bd	54206.0	0.0	0.0306	0.0001	17.3962	0.1453	7.0	0.9034	0.0114	35.6298	0.0183	131.0	0.8972	0.0076	S11	CSP
SN 2007bm	54223.0	0.0	0.0066	9.6733e-05	14.0347	0.0593	7.0	0.9531	0.0093						S11	CSP
SN 2007ca	54226.0	0.0	0.0142	6.3377e-05	15.6827	0.0606	25.0	1.1207	0.0208	34.3793	0.0199	219.0	1.0903	0.0155	S11,F15	F15
SN 2007co	54265.0	0.0	0.0278	0.0001	17.3075	0.1704	6.0	0.9565	0.0066						F15	F15
SN 2007cq	54280.0	0.0	0.0250	0.0001	16.5191	0.1213	6.0	1.0180	0.0077						F15	F15
SN 2007fb	54287.0	0.46	0.0177	6.3377e-05	16.1449	0.1691	2.0	0.8612	0.0204						F15	F15
SN 2007hx	54354.0	0.0	0.0797	0.0001	18.7298	0.1408	4.0	1.0219	0.0227						S11	CSP
SN 2007jg	54366.0	0.0	0.0369	0.0001	17.8823	0.1410	5.0	0.9440	0.0052	36.1739	0.0163	303.0	0.9308	0.0066	S11	CSP
SN 2007le	54398.0	0.0	0.0066	0.0001	13.9566	0.0290	46.0	1.1233	0.0103	32.3106	0.0088	500.0	1.0534	0.0056	S11,F15	F15
SN 2007nq	54397.0	0.46	0.0448	0.0001	17.7326	0.1013	6.0	0.8160	0.0185	36.2767	0.0133	238.0	0.7928	0.0055	S11	CSP
SN 2007on	54419.0	0.0	0.0058	3.3356e-05	13.2248	0.0270	25.0	0.5552	0.0053	31.5774	0.0063	453.0	0.5772	0.0032	S11	CSP
SN 2007rx	54442.0	0.07	0.0304	6.3377e-05	16.1862	0.0881	5.0	1.1738	0.0247						F15	F15
SN 2007sr	54446.0	0.46	0.0058	0.0001	13.3690	0.0380	31.0	1.1080	0.0295	31.8028	0.0159	405.0	1.1738	0.0109	F15	F15
SN 2008A	54479.0	0.0	0.0168	5.6705e-05	16.1057	0.1375	14.0	1.1890	0.0321						F15	F15
SN 2008C	54465.0	0.46	0.0166	2.6685e-05	16.0850	0.0594	21.0	0.9734	0.0201	34.2559	0.0139	291.0	0.9630	0.0071	S11	CSP
SN 2008R	54494.0	0.0	0.0130	7.3384e-05	15.4852	0.0876	5.0	0.6265	0.0098	33.7911	0.0157	88.0	0.6119	0.0101	S11	CSP
SN 2008Z	54514.0	0.0	0.0214	0.0002	16.6822	0.0509	44.0	1.2494	0.0109	35.2827	0.0241	258.0	1.0998	0.0194	F15	F15
SN 2008ae	54512.0	0.0	0.0300	0.0001	17.3464	0.1905	23.0	1.1890	0.0474						F15	F15
SN 2008bc	54549.0	0.0	0.0143	0.0001	15.8159	0.0508	11.0	1.0910	0.0127	34.0686	0.0137	223.0	1.0746	0.0106	S11	CSP
SN 2008bq	54563.0	0.0	0.0331	5.3370e-05	17.5143	0.1083	4.0	1.0779	0.0066	35.6580	0.0164	107.0	1.0584	0.0112	S11	CSP
SN 2008fp	54730.0	0.0	0.0056	0.0001	13.5452	0.0156	20.0	1.1005	0.0085						S11	CSP
SN 2008fr	54732.0	0.46	0.0490	5.3370e-05	18.4303	0.1410	6.0	1.0980	0.0270	36.1737	0.0198	114.0	1.0633	0.0115	F15	F15

Table B20. SN H-band “max_model” and Optical “EBV_model2” DM fits IV

Name	t_{max} MJD	$t_{\mathrm{max}}^{\mathrm{err}}$ MJD	z_{cmb}	$z_{\mathrm{cmb}}^{\mathrm{err}}$	H_{max} mag	$H_{\mathrm{max}}^{\mathrm{err}}$ mag	N_H	st_H	$\mathrm{st}_H^{\mathrm{err}}$	DM mag	$\mathrm{DM}^{\mathrm{err}}$ mag	N_{DM}	$\mathrm{st}_{\mathrm{DM}}$	$\mathrm{st}_{\mathrm{DM}}^{\mathrm{err}}$	Ref.	Samp.
SN 2008fv	54752.0	0.0	0.0104	5.0034e-05	14.9770	0.0884	3.0	0.7945	0.1208						F15	F15
SN 2008fx	54748.0	0.0	0.0536	8.3391e-05	18.4375	0.0864	5.0	2.8459	3.6366						F15	F15
SN 2008gb	54746.0	0.46	0.0374	4.3363e-05	17.5836	0.0642	14.0	1.0403	0.0272	36.0699	0.0244	108.0	1.0247	0.0138	F15	F15
SN 2008gl	54768.0	0.0	0.0339	0.0001	17.1915	0.0708	12.0	0.8623	0.0089	35.8164	0.0156	84.0	0.8529	0.0080	F15	F15
SN 2008gp	54778.0	0.0	0.0330	0.0001	17.4876	0.1439	9.0	1.1170	0.0227	35.6778	0.0185	136.0	1.0118	0.0100	S11	CSP
SN 2008hm	54804.0	0.0	0.0194	9.6733e-05	16.4553	0.0429	22.0	1.1217	0.0165	34.6207	0.0276	166.0	1.0605	0.0190	F15	F15
SN 2008hs	54812.0	0.0	0.0178	8.3391e-05	16.3559	0.0557	21.0	0.5631	0.0119	34.7115	0.0186	285.0	0.6318	0.0091	F15	F15
SN 2008hv	54816.0	0.0	0.0125	0.0001	15.5228	0.0475	45.0	0.8985	0.0065	33.8625	0.0081	633.0	0.8629	0.0034	S11,F15	F15
SN 2008hy	54800.0	0.07	0.0094	5.3370e-05	14.3333	0.0318	23.0	0.8590	0.0062						F15	F15
SN 2008ia	54812.0	0.0	0.0208	0.0001	16.3294	0.0525	14.0	0.8877	0.0061	34.8571	0.0141	135.0	0.8739	0.0057	S11	CSP
SN 2009D	54841.0	0.46	0.0243	4.3363e-05	16.6447	0.0226	24.0	1.1858	0.0244	35.0486	0.0346	138.0	1.1738	0.0224	F15	F15
SN 2009ad	54886.0	0.0	0.0280	1.6678e-05	16.9491	0.0334	20.0	1.0278	0.0095	35.4181	0.0185	150.0	1.0250	0.0105	F15	F15
SN 2009al	54896.0	0.0	0.0237	0.0001	16.5139	0.0494	22.0	1.1890	0.0194	34.9119	0.0398	146.0	0.9528	0.0240	F15	F15
SN 2009an	54898.0	0.0	0.0103	0.0001	14.9456	0.0218	29.0	0.8553	0.0057	33.3214	0.0117	205.0	0.8458	0.0055	F15	F15
SN 2009bv	54926.0	0.0	0.0374	8.0055e-05	17.5048	0.0551	13.0	1.1184	0.0287	36.3284	0.0361	100.0	1.1050	0.0255	F15	F15
SN 2009do	54945.0	0.46	0.0405	9.0062e-05	17.5947	0.0701	9.0	0.9442	0.0251	36.1226	0.0258	98.0	0.9419	0.0124	F15	F15
SN 2009ds	54960.0	0.0	0.0192	7.0048e-05	16.3271	0.1273	6.0	1.0917	0.0307	34.7650	0.0221	60.0	1.0673	0.0135	F15	F15
SN 2009fv	54995.0	0.46	0.0308	7.3384e-05	15.3593	0.2357	5.0	0.8541	0.0419						F15	F15
SN 2009ig	55080.0	0.0	0.0085	3.6692e-05	14.2541	0.1148	9.0	1.1211	0.0112	32.6931	0.0131	386.0	1.2016	0.0077	F15	F15
SN 2009im	55080.0	0.07	0.0127	0.0001	15.2484	0.0969	11.0	0.3646	0.0195						F15	F15
SN 2009jr	55119.0	0.0	0.0170	7.3384e-05	16.9568	0.1120	14.0	1.1222	0.0412						F15	F15
SN 2009kk	55126.0	0.46	0.0124	0.0001	15.6209	0.0516	17.0	0.8893	0.0186						F15	F15
SN 2009kq	55155.0	0.0	0.0126	6.0041e-05	15.3161	0.0512	11.0	0.9889	0.0056						F15	F15
SN 2009le	55165.0	0.0	0.0172	4.6698e-05	15.9717	0.1618	7.0	0.9510	0.0253	34.3196	0.0279	57.0	0.9845	0.0193	F15	F15
SN 2009lf	55148.0	0.46	0.0450	0.0004	17.3740	0.0795	16.0	0.8382	0.0253	35.8020	0.0295	98.0	0.8407	0.0145	F15	F15
SN 2009na	55201.0	0.0	0.0225	9.6733e-05	16.4678	0.1047	10.0	0.9575	0.0106	34.8519	0.0199	90.0	0.9368	0.0121	F15	F15
SN 2010Y	55247.0	0.0	0.0118	0.0001	15.2784	0.1619	10.0	0.5600	0.0120	33.7939	0.0181	250.0	0.6264	0.0092	F15	F15
SN 2010ag	55270.0	0.0	0.0347	0.0001	17.5835	0.0694	15.0	1.2168	0.0172	35.6109	0.0338	102.0	1.1477	0.0286	F15	F15
SN 2010ai	55277.0	0.0	0.0203	0.0001	16.4413	0.0523	17.0	0.8341	0.0078	35.1096	0.0161	135.0	0.8265	0.0073	F15	F15
SN 2010cr	55310.0	0.07	0.0237	0.0001	17.0052	0.0798	12.0	0.7050	0.0302	35.3168	0.0487	112.0	0.7320	0.0224	F15	F15
SN 2010dl	55339.0	0.46	0.0303	0.0001	17.1684	0.1575	3.0	1.2025	0.3537						F15	F15
SN 2010dm	55350.0	0.46	0.0333	5.3370e-05	17.5401	0.0438	6.0	1.2618	0.0367						BN12	BN12
SN 2010dw	55357.0	0.0	0.0384	0.0001	17.6592	0.1112	6.0	1.2268	0.0294	36.1366	0.0226	47.0	1.1890	0.0179	F15	F15
SN 2010ew	55381.0	0.46	0.0267	0.0001	16.2968	0.2599	4.0	0.6809	0.2243						F15	F15
SN 2010ex	55384.0	0.46	0.0227	7.6719e-05	16.6642	0.3633	2.0	0.6720	0.4208						F15	F15
SN 2010gn	55390.0	0.0	0.0313	0.0001	17.3258	0.0584	8.0	0.7433	0.0324	35.8145	0.0667	68.0	0.9088	0.0254	[b]	F15
SN 2010gy	55426.0	0.0	0.0660	0.0001	19.1345	0.1228	4.0	0.9039	0.0173	37.4639	0.0367	88.0	0.9044	0.0145	BN12	BN12

[a] F15,BN12

Table B21. SN H-band “max_model” and Optical “EBV_model2” DM fits V

Name	t_{max} MJD	$t_{\mathrm{max}}^{\mathrm{err}}$ MJD	z_{cmb}	$z_{\mathrm{cmb}}^{\mathrm{err}}$	H_{max} mag	$H_{\mathrm{max}}^{\mathrm{err}}$ mag	N_H	st_H	$\mathrm{st}_H^{\mathrm{err}}$	DM mag	$\mathrm{DM}^{\mathrm{err}}$ mag	N_{DM}	$\mathrm{st}_{\mathrm{DM}}$	$\mathrm{st}_{\mathrm{DM}}^{\mathrm{err}}$	Ref.	Samp.
SN 2010ho	55442.0	0.0	0.0410	0.0001	18.0124	0.0266	4.0	1.0393	0.0671						BN12	BN12
SN 2010hs	55454.0	0.0	0.0770	0.0001	19.3361	0.0627	4.0	2.8022	1.5224						BN12	BN12
SN 2010iw	55496.0	0.46	0.0217	4.0027e-05	16.2482	0.0523	18.0	1.0926	0.0383						F15	F15
SN 2010ju	55523.0	0.0	0.0151	1.3342e-05	15.5831	0.0360	19.0	1.1006	0.0430						F15	F15
SN 2010jv	55519.0	0.0	0.0137	8.6726e-05	15.3411	0.0335	3.0	0.9028	0.0888						F15	F15
SN 2010kg	55543.0	0.0	0.0163	3.6692e-05	15.8505	0.0333	27.0	0.9183	0.0123	34.0252	0.0543	117.0	0.8891	0.0190	F15	F15
SN 2011B	55583.0	0.0	0.0058	5.3370e-05	13.2626	0.0271	43.0	0.8821	0.0087	31.8837	0.0354	222.0	0.8714	0.0120	F15	F15
SN 2011K	55577.0	0.0	0.0145	0.0010	15.5041	0.0215	16.0	1.1738	0.0162						F15	F15
SN 2011aa	55597.0	0.46	0.0132	9.6733e-05	14.4136	0.0418	28.0	2.3910	0.0746						F15	F15
SN 2011ae	55619.0	0.46	0.0064	9.6733e-05	13.5068	0.0479	31.0	0.9401	0.0264						F15	F15
SN 2011ao	55639.0	0.0	0.0115	6.3377e-05	14.9166	0.0197	29.0	1.0105	0.0120	33.5312	0.0386	178.0	1.0382	0.0162	F15	F15
SN 2011at	55634.0	0.46	0.0066	8.0055e-05	14.0210	0.0460	14.0	0.8719	0.0273	32.4656	0.0340	76.0	0.8963	0.0135	F15	F15
SN 2011de	55711.0	0.0	0.0302	5.0034e-05	15.9985	0.0605	24.0	1.8041	0.0989						F15	F15
SN 2011df	55716.0	0.0	0.0155	0.0001	15.5810	0.0187	25.0	1.0897	0.0163						F15	F15
SN 2011fs	55833.0	0.07	0.0211	0.0001	16.1266	0.0365	4.0	1.1738	0.0291	34.6509	0.0209	39.0	1.1738	0.0256	W17	W17
SN 2011io	55894.0	0.46	0.0396	0.0004	18.2629	0.02	1.0	0.955	0.0137						W17	W17
SN 2012bh	56016.0	0.46	0.0267	8.3391e-05	16.9568	0.02	1.0	0.955	0.0137						W17	W17
SN 2012bp	56013.0	0.46	0.0282	0.0002	17.1040	0.02	1.0	0.955	0.0137						W17	W17
SN 2012em	56187.0	0.46	0.0379	0.0003	18.1196	0.02	1.0	0.955	0.0137						W17	W17
SN 2012fk	56223.0	0.07	0.0350	0.0003	17.4667	0.0460	3.0	0.6678	0.0147						W17	W17
SN 2013bs	56408.0	0.07	0.0275	0.0002	16.7795	0.1220	7.0	0.6541	0.0716	35.0202	0.3449	21.0	0.6562	0.0735	W17	W17
SN 2013bt	56408.0	0.0	0.0363	0.0003	17.5358	0.1733	5.0	0.8912	0.1206						W17	W17
SN 2013cs	56436.0	0.0	0.0093	7.3384e-05	14.5276	0.1007	4.0	1.0806	0.0224	32.7267	0.0430	137.0	1.0982	0.0343	W17	W17
SN 2013cv	56429.0	0.0	0.0350	0.0003	17.6428	0.0519	11.0	1.1110	0.0229	36.1481	0.0349	159.0	1.1136	0.0260	W17	W17
SN 2013fn	56572.0	0.46	0.0269	0.0002	17.1063	0.0543	3.0	0.9449	0.0309	35.1367	0.0780	42.0	0.9406	0.0401	W17	W17
iPTF13dge	56558.0	0.0	0.0156	3.3356e-05	15.9608	0.0693	8.0	0.9238	0.0094	33.9272	0.0362	452.0	0.8799	0.0113	W17	W17
iPTF13dkl	56566.0	0.46	0.0400	0.0004	18.4755	0.0937	2.0	0.7388	0.0534	36.3680	0.0654	12.0	0.8864	0.0324	W17	W17
iPTF13dkx	56568.0	0.46	0.0300	0.0003	17.3045	0.1426	4.0	0.9502	0.1274						W17	W17
iPTF13ebh	56623.0	0.0	0.0129	8.6726e-05	15.3236	0.1578	3.0	0.6234	0.0127	33.3952	0.0278	228.0	0.6094	0.0129	W17	W17

Table B22. SN H-band “max_model” and Optical “EBV_model2” DM fits VI - Overflow

Name	t_{max} MJD	$t_{\mathrm{max}}^{\mathrm{err}}$ MJD	z_{cmb}	$z_{\mathrm{cmb}}^{\mathrm{err}}$	H_{max} mag	$H_{\mathrm{max}}^{\mathrm{err}}$ mag	N_H	st_H	$\mathrm{st}_H^{\mathrm{err}}$	DM mag	DM$^{\mathrm{err}}$ mag	N_{DM}	$\mathrm{st}_{\mathrm{DM}}$	$\mathrm{st}_{\mathrm{DM}}^{\mathrm{err}}$	Ref.	Samp.
CSS121006:232854+085452	56207.0	0.07	0.0799	0.0008	19.9446	0.1677	2.0	0.955	0.0						W17	W17
CSS121009:011101-172841	56220.0	0.46	0.0600	0.0006	18.1625	2.0790	2.0	0.6660	0.9493						W17	W17
CSS121114:090202+101800	56252.0	0.46	0.0419	0.0004	17.9491	0.0930	3.0	1.1738	0.1094						W17	W17
SNF20080522-000	54621.0	0.0	0.0471	0.0004	17.4751	0.3081	3.0	1.1042	0.0441	36.2297	0.0565	58.0	1.1738	0.0503	F15	F15
SNF20080522-011	54617.0	0.46	0.0377	0.0003	17.7402	0.0889	9.0	1.0738	0.0332	36.1132	0.0339	86.0	1.0965	0.0227	F15	F15

Note. — This table contains SNeIa with names too long to fit in the tables in alphabetical order.

BIBLIOGRAPHY

Abazajian, K., Adelman-McCarthy, J. K., Agüeros, M. A., et al. 2003, AJ, 126, 2081

—. 2005, AJ, 129, 1755

Abazajian, K. N., Adelman-McCarthy, J. K., Agüeros, M. A., et al. 2009a, ApJS, 182, 543

—. 2009b, ApJS, 182, 543

Adelman-McCarthy, J. K., Agüeros, M. A., Allam, S. S., et al. 2006a, ApJS, 162, 38

—. 2006b, ApJS, 162, 38

—. 2008, ApJS, 175, 297

Akaike, H. 1974, IEEE Transactions on Automatic Control, 19, 716

Arbour, R., Masi, G., Nocentini, F., Schmeer, P., & Cortini, G. 2014, Central Bureau Electronic Telegrams, 3823

Arun, K., Gudennavar, S. B., & Sivaram, C. 2017, Advances in Space Research, 60, 166

Astier, P., Guy, J., Regnault, N., et al. 2006, A&A, 447, 31

Astier, P., Balland, C., Brescia, M., et al. 2014, A&A, 572, A80

Astropy Collaboration, Robitaille, T. P., Tollerud, E. J., et al. 2013a, A&A, 558, A33

—. 2013b, A&A, 558, A33

Baade, W. 1938, ApJ, 88, 285

Barden, S. C., Armandroff, T., Muller, G., et al. 1994, in Proc. SPIE, Vol. 2198, Instrumentation in Astronomy VIII, ed. D. L. Crawford & E. R. Craine, 87–97

Barden, S. C., Sawyer, D. G., & Honeycutt, R. K. 1998, in Proc. SPIE, Vol. 3355, Optical Astronomical Instrumentation, ed. S. D'Odorico, 892–899

Barone-Nugent, R. L., Lidman, C., Wyithe, J. S. B., et al. 2012, MNRAS, 425, 1007

Belligoli, R., Castellani, F., Denisenko, D., et al. 2012, Central Bureau Electronic Telegrams, 3272, 1

Bernardi, M., Shankar, F., Hyde, J. B., et al. 2010, MNRAS, 404, 2087

Bershady, M., Barden, S., Blanche, P.-A., et al. 2008, in Proc. SPIE, Vol. 7014, Ground-based and Airborne Instrumentation for Astronomy II, 70140H

Bershady, M. A., Andersen, D. R., Harker, J., Ramsey, L. W., & Verheijen, M. A. W. 2004, PASP, 116, 565

Bershady, M. A., Andersen, D. R., Verheijen, M. A. W., et al. 2005, ApJS, 156, 311

Bertin, E., & Arnouts, S. 1996, A&AS, 117, 393

Betoule, M., Kessler, R., Guy, J., et al. 2014, A&A, 568, A22

Bianchi, L., Conti, A., & Shiao, B. 2014, Advances in Space Research, 53, 900

Blagorodnova, N., Walton, N., Fraser, M., et al. 2014a, Central Bureau Electronic Telegrams, 3823

—. 2014b, Central Bureau Electronic Telegrams, 3999

Blanton, M. R., & Roweis, S. 2007, AJ, 133, 734

Blanton, M. R., Brinkmann, J., Csabai, I., et al. 2003a, AJ, 125, 2348

Blanton, M. R., Hogg, D. W., Bahcall, N. A., et al. 2003b, ApJ, 594, 186

Bottinelli, L., Durand, N., Fouque, P., et al. 1993, A&AS, 102, 57

Box, G. E. P., & Jenkins, G. M., eds. 1976, Time series analysis. Forecasting and control

Brimacombe, J., Holoien, T. W.-S., Stanek, K. Z., et al. 2015a, The Astronomer's Telegram, 7413

Brimacombe, J., Kiyota, S., Holoien, T. W.-S., et al. 2015b, The Astronomer's Telegram, 7228

Bruzual, G., & Charlot, S. 2003, MNRAS, 344, 1000

Burns, C. R., Stritzinger, M., Phillips, M. M., et al. 2011, AJ, 141, 19

—. 2014, ApJ, 789, 32

Buton, C., Feindt, U., Kerschhaggl, M., et al. 2012, The Astronomer's Telegram, 4497

Cai, Y.-F., Saridakis, E. N., Setare, M. R., & Xia, J.-Q. 2010, Phys. Rep., 493, 1

Campbell, H., Fraser, M., & Gilmore, G. 2016, MNRAS, 457, 3470

Cao, Y., Nugent, P. E., Goobar, A., Johannson, J., & Gorbikov, E. 2013a, The Astronomer's Telegram, 5405, 1

Cao, Y., Sesar, B., Perley, D., et al. 2013b, The Astronomer's Telegram, 5366

Cao, Y., Hsiao, E. Y., Phillips, M. M., et al. 2013c, The Astronomer's Telegram, 5580, 1

Cao, Y., Kulkarni, S. R., Howell, D. A., et al. 2015, Nature, 521, 328

Capozziello, S., & Fang, L. Z. 2002, International Journal of Modern Physics D, 11, 483

Carroll, B. W., & Ostlie, D. A. 2006, An introduction to modern astrophysics and cosmology (Pearson Education, Inc. as Addison-Wesley)

Carroll, S. M., Duvvuri, V., Trodden, M., & Turner, M. S. 2004, Phys. Rev. D, 70, 043528

Cellier-Holzem, F., Canto, A., Antilogus, P., et al. 2012, The Astronomer's Telegram, 4566

Cenko, S. B., Filippenko, A. V., Silverman, J. M., et al. 2012, Central Bureau Electronic Telegrams, 3111, 2

Chambers, K. C., Magnier, E. A., Metcalfe, N., et al. 2016, ArXiv e-prints, arXiv:1612.05560

Childress, M., Aldering, G., Antilogus, P., et al. 2013a, ApJ, 770, 107

—. 2013b, ApJ, 770, 108

Childress, M. J., Wolf, C., & Zahid, H. J. 2014, MNRAS, 445, 1898

Ciabattari, F., Mazzoni, E., Gonzalez Carballo, J.-L., et al. 2013, Central Bureau Electronic Telegrams, 3654, 1

Cid Fernandes, R., Mateus, A., Sodré, L., Stasińska, G., & Gomes, J. M. 2005, MNRAS, 358, 363

Claver, C. F., Corson, C., Gomez, Jr., R. R., et al. 2003, in Society of Photo-Optical Instrumentation Engineers (SPIE) Conference Series, Vol. 4837, Large Ground-based Telescopes, ed. J. M. Oschmann & L. M. Stepp, 438–447

Conley, A., Guy, J., Sullivan, M., et al. 2011, ApJS, 192, 1

Contreras, C., Hamuy, M., Phillips, M. M., et al. 2010, AJ, 139, 519

Cortese, L., Minchin, R. F., Auld, R. R., et al. 2008, MNRAS, 383, 1519

Cox, L., Newton, J., Puckett, T., et al. 2011, Central Bureau Electronic Telegrams, 2939, 1

Dale, D. A., Giovanelli, R., Haynes, M. P., et al. 1997, AJ, 114, 455

D'Andrea, C. B., Gupta, R. R., Sako, M., et al. 2011, ApJ, 743, 172

de Vaucouleurs, G., de Vaucouleurs, A., Corwin, Jr., H. G., et al. 1991, Third Reference Catalogue of Bright Galaxies. Volume I: Explanations and references. Volume II: Data for galaxies between 0^h and 12^h. Volume III: Data for galaxies between 12^h and 24^h. (Springer, New York, NY (USA))

Dvali, G., Gabadadze, G., & Porrati, M. 2000, Physics Letters B, 485, 208

Elias-Rosa, N., Cappellaro, E., Benetti, S., et al. 2014, The Astronomer's Telegram, 6628

Falco, E., Willner, S., Challis, P., et al. 2015a, The Astronomer's Telegram, 7420

—. 2015b, The Astronomer's Telegram, 7432

Falco, E. E., Kurtz, M. J., Geller, M. J., et al. 1999, PASP, 111, 438

Ferretti, R., Fremling, C., Johansson, J., et al. 2014, The Astronomer's Telegram, 6764

Filippenko, A. V., Li, W. D., Treffers, R. R., & Modjaz, M. 2001, in Astronomical Society of the Pacific Conference Series, Vol. 246, IAU Colloq. 183: Small Telescope Astronomy on Global Scales, ed. B. Paczynski, W.-P. Chen, & C. Lemme, 121

Filippenko, A. V., Richmond, M. W., Matheson, T., et al. 1992a, ApJ, 384, L15

Filippenko, A. V., Richmond, M. W., Branch, D., et al. 1992b, AJ, 104, 1543

Fitzpatrick, E. L. 1999, PASP, 111, 63

Flewelling, H. A., Magnier, E. A., Chambers, K. C., et al. 2016, ArXiv e-prints, arXiv:1612.05243

Folatelli, G., Phillips, M. M., Burns, C. R., et al. 2010, AJ, 139, 120

Foreman-Mackey, D., Hogg, D. W., Lang, D., & Goodman, J. 2013, PASP, 125, 306

Foreman-Mackey, D., Price-Whelan, A., Ryan, G., et al. 2014, triangle.py v0.1.1, doi:10.5281/zenodo.11020

Friedman, A. S., Wood-Vasey, W. M., Marion, G. H., et al. 2015, ApJS, 220, 9

Frieman, J. A., Bassett, B., Becker, A., et al. 2008, AJ, 135, 338

G., Tomasella, L., Benetti, S., et al. 2014, Central Bureau Electronic Telegrams, 3823

Gal-Yam, A., Nugent, P., Walker, E., Cenko, S. B., & Fox, O. 2012, The Astronomer's Telegram, 4363, 1

Galbany, L., Miquel, R., Östman, L., et al. 2012, ApJ, 755, 125

Gallagher, J. S., Garnavich, P. M., Caldwell, N., et al. 2008, ApJ, 685, 752

Garland, C. A., Williams, J. P., Pisano, D. J., et al. 2005, ApJ, 624, 714

Gelman, A., Hwang, J., & Vehtari, A. 2014, Statistics and computing, 24

Giovanelli, R., & Haynes, M. P. 1993, AJ, 105, 1271

Goodman, J., & Weare, J. 2010, Comm. App. Math. and Comp. Sci, 5

Greggio, L. 2005, A&A, 441, 1055

Greggio, L., Renzini, A., & Daddi, E. 2008, MNRAS, 388, 829

Guillochon, J., Parrent, J., Kelley, L. Z., & Margutti, R. 2017, ApJ, 835, 64

Gupta, R. R., D'Andrea, C. B., Sako, M., et al. 2011, ApJ, 740, 92

Guy, J., Astier, P., Baumont, S., et al. 2007, A&A, 466, 11

Guy, J., Sullivan, M., Conley, A., et al. 2010, A&A, 523, A7

Hamuy, M., Phillips, M. M., Maza, J., et al. 1995, AJ, 109, 1

Harbeck, D. R., Boroson, T., Lesser, M., et al. 2014, in Proc. SPIE, Vol. 9147, Ground-based and Airborne Instrumentation for Astronomy V, 91470P

Hayden, B. T., Gupta, R. R., Garnavich, P. M., et al. 2013, ApJ, 764, 191

Helbig, P. 2015, MNRAS, 453, 3975

Hernandez, M., Meikle, W. P. S., Aparicio, A., et al. 2000, MNRAS, 319, 223

Hinshaw, G., Larson, D., Komatsu, E., et al. 2013, ApJS, 208, 19

Hogg, D. W., Baldry, I. K., Blanton, M. R., & Eisenstein, D. J. 2002, ArXiv Astrophysics e-prints, astro-ph/0210394

Howell, D. A., Sand, D., Valenti, S., & Arcavi, I. 2013, Central Bureau Electronic Telegrams, 3681

Howell, D. A., Sullivan, M., Brown, E. F., et al. 2009, ApJ, 691, 661

Howerton, S., Drake, A. J., Djorgovski, S. G., et al. 2011, Central Bureau Electronic Telegrams, 2881, 2

—. 2013, Central Bureau Electronic Telegrams, 3662, 1

Hsiao, E. Y., Conley, A., Howell, D. A., et al. 2007, ApJ, 663, 1187

Hsiao, E. Y., Marion, G. H., Phillips, M. M., et al. 2013, ApJ, 766, 72

Hsiao, E. Y., Burns, C. R., Contreras, C., et al. 2015, A&A, 578, A9

Huchra, J. P., Vogeley, M. S., & Geller, M. J. 1999, ApJS, 121, 287

Huchra, J. P., Macri, L. M., Masters, K. L., et al. 2012, ApJS, 199, 26

Hunter, J. D. 2007, Computing In Science & Engineering, 9, 90

Husemann, B., Kamann, S., Sandin, C., et al. 2012, A&A, 545, A137

Huterer, D., & Cooray, A. 2005, Phys. Rev. D, 71, 023506

Jha, S., Riess, A. G., & Kirshner, R. P. 2007, ApJ, 659, 122

Jha, S., Garnavich, P. M., Kirshner, R. P., et al. 1999, ApJS, 125, 73

Jin, Z., & Gao, X. 2011, Central Bureau Electronic Telegrams, 2871, 1

Jin, Z., Gao, X., Koff, R. A., et al. 2013, Central Bureau Electronic Telegrams, 3681

Johansson, J., Thomas, D., Pforr, J., et al. 2013, MNRAS, 435, 1680

Johansson, J., Ferretti, R., Fremling, C., et al. 2014, The Astronomer's Telegram, 6534

Jones, D. H., Read, M. A., Saunders, W., et al. 2009, MNRAS, 399, 683

Jones, D. O., Riess, A. G., & Scolnic, D. M. 2015, ArXiv e-prints, arXiv:1506.02637

Jones, D. O., Rodney, S. A., Riess, A. G., et al. 2013, ApJ, 768, 166

Jones, D. O., Scolnic, D. M., Riess, A. G., et al. 2017, ApJ, 843, 6

Kandrashoff, M., Cenko, S. B., Li, W., et al. 2012, Central Bureau Electronic Telegrams, 3111, 1

Kankare, E., Kangas, T., Mattila, S., et al. 2013, The Astronomer's Telegram, 5392, 1

Kasen, D. 2006, ApJ, 649, 939

Kattner, S., Leonard, D. C., Burns, C. R., et al. 2012, PASP, 124, 114

Kauffmann, G., Heckman, T. M., White, S. D. M., et al. 2003, MNRAS, 341, 33

Kelly, P. L., Filippenko, A. V., Burke, D. L., et al. 2015, Science, 347, 1459

Kelly, P. L., Hicken, M., Burke, D. L., Mandel, K. S., & Kirshner, R. P. 2010, ApJ, 715, 743

Kent, B. R., Giovanelli, R., Haynes, M. P., et al. 2008, AJ, 136, 713

Kessler, R., Bernstein, J. P., Cinabro, D., et al. 2009, PASP, 121, 1028

—. 2010, Astrophysics Source Code Library, ascl:1010.027

Kim, A., Deustua, S., Gabi, S., et al. 1996, ArXiv Astrophysics e-prints, astro-ph/9602123

Kim, A. G., Thomas, R. C., Aldering, G., et al. 2013, ApJ, 766, 84

Kim, A. G., Aldering, G., Antilogus, P., et al. 2014, ApJ, 784, 51

Kirshner, R. P. 2012, RAISIN: Tracers of cosmic expansion with SN IA in the IR HST Proposal 13046

Kiyota, S., Brimacombe, J., Holoien, T. W.-S., et al. 2015, The Astronomer's Telegram, 7426

Kowal, C. T. 1968, AJ, 73, 1021

Krisciunas, K., Hastings, N. C., Loomis, K., et al. 2000, ApJ, 539, 658

Krisciunas, K., Phillips, M. M., & Suntzeff, N. B. 2004a, ApJ, 602, L81

Krisciunas, K., Phillips, M. M., Suntzeff, N. B., et al. 2004b, AJ, 127, 1664

Krisciunas, K., Marion, G. H., Suntzeff, N. B., et al. 2009, AJ, 138, 1584

Lackner, C. N., & Gunn, J. E. 2012, MNRAS, 421, 2277

Lampeitl, H., Smith, M., Nichol, R. C., et al. 2010, ApJ, 722, 566

Leibundgut, B., Kirshner, R. P., Phillips, M. M., et al. 1993, AJ, 105, 301

Li, W. D., Filippenko, A. V., Treffers, R. R., et al. 2000, in American Institute of Physics Conference Series, Vol. 522, American Institute of Physics Conference Series, ed. S. S. Holt & W. W. Zhang, 103–106

Liddle, A. R. 2007, MNRAS, 377, L74

LSST Science Collaboration, Abell, P. A., Allison, J., et al. 2009, ArXiv e-prints, arXiv:0912.0201

Magnier, E. A., Sweeney, W. E., Chambers, K. C., et al. 2016, ArXiv e-prints, arXiv:1612.05244

Malmquist, K. G. 1936, Stockholms Observatoriums Annaler, 12, 7

Mannucci, F., Della Valle, M., & Panagia, N. 2006, MNRAS, 370, 773

Mannucci, F., Della Valle, M., Panagia, N., et al. 2005, A&A, 433, 807

Maoz, D., Mannucci, F., & Nelemans, G. 2014, ARA&A, 52, 107

Marion, G. H., & Berlind, P. 2011a, Central Bureau Electronic Telegrams, 2880, 2

—. 2011b, Central Bureau Electronic Telegrams, 2892, 3

—. 2011c, Central Bureau Electronic Telegrams, 2939, 2

Marion, G. H., Kirshner, R. P., Foley, R. J., Challis, P., & Irwin, J. 2012, Central Bureau Electronic Telegrams, 3111, 3

Marion, G. H., Sand, D. J., Hsiao, E. Y., et al. 2015, ApJ, 798, 39

Marzke, R. O., Huchra, J. P., & Geller, M. J. 1996, AJ, 112, 1803

Meixner, M., Smee, S., Doering, R. L., et al. 2010, PASP, 122, 451

Metropolis, N., Rosenbluth, A. W., Rosenbluth, M. N., Teller, A. H., & Teller, E. 1953, J. Chem. Phys., 21, 1087

Miknaitis, G., Pignata, G., Rest, A., et al. 2007, ApJ, 666, 674

Milisavljevic, D. 2013, Central Bureau Electronic Telegrams, 3662, 1

Milne, P. A., Foley, R. J., Brown, P. J., & Narayan, G. 2015, ApJ, 803, 20

Mo, J., Zhao, X., Wang, X., & Zhang, T. 2013, Central Bureau Electronic Telegrams, 3662, 1

Moreno-Raya, M. E., Mollá, M., López-Sánchez, Á. R., et al. 2016, ApJ, 818, L19

Moustakas, J., Coil, A. L., Aird, J., et al. 2013, ApJ, 767, 50

Nakano, S. 2011, Central Bureau Electronic Telegrams, 2892, 1

Nakano, S., Itagaki, K., Kiyota, S., et al. 2014, Central Bureau Electronic Telegrams, 3996

Nayak, I., Cenko, S. B., Li, W., et al. 2011, Central Bureau Electronic Telegrams, 2901, 1

Nishiura, S., Shimada, M., Ohyama, Y., Murayama, T., & Taniguchi, Y. 2000, AJ, 120, 1691

Noebauer, U., Ishida, E., Taubenberger, S., et al. 2015, The Astronomer's Telegram, 7219

Nugent, P., Kim, A., & Perlmutter, S. 2002, PASP, 114, 803

Ochner, P., Pastorello, A., Benetti, S., et al. 2012, Central Bureau Electronic Telegrams, 3303, 2

Ochner, P., Tomasella, L., Benetti, S., et al. 2015, The Astronomer's Telegram, 7222

Oke, J. B., & Sandage, A. 1968, ApJ, 154, 21

Olling, R. P., Mushotzky, R., Shaya, E. J., et al. 2015, Nature, 521, 332

Osterbrock, D. E., Fulbright, J. P., Martel, A. R., et al. 1996, PASP, 108, 277

Pan, Y.-C., Sullivan, M., Maguire, K., et al. 2014, MNRAS, 438, 1391

Pastorello, A., Mazzali, P. A., Pignata, G., et al. 2007a, MNRAS, 377, 1531

Pastorello, A., Taubenberger, S., Elias-Rosa, N., et al. 2007b, MNRAS, 376, 1301

Pearson, K. 1894, Phil. Trans. Roy. Soc. London, A, 71

Peebles, P. J. E., & Ratra, B. 1988, ApJ, 325, L17

Perlmutter, S., Aldering, G., Goldhaber, G., et al. 1999, ApJ, 517, 565

Perrett, K., Balam, D., Sullivan, M., et al. 2010, AJ, 140, 518

Persson, S. E., Murphy, D. C., Krzeminski, W., Roth, M., & Rieke, M. J. 1998, AJ, 116, 2475

Phillips, M. M. 1993, ApJ, 413, L105

Phillips, M. M., Wells, L. A., Suntzeff, N. B., et al. 1992, AJ, 103, 1632

Phillips, M. M., Krisciunas, K., Suntzeff, N. B., et al. 2006, AJ, 131, 2615

Phillips, M. M., Li, W., Frieman, J. A., et al. 2007, PASP, 119, 360

Pignata, G., Maza, J., Hamuy, M., et al. 2008, Central Bureau Electronic Telegrams, 1545

Planck Collaboration, Ade, P. A. R., Aghanim, N., et al. 2016, A&A, 594, A13

Ponder, K. A., Wood-Vasey, W. M., & Zentner, A. R. 2016, ApJ, 825, 35

Rau, A., Kulkarni, S. R., Law, N. M., et al. 2009, PASP, 121, 1334

Rest, A., Scolnic, D., Foley, R. J., et al. 2014, ApJ, 795, 44

Rich, D., Dennefeld, M., Pizzella, A., et al. 2012a, Central Bureau Electronic Telegrams, 3227, 2

Rich, D., Koff, R. A., Koishikawa, M., et al. 2012b, Central Bureau Electronic Telegrams, 3303, 1

Riess, A. G., Press, W. H., & Kirshner, R. P. 1996, ApJ, 473, 88

Riess, A. G., Filippenko, A. V., Challis, P., et al. 1998, AJ, 116, 1009

Rigault, M., Copin, Y., Aldering, G., et al. 2013, A&A, 560, A66

Rigault, M., Aldering, G., Kowalski, M., et al. 2015, ApJ, 802, 20

Roman, M., Hardin, D., Betoule, M., et al. 2017, ArXiv e-prints, arXiv:1706.07697

Rubin, D., Aldering, G., Barbary, K., et al. 2015, ApJ, 813, 137

Saintonge, A., Giovanelli, R., Haynes, M. P., et al. 2008, AJ, 135, 588

Sako, M., Bassett, B., Becker, A. C., et al. 2014, ArXiv e-prints, arXiv:1401.3317

Sánchez Almeida, J., Aguerri, J. A. L., Muñoz-Tuñón, C., & Huertas-Company, M. 2011, ApJ, 735, 125

Scannapieco, E., & Bildsten, L. 2005, ApJ, 629, L85

Schlafly, E. F., & Finkbeiner, D. P. 2011, ApJ, 737, 103

Schwarz, G. 1978, Ann. Statist., 6, 461

Scolnic, D., Rest, A., Riess, A., et al. 2014, ApJ, 795, 45

SDSS Collaboration, Albareti, F. D., Allende Prieto, C., et al. 2016, ArXiv e-prints, arXiv:1608.02013

Sersic, J. L. 1968, Atlas de galaxias australes

Shimasaku, K., Fukugita, M., Doi, M., et al. 2001, AJ, 122, 1238

Shivvers, I., & Filippenko, A. V. 2014, Central Bureau Electronic Telegrams, 3996

Shivvers, I., Zheng, W., Van Dyk, S. D., et al. 2017, ArXiv e-prints, arXiv:1704.04316

Silverman, J. M., Vinko, J., Quimby, R., et al. 2013, Central Bureau Electronic Telegrams, 3470, 1

Skrutskie, M. F., Cutri, R. M., Stiening, R., et al. 2006, AJ, 131, 1163

Smee, S. A., Barkhouser, R. H., Scharfstein, G. A., et al. 2011, PASP, 123, 87

Smith, K. W., Wright, D., Smartt, S. J., et al. 2015, The Astronomer's Telegram, 7212

Spergel, D., Gehrels, N., Baltay, C., et al. 2015, ArXiv e-prints, arXiv:1503.03757

Spiegelhalter, D. J., Best, N. G., Carlin, B. P., & van der Linde, A. 2002, Journal of the Royal Statistical Society, 64, 583

Stanishev, V., Goobar, A., Benetti, S., et al. 2007, A&A, 469, 645

Stanishev, V., Goobar, A., Amanullah, R., et al. 2015, ArXiv e-prints, arXiv:1505.07707

Stoughton, C., Lupton, R. H., Bernardi, M., et al. 2002, AJ, 123, 485

Strateva, I., Ivezić, Ž., Knapp, G. R., et al. 2001, AJ, 122, 1861

Stritzinger, M. D., Phillips, M. M., Boldt, L. N., et al. 2011, AJ, 142, 156

Sugiura, N. 1978, Commun. Stat. A-Theor., 7, 13

Sullivan, M., Le Borgne, D., Pritchet, C. J., et al. 2006, ApJ, 648, 868

Sullivan, M., Conley, A., Howell, D. A., et al. 2010, MNRAS, 406, 782

Taubenberger, S., Klauser, M., Hachinger, S., et al. 2011, Central Bureau Electronic Telegrams, 2871, 3

Theureau, G., Bottinelli, L., Coudreau-Durand, N., et al. 1998, A&AS, 130, 333

Theureau, G., Coudreau, N., Hallet, N., et al. 2005, A&A, 430, 373

Tonry, J. L., Stubbs, C. W., Lykke, K. R., et al. 2012, ApJ, 750, 99

Tremonti, C. A., Heckman, T. M., Kauffmann, G., et al. 2004, ApJ, 613, 898

Tripp, R. 1998, A&A, 331, 815

Walton, N., Fraser, M., Blagorodnova, N., et al. 2014, The Astronomer's Telegram, 5970

Webbink, R. F. 1984, ApJ, 277, 355

Weinberg, D. H., Mortonson, M. J., Eisenstein, D. J., et al. 2013, Phys. Rep., 530, 87

Weyant, A., Wood-Vasey, W. M., Allen, L., et al. 2014, ApJ, 784, 105

Weyant, A., Wood-Vasey, W. M., Joyce, R., et al. 2017, ArXiv e-prints, arXiv:1703.02402

Whelan, J., & Iben, Jr., I. 1973, ApJ, 186, 1007

Wolf, R. C., D'Andrea, C. B., Gupta, R. R., et al. 2016, ApJ, 821, 115

Wood, C. M., Bershady, M. A., Eigenbrot, A. D., et al. 2012, in Proc. SPIE, Vol. 8446, Ground-based and Airborne Instrumentation for Astronomy IV, 84462W

Wood-Vasey, W. M., Miknaitis, G., Stubbs, C. W., et al. 2007, ApJ, 666, 694

Wood-Vasey, W. M., Friedman, A. S., Bloom, J. S., et al. 2008, ApJ, 689, 377

Woods, D. F., Geller, M. J., & Barton, E. J. 2006, AJ, 132, 197

Wright, D., Chen, T.-W., Fraser, M., et al. 2012, The Astronomer's Telegram, 4516

Zaggia, S., Tomasella, L., Benetti, S., et al. 2012, Central Bureau Electronic Telegrams, 3272, 2

Zanutta, A., Landoni, M., Bianco, A., et al. 2013, Central Bureau Electronic Telegrams, 3654, 1

Zentner, A. R., & Bhattacharya, S. 2009, ApJ, 693, 1543

Zhan, H., & Tyson, J. A. 2017, ArXiv e-prints, arXiv:1707.06948

Zhang, T., Chen, J., Wang, X., Lin, L., & Kong, X. 2011a, Central Bureau Electronic Telegrams, 2871, 4

Zhang, T., Zhou, X., Zhou, L., et al. 2013, Central Bureau Electronic Telegrams, 3470, 1

Zhang, T.-M., Zhang, J.-J., & Wang, X.-F. 2011b, Central Bureau Electronic Telegrams, 2901, 2